

VOLUME 78 NOVEMBER 21, 1974 ✓ NUMBER 24

JPCHAX

THE JOURNAL OF

PHYSICAL

CHEMISTRY

PUBLISHED BIWEEKLY BY THE AMERICAN CHEMICAL SOCIETY

THE JOURNAL OF PHYSICAL CHEMISTRY

BRYCE CRAWFORD, Jr., *Editor*

WILMER G. MILLER, *Associate Editor*

ROBERT W. CARR, Jr., **FREDERIC A. VAN-CATLEDGE,** *Assistant Editors*

EDITORIAL BOARD: A. O. ALLEN (1970-1974), C. A. ANGELL (1973-1977), F. C. ANSON (1974-1978), V. A. BLOOMFIELD (1974-1978), J. R. BOLTON (1971-1975), L. M. DORFMAN (1974-1978), M. FIXMAN (1970-1974), H. S. FRANK (1970-1974), R. R. HENTZ (1972-1976), W. J. KAUZMANN (1974-1978), R. L. KAY (1972-1976), D. W. McCLURE (1974-1978), R. M. NOYES (1973-1977), J. A. POPLE (1971-1975), B. S. RABINOVITCH (1971-1975), H. REISS (1970-1974), S. A. RICE (1969-1975), F. S. ROWLAND (1973-1977), R. L. SCOTT (1973-1977), A. SILBERBERG (1971-1975), J. B. STOTHERS (1974-1978), W. A. ZISMAN (1972-1976)

AMERICAN CHEMICAL SOCIETY, 1155 Sixteenth St., N.W., Washington, D. C. 20036

Books and Journals Division

JOHN K. CRUM *Director*

RUTH REYNARD *Assistant to the Director*

CHARLES R. BERTSCH *Head, Editorial Processing Department*

D. H. MICHAEL BOWEN *Head, Journals Department*

BACIL GUILLEY *Head, Graphics and Production Department*

SELDON W. TERRANT *Head, Research and Development Department*

©Copyright, 1974, by the American Chemical Society. Published biweekly by the American Chemical Society at 20th and Northampton Sts., Easton, Pa. 18042. Second-class postage paid at Washington, D. C., and at additional mailing offices.

All manuscripts should be sent to *The Journal of Physical Chemistry*, Department of Chemistry, University of Minnesota, Minneapolis, Minn. 55455.

Additions and Corrections are published once yearly in the final issue. See Volume 77, Number 26 for the proper form.

Extensive or unusual alterations in an article after it has been set in type are made at the author's expense, and it is understood that by requesting such alterations the author agrees to defray the cost thereof.

The American Chemical Society and the Editor of *The Journal of Physical Chemistry* assume no responsibility for the statements and opinions advanced by contributors.

Correspondence regarding accepted copy, proofs, and reprints should be directed to Editorial Processing Department, American Chemical Society, 20th and Northampton Sts., Easton, Pa. 18042. Department Head: CHARLES R. BERTSCH. Assistant Department Head: MARIANNE C. BROGAN. Assistant Editor: CELIA B. McFARLAND. Editorial Assistant: JOSEPH E. YURVATI.

Advertising Office: Centcom, Ltd., 50 W. State St., Westport, Conn. 06880.

Business and Subscription Information

Send all new and renewal subscriptions with payment to: Office of the Controller, 1155 16th Street, N.W., Washington, D. C. 20036. Subscriptions should be renewed promptly to avoid a break in your

series. All correspondence and telephone calls regarding changes of address, claims for missing issues, subscription service, the status of records, and accounts should be directed to Manager, Membership and Subscription Services, American Chemical Society, P.O. Box 3337, Columbus, Ohio 43210. Telephone (614) 421-7230.

On changes of address, include both old and new addresses with ZIP code numbers, accompanied by mailing label from a recent issue. Allow four weeks for change to become effective.

Claims for missing numbers will not be allowed (1) if loss was due to failure of notice of change in address to be received before the date specified, (2) if received more than sixty days from date of issue plus time normally required for postal delivery of journal and claim, or (3) if the reason for the claim is "issue missing from files."

Subscription rates (1974): members of the American Chemical Society, \$20.00 for 1 year; to nonmembers, \$60.00 for 1 year. Those interested in becoming members should write to the Admissions Department, American Chemical Society, 1155 Sixteenth St., N.W., Washington, D. C. 20036. Postage to Canada and countries in the Pan-American Union, \$5.00; all other countries, \$6.00. Air freight rates available on request. Single copies for current year: \$3.00. Rates for back issues from Volume 56 to date are available from the Special Issues Sales Department, 1155 Sixteenth St., N.W., Washington, D. C. 20036.

Subscriptions to this and the other ACS periodical publications are available on microfilm. Supplementary material not printed in this journal is now available in microfiche form on a current subscription basis. For information on microfilm or microfiche subscriptions, write Special Issues Sales Department at the address above.

THE JOURNAL OF PHYSICAL CHEMISTRY

Volume 78, Number 24 November 21, 1974

JPCHAx 78(24) 2417-2526 (1974)

ISSN 0022-3654

Reactions of CH_3O_2 with NO and NO_2	R. Simonaitis* and Julian Heicklen	2417
Ion-Molecule Reactions in Methylsilane	T. M. Mayer and F. W. Lampe*	2422
Kinematics of Hydride Transfer Reactions in Methylsilane	T. M. Mayer and F. W. Lampe*	2429
Ion-Molecule Reactions in Monosilane-Ethylene Mixtures	T. M. Mayer and F. W. Lampe*	2433
Inelastic Scattering of Vibrationally Excited Potassium Bromide by Polyatomic Partners F. F. Crim, H. B. Bente, and G. A. Fisk*		2438
Photochemistry in the Adsorbed Layer. I. Photolyses of the Alkyl Ketones in the Presence of Nitric Oxide Yutaka Kubokawa* and Masakazu Anpo		2442
Photochemistry in the Adsorbed Layer. II. Energy Transfer in the Adsorbed Layer Masakazu Anpo and Yutaka Kubokawa*		2446
Dissociation Field Effect and Temperature-Jump Kinetics of Ethanolic and Aqueous Phenolphthalein M. S. Massey, Jr., and Z. A. Schelly*		2450
Energy Level Structure and Mobility of Excess Electrons in γ -Irradiated 5 M Potassium Carbonate Aqueous Glasses. Effect of Ions on Trapped and Mobile Electrons in Aqueous Glasses Shoji Noda and Larry Kevan*		2454
Interactions of Aqueous Electrolytes with Nonelectrolytes. The Enthalpy of Dilution of Urea and <i>tert</i> -Butyl Alcohol in Salt Solutions R. B. Cassel and R. H. Wood*		2460■
Heat of Mixing Aqueous Nonelectrolytes at Constant Molality. Sucrose, Urea, and Glycine R. B. Cassel and R. H. Wood*		2465
Theory of Micelle Formation in Aqueous Solutions Charles Tanford		2469
Micelle Formation by Ionic Surfactants. II. Specificity of Head Groups, Micelle Structure Dirk Stigter		2480
Oxidation of Titanium, Tantalum, and Niobium Films by Oxygen and Nitrous Oxide Jalal M. Saleh* and Mohammed Hashim Matloob		2486
Nitric Oxide and Carbon Monoxide Chemisorption on Cobalt-Containing Spinel H. C. Yao* and M. Shelef		2490
Studies of Compound Formation on Alkali/ γ -Aluminum Oxide Catalyst Systems Using Chromium, Iron, and Manganese Luminescence W. H. J. Stork* and G. T. Pott		2496
Nitrogen-15 Nuclear Magnetic Resonance Spectroscopy. Nitrogen-15 Chemical Shifts Determined from Natural-Abundance Spectra John P. Warren and John D. Roberts*		2507
Electron Nuclear Double Resonance Study of 9-Arylxanthyl Radicals Yoshio Yamada,* Sadaharu Toyoda, and Koji Ouchi		2512■
Bubble Solution Method for Diffusion Coefficient Measurements. An Experimental Evaluation William F. Pfeiffer* and Irvin M. Krieger		2516
Conductance Studies of the Alkali Metal Chlorides in Aluminum Chloride-Propylene Carbonate Solution Jacob Jorne* and Charles W. Tobias		2521

COMMUNICATIONS TO THE EDITOR

- Effect of Surface-Active Materials in Water on Ortho-Positronium Lifetime and Its Connection
to the Bubble Model **Béla Lévy*** and **Attila Vértes** 2526

■ Supplementary material for this paper is available separately, in photocopy or microfiche form. Ordering information is given in the paper.

* In papers with more than one author, the asterisk indicates the name of the author to whom inquiries about the paper should be addressed.

AUTHOR INDEX

- | | | | |
|---------------------------|--------------------------------|-----------------------|-------------------------|
| Anpo, M., 2442, 2446 | Kevan, L., 2454 | Ōuchi, K., 2512 | Stork, W. H. J., 2496 |
| Bente, H. B., 2438 | Krieger, I. M., 2516 | Pfeiffer, W. F., 2516 | Tanford, C., 2469 |
| Cassel, R. B., 2460, 2465 | Kubokawa, Y., 2442, 2446 | Pott, G. T., 2496 | Tobias, C. W., 2521 |
| Crim, F. F., 2438 | Lampe, F. W., 2422, 2429, 2433 | Roberts, J. D., 2507 | Toyoda, S., 2512 |
| Fisk, G. A., 2438 | Lévy, B., 2526 | Saleh, J. M., 2486 | Vértes, A., 2526 |
| Heicklen, J., 2417 | Massey, M. S., Jr., 2450 | Schelly, Z. A., 2450 | Warren, J. P., 2507 |
| Jorne, J., 2521 | Matloob, M. H., 2486 | Shelef, M., 2490 | Wood, R. H., 2460, 2465 |
| | Mayer, T. M., 2422, 2429, 2433 | Simonaitis, R., 2417 | Yamada, Y., 2512 |
| | Noda, S., 2454 | Stigter, D., 2480 | Yao, H. C., 2490 |

THE JOURNAL OF PHYSICAL CHEMISTRY

Registered in U. S. Patent Office © Copyright, 1974, by the American Chemical Society

VOLUME 78, NUMBER 24 NOVEMBER 21, 1974

Reactions of CH_3O_2 with NO and NO_2

R. Simonaitis* and Julian Heicklen

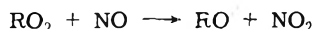
Department of Chemistry, Ionosphere Research Laboratory and Center for Air Environment Studies, The Pennsylvania State University, University Park, Pennsylvania 16802 (Received December 14, 1973; Revised Manuscript Received August 1, 1974)

Publication costs assisted by the National Science Foundation

The reactions of CH_3O_2 radicals with NO and NO_2 were examined at 25° . The CH_3O_2 radicals were produced from the photolysis of $\text{N}_2\text{O}-\text{CH}_4-\text{O}_2$ mixtures at 2139 Å. With NO present NO_2 and CH_3ONO were produced with no induction period and initial quantum yields of $\Phi\{\text{NO}_2\} = 1.43 \pm 0.13$ and $\Phi\{\text{CH}_3\text{ONO}\} = 1.5$. Therefore it is deduced that when NO reacts with CH_3O_2 , $80 \pm 15\%$ of the reaction proceeds *via* $\text{CH}_3\text{O}_2 + \text{NO} \rightarrow \text{CH}_3\text{O} + \text{NO}_2$ (1a). When both NO and NO_2 are present, $\Phi\{\text{NO}_2\}$ can either increase or decrease depending on the ratio $[\text{NO}]/[\text{NO}_2]$. For a ratio of about 0.85, $\Phi\{\text{NO}_2\} = 0$, from which it could be concluded that $k_{1a}/k_3 = 2.2$ where reaction 3 is the reaction between NO_2 and CH_3O_2 . The quantum yield of NO_2 removal of 2.15 when NO was absent showed that NO_3 could not be important in this system and that the two possible channels for reaction 3 are $\text{CH}_3\text{O}_2 + \text{NO}_2 \rightarrow \text{CH}_3\text{O}_2\text{NO}_2$ (3a) and $\text{CH}_3\text{O}_2 + \text{NO}_2 \rightarrow \text{CH}_2\text{O} + \text{HONO}_2$ (3b).

Introduction

The reactions between alkylperoxy radicals and nitrogen oxides are believed to be important in polluted atmosphere chemistry. Of particular importance is the suspected reaction of RO_2 with NO

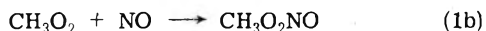


which has been postulated to be responsible for the chain conversion of NO to NO_2 .¹ The methylperoxy radical is also an important constituent in the stratosphere, where it is produced from CH_4 oxidation, and may play a role in the overall O_3 balance of the stratosphere.

In spite of the importance of these reactions only one laboratory study of the reactions of CH_3O_2 with NO and NO_2 has been performed.² Contrary to every expectation from atmospheric chemistry models as well as smog chamber results, no evidence was found for the all-important reaction



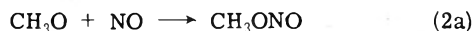
Instead the results indicated that the competing reaction paths



and



were important with reaction 1b occurring $60 \pm 10\%$ of the time, reaction 1c occurring $40 \pm 10\%$ of the time, and reaction 1a occurring $<2\%$ of the time. The conclusion of Spicer, *et al.*,² that reaction 1a is unimportant was based on the absence of CH_3ONO as a reaction product. If reaction 1a had been important, then CH_3ONO should have been produced *via*



The reaction of CH_3O_2 with NO_2 was found² to produce CH_3ONO_2 $75 \pm 5\%$ of the time from which Spicer, *et al.*, concluded that the reaction steps were



and



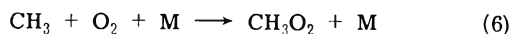
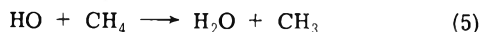
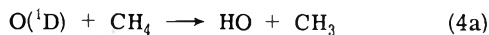
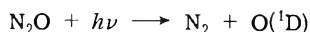
The $\text{CH}_3\text{O}_2\text{NO}_2$ presumably converted to CH_3ONO_2 all the time so that $k_{3a}/k_3 = 0.75$. The third alternative



was considered to be unimportant because it is endothermic by ~ 4.5 kcal/mol.

Because of the unexpected results found in the earlier work performed in our research group² we have continued studies on these systems.

We have now reexamined these important reactions in a different system than used by Spicer, *et al.*² They used $\text{CH}_3\text{N}_2\text{CH}_3$ and CH_3I photooxidation as CH_3O_2 sources and analyzed for CH_3ONO_2 and CH_3ONO by gas chromatography and mass spectroscopy. In the system used in our study presented here, NO_2 is analyzed photometrically and CH_3ONO and CH_3ONO_2 are analyzed by gas chromatography. The CH_3O_2 is produced *via* the sequence of reactions



The results reported here complement and partly supercede those of Spicer, *et al.* One very important difference is that CH_3ONO is found in the CH_3O_2 -NO system in this study whereas it was not found in the previous work. Thus the relative importance of reactions 1a and 1b is reversed.

Experimental Section

Mixtures of N_2O , CH_4 , O_2 , and NO or NO_2 or both are irradiated at 2139 Å and 25°, and the NO_2 monitored photometrically. The detailed experimental procedure has been described previously for the system in which H_2 replaced CH_4 .^{3,4} For some runs the reaction mixture was analyzed for CH_3ONO and CH_3ONO_2 by gas chromatography with a 10 ft \times 1/4 in. propylene carbonate column. For CH_3ONO analysis the column was maintained at 0°, whereas for CH_3ONO_2 analysis the column temperature was 69°.

Actinometry was done in separate experiments by either photolysis of N_2O and monitoring the N_2 produced,³ or by using H_2 in place of CH_4 and monitoring NO_2 . In the absence of NO the quantum yield of NO_2 removal in the H_2 system is 2.0.⁴

The CH_4 used here was ultra-high-purity grade from the Matheson Co., and was used without further purification. Methyl nitrite was prepared by the dropwise addition of 50% H_2SO_4 to a saturated solution of NaNO_2 in 75% methyl alcohol-water solution. The product was purified by fractional distillation from a trap at -130° to a trap maintained at -196°. The identity of the product was verified by mass spectral analysis.

Results

Reaction of CH_3O_2 with NO. Irradiation of mixtures of N_2O - O_2 - CH_4 in the presence of small amounts of NO at 2139 Å and 25° leads to the production of NO_2 with no induction period, CH_3ONO , and small amounts of CH_3ONO_2 . The NO_2 pressure initially rises linearly with time but as the reaction proceeds the rate decreases and a maximum in the NO_2 pressure is reached at about one-third of the initial NO pressure. On further irradiation the NO_2 is consumed at nearly a constant rate until the NO_2 is exhausted. Figure 1 shows a plot of the NO_2 pressure *vs.* irradiation time for a typical run. Values for the initial rate of NO_2 formation, $+\Phi_i\{\text{NO}_2\}$, the final rate of NO_2 removal, $-\Phi_f\{\text{NO}_2\}$, and the corresponding quantum yields are given in Table I.

Examination of Table I shows that $+\Phi_i\{\text{NO}_2\}$ and $-\Phi_f\{\text{NO}_2\}$ are each independent of changes in O_2 and initial NO pressures, which were varied from 3.3 to 36 torr and from 23 to 173 mTorr, respectively. The average value of $+\Phi_i\{\text{NO}_2\}$ is 1.44 ± 0.2 and the average value of $-\Phi_f\{\text{NO}_2\}$ is

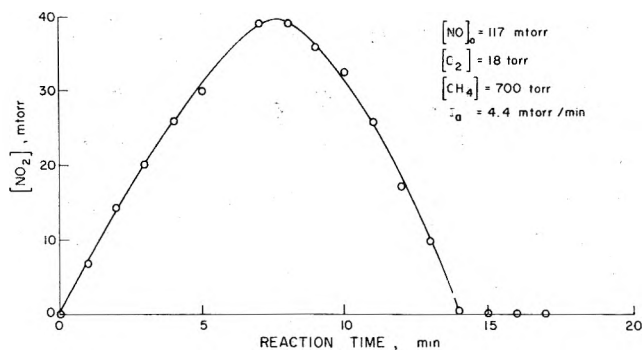


Figure 1. Plot of $[\text{NO}_2]$ *vs.* reaction time in the photolysis of N_2O - O_2 - CH_4 mixtures in the presence of small amounts of NO at 25° and 2139 Å.

2.1 ± 0.3 . $+\Phi_i\{\text{NO}_2\}$ may be somewhat lower at the highest NO pressures, the average value for $[\text{NO}]_0 > 150$ mTorr being about 1.2. A few runs were done at lower absorbed light intensity, I_a , and lower N_2O pressures. Measurement errors increased significantly at lower I_a and lower $[\text{N}_2\text{O}]$ due to the slower rate of photolysis so that the slightly higher than average values of $+\Phi_i\{\text{NO}_2\}$ observed are not significant.

The quantum yields of CH_3ONO and CH_3ONO_2 production as a function of time, but otherwise similar conditions, are presented in Table II. It is evident that $\Phi\{\text{CH}_3\text{ONO}\}$ declines and $\Phi\{\text{CH}_3\text{ONO}_2\}$ increases with the time of irradiation, however, the sum is approximately constant. Clearly CH_3ONO_2 is a secondary product of the reaction of CH_3O_2 with NO (see below).

A few qualitative runs were done with azomethane- O_2 mixtures as the source of CH_3O_2 radicals² and the products analyzed for CH_3ONO . In this system also CH_3ONO was found to be a product, contrary to the observations of Spicer, *et al.*² In the present paper a different chromatographic technique was employed, which presumably accounts for the difference between the present results and those of Spicer, *et al.* We observed that with the Spicer, *et al.*, chromatographic conditions the lower limit for CH_3ONO detection was considerably greater than claimed by them. In a typical run a mixture of 6.6 Torr of azomethane, 150 mTorr of NO, and 10 Torr of O_2 irradiated for 30 sec with a medium-pressure Hg lamp (effective radiation mainly at 3660 Å) gave 24 mTorr of CH_3ONO . Since the absorbed light intensity was determined to be 80 mTorr/min, $\Phi\{\text{CH}_3\text{ONO}\} \sim 0.6$. The conversion in this particular experiment approximately corresponds to the 21-min run in Table II. The agreement between the quantum yields is satisfactory.

Reaction of CH_3O_2 with NO_2 . Irradiation of mixtures of N_2O - O_2 - CH_4 in the presence of small amounts of NO_2 at 2139 Å and 25° leads to the consumption of NO_2 and the production of CH_3ONO_2 . That CH_3ONO_2 is a major product is in agreement with the results of Spicer, *et al.*² Figure 2 shows a plot of the NO_2 pressure *vs.* irradiation time for an experiment in which the initial NO_2 pressure, $[\text{NO}_2]_0$, was 50 mTorr. The consumption is linear with irradiation time down to 2–3 mTorr of NO_2 pressure. Values for $-\Phi_f\{\text{NO}_2\}$ are presented in Table III, $-\Phi_f\{\text{NO}_2\}$ appears to be approximately independent of the changes in the initial NO_2 and O_2 pressures. The average value of $-\Phi_f\{\text{NO}_2\}$ is 2.1 ± 0.3 in agreement with the value obtained in the experiments where NO is initially present.

Extensive measurements of CH_3ONO_2 production were not made because presumably the results of Spicer, *et al.*,

TABLE I: Quantum Yields for NO₂ from the Reaction of CH₃O₂ with NO^a

[NO] ₀ , mTorr	[O ₂], Torr	I _a , mTorr/min	+R _i {NO ₂ }, mTorr/min	-R _r {NO ₂ }, mTorr/min	+Φ _i {NO ₂ } ^b	-Φ _r {NO ₂ } ^b
23	10.5	4.40	6.2	8.0	1.45	1.90
32	12.0	2.85	4.3	5.3	1.50	1.86
34	23	2.42	4.2	3.9	1.74	1.61
42	15	2.90	3.0	5.5	1.20	2.1
43	22	2.55	4.3	5.9	1.64	2.3
44	8.0	2.42	3.6	3.9	1.48	1.61
51	18	4.45	6.6		1.38	
54	13	2.90	4.3		1.70	
57	36	4.40	6.5	12.0	1.50	2.70
57	16	4.60	5.9	9.0	1.39	2.10
59	21	4.40	5.5	8.9	1.34	2.16
59	6.7	2.55	3.3	5.5	1.30	2.16
61	3.3	4.40	6.6		1.52	
65	13	4.35	6.0	8.4	1.41	1.96
67	7.4	4.40	6.2	10.8	1.33	2.37
72 ^c	7.1	0.61	1.1		1.72	
78 ^d	12	1.80	3.0	4.0	1.66	2.20
78	16	4.45	6.1	7.9	1.42	1.78
80	14	2.85	3.7	6.3	1.27	2.20
85	14	2.90	4.1	5.0	1.57	1.95
93	14	2.90	3.3	5.3	1.30	2.10
95	6.0	4.40	5.7		1.48	
103	14	4.35	5.8	8.85	1.45	2.22
117	18	4.40	6.1	9.2	1.46	2.20
125	17	2.42	3.2		1.33	
133	11	2.85	3.9	6.5	1.38	2.30
155	14	2.90	3.5	5.4	1.35	2.00
160	10	4.45	4.9	7.9	1.10	1.78
173	11.5	2.85	3.65	6.0	1.30	2.15
173	5.5	2.65	3.2	6.0	1.15	2.26

^a [CH₄] = 700 ± 20 Torr; [N₂O] = 55 ± 5 Torr. ^b Φ's corrected for small differences in [N₂O]. ^c [N₂O] = 8.1 Torr. ^d [N₂O] = 24 Torr.

TABLE II: Quantum Yields for CH₃ONO and CH₃ONO₂ from the Reaction of CH₃O₂ with NO^a

[NO] ₀ , mTorr	[O ₂], Torr	I _a , mTorr/min	Irradiation time, min	Φ{CH ₃ ONO}	Φ{CH ₃ ONO ₂ }
108	16	3.3	4.0	1.3	
180	17	3.3	4.0	1.3	
205	21	2.8	8.0	1.1	
175	14	3.3	9.0	1.1	
160	22	3.2	21.0	0.69	
170	16	3.0	8.0		0.23
179	16	3.5	30.0		0.77

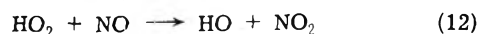
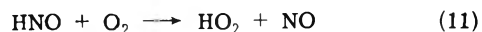
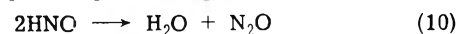
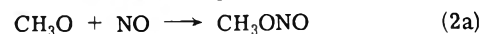
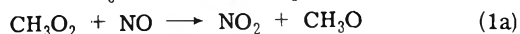
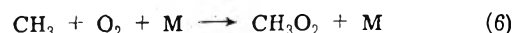
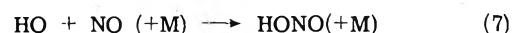
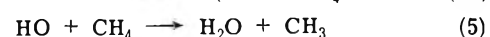
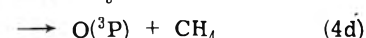
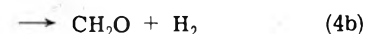
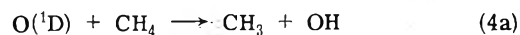
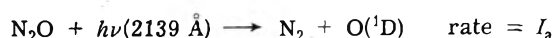
^a [N₂O] = 55 ± 5 Torr, [CH₄] = 680 ± 20 Torr.

are correct. However, it was noted that Φ{CH₃ONO₂} is between 1 and 2 in agreement with Spicer, *et al.*, who obtained Φ{CH₃ONO₂} = 1.4 ± 0.2.

Reaction of CH₃O₂ with NO and NO₂ Mixtures. Three runs were done in which both NO and NO₂ were initially present. Table IV presents the values of Φ_i{NO₂} and -Φ_r{NO₂}. It is apparent that as the [NO]₀/[NO₂]₀ ratio declines Φ_i{NO₂} goes from positive to negative. It is estimated from linear interpolation that Φ_i{NO₂} = 0 at [NO]₀/[NO₂]₀ = 0.85. The average value for -Φ_r{NO₂} is 2.2 in close agreement with the experiments in which only NO or NO₂ is initially present.

Discussion

CH₃O₂ + NO. In experiments with NO₂ initially absent, the initial stages of the reaction can be discussed in terms of the following mechanism



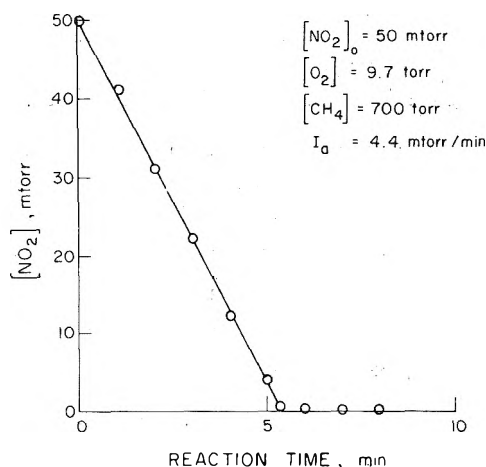


Figure 2. Plot of $[\text{NO}_2]$ vs. time in the photolysis of $\text{N}_2\text{O}-\text{O}_2-\text{CH}_4$ mixtures in the presence of small amounts of NO_2 at 25° and 2139 Å.

TABLE III: Reaction of CH_3O_2 with NO_2^a

$[\text{NO}_2]_0$, mTorr	$[\text{O}_2]$, Torr	I_a , mTorr/ min	$-R_r$, $\{\text{NO}_2\}$, mTorr/ min	$-\Phi_i$, $\{\text{NO}_2\}^b$
12	17.6	4.35	7.7	1.78
12.8	21.6	4.35	7.8	1.93
41	19.6	2.85	7.3	2.37
49	56	4.35	9.2	2.14
50	9.7	4.35	9.4	2.16
53	24.3	4.35	7.2	2.12
102	19.8	4.35	9.3	2.25

^a $[\text{N}_2\text{O}] = 58 \pm 3$ Torr, $[\text{CH}_4] = 700 \pm 20$ Torr. ^b Quantum yields corrected for the small differences in $[\text{N}_2\text{O}]$.

The initial photolytic act together with reactions 4a, 5, and 6 constitute the means of CH_3O_2 production.

The $\text{O}(^1\text{D})$ atoms produced by N_2O photolysis are removed predominantly by reaction with CH_4 , though a small fraction are removed by reaction with N_2O . The relative efficiency for $\text{O}(^1\text{D})$ removal by CH_4 and N_2O is 2.3.⁵⁻⁷ The $[\text{CH}_4]/[\text{N}_2\text{O}]$ ratio used here is 12, so that only 3% of the $\text{O}(^1\text{D})$ are removed by N_2O . Many laboratory experiments have now shown that O_2 is even less efficient than N_2O in removing $\text{O}(^1\text{D})$. Since $[\text{CH}_4]/[\text{O}_2] > 21$ in all experiments, $\text{O}(^1\text{D})$ removal by O_2 is completely negligible.

It is still not certain exactly what fraction of reaction 4 goes via channel 4a. Greenberg and Heicklen⁷ report 95 \pm 5%, but Lin and DeMore⁸ report about 88% with 9% going via channel 4b. However it is clear that a large percentage of the reaction does go through channel 4a, and whether this is 88 or 100% will not significantly influence the results of this study.

The HO radicals produced in reaction 4a react essentially entirely with CH_4 via reaction 5, the rate coefficient being 1.1×10^{-14} ml/sec.⁹ The only possible competing reaction is reaction 7. There is considerable uncertainty in the rate coefficient for this reaction, but at 1 atm pressure at 25° , it is between^{3,10,11} 1.2×10^9 and $1.2 \times 10^{10} \text{ M}^{-1} \text{ sec}^{-1}$. Even if the high value is correct, reaction 7 plays only a minor role since in these studies $[\text{CH}_4]/[\text{NO}] > 4000$, and usually very much greater. The experimental evidence also indicates that reaction 7 is minor since $\Phi_i\{\text{NO}_2\}$ is independent of the NO pressure.

The methyl radicals produced in reactions 4a and 5

might react with either O_2 or NO via reactions 6 and 8, respectively. The respective rate coefficients are $3.6 \times 10^{10} \text{ M}^{-2} \text{ sec}^{-1}$,¹² and $2.4 \times 10^9 \text{ M}^{-1} \text{ sec}^{-1}$.¹³ The lowest $[\text{O}_2]/[\text{NO}]$ ratio used was 32, so that at least 95% of the reaction went via reaction 6.

The current study shows that NO_2 and CH_3ONO are initial products, so that at least part of the time reaction 1a must occur. This conflicts with the conclusion of Spicer, *et al.*,² who based their conclusion on the absence of CH_3ONO . Evidently this conclusion was erroneous since we have found CH_3ONO is also produced when azomethane- O_2 mixtures are the source of CH_3O_2 radicals. Their observation that CH_3ONO_2 was the major product formed with an induction period suggests that it was formed in a secondary reaction with NO_2 just as it is produced in the present system upon extended irradiation.

The CH_3O radicals can be removed by reaction 2 or 9. The relative importance of reactions 2 and 9 can be estimated by comparing the quantities $\Phi_i\{\text{CH}_3\text{ONO}\}k_2/k_{2a}$ and $\Phi_i\{\text{NO}_2\}$. The ratio k_{2a}/k_2 is known to be 0.85^{14,15} and $\Phi_i\{\text{CH}_3\text{ONO}\} = 1.3$. Therefore $\Phi_i\{\text{CH}_3\text{ONO}\}k_2/k_{2a} = 1.52$. Thus reaction 9 is negligible, since $\Phi_i\{\text{NO}_2\} = 1.44$. Furthermore $\Phi_i\{\text{NO}_2\}$ is independent of the $[\text{O}_2]/[\text{NO}]$ ratio, contrary to expectation if reaction 9 was important. These observations are entirely consistent with the measured value for the ratio $k_9/k_2 = 4.7 \times 10^{-5}$,¹⁶ since the highest value of $[\text{O}_2]/[\text{NO}]$ used was 1460.

Similarly, since within experimental error $\Phi_i\{\text{CH}_3\text{ONO}\}k_2/k_{2a} = \Phi_i\{\text{NO}_2\}$ reaction 11 must be unimportant compared to reaction 10. This conclusion is also consistent with the observation that $\Phi_i\{\text{NO}_2\}$ is independent of the O_2 pressure, which was varied by a factor of 10. Furthermore these observations are consistent with the measured value for the ratio k_{10}/k_{11} ¹² = 340 M sec.¹⁶ Calculation shows that even at the highest pressures of O_2 used reaction 11 is <10% of reaction 10.

From the mechanism with reactions 7-9 and 11 omitted, because they are negligible, the following rate laws are obtained

$$\Phi_i\{\text{NO}_2\} = 2k_{4a}k_{1a}/k_4k_1 \quad (a)$$

$$\Phi_i\{\text{CH}_3\text{ONO}\} = 2k_{4a}k_{1a}k_{2a}/k_4k_1k_2 \quad (b)$$

$\Phi_i\{\text{NO}_2\}$ has a mean value of 1.43 with a mean deviation of ± 0.13 . Also k_{4a}/k_4 is between 0.88 and 1.0. If the mean value for $\Phi_i\{\text{NO}_2\}$ is used then k_{1a}/k_1 is computed from eq a to lie between 0.82 and 0.72. The ratio k_{1a}/k_1 can also be estimated from eq b. If the data of Table II for $\Phi_i\{\text{CH}_3\text{ONO}\}$ are linearly extrapolated to zero time, then $\Phi_i\{\text{CH}_3\text{ONO}\}$ becomes 1.50. Since k_{2a}/k_2 is known accurately^{14,15} to be 0.85, then eq b leads to a value for k_{1a}/k_1 lying between 0.88 and 1.0. The former value is more reliable because much more data are available. We conclude that $k_{1a}/k_1 = 0.80 \pm 0.15$. After this manuscript was submitted for publication we became aware of an unpublished study by Finlayson and Pitts¹⁷ who found $k_{1a}/k_1 = 1.0$.

$\text{CH}_3\text{O}_2 + \text{NO}_2$. In the presence of NO_2 the following additional reactions are possible

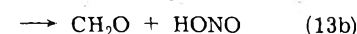
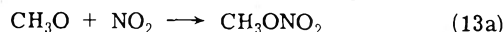
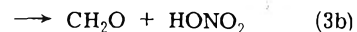
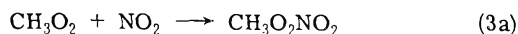


TABLE IV: Reaction of CH₃O₂ with NO and NO₂^a

[NO] ₀ , mTorr	[NO ₂] ₀ , mTorr	[NO] ₀ /[NO ₂] ₀	[O ₂], Torr	R _i {NO ₂ }, mTorr/min	-R _r {NO ₂ }, mTorr/min	Φ _i {NO ₂ } ^b	-Φ _r {NO ₂ } ^b
71	89.5	0.80	17.3	-0.94	8.2	-0.24	2.10
44	46	0.94	23.4	+1.45	10.0	+0.33	2.34
79	23	3.43	11.0	+4.00	9.0	+0.97	2.18

^a [N₂O] = 56 ± 3 Torr, [CH₄] = 700 ± 20 Torr. ^b Φ's corrected for small differences in [N₂O].



The high-pressure limiting rate coefficient for reaction 14 is $18.4 \times 10^9 \text{ M}^{-1} \text{ sec}^{-1}$. Thus under all of our conditions, reaction 14 is negligible.

With reactions 3, 13, and 15 included, but reactions 3c and 16 omitted, the rate law for NO₂ formation becomes

$$\Phi\{\text{NO}_2\} = \left(\frac{k_2[\text{NO}]}{(k_2[\text{NO}] + k_{13}[\text{NO}_2])} - \frac{k_3[\text{NO}_2]}{k_{1a}[\text{NO}]} \right) \times \frac{k_{1a}[\text{NO}]k_{4a}/k_4}{(k_1[\text{NO}] + k_3[\text{NO}_2])} \quad (c)$$

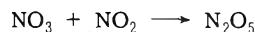
This expression ignores any contribution resulting from reaction 11. However, we saw above that reaction 11 is negligible compared to reaction 10. Any contribution is further reduced here because less HNO is produced since some of the CH₃O radicals are removed by NO₂. Furthermore the HO₂ produced in reaction 11 can both produce NO₂ via reaction 12 or remove NO₂ via reaction 15. These reactions tend to compensate each other, thus further reducing any contribution to net NO₂ production. Equation c shows that the only way Φ_i{NO₂} can become negative is if reaction 3 participates. This would be true even if reaction 11 were included, since without reaction 3, the only removal processes for NO₂ involve CH₃O directly or as a precursor and CH₃O and NO₂ are produced on a 1/1 basis. Thus reaction 3 must occur.

The extinction coefficients for N₂O and NO₂ at 213.9 nm and 25° are 0.090 and 9.00 atm⁻¹ cm⁻¹, respectively. Consequently in the runs in which the initial pressures of NO₂ were about 50 and 100 mTorr as much as 8 and 16% of the light could have been absorbed by the NO₂. The experimental data however do not show any evidence of NO₂ photolysis. The rate of NO₂ removal was constant throughout the whole course of the reaction at all initial pressures of NO₂ (see Figure 2). If NO₂ photolysis was important the rate would have changed as the reaction proceeded. Furthermore there is no clear trend in Φ_r{NO₂} with the initial NO₂ pressure (Table III) or the initial [NO]₀/[NO₂]₀ ratio (Table IV). Thus reaction 16 appears to be unimportant.

With mixtures of NO and NO₂, Φ_i{NO₂} becomes zero for [NO]/[NO₂] = 0.85. The ratio $k_2/k_{13} = 1.2^{16}$ Thus $k_{1a}/k_3 = 2.3$. This result is in contrast to the conclusion of Spicer, *et al.*,² that $k_{1a} \ll k_3$. If we include the possibility that NO₂ is photodecomposing via reaction 16, then the right-hand side of eq c should become zero when Φ_r{NO₂} ~ 0.1, i.e., when [NO]/[NO₂] ~ 0.9. The computed value of k_{1a}/k_3 is reduced to 2.1.

The remaining question is whether reaction 3c can be neglected. This question can be answered affirmatively by examining the results in the absence of NO. If reaction 3c is

included, then additional NO₂ is removed via



and the rate law for NO₂ removal becomes

$$-\Phi_r\{\text{NO}_2\} = \frac{2k_{4a}}{k_4} \left(1 + \frac{2k_{3c}}{k_3} \right) \quad (d)$$

It was observed that -Φ_r{NO₂} = 2.15. Since $k_{4a}/k_4 > 0.88$, $k_{3c}/k_3 < 0.11$, i.e., channel 3c is unimportant. In fact, any mechanism producing NO₃ must be unimportant, since it would tend to give values of -Φ_r{NO₂} much greater than the observed value of 2.15. Thus the route for CH₃O₂NO₂ transformation to CH₃ONO₂ proposed by Spicer, *et al.*, cannot be correct. In conclusion the results here confirm that NO₂ reacts with CH₃O₂, and that channel 3c is unimportant. Our results do not give any evidence on the relative efficiencies of reactions 3a and 3b; presumably the values of Spicer, *et al.*, are correct (i.e., $k_{3a}/k_3 = 0.75 \pm 0.05$). However, the mechanism of conversion of CH₃O₂NO₂ to CH₃ONO₂ is still obscure. Theoretically -Φ_r{NO₂} should be 2.0 rather than 2.15, if reaction 16 is ignored. If reaction 16 is playing some role, then on the average, a quantum yield contribution of 0.25 (3 × 0.08) can be attributed to it. Thus -Φ_r{NO₂} would become slightly less than 2.0.

Acknowledgment. This work was supported by the Atmospheric Sciences Section of the National Science Foundation through Grant No. GA-12385 and the Environmental Protection Agency through Grant No. 800874 for which we are grateful.

References and Notes

- (1) J. Heicklen, K. Westberg, and N. Cohen, "Chemical Reactions in the Upper Atmosphere," C. Tuesday, Ed., American Elsevier, New York, N.Y., 1971, p 55.
- (2) C. W. Spicer, A. Villa, H. A. Wiebe, and J. Heicklen, *J. Amer. Chem. Soc.*, **95**, 13 (1973).
- (3) R. Simonaitis and J. Heicklen, *J. Phys. Chem.*, **77**, 1096 (1973).
- (4) R. Simonaitis and J. Heicklen, *J. Phys. Chem.*, **78**, 653 (1974).
- (5) W. B. DeMore, *J. Phys. Chem.*, **73**, 391 (1969).
- (6) G. Paraskevopoulos and R. J. Cvetanović, *J. Amer. Chem. Soc.*, **91**, 7572 (1969).
- (7) R. I. Greenberg and J. Heicklen, *Int. J. Chem. Kinet.*, **4**, 417 (1972).
- (8) C. L. Lin and W. B. DeMore, *J. Phys. Chem.*, **77**, 863 (1973).
- (9) W. E. Wilson and A. A. Westenberg, *Symp. (Int.) Combust.*, [Proc.], **11th**, 1966, 1143 (1967).
- (10) F. Stuhl and H. Niki, presented at the 10th Informal Conference on Photochemistry, Oklahoma State University, 1972.
- (11) C. Morley and I. W. M. Smith, *J. Chem. Soc., Faraday Trans. 2*, 1016 (1972).
- (12) W. C. Sleppy and J. G. Calvert, *J. Amer. Chem. Soc.*, **81**, 769 (1959).
- (13) N. Basco, D. G. L. James, and R. D. Stuart, *Int. J. Chem. Kinet.*, **2**, 215 (1970).
- (14) G. E. McGraw and H. S. Johnston, *Int. J. Chem. Kinet.*, **1**, 89 (1969).
- (15) H. A. Wiebe and J. Heicklen, *J. Amer. Chem. Soc.*, **95**, 1 (1973).
- (16) H. A. Wiebe, A. Villa, T. M. Hellman, and J. Heicklen, *J. Amer. Chem. Soc.*, **95**, 7 (1973).
- (17) B. Finlayson and J. W. Pitts, Jr., private communication.
- (18) R. Simonaitis and J. Heicklen, *Int. J. Chem. Kinet.*, **4**, 529 (1972).

Ion-Molecule Reactions in Methylsilane¹

T. M. Mayer and F. W. Lampe*

Davey Laboratory, Department of Chemistry, The Pennsylvania State University, University Park, Pennsylvania 16802
(Received April 29, 1974)

Publication costs assisted by the U. S. Atomic Energy Commission

Positive ion-molecule reactions in methylsilane have been investigated by tandem and high-pressure mass spectrometry. Reaction identification and rate constants for exothermic bimolecular reactions of all primary ions have been obtained for reactant ion energies of 1.0 eV in the center-of-mass system. A number of endothermic reactions have been observed. The dominant mode of reaction is that involving the transfer of an H⁺ species, giving CH₃SiH₂⁺ product. It is concluded that, in general, the methyl group does not play an active role in the ionic chemistry of methylsilane, in that there appears to be no scrambling of H atoms bound to the carbon and silicon atoms, and in that H⁺ or H abstraction comes exclusively from the silicon end of the molecule. High-pressure mass spectra, up to 0.3 Torr, reveal a number of termolecular association reactions, the rate constants of which have been measured.

Introduction

Following the rather extensive study of the ion-molecule chemistry of hydrocarbons in the past decade,² hydrides of group IV elements other than carbon have attracted interest in recent years. To date, ion-molecule reactions in monosilane,³⁻⁶ disilane,⁷ monogermane,⁸ and a few mixtures of monosilane and simple organic compounds⁹⁻¹² have received extensive study; simple alkylsilanes^{13,14} have received less extensive examination.

A previous study of positive ion-molecule reactions in methylsilane¹³ performed in this laboratory reported a number of reactions of the CH₃SiH⁺ ion and their rate constants, along with considerable thermochemical information concerning the ions formed by electron impact on methylsilane. This study was carried out in a single source mass spectrometer and was limited to source pressures below 6×10^{-3} Torr. Later studies of several ion-molecule reaction systems^{4,10-12} using ion-cyclotron resonance and high-pressure and tandem mass spectrometry have shown that the low-pressure single-source experiments may be quite incomplete in describing the ion-molecule chemistry of systems containing more than one or two possible reactant ions and neutral reactant molecules. In general the ion-molecule chemistry of the silanes has been much more complex than our earlier studies indicated. Accordingly we have undertaken further studies of the methylsilane system with the intention of presenting a complete picture of the ion-molecule chemistry of methylsilane. The effect of the addition of an alkyl group, and the similarities to the ion-molecule chemistry of monosilane, are of interest to the general behavior of group IV hydrides.

Experimental Section

The tandem mass spectrometer used in this study has been described previously.^{3,6} The apparatus permits injection of mass selected ions having kinetic energies variable down to about 1 eV, with energy spread of about 1 eV, into a collision chamber containing the neutral target gas. Products scattered into the forward direction are collected with an acceptance angle of $\sim 10^\circ$. The collision chamber pressure in all experiments was 1.0×10^{-3} Torr, as measured with a CGS Barocel capacitance manometer. Collection ef-

ficiency of the analyzer was found to be mass dependent over the rather large range of masses involved in this study, and corrections were made for this in the calculation of relative cross sections and rate constants.

Measurements of ionic abundance as a function of source pressure were carried out in a modified Nuclide Associates 12-90G sector field mass spectrometer which has been described previously.³ Pressures in the ion source were measured with a Granville-Phillips capacitance manometer which had been calibrated with a McLeod gauge. The calibration was checked by observing the pressure-dependent formation of CH₅⁺ in methane. The known specific reaction rate¹⁵ indicated that our pressure readings are accurate to within $\pm 10\%$. The ionizing electron energy was 100 eV, and all experiments were carried out with a repeller field of 6.25 V/cm, which lead to free-drift ion-exit energy of 1.9 eV. The temperature of the ion source was about 100° in all experiments.

Methylsilane (CH₃SiH₃), obtained from the Peninsular ChemResearch Company, was fractionated on the vacuum line and checked mass spectrometrically for satisfactory purity. Methylsilane-*d*₃ (CH₃SiD₃) was synthesized by the reduction of CH₃SiCl₃, obtained from Alfa Inorganics, by LiAlD₄ in di-*n*-butyl ether solution.¹⁶ The product was purified in the same manner as methylsilane.

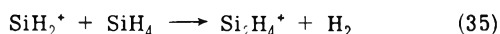
All data were corrected for the presence of ²⁹Si and ³⁰Si isotopes and all data presented represent only ions containing the major ²⁸Si isotope. Corrections for ¹³C isotopes were not made.

Results and Discussion

Electron impact ionization of methylsilane yields nine ions with abundances greater than 3%, all of which can be considered as possible reactant ions. The earlier studies of Potzinger and Lampe¹³ indicated that only the major CH₃SiH⁺ ion and, to a small extent, the minor SiH₂⁺ ions were reactive in this system. All observed product ions were attributed to reactions of these two ions. We have found this to be an incomplete description of the ion-molecule chemistry of this system, and, indeed, all primary ions are found to react with methylsilane. The bimolecular reactions of various primary ions will be discussed in detail fol-

lowed by an analysis of reactions occurring at elevated pressures in the single-source instrument.

Tandem Mass-Spectrometric Studies. Reaction identification and the dependence of reaction cross section on ion energy in the range 0.5–5 eV CM were carried out in the tandem mass spectrometer. Heats of formation of many of the species involved are not known, but the shape of the cross-section curves as a function of energy in general allows one to determine whether a reaction is exo- or endothermic.¹⁷ Exothermic bimolecular reactions observed for the various primary ions with methylsilane are listed in Table I. Specific reaction rates for the reactions in Table I were obtained by measuring relative cross sections for all reactions at 1.0 eV (CM) and comparing these to the cross section obtained for reaction 35



for which the specific reaction rate has been measured.³ The values obtained were checked relative to the formation rates of $(\text{CH}_3)_2\text{SiH}^+$ and $(\text{CH}_3)_2\text{Si}_2\text{H}_2^+$, represented by reactions 5 and 10, and to the total reaction rate of CH_3SiH^+ in the Nuclide mass spectrometer. Rate constants calculated by the two different methods were found to agree within experimental error. Although the collision energy obtaining in the Nuclide mass spectrometer is generally quite a bit lower than the 1.0 eV used in the tandem machine, phenomenological rate constants should be quite insensitive to ion kinetic energy, as predicted by the polarization theory of ion-molecule reactions.² The good agreement between the two greatly different methods of measuring rate constants attests to the validity of this assumption and to the overall internal consistency of this work. Standard enthalpy changes were calculated using existing thermochemical information.^{18,19} The neutral products of all reactions have been written arbitrarily to yield products that give the greatest exothermicity, or require the least amount of rearrangement. In the last column of Table I are listed the results of Potzinger and Lampe¹³ for reactions observed in both studies. The agreement between this work and the earlier results is quite good. It is seen from the table that the earlier study, while giving reliable rate constants, was very incomplete with regard to reaction identification.

Endothermic reactions observed in the range 0.5–5 eV are listed in Table II. Phenomenological rate constants cannot be calculated in the manner used for the exothermic reactions, because the polarization theory does not predict the behavior of cross sections of endothermic reactions. Relative cross sections at 1.0 eV (CM) collision energy are listed and may be compared with the relative cross sections listed in Table I.

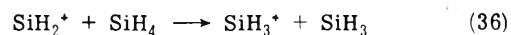
(a) $\text{CH}_2\text{SiH}_2^+$. This ion comprises about 24% of the total ions produced by impact of 100-eV electrons on methylsilane. We write the structure of the ion as such on the basis that the dissociation energy of Si–H bonds are generally lower than the corresponding C–H bonds.²⁰ In the mass spectrum of CH_3SiD_3 the peak at m/e 47, corresponding to $\text{CH}_3\text{SiD}_2^+$, is about ten times as large as the peak at m/e 48, corresponding to $\text{CH}_2\text{SiD}_3^+$; thus we conclude that $\text{CH}_3\text{SiH}_2^+$ is the most probable structure of this ion.

When $\text{CH}_3\text{SiH}_2^+$ is injected into methylsilane we observe two reactions to occur, namely reactions 1 and 2 shown in Table I. Reaction 1 involves the transfer of an H^- ion and yields products identical with the reactants. We were able

to observe this reaction in the tandem mass spectrometer by using CH_3SiD_3 as the target gas. The corresponding reaction of the SiH_3^+ ion in monosilane has been shown⁶ to proceed predominantly via a direct H^- stripping type reaction. This same process in methylsilane- d_3 should lead to products at m/e 47, $\text{CH}_3\text{SiD}_2^+$, and m/e 48, $\text{CH}_2\text{SiD}_3^+$, if the H^- is stripped from the silicon or carbon end of the molecule, respectively. We observe that the bulk of the product lies at m/e 47 with only a very small amount of m/e 48. The virtual absence of m/e 48 in the product spectrum indicates that the hydride which is transferred comes exclusively from the silicon end of the molecule. This fact is undoubtedly due to the hydridic nature of the Si–H bonds²⁰ and is consistent with the observation that H^- transfer is by far the dominant mode of reaction in other silane systems.

Reaction 2 was observed to occur with much smaller cross section than the H^- transfer reaction. Potzinger and Lampe¹³ observed $(\text{CH}_3)_2\text{Si}_2\text{H}_3^+$ as a product ion but were unable to identify correctly its precursor, presumably because $\text{CH}_3\text{SiH}_2^+$ is also a product ion from other reactions, a fact which masked its reactivity in the low-pressure single-source instrument.

(b) CH_3SiH^+ . Potzinger and Lampe¹³ observed this ion to be reactive in CH_3SiH_3 and our measurements are in good agreement with their's for reactions 3–10. This is the major primary ion in methylsilane, comprising about 34% of the 100-eV mass spectrum, and to a large extent its reactions characterize the overall ion-molecule chemistry of the system. Again the net hydride transfer reaction (3) proceeds with large cross section. In monosilane it was pointed out⁶ that the analogous reaction



proceeds through a variety of mechanisms, including H^- transfer, H atom transfer, and an intermediate complex. The details of the dynamics of reaction 3 will be treated in a following paper, but it should be noted that when CH_3SiD_3 is used as a target gas, only trace amounts of $\text{CH}_2\text{SiD}_3^+$ are observed, indicating again that the hydrogens bound to the carbon atom are not involved in the reaction.

In the case of reactions 4 and 5 there is some ambiguity about the identity of the products. An m/e value of 58 can be assigned to either $(\text{CH}_3)_2\text{Si}^+$ or Si_2H_2^+ and m/e 59 can be either $(\text{CH}_3)_2\text{SiH}^+$ or Si_2H_3^+ . As noted by Potzinger and Lampe,¹³ however, reactions leading to Si_2H_2^+ and Si_2H_3^+ have enthalpy changes of –1 and +7 kcal, respectively, while reactions 4 and 5 as written are highly exothermic. Furthermore, when CH_3SiD_3 is used as target gas no ion above m/e 60 is observed, whereas if Si_2H_3^+ was formed, products at m/e 61 and 62 (Si_2HD_2^+ and Si_2D_3^+) would be expected. The large rate constant for reaction 5, probably reflecting the high stability of the $(\text{CH}_3)_2\text{SiH}^+$ ion, is interesting and somewhat suggestive of a direct mechanism for this reaction. It can be seen in Tables I and II that reactions proceeding presumably through a direct mechanism, namely H^- transfer or H atom transfer, generally have rate constants between 5 and 10 times larger than reactions involving a complex formation. The magnitude of the rate of reaction 5 suggests that this may proceed through a direct CH_3 group transfer. Isotopic distribution of the product ions obtained when CH_3SiD_3 is used as a target gas support this conjecture. If, indeed, the hydrogens attached to the carbon are not reactive and reaction 5 proceeds through a randomized complex, then products should be observed at

TABLE I: Exothermic Bimolecular Reactions in CH_3SiH_3

Reaction no.	Reaction	Product m/e	ΔH° , kcal/mol	σ^a	$10^{10}k$, cm^3/sec (this work)	$10^{10}k$, cm^3/sec (ref 13)
1	$\text{CH}_3\text{SiH}_2^+ + \text{CH}_3\text{SiH}_3$					
	$\rightarrow \text{CH}_3\text{SiH}_2^+ + \text{CH}_3\text{SiH}_3$	45	0	13.5	2.9 ± 0.7	
2	$\rightarrow (\text{CH}_3)_2\text{SiH}_2^+ + \text{H}_2$	89		1.14	0.30 ± 0.1	
3	$\text{CH}_3\text{SiH}^+ + \text{CH}_3\text{SiH}_3$					
	$\rightarrow \text{CH}_3\text{SiH}_2^+ + \text{CH}_3\text{SiH}_2$	45	-1	46	9.9 ± 2	6.4
4	$\rightarrow (\text{CH}_3)_2\text{Si}^+ + \text{SiH}_4$	58	-26	3.7	0.74 ± 0.2	0.44
5	$\rightarrow (\text{CH}_3)_2\text{SiH}^+ + \text{SiH}_3$	59	-26	40	8.6 ± 2	3.8
6	$\rightarrow \text{CH}_3\text{Si}_2^+ + \text{CH}_3 + 2\text{H}_2$	71		1.5	0.33 ± 0.1	0.42
7	$\rightarrow \text{CH}_3\text{Si}_2\text{H}_2^+ + \text{CH}_3 + \text{H}_2$	73		4.0	0.90 ± 2	1.0
8	$\rightarrow \text{CH}_3\text{Si}_2\text{H}_3^+ + \text{CH}_4$	74		3.2	0.70 ± 0.4	0.46
9	$\rightarrow (\text{CH}_3)_2\text{Si}_2^+ + 2\text{H}_2$	86		4.8	1.1 ± 0.3	0.46
10	$\rightarrow (\text{CH}_3)_2\text{Si}_2\text{H}_2^+ + \text{H}_2$	88		10.2	2.2 ± 0.6	0.92
	\rightarrow total product production				24.5 ± 6	17.2
11	$\text{CH}_3\text{Si}^+ + \text{CH}_3\text{SiH}_3$					
	$\rightarrow \text{CH}_3\text{SiH}^+ + \text{CH}_3\text{SiH}_2$	44	+30	54	10.8 ± 3	
12	$\rightarrow \text{CH}_3\text{Si}_2\text{CH}_2^+ + 2\text{H}_2$	85		1.6	0.32 ± 0.1	
13	$\rightarrow (\text{CH}_3)_2\text{Si}_2^+ + \text{H}_2 + \text{H}$	86		2.4	0.51 ± 0.1	
14	$\rightarrow (\text{CH}_3)_2\text{Si}_2\text{H}^+ + \text{H}_2$	87		3.0	0.64 ± 0.1	
15	$\rightarrow (\text{CH}_3)_2\text{Si}_2\text{H}_2^+ + \text{H}$	88		1.3	0.28 ± 0.05	
16	$\text{CH}_2\text{Si}^+ + \text{CH}_3\text{SiH}_3$					
	$\rightarrow \text{CH}_2\text{Si}^+ + \text{CH}_3\text{SiH}_2$	43		2.7	0.60 ± 0.2	
17	$\rightarrow \text{CH}_3\text{Si}_2\text{H}_2^+ + \text{CH}_3$	73		5.0	1.1 ± 0.2	
18	$\text{CHSi}^+ + \text{CH}_3\text{SiH}_3$					
	$\rightarrow \text{CH}_2\text{Si}^+ + \text{CH}_3\text{SiH}$	43		8.8	1.9 ± 0.3	
19	$\text{SiH}_3^+ + \text{CH}_3\text{SiH}_3$					
	$\rightarrow \text{CH}_3\text{SiH}_2^+ + \text{SiH}_4$	45	-11	17.5	3.6 ± 0.7	
20	$\text{SiH}_2^+ + \text{CH}_3\text{SiH}_3$					
	$\rightarrow \text{CH}_3\text{SiH}^+ + \text{SiH}_4$	44	-12	3.3	0.84 ± 0.1	
21	$\rightarrow \text{CH}_3\text{SiH}_2^+ + \text{SiH}_3$	45	-11	26.5	6.9 ± 1	
22	$\rightarrow \text{CH}_3\text{Si}_2\text{H}_3^+ + \text{H}_2$	74		2.0	0.52 ± 0.2	
23	$\text{SiH}^+ + \text{CH}_3\text{SiH}_3$					
	$\rightarrow \text{CH}_2\text{Si}^+ + \text{SiH}_4$	43	-22	14	3.6 ± 0.7	
24	$\rightarrow \text{CH}_3\text{Si}_2\text{H}_2^+ + \text{H}_2$	73		36	9.5 ± 2	
25	$\text{Si}^+ + \text{CH}_3\text{SiH}_3$					
	$\rightarrow \text{CH}_3\text{SiH}_2^+ + \text{SiH}$	35	+10	14	3.8 ± 0.8	
26	$\rightarrow \text{CH}_3\text{Si}_2\text{H}^+ + \text{H}_2$	72		23		

^a Relative cross section at 1.0 eV (CM).TABLE II: Endothermic Bimolecular Reactions in CH_3SiH_3

Reaction no.	Reaction	Product m/e	ΔH° , kcal/mol	Relative cross section σ at 1.0 eV CM
27	$\text{CH}_2\text{Si}^+ + \text{CH}_3\text{SiH}_3 \rightarrow \text{CH}_3\text{SiH}^+ + \text{CH}_3\text{SiH}$	44		4.0
28	$\rightarrow \text{CH}_3\text{Si}_2^+ + \text{CH}_3 + \text{H}_2$	71		4.4
29	$\text{CHSi}^+ + \text{CH}_3\text{SiH}_3 \rightarrow \text{CH}_2\text{Si}^+ + \text{CH}_3\text{SiH}_2$	42		51
30	$\rightarrow \text{CH}_3\text{SiH}_2^+ + \text{CH}_2\text{Si}$	45		17.5
31	$\text{SiH}_2^+ + \text{CH}_3\text{SiH}_3 \rightarrow \text{CH}_3\text{Si}_2\text{H}^+ + 2\text{H}_2$	72		2.4
32	$\text{SiH}^+ + \text{CH}_3\text{SiH}_3 \rightarrow \text{CH}_3\text{SiH}_2^+ + \text{SiH}_2$	45	+17	32.5
33	$\rightarrow \text{CH}_3\text{Si}_2^+ + 2\text{H}_2$	71		18
34	$\text{Si}^+ + \text{CH}_3\text{SiH}_3 \rightarrow \text{CH}_3\text{Si}^+ + \text{SiH}_3$	43	+30	66.5

masses 59, $(\text{CH}_3)_2\text{SiH}^+$, and 60, $(\text{CH}_3)_2\text{SiD}^+$, in the ratio 1:3, respectively. Figure 1 shows the observed isotopic products as a function of collision energy. The fact that the product containing hydrogen, $(\text{CH}_3)_2\text{SiH}$, is by far the most abundant in the energy range 1.5 \rightarrow 5.2 eV suggests that this reaction involves a more or less direct transfer of CH_3 from the target to the projectile ion. The inversion of product contributions at low energies is likely due to transition to a mechanism more complex in nature. This type of complex-to-direct mechanism transition has been observed fairly often in ion-molecule reactions.^{21,22} The behavior of isotope distributions above 3 eV is puzzling and we are unable to explain the predominance of the deuterated product at high energies. It should be noted however that the total cross section for product production decreases with

increasing collision energy, and is quite small in the region above 5 eV. Further investigations are needed to resolve this problem.

Reactions 6-8 are observed to be exothermic reactions that presumably proceed through a complex type of mechanism. The neutral products of these reactions are written rather arbitrarily, as either the ones giving greatest exothermicity or requiring the least rearrangement of atoms. The cross sections for reactions 6-8 exhibit unusual behavior as shown in Figure 2. The initial decrease in cross section at low energies is normal behavior for exothermic reactions, however, particularly for reactions 6 and 8 the cross section goes through a minimum at about 1-eV CM energy and then rises to a broad maximum at about 2.2-2.5 eV. This type of behavior is usually indicative of the onset of

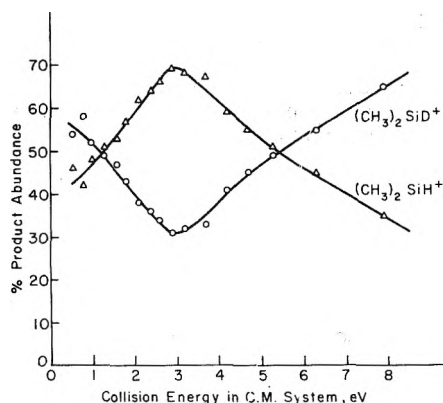


Figure 1. Isotopic distribution of products of reaction 5 using CH_3SiD_3 as target.

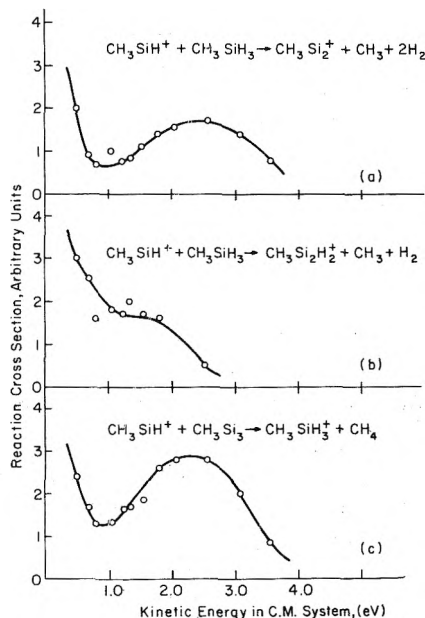


Figure 2. Relative cross sections as a function of collision energy: (a) reaction 6; (b) reaction 7; (c) reaction 8.

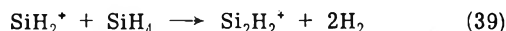
an endothermic channel for the production involved. We suspect that this behavior is due to the dissociation of neutral products. The neutral products of reaction 6 have been written as $\text{CH}_3 + 2\text{H}_2$ but, energetically, $\text{CH}_4 + \text{H}_2 + \text{H}$ are just as plausible. The dissociation of whatever set of neutral molecular products are involved, e.g.



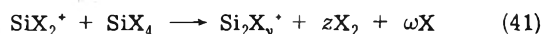
may account for the rise in the cross section of reaction 6. Both processes require about 4-eV energy. Since the heat of formation of CH_3Si_2^+ is not known, we cannot predict a threshold for these processes, but, in any case, the apparent threshold of about 1 eV, evident from Figure 2a, is almost surely too low. The apparent exothermic behavior at low energy may be due to excitation in the reactant ion, but lack of information concerning possible excited states of the reactant ion, and of the energetics of the species involved, preclude further speculation about this reaction. Similar considerations apply to the behavior with energy of the cross section of reaction 8. Reaction 7 exhibits more typical exothermic behavior as shown in Figure 2b. The slight leveling off of cross section at about 1.5 eV may be

indicative of some alternative process taking place, but we do not have enough information to speculate further.

Reactions 9 and 10 are observed as exothermic reactions most probably involving the liberation of hydrogen molecules as neutral products. Measured rate constants for these reactions are in reasonably good agreement with those reported by Potzinger and Lampe. These reactions appear to be analogous to those of the SiH_2^+ ion reported in monosilane,^{3,4} namely



the products of which are the major two-silicon atom products of reaction of SiH_2^+ . It is of interest here to observe the effect of addition of an alkyl group to the molecule. If the methyl group plays an active role in the chemistry of methylsilane, then one would expect that there would be scrambling of the H atoms bound to the carbon and silicon atoms and that H atoms from both should appear among the neutral fragments. The extent of methyl group participation in reactions 9 and 10 can be determined from isotopic labeling of the methylsilane. Tables III and IV give the expected isotopic distribution of product ions of reactions 9 and 10 using CH_3SiD_3 as target gas, assuming first that the methyl groups are intimately involved in the complex, that hydrogen atoms are completely scrambled, and that dissociation of the complex is completely statistical; and second, that the methyl groups are not involved in the chemistry of the complex and the liberated hydrogen comes exclusively from the silicon atoms. The observed isotope distribution at 1.0-eV collision energy for reaction 9, shown in Table III, is in excellent agreement with the second prediction, while the distribution for reaction 10, shown in Table IV, while not as clear, is considerably closer to the second prediction. These observations, together with those for reactions 1 and 3 offer convincing evidence that the methyl group acts as a more-or-less inert unit and does not play a major role in the chemistry of the system. The reactions involving a complex, namely (6)–(10), then appear as the general type reaction



where X is either CH_3 or H and $y + 2z + \omega = 6$. Considered in this fashion, the reactions of the CH_3SiH^+ ion in methylsilane are very similar to those of SiH_2^+ in monosilane.

(c) CH_3Si^+ , CH_2Si^+ , and CHSi^+ . These ions are all relatively minor primary ions comprising 11.2, 5.5, and 3.0%, respectively, of the primary mass spectrum. Reactions of these ions observed to be exothermic are listed in Table I. While the cross section of (11) exhibits exothermic behavior, using existing thermochemical data, we calculate this reaction to be endothermic by 30 kcal. This contradiction is perhaps due to internal excitation of the CH_3Si^+ primary ion. The large rate constant is indicative of a direct mechanism which could be either H atom or H_2^- transfer. The reactions of CH_2Si^+ and CHSi^+ are of relatively minor importance and will not be treated in detail, however, it is significant to note that the two endothermic reactions of CHSi^+ , namely (29) and (30), proceed with rather large cross sections at 1.0 eV. Based on previous observations we suspect that these are direct H atom and H^- transfer reactions, and even though they exhibit clearly endothermic behavior, the direct nature of the reaction results in a large cross section.

(d) SiH_3^+ , SiH_2^+ , SiH^+ , and Si^+ . The reactions of these

TABLE III: Isotopic Distributions for Reaction 9 Using CH_3SiD_3 as Target

m/e	Product ion	Obsd intensity	Predicted intensity based on scrambling of all H and D atoms	Predicted intensity based on scrambling only of H and D atoms bound to Si
86	$\text{Si}_2\text{C}_2\text{H}_6^+$	100	0.83	100
87	$\text{Si}_2\text{C}_2\text{H}_5\text{D}^+$		5	
88	$\text{Si}_2\text{C}_2\text{H}_4\text{D}_2^+$		75	
89	$\text{Si}_2\text{C}_2\text{H}_3\text{D}_3^+$		100	

TABLE IV: Isotopic Distributions for Reaction 10 Using CH_3SiD_3 as Target

m/e	Product ion	Obsd intensity	Predicted intensity based on scrambling of all H and D atoms	Predicted intensity based on scrambling only of H and D atoms bound to Si
89	$\text{Si}_2\text{C}_2\text{H}_7\text{D}^+$	69	14	100
90	$\text{Si}_2\text{C}_2\text{H}_6\text{D}_2^+$	100	49	100
91	$\text{Si}_2\text{C}_2\text{H}_5\text{D}_3^+$	25	100	

minor ions are listed in Tables I and II as reactions 19–26 and 31–34, and again are dominated by the reactions involving transfer of H^- or H_2^- . Of particular interest here are the reactions of the Si^+ ion. Reaction 25, an H^- transfer reaction, which from available thermochemical data we calculate to be endothermic by 10 kcal for ground state reactants, is observed to have a cross section that shows exothermic behavior in the low-energy region, with a subsequent rise in cross section beginning at about 1 eV CM as shown in Figure 3a. The shape of the cross-section curve is indicative of superimposed exo- and endothermic processes. An extrapolation of the onset of the endothermic process is in good agreement with the calculated endothermicity of the reaction. The superimposed exothermic process giving a decreasing cross section at low energies is undoubtedly due to reactions of an electronically excited state of the Si^+ ion. The first excited states of the Si^+ ion, namely ($3p^2$, ^4P), lie 5.4 eV above the ground state²³ and could easily supply the needed energy. Independent measurements in this laboratory²⁴ have indicated that as much as 25% of the Si^+ ions formed by 100-eV electron impact on monosilane are formed in electronically excited states. Assuming a similar situation obtaining in methylsilane, this could easily account for the observed exothermic behavior of reaction 25. Reaction 34 in Table II is calculated to be endothermic by 30 kcal/mol for ground state reactants. The cross section as a function of collision energy is shown in Figure 3b, and displays typical endothermic behavior. Despite the endothermic shape of its dependence on energy, the cross section has a fairly high value even at the lowest energies we can measure. The fact that this reaction has an onset well below the calculated onset of 1.30 eV, in the center-of-mass system, is a further indication of internal excitation of the Si^+ ion. The magnitude of the cross section is indicative of a direct reaction.

High-Pressure Studies. Single-source mass-spectrometric studies of methylsilane are in general agreement with the tandem mass-spectrometric results with regard to the total reaction rates of the primary ions. However, the secondary ion spectra is so complex that unambiguous reac-

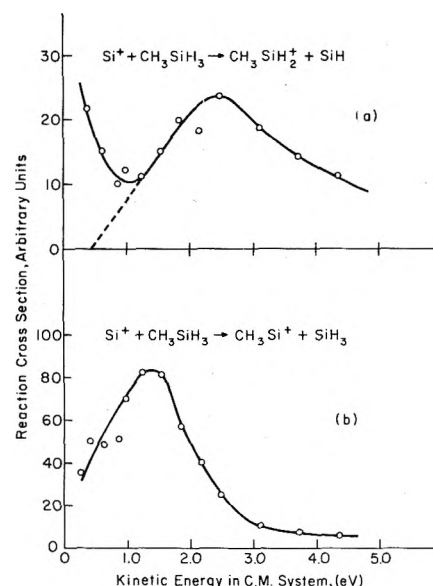


Figure 3. Relative cross sections as a function of collision energy: (a) reaction 25; (b) reaction 35.

tion assignments and calculation of rate constants from the single-source data can be made for only a few reactions. The principal advantage of the high-pressure mass spectra is the possibility of observing higher order reactions not observable in the tandem machine. The high-pressure studies are more likely to give a closer view of the overall ionic chemistry of the system in a situation where multiple collisions are possible, such as in gas-phase radiolysis situations. Thus in addition to the bimolecular processes observed in the tandem studies we have observed a great number of tertiary and higher order product ions.

The percentage ion abundances of the major primary ions ($\text{CH}_3\text{SiH}_2^+$, CH_3SiH^+ , and CH_3Si^+) are shown in Figure 4 as a function of source pressure. The CH_3SiH^+ ion, the major reactant ion observed by Potzinger and Lampe,¹³ and by us in the present tandem studies, is seen to react very rapidly. The decay rate constant measured from the initial slope of the decay of CH_3SiH^+ is calculated to be $20.0 (\pm 3) \times 10^{-10} \text{ cm}^3/\text{sec}$, in good agreement with the total rate constant for reaction of CH_3SiH^+ in Table I, and also with that of Potzinger and Lampe. The $\text{CH}_3\text{SiH}_2^+$ and CH_3Si^+ ions show an initial rise in abundance indicating that they are formed as products, consistent with reactions 3, 15–18, 19, 20, 23, 25, and 32. Above about 0.01 Torr their decreasing abundance indicates further reactions of these ions.

Reactions leading to formation of $\text{CH}_3\text{SiH}_2^+$ from Table I indicate that $\text{CH}_3\text{SiH}_2^+$ should reach a maximum abundance of between 45 and 50% of the total ions present. As seen in Figure 4, however, the $\text{CH}_3\text{SiH}_2^+$ abundance peaks at about 0.01 Torr with a value of 40%. Further reactions of this ion prevent it from reaching its maximum-possible

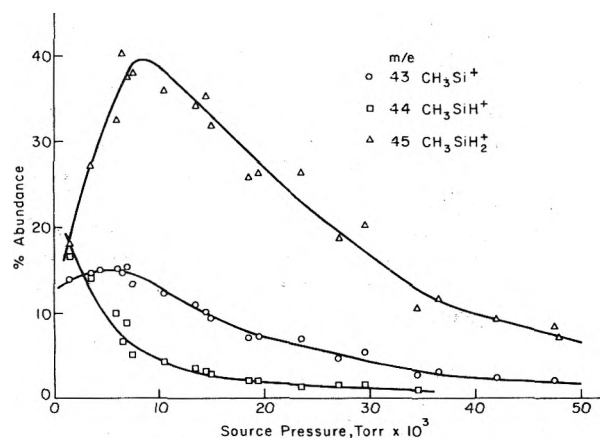
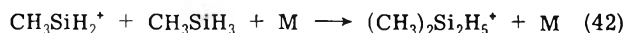


Figure 4. Major primary ion abundances as a function of source pressure.

abundance. The only bimolecular reaction observed in the tandem machine that depletes $\text{CH}_3\text{SiH}_2^+$ is reaction 2. As shown in Figure 5 this product, $(\text{CH}_3)_2\text{Si}_2\text{H}_3^+$, rises rapidly and reaches a maximum of about 10%. This is clearly not sufficient to explain the total depletion of $\text{CH}_3\text{SiH}_2^+$. Similar to the situation for SiH_3^+ in monosilane,³ we conclude that $\text{CH}_3\text{SiH}_2^+$ undergoes a third-order reaction leading to the ion at mass 91, $(\text{CH}_3)_2\text{Si}_2\text{H}_5^+$, which above 0.025 Torr is the major ion in the spectrum, *viz.*



The $(\text{CH}_3)_2\text{Si}_2\text{H}_5^+$ ion, shown in Figure 6, is seen to have a pressure dependence consistent with a third-order formation process; it reaches a maximum abundance of about 40% and appears to be unreactive toward CH_3SiH_3 up to 0.25 Torr. It can be seen from the abundances of $\text{CH}_3\text{SiH}_2^+$, $(\text{CH}_3)_2\text{Si}_2\text{H}_3^+$, and $(\text{CH}_3)_2\text{Si}_2\text{H}_5^+$ that in the region of 0.01–0.04 Torr, where further reactions are negligible, that the sum of the abundances of these three ions is constant, satisfying the stoichiometric requirements of the proposed reaction scheme.

The total rate equation for $\text{CH}_3\text{SiH}_2^+$ formation and reaction can be written as

$$dX_{\text{CH}_3\text{SiH}_2^+}/dt =$$

$$\sum_i k_i X_i [M] - k_2 X_{\text{CH}_3\text{SiH}_2^+} [M] - k_{42} X_{\text{CH}_3\text{SiH}_2^+} [M]^2 \quad (43)$$

where X_i is the per cent abundance of the various ions and $[M]$ is the number density of methylsilane. Above about 0.01 Torr the processes leading to formation of $\text{CH}_3\text{SiH}_2^+$, indicated by the first term in eq 43, can be ignored, as the abundances of the primary ions, X_i , have been nearly totally depleted. Then the equation becomes

$$-dX_{\text{CH}_3\text{SiH}_2^+}/dt = k_2 X_{\text{CH}_3\text{SiH}_2^+} [M] + k_{42} X_{\text{CH}_3\text{SiH}_2^+} [M]^2 \quad (44)$$

and with simple integration

$$\ln X_{\text{CH}_3\text{SiH}_2^+}^0 - \ln X_{\text{CH}_3\text{SiH}_2^+} = [k_2 [M] + k_{42} [M]^2] \tau \quad (45)$$

where $X_{\text{CH}_3\text{SiH}_2^+}^0$ is the maximum abundance of $\text{CH}_3\text{SiH}_2^+$ and τ is the residence time in the ion source. A plot of $1/[M] \ln X_{\text{CH}_3\text{SiH}_2^+}^0/X_{\text{CH}_3\text{SiH}_2^+}$ vs. $[M]$ should then be linear in pressure regions where $\text{CH}_3\text{SiH}_2^+$ is no longer formed and permit calculation of k_{42} . Figure 7 shows this plot and the rate constant calculated from this treatment is given in Table V. The residence time used in the calculation is the residence time of the free drift of the $\text{CH}_3\text{SiH}_2^+$ in the repeller field.

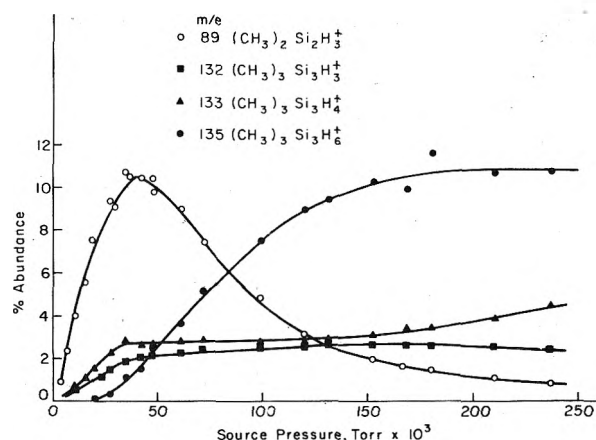


Figure 5. Major product ion abundances as a function of source pressure.

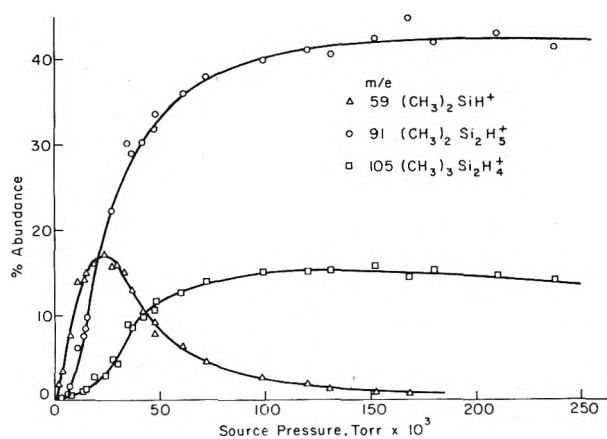


Figure 6. Major product ion abundances as a function of source pressure.

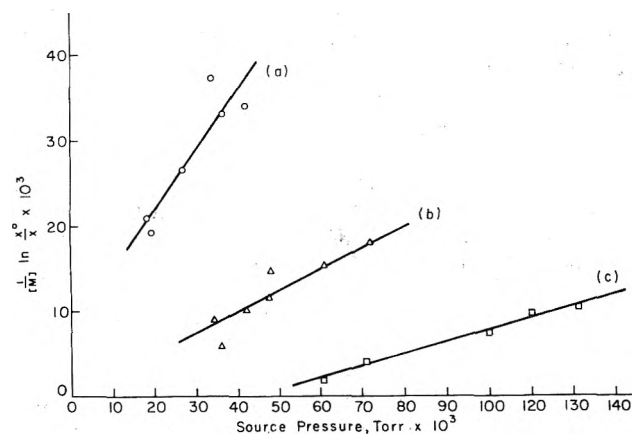


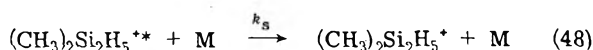
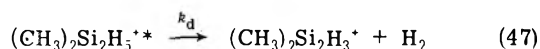
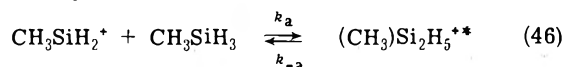
Figure 7. Termolecular decay of (a) $\text{CH}_3\text{SiH}_2^+$, (b) $(\text{CH}_3)_2\text{SiH}^+$, and (c) $(\text{CH}_3)_2\text{Si}_2\text{H}_3^+$.

This quantity is expected to be quite uncertain. At pressures below 0.05 Torr it is expected that diffusion effects will not lengthen the residence time a great deal, but the path length of the ion in the source is not well known. Since $\text{CH}_3\text{SiH}_2^+$ is formed as a product ion, the assumption that the path length is the distance between the electron beam and the exit slit is not valid. However, the uncertainties in path length and diffusion effects tend to offset one another. As a result we feel the residence time is uncertain to at least 50% leading to a large uncertainty assigned to k_{42} .

TABLE V: Third-Order Reactions in Methylsilane

Reaction	$10^{25} k$, cm ⁶ /molecule sec
$\text{CH}_3\text{SiH}_2^+ + \text{CH}_3\text{SiH}_3 \xrightarrow{\text{M}} (\text{CH}_3)_2\text{Si}_2\text{H}_5^+$	5.2 ± 4
$(\text{CH}_3)_2\text{SiH}^+ + \text{CH}_3\text{SiH}_3 \xrightarrow{\text{M}} (\text{CH}_3)_3\text{Si}_2\text{H}_4^+$	1.8 ± 1
$(\text{CH}_3)_2\text{Si}_2\text{H}_3^+ + \text{CH}_3\text{SiH}_3 \xrightarrow{\text{M}} (\text{CH}_3)_3\text{Si}_3\text{H}_6^+$	0.59 ± 0.4

The third-order formation of $(\text{CH}_3)_2\text{Si}_2\text{H}_5^+$ can be viewed as the collisional stabilization of an energetic complex formed by the association of $\text{CH}_3\text{SiH}_2^+$ and CH_3SiH_3 , and thus the overall process of reaction of $\text{CH}_3\text{SiH}_2^+$ may be described by



Assuming this mechanism we can then write the rate constants for reactions 2 and 42 as

$$k_2 = \frac{k_a k_d}{k_{-a} + k_a + k_s [\text{M}]} = 0.3 \times 10^{-10} \text{ cm}^3/\text{molecule sec} \quad (49)$$

$$k_{42} = \frac{k_a k_s}{k_{-a} + k_d + k_s [\text{M}]} = 5.2 \times 10^{-25} \text{ cm}^6/\text{molecule sec} \quad (50)$$

Thus the ratio k_s/k_d can be gotten from k_{42}/k_2 , or

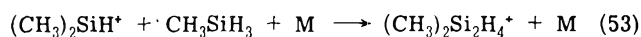
$$\frac{k_{42}}{k_2} = \frac{k_s}{k_d} = 17.3 \times 10^{-15} \text{ cm}^3/\text{molecule} \quad (51)$$

The same ratio can be obtained from a plot of $X_{(\text{CH}_3)_2\text{Si}_2\text{H}_5^+}/X_{(\text{CH}_3)_2\text{Si}_2\text{H}_3^+}$ vs. $[\text{M}]$ from the pressure data. The slope of this line gives directly the ratio k_s/k_d . The value derived from this plot is $4.0 \times 10^{-15} \text{ cm}^3/\text{molecule}$. The agreement is satisfactory considering the large error limits on k_{42} and the fact that k_2 was obtained in a completely different apparatus. We may estimate the mean lifetime of the complex involved in the collisional stabilization model to be represented by $(k_{-a} + k_d)^{-1}$. If we assume k_a and k_s to be of the order of magnitude of the polarization theory rate constant,² namely $\sim 1 \times 10^{-9} \text{ cm}^3/\text{molecule sec}$, then from eq 51

$$\tau^* \approx \frac{1}{k_{-a} + k_d} = \frac{k_{42}}{k_a k_s} \approx 5 \times 10^{-7} \text{ sec} \quad (52)$$

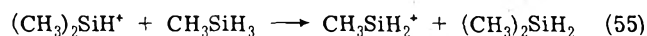
The magnitude of the constants k_2 and k_{42} demands that $k_{-a} \gg k_d$ so that the mean lifetime of the complex with respect to decomposition to original reactants is of the order of $5 \times 10^{-7} \text{ sec}$. This time is a great deal longer than the few rotational periods usually assumed to be necessary to obtain randomization of energy within the complex.²² We can thus conclude that this and similar reactions in methylsilane proceed through a randomized complex mechanism. The lifetime of the complex is short enough to preclude its observation in the tandem mass spectrometer, where multiple collisions are quite infrequent, and indeed it was not observed.

Other condensation reactions similar to reaction 42 are observed at elevated pressures in methylsilane. From stoichiometric considerations alone it can be inferred that the two additional condensation-type reactions 53 and 54, take



place. The abundances of these ions are shown in Figures 5 and 6. Similar treatment as that performed on reaction 42 and shown in Figure 7 yields third-order rate constants for these two reactions that are listed in Table V. The residence times were taken to be the free-drift residence times of the $(\text{CH}_3)_2\text{SiH}^+$ and $(\text{CH}_3)_2\text{Si}_2\text{H}_3^+$ ions. Again these are not likely to be very accurate, but for lack of information concerning the mobility of these ions in the gas and unspecified path length, a better estimate cannot be made.

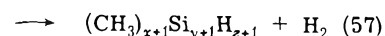
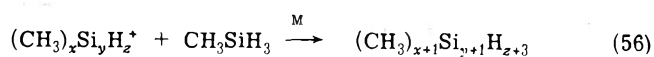
In the case of reaction 53, it can be shown from the ion abundance curve in Figure 6 that above 0.03 Torr the disappearance of $(\text{CH}_3)_2\text{SiH}^+$ is clearly due to a bimolecular process, while the formation of $(\text{CH}_3)_3\text{Si}_2\text{H}_4^+$ is clearly due to a termolecular process. This indicates to us that $(\text{CH}_3)_2\text{SiH}^+$ is being depleted, in addition to reaction 53, by a bimolecular reaction which is not immediately evident in the spectra. In view of the fact that all other monosilicon ions readily undergo a hydride transfer reaction with methylsilane, it is tempting to postulate that the bimolecular process depleting $(\text{CH}_3)_2\text{SiH}^+$ is the H^- transfer reaction 55. However, the most recent thermochemical data¹⁹ indi-



cate (55) to be endothermic by 16 kcal. At present we simply do not know the identity of the other product(s) of this bimolecular depletion of $(\text{CH}_3)_2\text{SiH}^+$.

It should be noted that the third-order rate constants for $\text{CH}_3\text{SiH}_2^+$ and $(\text{CH}_3)_2\text{SiH}^+$ are about an order of magnitude higher than those observed for similar reactions in monosilane³ and monogermane.⁸ The fact that the ratio k_s/k_d calculated for reaction 42 is nearly the same as that observed for the analogous reaction in monosilane leads us to the conclusion that k_{-a} , the rate of decomposition back to reactants, is about an order of magnitude slower in reaction 42. This is undoubtedly due to the greater ability of the complex to distribute the internal excitation among its many degrees of internal freedom (42 for $(\text{CH}_3)_2\text{Si}_2\text{H}_5^+$ compared to 24 for Si_2H_7^+ and Ge_2H_7^+) thus giving the complex a longer lifetime.

As indicated in Figures 5 and 6, the products of these condensation reactions appear to be unreactive up to 0.3 Torr, as shown by their constant abundance with increasing pressure. These three ions account for 68% of the total ion current at 0.2 Torr. At pressures up to 0.5 Torr we have observed many smaller product ions ranging up to m/e 225, presumably containing at least five silicon atoms. Because of the complexity of the spectra it is impossible to extract a detailed reaction scheme, but the general appearance of the spectra seems to indicate an ionic polymerization chain, most probably proceeding through the general type of reactions



Above about 0.3 Torr the spectra become further obscured by reactions with residual water in the mass spectrometer, such that at 0.5 Torr these water-containing ions account for at least 46% of the total ions present. This tendency to react with even very small amounts of water in the mass spectrometer at high pressures has also been noted to occur in monosilane³ and methane.²⁵

Acknowledgments. This work was supported by the U. S. Atomic Energy Commission under Contract No. AT(11-1)-3416. We also wish to thank the National Science Foundation for providing funds to assist in the original purchase of the Nuclide mass spectrometer and the Education Committee of the Gulf Oil Corporation for a grant that assisted in the construction of the tandem mass spectrometer.

References and Notes

- (1) U.S. Atomic Energy Commission Document No. COO-3416-15.
- (2) Recent reviews include J. H. Futrell and T. O. Tiernan, "Fundamental Processes in Radiation Chemistry," P. Ausloos, Ed., Interscience, New York N.Y., 1968; P. Ausloos and S. G. Lias, "Ion-Molecule Reactions," J. L. Franklin, Ed., Plenum Press, New York, N.Y., 1972.
- (3) T.-Y. Yu, T. M. H. Cheng, V. Kempter, and F. W. Lampe, *J. Phys. Chem.*, **76**, 3321 (1972).
- (4) J. M. S. Henis, G. W. Stewart, M. K. Tripodi, and P. P. Gaspar, *J. Chem. Phys.*, **57**, 389 (1972).
- (5) J. M. S. Henis, G. W. Stewart, and P. P. Gaspar, *J. Chem. Phys.*, **58**, 3639 (1973).
- (6) T. M. Mayer and F. W. Lampe, *J. Phys. Chem.*, **78**, 2195 (1974).
- (7) T.-Y. Yu, T. M. H. Cheng, and F. W. Lampe, *J. Phys. Chem.*, **78**, 1184 (1974).
- (8) J. K. Northrop and F. W. Lampe, *J. Phys. Chem.*, **77**, 30 (1973).
- (9) D. P. Beggs and F. W. Lampe, *J. Phys. Chem.*, **73**, 4194, 3307, 3315 (1969).
- (10) T.-Y. Yu, T. M. H. Cheng, and F. W. Lampe, *J. Phys. Chem.*, **77**, 2587 (1973).
- (11) G. W. Stewart, J. M. S. Henis, and P. P. Gaspar, *J. Chem. Phys.*, **57**, 1990, 2247 (1972).
- (12) T. M. Mayer and F. W. Lampe, *J. Phys. Chem.*, submitted for publication.
- (13) P. Potzinger and F. W. Lampe, *J. Phys. Chem.*, **74**, 587 (1970).
- (14) P. Potzinger and F. W. Lampe, *J. Phys. Chem.*, **75**, 13 (1971).
- (15) M. J. Henchman, "Ion-Molecule Reactions," J. L. Franklin, Ed., Plenum Press, New York, N.Y., 1972.
- (16) E. A. Finholt, A. C. Bond, K. E. Wilzbach, and H. I. Schlesinger, *J. Amer. Chem. Soc.*, **69**, 2692 (1947).
- (17) T. M. H. Cheng and F. W. Lampe, *Chem. Phys. Lett.*, **19**, 532 (1973).
- (18) J. L. Franklin, J. G. Dillard, H. M. Rosenstock, J. T. Herron, K. Drexel, and F. H. Field, *Nat. Bur. Stand. Ref. Data Ser., Nat. Bur. Stand.*, **No. 26**, June (1969).
- (19) P. Potzinger and F. W. Lampe, *J. Phys. Chem.*, **73**, 3912 (1969); **74**, 719 (1970).
- (20) E. A. V. Ebsworth, "Volatile Silicon Compounds," Pergamon Press, London, 1963, pp 16-17.
- (21) A. Henglein, *Proc. Int. Sch. Phys., "Enrico Fermi," No. 43*, (1969).
- (22) Z. Herman and R. Wolfgang, "Ion-Molecule Reactions," J. L. Franklin, Ed., Plenum Press, New York, N.Y., 1972.
- (23) C. E. Moore, *Nat. Bur. Stand. U.S., Circ.*, **No. 467** (1949).
- (24) W. N. Allen and F. W. Lampe, unpublished results.
- (25) M. Vestal, private communication.

Kinematics of Hydride Transfer Reactions in Methylsilane¹

T. M. Mayer and F. W. Lampe*

Davey Laboratory, Department of Chemistry, The Pennsylvania State University, University Park, Pennsylvania 16802

(Received April 29, 1974)

Publications costs assisted by the U. S. Atomic Energy Commission

Kinematics of hydride transfer reactions in methylsilane have been investigated by isotopic distribution measurements and kinetic energy analysis of product ions in a tandem mass spectrometer. Reactions are observed to proceed predominately *via* a direct stripping type process, yielding an $\text{CH}_3\text{SiD}_2^+$ or $\text{CH}_3\text{SiH}_2^+$ ion with very little kinetic energy, and by a complex formation mechanism that is particularly prominent at low collision energies. The process is interpreted as making a transition from complex in nature at low energies to direct at high collision energies.

Introduction

In a preceding paper² we have presented data and rate constants for a large number of ion-molecule reactions in methylsilane. The bimolecular reactions occurring in this system are dominated by those involving the net transfer of small particles, H^- , H_2^- , H . It has been shown³ that these type reactions, which are also dominant in various other silane systems, for the most part occur *via* direct stripping type mechanisms. For example, at the lowest collision energies studied, the reaction



was shown to proceed predominately through both direct H^- and H atom transfer mechanisms, while about 20% of the observed product could be attributed to the formation of a long-lived complex.

This paper examines similar reactions in methylsilane in order to further characterize the nature of these reactions

and to observe the effects of an addition of an alkyl group to the silane system.

Experimental Section

The tandem mass spectrometer used in this study has been described previously.^{3,4} The experimental procedure consists of injecting mass selected ions with kinetic energies variable down to ~ 1 eV into a collision chamber containing the neutral target gas. Products scattered into the forward direction are collected, energy analyzed in a retarding-field energy analyzer, mass analyzed, and detected. Performance of the energy analyzer has been described previously.³

Methylsilane (CH_3SiH_3) gas, obtained from Peninsular ChemResearch, was fractionated on the vacuum line and checked mass spectrometrically for satisfactory purity. Methylsilane- d_3 (CH_3SiD_3) was synthesized by reduction of CH_3SiCl_3 with LiAlD_4 in di-*n*-butyl ether solution.⁵ It was purified in the same manner as CH_3SiH_3 .

TABLE I: Hydride Transfer Reactions in Methylsilane

Reaction no.	Reaction	ΔH° , kcal/mol
4	$\text{CH}_3\text{SiH}_2^+ + \text{CH}_3\text{SiH}_3 \rightarrow \text{CH}_3\text{SiH}_2^+ + \text{CH}_3\text{SiH}_3$	0
5	$\text{CH}_3\text{SiH}^+ + \text{CH}_3\text{SiH}_3 \rightarrow \text{CH}_3\text{SiH}_2^+ + \text{CH}_3\text{SiH}_2$	-1
6	$\text{SiH}_3^+ + \text{CH}_3\text{SiH}_3 \rightarrow \text{CH}_3\text{SiH}_2^+ + \text{SiH}_4$	-11
7	$\text{SiH}_2^+ + \text{CH}_3\text{SiH}_3 \rightarrow \text{CH}_3\text{SiH}_2^+ + \text{SiH}_3$	-11
8	$\text{Si}^+ + \text{CH}_3\text{SiH}_3 \rightarrow \text{CH}_3\text{Si}^+ + \text{SiH}_3$	+30
9	$\text{Si}^+ + \text{CH}_3\text{SiH}_3 \rightarrow \text{CH}_3\text{SiH}_2^+ + \text{SiH}$	+10

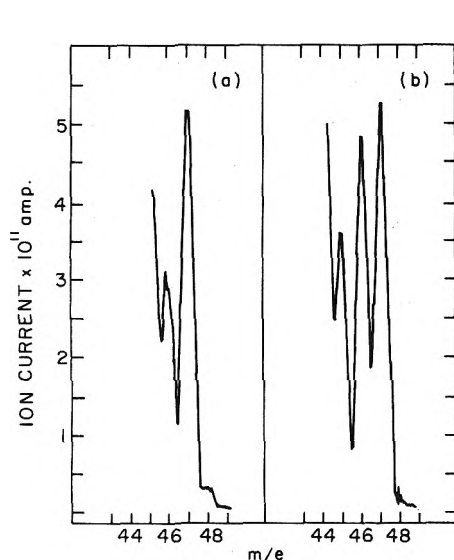


Figure 1. Isotopic distributions of products using CH_3SiD_3 as target gas: (a) reaction 4, collision energy = 0.94 eV, center of mass; (b) reaction 5, collision energy = 1.4 eV, center of mass.

Results and Discussion

In previous work in this laboratory³ we interpreted the kinematics of H and H^- transfer reactions in monosilane in terms of two models. In the spectator stripping model,⁶ in which the transfer of a particle takes place with little or no redistribution of energy among the reactants, the "spectator" particle is left with essentially the same energy it possessed before reaction. Then for a reaction involving transfer of a neutral particle from the target to the projectile ion we can predict the kinetic energy of the product ion, namely

$$E_3(s) = (m_1/m_3)E_1 \quad (2)$$

where m_1 and E_1 are the mass and energy of the projectile, respectively, and m_3 and $E_3(s)$ are the mass and energy of the product predicted by the stripping model.²

The complex-formation model refers to the formation of a persistent association product of the reactants which moves with velocity of the center of mass, and in which there occurs a randomization of the internal energy that is followed by a unimolecular dissociation to the observed products. If the lifetime of this complex is longer than a rotational period, the angular distribution and kinetic energy distribution of the dissociation products will be symmetric⁷ around the velocity of the center of mass. In such a case the kinetic energies of the products that are collected into a wide angle in the forward direction are expected to lie in a broad band centered on the kinetic energy of the center of mass as shown by

$$E_3(c) = \frac{m_1 m_3}{(m_1 + m_2)^2} E_1 \quad (3)$$

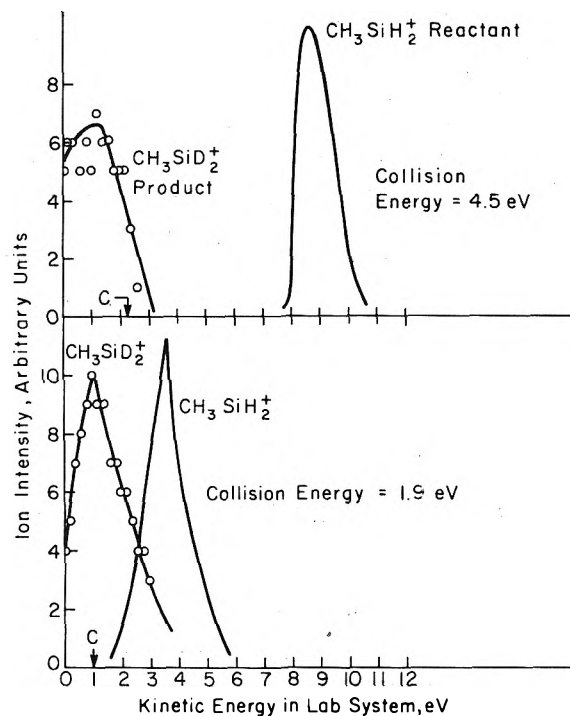
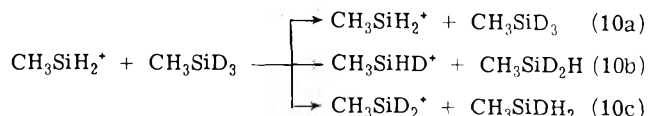


Figure 2. Product kinetic energy distributions of $\text{CH}_3\text{SiD}_2^+$ from reaction 4.

where m_1 and E_1 are the mass and energy of the projectile ion, respectively, m_2 is the mass of the target, and m_3 and $E_3(c)$ are the mass and kinetic energy of the product ion, respectively, predicted by the complex model.

Table I lists the major reactions observed in methylsilane that can be described as net transfers of one or more hydrogenic particles. In the remainder of this paper we discuss for each reactant ion the kinematics of the reactions shown.

(a) $\text{CH}_3\text{SiH}_2^+$ (m/e 45). As indicated previously² we believe the most probable structure of the m/e 45 ion, formed by electron impact on CH_3SiH_3 , to be as written. When $\text{CH}_3\text{SiH}_2^+$ is injected into CH_3SiD_3 products of reaction 4 are observed at m/e 46 (CH_3SiHD^+) and m/e 47 ($\text{CH}_3\text{SiH}_2^+$ is injected into CH_3SiD_3 products of reaction 4 since it is not observed when $\text{CH}_3\text{SiH}_2^+$ reacts with $\text{CH}_3\text{SiH}_2^+$ is injected into CH_3SiD_3 products of reaction 4 energies of 0.94 eV, center of mass, is shown in Figure 1a. The fact that virtually no product is observable at m/e 48 indicates that hydrogens bound to the carbon atoms are not participating in the reaction. Formation of a complex followed by dissociation with complete scrambling of H and D atoms bound to silicon atoms only would yield products indicated by reactions 10a-c, in the ratio a:b:c = 1:6:3.



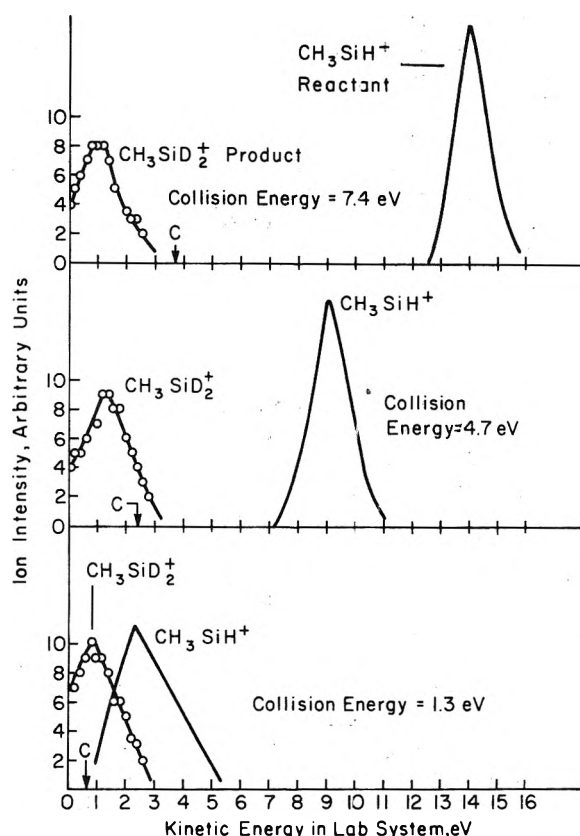
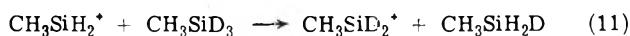


Figure 3. Product kinetic energy distributions of $\text{CH}_3\text{SiD}_2^+$ from reaction 5.

As is evident from Figure 1a, $\text{CH}_3\text{SiD}_2^+$ is present in much greater abundance than would be the case for a randomized complex mechanism. As in the analogous reaction in monosilane³ we conclude that this ion arises predominately *via* a direct D^- transfer from the target to the projectile indicated by reaction 11. The kinetic energy distribution of



product ions at m/e 47, shown in Figure 2 for two different collision energies, confirms this conclusion. In the framework of the spectator stripping model, the product ion is the spectator to the reaction. It receives therefore very little momentum from the projectile, and thus should have a very low (thermal) kinetic energy and, moreover, this kinetic energy should be independent of collision energy. This is seen to be the case in Figure 2. The point marked C indicates the most probable energy expected from the complex model, calculated from eq 3. As noted previously,³ the collection and energy measurement of very low-energy ions is very difficult. For this reason we expect that the exact location of the peak in the product-ion energy distribution may be determined by instrumental factors. We do not, therefore, place emphasis on the position of the peak but rather on the facts that the product-ion energy distribution of the D^- -stripping process is independent of primary-ion energy and at higher energies the entire band lies at energies below the C point.

High-pressure mass spectrometric experiments with methylsilane² have shown that at an average collision energy of 0.4 eV, $\text{CH}_3\text{SiH}_2^+$ will associate with CH_3SiH_3 to yield a complex having a lifetime as long as 5×10^{-7} sec. Further, in the absence of a stabilizing collision most of these complexes revert to reactants. If we then assume that

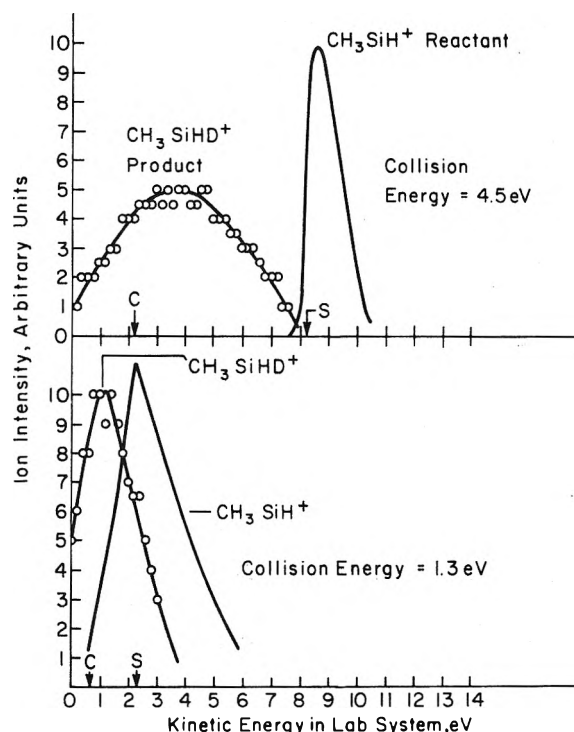
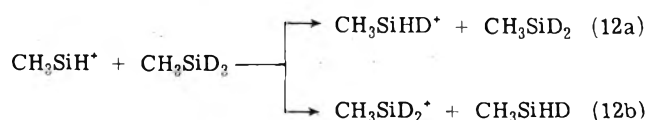


Figure 4. Product kinetic energy distributions of CH_3SiHD^+ from reaction 5.

the observed product CH_3SiHD^+ is formed exclusively by the complex-formation mechanism, one may estimate, from the relative intensities of m/e 46 and 47, the contributions from complex and impulsive processes to the total product-ion formation.

At the lowest energies measured, 0.5 eV center of mass, about 60% of the total product may be accounted for by the complex process resulting in scrambling of H and D atoms. This contribution from the complex process decreases rapidly with increasing collision energy such that at 2.0-eV collision energy, the complex accounts for only 20% of the total product production, the remainder occurring *via* the direct D^- transfer. This transition from complex to direct processes as collision energy increases has been observed quite frequently,^{3,8,9} and is due to the inability of the complex to accommodate the internal energy it acquires at increased collision energies.

(b) CH_3SiH^+ (m/e 44). The major reaction of this ion was reported² to be that involving the net transfer of either H^- or H from target to projectile as shown by reaction 5 in Table I. This particular reaction is of great interest because of the variety of possible mechanisms leading to the same product ion. The equivalent reaction in monosilane, indicated by reaction 1, was reported to proceed *via* direct H atom and H^- transfer, as well as through a complex. The various isotopic products expected for these mechanisms when CH_3SiD_3 is used as target, and when it is assumed that the methyl hydrogens are not involved, are illustrated in reaction (12). The product in (12a) would be expected



from a D-atom transfer process, while that of (12b) is formed *via* D^- transfer. A complex mechanism statistically

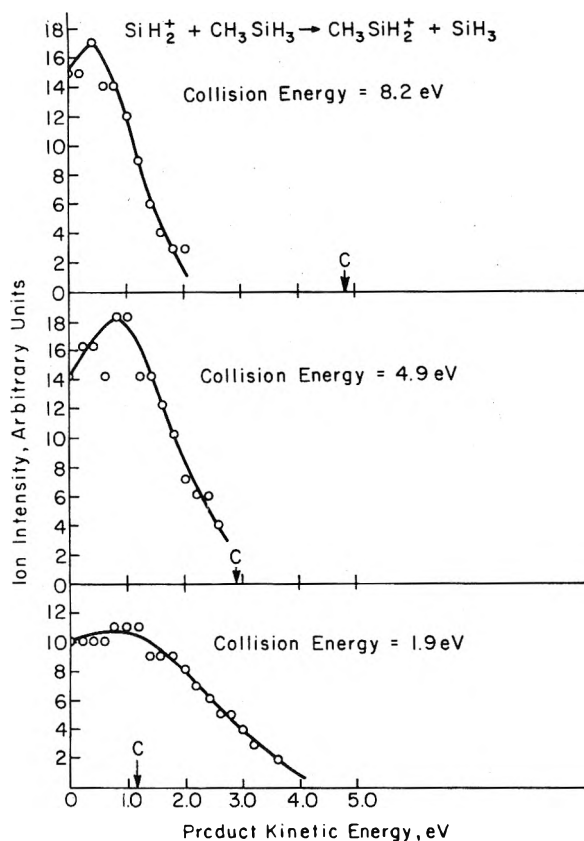


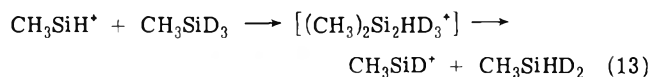
Figure 5. Product kinetic energy distributions of $\text{CH}_3\text{SiH}_2^+$ from reaction 7.

would yield both species in the ratio $a:b = 1:1$. Figure 1b shows a typical product mass spectrum at 1.4 eV, center of mass. As evident from the figure both isotopic species are present in nearly equal amounts. The ratio of $a:b$ remains fairly constant as a function of collision energy up to about 5 eV with the $\text{CH}_3\text{SiD}_2^+$ product becoming dominant at energies higher than 5-eV center of mass. Product energy distributions for these ions are shown in Figures 3 and 4. It can be seen that the $\text{CH}_3\text{SiD}_2^+$ ion displays energy distributions characteristic of a direct D^- transfer reaction. At the lowest energies, the product energy resolution is insufficient to indicate a direct or complex distinction, but clearly at higher energies the reaction is direct, leaving the product with very little energy and specifically with less energy than predicted for a complex mechanism.

The product energies of the CH_3SiHD^+ appear quite different. At low collision energy the product energy band is nearly centered on the C point, and at higher collision energies, the band becomes very broad and is centered on an energy about 1.5 eV above the C point. The broadening of the band is an indication of a great deal of energy partitioning among the reactant partners, and the position of the band indicates a mechanism much closer to that of complex formation than to direct D atom transfer. The analogous reaction³ in monosilane was shown to proceed through a direct D atom transfer that approaches the spectator stripping model prediction, *i.e.*, S point, at higher collision energies. Clearly, this appears not to be the case in methylsilane. Although the center of the product energy band lies at greater energy than predicted by the complex model, it is far from that of the stripping prediction. At energies greater than the 4.5-eV collision energy shown in Figure 4

the intensity of CH_3SiHD^+ drops off sharply, further indicating that a direct D atom transfer is not a very likely reaction in this system.

Additional evidence for the existence of a randomized complex is the appearance of the ion at m/e 45, shown in Figure 1b. This ion most probably represents the dissociation of a complex back to reactants that follows scrambling of the H and D atoms in the complex as illustrated by reaction (13). The cross section for formation of this ion drops



off much more rapidly with increasing collision energy than the products of reaction 12, consistent with previous observations^{3,8,9} of transition from complex to direct mechanisms with increasing collision energy.

(c) SiH_3^+ (m/e 31). The hydride transfer reaction of SiH_3^+ with CH_3SiH_3 , reaction 6, appears to be very similar to other direct H^- transfer reactions observed. The $\text{CH}_3\text{SiH}_2^+$ is formed with very little kinetic energy which, furthermore, is independent of collision energy.

(d) SiH_2^+ (m/e 30). The interpretation that these reactions undergo a transition from complex to direct mechanism as the collision energy increases is clearly borne out by the kinetic energy distribution of the product ion of reaction 7, shown in Figure 5. The reaction of SiH_2^+ with methylsilane was studied in detail only with CH_3SiH_3 as the target molecule. In this case the products of both direct and complex mechanisms will appear at the same mass. The breadth of this product ion kinetic energy band is a clear indication of the energy transfer processes taking place. At 1.93-eV center-of-mass collision energy, the product energy band is quite broad and centered on the energy prediction of the complex model. As one increases the collision energy, however, the band becomes increasingly narrow and moves closer to zero while the C point moves to higher energies. The broadness of the band at low energies is due to partitioning of the available energy of the system among internal and translational degrees of freedom during the lifetime of the complex. As one increases the collision energy, the reaction becomes more direct in character and little of the available energy of the system is redistributed and deposited into translation of the product ion or "spectator." The available energy of the system remains largely in translation of the neutral product.

The apparent inability of the methylsilane system to undergo H atom transfer reactions, as opposed to the case of monosilane,³ is also evident in the failure to observe a D-atom transfer reaction between SiH_2^+ and CH_3SiD_3 . Although the energetics are favorable (from the most recent data¹⁰ we calculate the H atom transfer to be exothermic by at least 5 kcal) only very small amounts of this product have been observed, and only at collision energies above about 2.5-eV center of mass.

(e) Si^+ . Reactions 8 and 9 in Table I were observed to occur in methylsilane with quite large cross section despite their endothermicity. This was attributed to the presence of a high percentage of electronically excited Si^+ ions in the reactant beam. Reaction 8 is of particular interest as it involves the net transfer of more than one atom. Although transfer reactions involving more than one hydridic particle are not uncommon in hydrocarbons¹¹ and silanes,⁴ because of the considerable rearrangement involved in the transfer of three atoms or, alternatively, the transfer of a

methyl group, it would appear less likely to proceed through the direct stripping type mechanism evident in hydridic transfer reactions involving transfer of only one atom. However, our measurements of the kinetic energies of CH_3Si^+ product of reaction 8 appear identical with the observations of reaction 7 indicating that the silicon atom in the CH_3Si^+ product is the one originally contained in the neutral molecule, and that the reaction proceeds *via* transfer of an H_3^- species which approaches a direct stripping type mechanism at high collision energies. Reaction 9 is also observed to proceed predominantly *via* the direct H^- transfer mechanism.

Acknowledgment. This work was supported by the U. S. Atomic Energy Commission under Contract No. AT(11-1)-3416. We also wish to thank the Gulf Oil Corporation

and its Education Committee for a grant that assisted in the construction of the tandem mass spectrometer.

References and Notes

- (1) U. S. Atomic Energy Commission Document No. C00-3416-16.
- (2) T. M. Mayer and F. W. Lampe, *J. Phys. Chem.*, **78**, 2422 (1974).
- (3) T. M. Mayer and F. W. Lampe, *J. Phys. Chem.*, **78**, 2195 (1974).
- (4) T. Y. Yu, T. M. H. Cheng, V. Kempter, and F. W. Lampe, *J. Phys. Chem.*, **76**, 3321 (1972).
- (5) A. E. Finholt, A. C. Bond, K. E. Wilzbach, and H. I. Schlesinger, *J. Amer. Chem. Soc.*, **69**, 2692 (1947).
- (6) A. Henglein, *J. Phys. Chem.*, **76**, 3883 (1972).
- (7) W. B. Miller, S. A. Safron, and D. R. Herschbach, *Discuss. Faraday Soc.*, **44**, 108 (1967).
- (8) Z. Herman and R. Wolfgang, "Ion-Molecule Reactions," J. L. Franklin, Ed., Plenum Press, New York, N.Y., 1972.
- (9) G. Eisele, A. Henglein, and G. Bosse, *Ber. Bunsenges. Phys. Chem.*, **78**, 140 (1974).
- (10) P. Potzinger and F. W. Lampe, *J. Phys. Chem.*, **74**, 719, 5871 (1970).
- (11) P. Ausloos, *Progr. React. Kinet.*, **5**, 113 (1969).

Ion-Molecule Reactions in Monosilane-Ethylene Mixtures¹

T. M. Mayer and F. W. Lampe*

Davey Laboratory, Department of Chemistry, The Pennsylvania State University, University Park, Pennsylvania 16802
(Received May 13, 1974)

Publication cost assisted by the U. S. Atomic Energy Commission

The reactions of Si^+ , SiH^+ , SiH_2^+ , and SiH_3^+ with C_2H_4 and the reactions of C_2H_2^+ , C_2H_3^+ , and C_2H_4^+ with SiH_4 have been studied by tandem and high-pressure mass spectrometry. Phenomenological rate constants have been measured at a reactant ion kinetic energy of 1.4 eV in the laboratory system and reaction cross sections have been studied over the range of 0.4 to 3.0 eV in the center-of-mass system. A persistent or "sticky" complex SiC_2H_7^+ is observed in collisions of SiH_3^+ with C_2H_4 with a cross section that decreases to zero at a center-of-mass energy of 1.3 eV. Formation of this complex in bimolecular reactions is confirmed in the high-pressure mass spectrometric studies. It further is shown that at higher pressures the complex SiC_2H_7^+ successively adds two more molecules of C_2H_4 and it is suggested that all these adducts have the ultimate form of alkylsiliconium ions, namely, $\text{C}_2\text{H}_5\text{SiH}_2^+$, $(\text{C}_2\text{H}_5)_2\text{SiH}^+$, and $(\text{C}_2\text{H}_5)_3\text{Si}^+$.

Introduction

A previous study² of ion-molecule reactions in the SiH_4 - C_2H_4 system was carried out at pressures below 5×10^{-3} Torr in a single source mass spectrometer system, relying principally on appearance potential measurements of product ions for reaction identification. In-as-much as more recent reports³⁻⁵ of ion-molecule reactions in similar systems have demonstrated that the application of such techniques to complex systems involving more than one neutral reactant leads to a very incomplete picture of the ionic chemistry of the system, a reinvestigation of the SiH_4 - C_2H_4 system was felt to be warranted. Accordingly we have conducted studies of the ion-molecule reactions in this system using both tandem mass spectrometry and high-pressure mass spectrometry up to about 0.3 Torr. This paper constitutes a report of our findings.

Experimental Section

The tandem mass spectrometer, which has been described previously,⁶ consists of two quadrupole mass filters,

separated by a collision chamber and ion lenses, mounted in an "in-line" configuration. It permits the injection of mass-selected reactant ions, having kinetic energies variable down to about 1 eV, into the collision chamber containing the reactant molecule and mass analysis of the product ions emerging from the collision chamber. Retarding field measurements show the energy spread of the reactant ion beam to be generally about 1 eV, but dependent on the cleanliness (past history) of the ion source.

Relative cross sections of the various ion-molecule reactions were studied as a function of collision energy in the range of 0.4-3 eV. As described previously,^{4,6,7} the shapes of the cross section *vs.* energy curves were used to differentiate between exothermic and endothermic processes. Phenomenological rate constants and cross sections of the various reactions were determined by direct comparison of relative cross sections for 1.4 eV (lab) reactant ions with the cross sections for reactions (1) and (2), the rate constants of

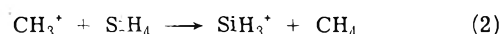
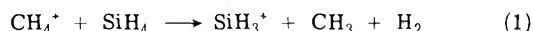


TABLE I: Exothermic Ion-Molecule Reactions in $\text{SiH}_4\text{-C}_2\text{H}_4$ Mixtures for 1.4-eV (lab) Reactant Ions

Reaction no.	Reaction	ΔH° , kcal	$10^{10}k$, cm^3/sec	
			This work	Ref 2
3	$\text{SiH}_3^+ + \text{C}_2\text{H}_4 \rightarrow \text{SiC}_2\text{H}_5^+ + \text{H}_2$		0.67 ± 0.20	Not detected
4	$\rightarrow \text{SiC}_2\text{H}_7^+$		0.78 ± 0.23	Not detected
5	$\text{SiH}_3^+ + \text{C}_2\text{H}_4 \rightarrow \text{SiCH}_3^+ + \text{CH}_3$	$+14^a$	4.8 ± 1.4	4.2 ± 1.1
6	$\rightarrow \text{SiC}_2\text{H}_3^+ + \text{H}_2 + \text{H}$		2.6 ± 0.8	0.3 ± 0.08
7	$\rightarrow \text{SiC}_2\text{H}_4^+ + \text{H}_2$		2.4 ± 0.8	0.2 ± 0.05
8	$\rightarrow \text{SiC}_2\text{H}_5^+ + \text{H}$		1.0 ± 0.3	Not detected
9	$\text{SiH}^+ + \text{C}_2\text{H}_4 \rightarrow \text{SiC}_2\text{H}_3^+ + \text{H}_2$		2.8 ± 0.8	Not detected
10	$\text{Si}^+ + \text{C}_2\text{H}_4 \rightarrow \text{SiC}_2\text{H}_3^+ + \text{H}$		0.74 ± 0.20	Not detected
11	$\text{C}_2\text{H}_4^+ + \text{SiH}_4 \rightarrow \text{C}_2\text{H}_5^+ + \text{SiH}_3$	-2 to -4^b	5.1 ± 1.5	Not detected
12	$\rightarrow \text{SiH}_2^+ + \text{C}_2\text{H}_6$	$+1^a$	2.0 ± 0.7	8.7 ± 2.2
13	$\rightarrow \text{SiH}_3^+ + \text{C}_2\text{H}_5$	$+3^a$	6.2 ± 2.0	Not detected
14	$\rightarrow \text{SiC}_2\text{H}_4^+ + 2\text{H}_2$		0.11 ± 0.03	0.7 ± 0.2
15	$\rightarrow \text{SiC}_2\text{H}_5^+ + \text{H}_2 + \text{H}$		0.11 ± 0.03	Not detected
16	$\rightarrow \text{SiC}_2\text{H}_6^+ + \text{H}_2$		0.24 ± 0.08	2.1 ± 0.5
17	$\rightarrow \text{SiC}_2\text{H}_7^+ + \text{H}$		0.33 ± 0.10	Not detected
18	$\text{C}_2\text{H}_3^+ + \text{SiH}_4 \rightarrow \text{SiH}_2^+ + \text{C}_2\text{H}_4$	-21	2.5 ± 0.8	Not detected
19	$\rightarrow \text{SiH}_3^+ + \text{C}_2\text{H}_2$	-1	0.34 ± 0.11	Not detected
20	$\text{C}_2\text{H}_2^+ + \text{SiH}_4 \rightarrow \text{Si}^+ + \text{C}_2\text{H}_4 + \text{H}_2$	-15	0.69 ± 0.15	Not detected
21	$\rightarrow \text{SiH}^+ + \text{C}_2\text{H}_5$	$+8^a$	0.46 ± 0.14	Not detected
22	$\rightarrow \text{SiH}_2^+ + \text{C}_2\text{H}_4$	-30	1.7 ± 0.5	14 ± 4
23	$\rightarrow \text{SiH}_3^+ + \text{C}_2\text{H}_3$	-21	7.3 ± 2.3	Not detected
24	$\rightarrow \text{SiCH}_3^+ + \text{CH}_3$	-16	0.22 ± 0.07	2.1 ± 0.5
25	$\rightarrow \text{SiC}_2\text{H}^+ + 2\text{H}_3 + \text{H}$		0.10 ± 0.04	Not detected
26	$\rightarrow \text{SiC}_2\text{H}_3^+ + \text{H}_2 + \text{H}$		0.44 ± 0.13	1.1 ± 0.3
27	$\rightarrow \text{SiC}_2\text{H}_3^+ + \text{H}$		0.16 ± 0.05	2.0 ± 0.5

^a See text. ^b P. Potzinger, private communication, to be submitted for publication.

which have been previously determined.⁴ Collision chamber pressures of the order of 1×10^{-3} Torr and ionization chamber pressures of the order of $1\text{--}5 \times 10^{-3}$ Torr were used.

The high-pressure mass-spectrometric experiments were carried out in a Nuclide Associates 12-90G sector-field mass spectrometer.⁶ In these experiments the ionic abundances in a mixture containing 10% C_2H_4 were measured over the pressure range of 0.02–0.3 Torr. The energy of the ionizing electron beam was 100 eV, the trap current was very small and not measured, and the ion-accelerating potential was 2500 V. In all experiments the ion-exit energy from the source was 1.9 eV and the ion-source temperature was 100°. Ion-source pressures were measured with a Granville-Phillips capacitance manometer that was calibrated against a McCleod gauge, which in turn was checked by measurement of the known pressure-dependent formation of CH_5^+ in CH_4 . We estimate our source pressure to be accurate to $\pm 10\%$.

Monosilane, purchased from the Matheson Co., was purified by fractionation on a vacuum line prior to use. The ethylene was Phillips Research Grade and was used as received.

Results and Discussion

(1) *Nature of the Elementary Reactions.* The ion-molecule reactions in the $\text{SiH}_4\text{-C}_2\text{H}_4$ system found to be exothermic on the basis of the dependence of reaction cross section on collision energy are shown in Table I. Also shown in Table I are standard enthalpy changes calculated from thermochemical data⁸⁻¹⁰ and phenomenological rate constants determined at 1.4-eV ion-kinetic energy in the laboratory system. For comparison, the rate constants reported previously² are shown in the last column of the table. In all cases except one, namely, reaction 20, the neutral products are written arbitrarily as those that lead to

maximum exothermicity. Reactions exhibiting rate constants below 10^{-11} cm^3/sec are not shown in the table.

Before proceeding to a discussion of the individual elementary reactions shown in Table I, we must first make the general observation that only qualitative agreement with the previous results of Beggs and Lampe² is obtained, and that only for the cases of what would be the major reactant ions in an equimolar mixture, namely, SiH_2^+ , C_2H_2^+ , and C_2H_4^+ . This is not surprising when one considers the complexity of this system, with respect to ion-molecule reactions, and the fact that Beggs and Lampe² used a single-source mass spectrometer at pressures below 5×10^{-3} Torr with almost complete reliance on appearance potentials and energetics for reaction identification. The comparison makes it clear that these more primitive techniques are quite inadequate for a quantitative study of a system containing two components when both are more complex than diatomic molecules, and we must conclude that our present results supercede those of the earlier report of Beggs and Lampe.²

Secondly, we may point out once again the preeminence of hydride ion transfer processes leading to formation of SiH_3^+ , a phenomenon that has proven to be quite general when gaseous systems containing SiH_4 are subjected to the passage of ionizing radiation.

In the remainder of this section we discuss the characteristics of the reactions that occur when the various reactant pairs are brought together.

(a) $\text{SiH}_3^+ + \text{C}_2\text{H}_4$. When SiH_3^+ ions are injected into the collision chamber containing C_2H_4 , SiC_2H_5^+ and SiC_2H_7^+ ions are formed *via* reactions 3 and 4 shown in Table I. In addition, very small amounts of SiC_2H_3^+ are also observed. Neither of the rate constants of (3) and (4) are particularly large and so we must conclude that most of the Langevin encounters of this pair ($k_L = 1.25 \times 10^{-9}$ cm^3/sec) revert to the original reactants. Nonetheless, these reactions are of considerable interest because in ionized

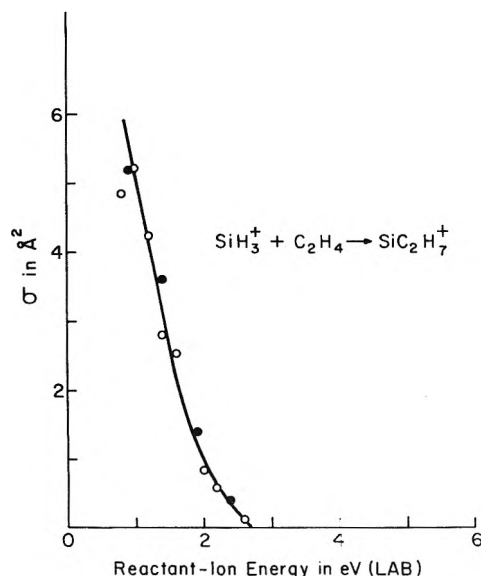


Figure 1. Dependence of cross section for SiC_2H_7^+ formation on kinetic energy of SiH_3^+ . Open and closed circles represent replicate experiments conducted 2 months apart.

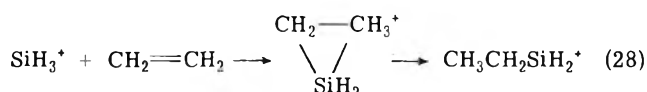
mixtures containing a large excess of SiH_4 , the predominance of hydride ion transfer from SiH_4 ensures that the SiH_3^+ ion will be the major ion leading to chemical conversion of the mixture.

The observation of (4) is of considerable interest in that the product of this reaction represents a persistent collision complex that contains all the atoms of the reactants. The observation of such persistent or "sticky" collision complexes is rather rare in ion-molecule reaction studies. The cross section of (4) decreases rapidly with increasing collision energy, as shown in Figure 1, becoming apparently zero at a relative collision energy of 1.3 eV. Previous observations of persistent complexes¹¹⁻¹³ have been made in single-source mass spectrometers and mostly, but not always, have been made on systems having more vibrational degrees of freedom than SiC_2H_7^+ .

Many complexes of this sort have been observed as a result of stabilizing collisions taking place before the complex can decompose and it may be argued that the SiC_2H_7^+ we have observed is the product of such a third-order process. However, if we make this assumption we immediately run into a number of contradictions. (1) The magnitude of the third-order rate constant necessary to produce this product in the amounts observed in the high-pressure experiments would require that the lifetime of the complex be of the order of 5×10^{-5} sec, which is appreciably larger than the ion residence time in the collision chamber and is of the order of magnitude of the total flight time in the tandem instrument, *i.e.*, it would be observed as a bimolecular product. (2) For a stabilization rate constant of about 10^{-10} cm³/mol sec, at 0.001 Torr pressure the mean distance travelled by the complex between collisions is on the order of 50 cm which is considerably more than the 2.0-cm total path length of the collision cell. (3) To the best of our knowledge, no other collision complexes of this nature have been observed in tandem mass spectrometers under similar conditions of collision cell pressure and total flight time.

In light of these arguments we think it most unlikely that the SiC_2H_7^+ observed is the result of a third-order process, but indeed is the result of a bimolecular process giving a very long-lived complex.

A loosely bound collision complex in which the reactants retain essentially their original identities, *i.e.*, $\text{C}_2\text{H}_4 \cdot \text{SiH}_3^+$, could not be expected¹⁴ to have a sufficient lifetime, relative to reversion to free reactants, to be detected in our system. In the absence of stabilizing collisions the reversion of a complex to reactants is always energetically feasible. However, if a chemical transformation takes place leading to a complex which lies in a deep potential-energy well relative to reactants, sufficient lifetime for detection ($\sim 10^{-5}$ sec) may well result. Although the evidence is not compelling, we suggest that the formation of SiC_2H_7^+ as a persistent complex occurs *via* a concerted proton transfer and addition of SiH_2 to the π -electron system of C_2H_4 , as shown by



It is proposed that a sufficiently large potential energy barrier separates the $\text{CH}_3\text{CH}_2\text{SiH}_2^+$ ion in (28) from the initial reactants for the lifetime of SiC_2H_7^+ to be longer than the detection time of the apparatus (10^{-5} sec). We rule out $\text{SiH}_3\text{CH}_2\text{CH}_2^+$ as the structure of the product of (28) in view of our experience with the mass spectrum of CH_3SiD_3 , in which we find $\text{CH}_3\text{SiD}_2^+$ to be much preferred over $\text{SiD}_3\text{CH}_2^+$. We write the cyclic structure as a possible intermediate in view of reports¹⁵⁻¹⁷ that singlet silylene radicals, (ground spin state) react with unsaturates in a fashion analogous to that of singlet methylene. The position of protonation of the cyclic structure is assumed in view of recent calculations by Hariharan, Radom, Pople, and Schleyer,¹⁸ showing that corner-protonated cyclopropane is the most stable form of a protonated cyclopropane ring. Some evidence for the linear structure in (28) comes from high-pressure mass spectrometric experiments, to be presented in a subsequent section, that indicate the rapid successive addition of three ethylene molecules to SiH_3^+ , forming presumably the stable $(\text{C}_2\text{H}_5)_3\text{Si}^+$ cation.

Regardless of whether the cyclic structure is involved as an intermediate in (28) or not, the protonation and addition must be concerted since simple proton transfer from SiH_3^+ to C_2H_4 is endothermic by 32 kcal/mol.^{9,10,19}

(b) $\text{SiH}_2^+ + \text{C}_2\text{H}_4$. Reactions 5-8, shown in Table I, are observed to occur when SiH_2^+ ions are injected into C_2H_4 . The dependence of reaction cross section on collision energy clearly shows that all reactions are exothermic, yet thermochemical calculations^{9,10} indicate that (5) should be endothermic by 14 kcal. These thermochemical calculations assume that SiCH_3^+ produced by the reaction of SiH_3^+ with C_2H_4 is the same species as one obtains from electron impact on CH_3SiH_3 , an assumption that may not be valid. Alternatively, it is possible that a significant fraction of the SiH_2^+ ions, formed by impact of 100-eV electrons on SiH_4 , contains sufficient internal energy to overcome the endothermicity. We cannot choose between the two alternatives on the basis of our data, but because the rate constant obtained is so large (and this is not typical of endothermic processes) we favor the idea that the SiCH_3^+ ion produced here is more stable than that formed by electron impact on CH_3SiH_3 and that the reaction observed is exothermic for ground-state reactants. We may note that the reaction is very efficient, some 85% of the Langevin encounters leading to products.

(c) $\text{SiH}^+ + \text{C}_2\text{H}_4$. When SiH^+ ions react with C_2H_4 , SiC_2H_3^+ ions are formed in the exothermic process shown

as reaction 9 in Table I; the reaction proceeds with a Langevin efficiency of $\sim 20\%$. An endothermic process forming SiC_2H_2^+ is observed at higher energies, with the threshold of the reaction being of the order of 1-eV center of mass.

(d) $\text{Si}^+ + \text{C}_2\text{H}_4$. Si^+ ions react exothermically with C_2H_4 to form SiC_2H_3^+ as shown by (10) in Table I. The reaction has a very low efficiency with only $\sim 5\%$ of the Langevin encounters leading to reaction products. In addition to (10), an apparently endothermic process with a threshold between 0.8 and 1.0 eV, center of mass, produces SiC_2H_2^+ .

(e) $\text{C}_2\text{H}_4^+ + \text{SiH}_4$. Reactions 11–17 are observed as exothermic processes when C_2H_4^+ ions are injected into SiH_4 . The total reaction of C_2H_4^+ with SiH_4 is very rapid with $\sim 100\%$ of the calculated Langevin encounters leading to products. The predominant processes, namely, some 94% of the total, involve the transfer of H, H_2^- , and H^- from SiH_4 , as shown by (11–13). This is quite typical of the reactions of hydrocarbon ions with silanes.^{4,5,7}

The ion, C_2H_5^+ , formed in (11), has the same m/e as SiH^+ but we choose C_2H_5^+ as the actual product observed at this m/e , since formation of SiH^+ would be endothermic by at least 70 kcal. Uncertainties in the thermochemical data may easily account for the calculated endothermicity of (12) and (13).

The calculated near-thermoneutral nature of (11–13), coupled with the large reaction rate constants and strong evidence of exothermicity from the dependence of cross section on energy, lead one immediately to the conclusion that the neutral products must be as written for any other set makes the ion formation very endothermic. This in turn leads to the mechanistic conclusion that (11–13) involve simple transfer from SiH_4 to C_2H_4^+ of H, H_2^- , and H^- , respectively.

(f) $\text{C}_2\text{H}_3^+ + \text{SiH}_4$. The only significant reactions of C_2H_3^+ with SiH_4 are those involving hydride ion transfer to form SiH_3^+ , as shown by (18), and proton transfer to form SiH_5^+ , as shown by (19). That SiH_3^+ is not a dissociation product of SiH_5^+ , but rather is formed in a completely different reaction channel, has been demonstrated in other systems by deuterium-labeling experiments.^{4,20,21} In this system the reaction sequence consisting of (19) followed by (29) is endothermic by 16 kcal/mol, and would hence not be



expected to yield SiH_3^+ with a rate constant as large as that shown in Table I.

(g) $\text{C}_2\text{H}_2^+ + \text{SiH}_4$. The reaction of C_2H_2^+ with SiH_4 is described by (20–27) shown in Table I. The magnitude of the rate constants indicates a very efficient reaction with some 80% of the Langevin encounters leading to products. Again the system is dominated by H^- and H_2^- transfer leading to formation of SiH_3^+ and SiH_2^+ , respectively, as shown by (22) and (23). The considerable uncertainty⁸ in the standard enthalpy of formation of SiH^+ is sufficient to account for the apparent endothermicity of 8 kcal for (21) shown in Table I. More recent estimates of limits to $\Delta H_f^\circ(\text{SiH}^+)$ suggest that (21) is actually exothermic.²²

It is possible that the product of (20) is not Si^+ but rather C_2H_4^+ , as these species have the same m/e . To produce C_2H_4^+ in an exothermic reaction would require a H_2 transfer process and since we have not often observed such processes but have often observed Si^+ formation in the reaction of hydrocarbon ions with SiH_4 , we favor (20).

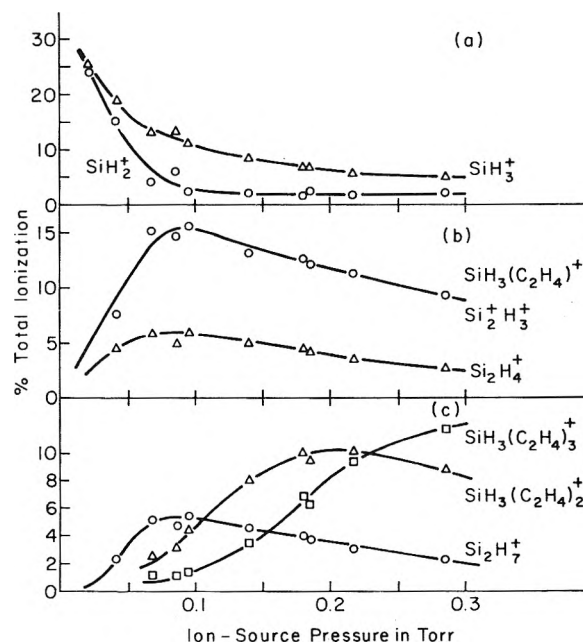


Figure 2. Relative abundances of major ions in a 90:10 $\text{SiH}_4:\text{C}_2\text{H}_4$ mixture as a function of ion-source pressure: (a) Δ , SiH_2^+ ; \circ , SiH_3^+ ; (b) Δ , Si_2H_4^+ ; \circ , $\text{SiC}_2\text{H}_7^+ + \text{Si}_2\text{H}_3^+$; (c) Δ , $\text{SiC}_4\text{H}_{11}^+$; \circ , Si_2H_7^+ ; \square , $\text{SiC}_6\text{H}_{15}^+$.

With a few exceptions the rate constants for reaction of C_2H_2^+ with SiH_4 shown in Table I agree within experimental error with those determined previously for reactions of C_2H_2^+ formed by electron impact on acetylene.⁵ The few exceptions can easily be rationalized by the possibility of greatly differing amounts of internal excitation contained in ions formed by electron impact on the two different molecules.

(2) *High-Pressure Mass Spectra.* The abundances of the major ions in a mixture of SiH_4 and C_2H_4 containing 10% C_2H_4 as a function of ion-source pressure are shown in Figure 2. To fully appreciate the implication of the results shown in Figure 2 one must first note the major features of such a plot for pure SiH_4 .^{6,23}

In pure SiH_4 ,⁶ the abundance of SiH_3^+ increases with increasing source pressure until at 0.06 Torr it passes through a maximum of about 50% of the total ionization. At pressures higher than 0.06 Torr, Si_2H_7^+ , which is formed by termolecular association of SiH_3^+ with SiH_4 , increases in abundance and attains a maximum at 0.19 Torr that represents about 35% of the total ionization. The SiH_2^+ abundance simply decays to very small values while Si_2H_4^+ , Si_2H_3^+ , and Si_2H_2^+ are the major secondary ions formed in bimolecular processes.

As shown in Figure 2 the addition of 10% of C_2H_4 has a large effect on this system. The maximum in SiH_3^+ , which is a result of hydride transfer reactions, must lie in this system below 0.02 Torr (Figure 2a), a fact that reflects the much more rapid reaction of SiH_3^+ with C_2H_4 , as shown by (3) and (4) in Table I, as compared with the termolecular association with SiH_4 that is the sole depletion channel in pure SiH_4 . Consistent with this is the fact that, as shown in Figure 2b, m/e 59 comprising SiC_2H_7^+ and Si_2H_3^+ exhibits a larger initial slope (bimolecular rate constant) than Si_2H_4^+ (m/e 60), whereas in pure SiH_4 , the ratio of initial slopes is $i_{59}/i_{60} = 0.41$.²³ Correction of the initial slope of m/e 59 (Figure 2b) for formation of Si_2H_3^+ and use of the known rate constant for formation of Si_2H_4^+ leads to a bi-

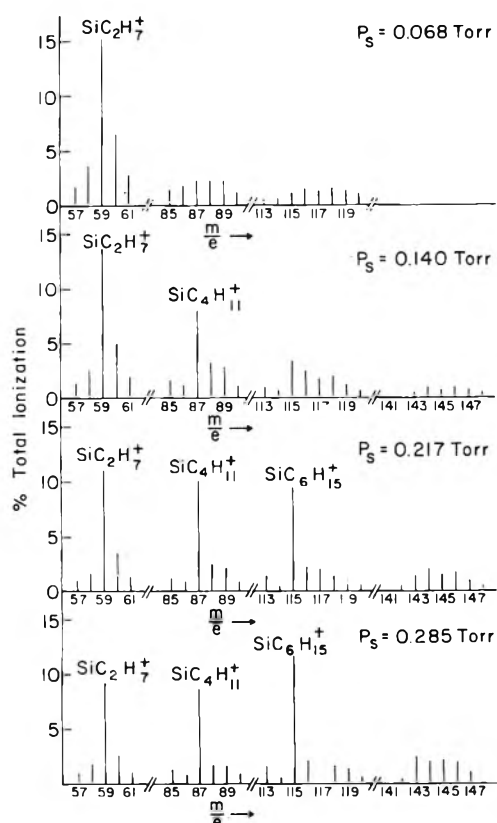
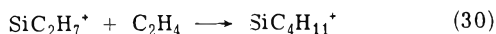


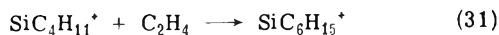
Figure 3. Patterns of selected mass groups as a function of ion-source pressure.

molecular rate constant of 1.6×10^{-10} for formation of SiC_2H_7^+ via (4). Considering the lower average energy of reactant ions in the high-pressure studies as compared with the tandem studies (0.7 vs. 1.4 eV) and the strong dependence of the cross section of (4) on energy, one must consider this agreement as satisfactory. The product of the competing reaction of SiH_3^+ , namely, Si_2H_7^+ , attains a maximum abundance of only 5% in the mixture as opposed to 35% in pure SiH_4 , again underscoring the rapidity of (4) relative to termolecular association.

Comparison of Figure 2b and 2c shows that with increasing pressure the maximum and the subsequent decay of SiC_2H_7^+ is accompanied by formation of $\text{SiC}_4\text{H}_{11}^+$ and $\text{SiC}_6\text{H}_{15}^+$, produced by the processes

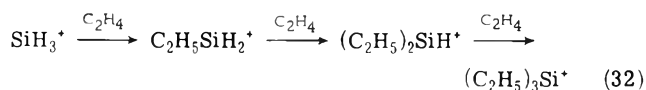


and



As shown in Figure 3, the species SiC_2H_7^+ , $\text{SiC}_4\text{H}_{11}^+$, and $\text{SiC}_6\text{H}_{15}^+$ become the most abundant ions in the system, appear to go through consecutive maxima, and overwhelmingly dominate the m/e patterns of their respective mass groups, which is an expected feature of alkylsiliconium

ions. An ion of m/e 143, which could be $\text{SiC}_8\text{H}_{19}^+$, is observed at the higher pressure but this ion never becomes the overwhelmingly dominant one in its mass group as do the former three species; moreover, there are essentially no ions of m/e less than 143. We believe, therefore, that the ultimate ion products of (4), (30), and (31) are ethylsiliconium ions formed by the sequence shown below, which may proceed via protonated cyclic intermediates



Such a sequence would be expected to stop at the triethylsiliconium ion, since further addition of ethylene would destroy the siliconium ion center leading to a less stable ionic species. This mechanism receives some additional support from the observation that diethylsilane is formed via non-free-radical processes in the radiolysis of SiH_4 - C_2H_4 mixtures.²⁴

Acknowledgment. This work was supported by the U. S. Atomic Energy Commission under Contract No. AT(11-1)-3416. We also wish to thank the National Science Foundation for providing funds to assist in the original purchase of the Nuclide mass spectrometer and the Gulf Oil Corporation for a grant that assisted in the construction of the tandem mass spectrometer.

References and Notes

- U. S. Atomic Energy Commission Document No. COO-3416-17.
- D. P. Beggs and F. W. Lampe, *J. Phys. Chem.*, **73**, 3315 (1969).
- G. W. Stewart, J. M. S. Henis, and P. P. Gaspar, *J. Chem. Phys.*, **57**, 1990 (1972).
- T. M. H. Cheng, Tung-Yang Yu, and F. W. Lampe, *J. Phys. Chem.*, **77**, 2587 (1973).
- T. M. Mayer and F. W. Lampe, *J. Phys. Chem.*, in press.
- Tung-Yang Yu, T. M. H. Cheng, V. Kemper, and F. W. Lampe, *J. Phys. Chem.*, **76**, 3321 (1972).
- T. M. H. Cheng and F. W. Lampe, *Chem. Phys. Lett.*, **19**, 532 (1973).
- P. Potzinger and F. W. Lampe, *J. Phys. Chem.*, **73**, 3912 (1969).
- P. Potzinger and F. W. Lampe, *J. Phys. Chem.*, **74**, 719 (1970).
- J. L. Franklin, J. G. Dillard, H. M. Rosenstock, J. T. Herron, K. Drexler, and F. H. Field, *Nat. Stand. Ref. Data Ser., Nat. Bur. Stand. No. 26* (June 1969).
- R. F. Pottle and W. H. Hamill, *J. Phys. Chem.*, **63**, 877 (1959).
- A. Henglein, *Z. Naturforsch. A*, **17**, 44 (1972).
- A. Henglein, G. Jacobs, and G. A. Muccini, *Z. Naturforsch. A*, **18**, 98 (1963).
- H. S. Johnston, "Gas-Phase Reaction Rate Theory," Ronald Press, New York, N.Y., 1966, pp 280 ff.
- P. S. Skell and E. J. Goldstein, *J. Amer. Chem. Soc.*, **86**, 1442 (1964).
- W. H. Atwell and D. R. Weyenberg, *J. Amer. Chem. Soc.*, **90**, 3438 (1968).
- Y. N. Tang, G. P. Gennaro, and Y. Y. Su, *J. Amer. Chem. Soc.*, **94**, 4355 (1972).
- P. C. Hariharan, L. Radom, J. A. Pople, and R. v. R. Schleyer, *J. Amer. Chem. Soc.*, **96**, 599 (1974).
- M. Bowrey and J. H. Purnell, *Proc. Roy. Soc., Ser. A*, **321**, 341 (1971).
- G. W. Stewart, J. M. S. Henis, and P. P. Gaspar, *J. Chem. Phys.*, **57**, 2247 (1972).
- T. M. H. Cheng and F. W. Lampe, *J. Phys. Chem.*, **77**, 2841 (1973).
- T. M. H. Cheng, T.-Y. Yu, and F. W. Lampe, *J. Phys. Chem.*, **78**, 1184 (1974).
- G. G. Hess and F. W. Lampe, *J. Chem. Phys.*, **44**, 2257 (1966).
- J. F. Schmidt and F. W. Lampe, *J. Phys. Chem.*, **73**, 2706 (1969).
- J. F. Schmidt and F. W. Lampe, *J. Phys. Chem.*, **73**, 2706 (1969).

Inelastic Scattering of Vibrationally Excited Potassium Bromide by Polyatomic Partners

F. F. Crim, H. B. Bente, and G. A. Fisk*¹

Department of Chemistry, Cornell University, Ithaca, New York 14850 (Received July 1, 1974)

Publication costs assisted by Sandia Laboratories

A molecular beam study of energy transfer from highly vibrationally excited (~ 41 kcal/mol) potassium bromide, KBr^\dagger , to the partners CH_3NO_2 , $(\text{CH}_3)_2\text{O}$, $\text{C}_2\text{H}_5\text{OH}$, and C_3H_8 is reported. An energy randomizing complex is formed in collisions of KBr^\dagger with CH_3NO_2 . Several internal modes of this partner participate in energy redistribution, in contrast to the behavior observed with the partners H_2O , NH_3 , and CH_3OH . $(\text{CH}_3)_2\text{O}$, $\text{C}_2\text{H}_5\text{OH}$, and C_3H_8 all exhibit similar dynamics with KBr^\dagger . Velocity spectra obtained for these partners show some features reminiscent of two interaction mechanisms explored earlier and cannot be explained in terms of any single, simple model.

Introduction

A growing interest in collisional energy transfer has motivated recent studies in which the details of inelastic collisions between uncharged species are probed by molecular beam techniques.^{2,3} A tandem molecular beam method has been employed in earlier work in this laboratory to study vibration-translation, V-T, energy transfer from highly vibrationally excited (~ 41 kcal/mol) potassium bromide, KBr^\dagger , in collisions with small polar^{2a} and nonpolar^{2b} partners. Rather different dynamics are responsible for the observed inelastic scattering from these two types of partners. Strong long-range attractions, which arise from the interaction of the KBr^\dagger and partner charge asymmetries, cause the inelastic scattering with polar partners to proceed through an energy randomizing complex. Nonpolar partners, on the other hand, have only weak attractive interactions with KBr^\dagger and the collisional interaction is primarily short-range repulsion. In this paper, we report the results of tandem molecular beam experiments for the energy transfer partners nitromethane, propane, dimethyl ether, and ethanol.

Nitromethane is an interesting partner because it has both a large dipole moment⁴ ($\mu = 3.5$ D) and several low-frequency skeletal vibrations.⁵ Complex formation is very likely in the scattering of KBr^\dagger with CH_3NO_2 , and the existence of low-frequency skeletal vibrations permits investigation of an important aspect of energy redistribution in collision complexes. Vibrational modes of the partner molecules do not participate in energy randomization in complexes formed between KBr^\dagger and NH_3 , H_2O , or CH_3OH . Apparently the partner vibrations are excluded by the large difference between their frequencies and that of KBr^\dagger (~ 100 cm^{-1}).² Because a much smaller frequency gap exists between the three low-frequency modes⁵ in nitromethane and the KBr^\dagger vibration, it is reasonable to expect some partner modes to be involved in energy randomization in a $(\text{KBrCH}_3\text{NO}_2)^\dagger$ complex.

Propane, dimethyl ether, and ethanol are the most structurally complicated energy transfer partners so far studied. Propane is nonpolar, and dimethyl ether and ethanol have dipole moments⁴ of 1.3 and 1.7 D, respectively. The molecular weights (MW) of two previously studied nonpolar partners,^{2b} Ar (MW = 40) and CO_2 (MW = 44), are close to those of C_3H_8 (MW = 44), $(\text{CH}_3)_2\text{O}$ (MW = 46), and $\text{C}_2\text{H}_5\text{OH}$ (MW = 46). These five partners form an

interesting series because they have nearly equal masses but different structures and charge distributions.

The experimental apparatus and procedure are essentially identical with those used for the first experiments with nonpolar partners.^{2b} A beam of KBr^\dagger , produced by the crossed beam reaction of K with Br_2 ,⁶ enters a scattering region where it intersects a beam of collision partner molecules. Scattered potassium bromide is detected using a surface ionization strip mounted behind a slotted disk velocity analyzer. Use of a Cary 31 vibrating reed electrometer increases the sensitivity of the detection system over that of earlier studies.^{2b} This permits data acquisition at laboratory scattering angles, θ , up to the physical rotation limits of the apparatus ($\theta = 60^\circ$). (Scattered intensities can be obtained only to $\theta = 50^\circ$ for nitromethane because the surface ionization filament is disturbed by CH_3NO_2 at larger angles.)

Nitromethane

The dipole moments of KBr^\dagger (~ 17 D)⁷ and nitromethane are large enough that collision complexes between these two species should be formed with large cross section,^{2a} and the observed scattering data are analyzed accordingly. Decay energetics and angular distributions arising from energy randomizing complexes are discussed elsewhere,^{2a,8-11} and only a few central points are repeated here. The probability of a final translational energy, E' , is

$$P(E') = A(E')N^+(E' - E')$$

where E' is the total energy of the system and $N^+(E' - E')$ is the energy level density of the active vibrations and rotations. In the limit of high total energy and low-frequency vibrations, the classical approximation

$$N^+(E' - E') \sim (E' - E')^n$$

is valid. $A(E')$ is determined by the force constants (C and C') in the entry and exit channels and the initial relative translational energy, E . The force constants are calculated using the Keesom-Linder¹² approximation for the interaction of two rotating dipoles. The exponent n is

$$n = s + \langle r/2 \rangle - 2$$

where s is the number of active vibrations in the complex, including the separation coordinate, and r is the number of active rotations. Angular distributions for decay products of long-lived complexes are determined by angular momen-

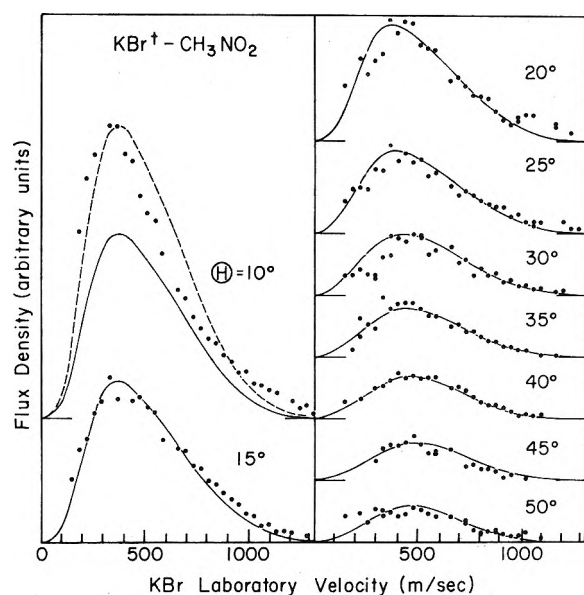


Figure 1. Scattered flux density of potassium bromide as a function of velocity at various laboratory angles. The points are experimental measurements, and the solid curves are the calculated distributions. No adjustments of the relative intensities for the solid curves are made; the broken curve is scaled to match the measurement at $\theta = 10^\circ$. The KBr^+ beam is at $\theta = 0^\circ$, and the CH_3NO_2 beam is at $\theta = 90^\circ$.

tum considerations.¹⁰ For short complex lifetimes, these distributions are modified using a factor¹¹ which is determined by the ratio, τ/τ_R , of the mean complex lifetime to the rotational period.

The data for $\text{KBr}^+-\text{CH}_3\text{NO}_2$ are compared with the collision complex model using a previously developed^{2a,8} computer program which transforms a calculated center of mass, CM, intensity distribution to the laboratory. The theory for the decay of energy randomizing collision complexes provides the CM inelastic scattering intensity for the transformation. A term to account for the nearly elastic small-angle scattering which occurs in collisions that do not lead to complex formation is added to that from complex decay. The computer program transforms the sum of these two terms at a given CM angle and CM velocity to the laboratory, taking into account the velocity distributions in each beam. The resulting laboratory intensity is convoluted with the transmission function of the velocity analyzer to give distributions for comparison with the experimental data. Most of the parameters of the model are determined uniquely once quantities such as dipole moments and initial temperatures are known. The two adjustable parameters are n and τ/τ_R . Shapes of the final velocity distributions are determined primarily by n and relative intensities by τ/τ_R .

Lin and Rabinovitch¹³ have called the temporary low-frequency modes of a complex which correlate with rotations and vibrations of the separated partners transitional modes. The analysis technique described above has been used previously to show that only the transitional modes and the KBr^+ vibration participate in energy randomization in complexes formed between KBr^+ and H_2O , NH_3 , or CH_3OH . If only the transitional modes and the KBr^+ vibration are active in a complex of KBr^+ with a nonlinear polyatomic, n lies in the range 2.5–4.5. The best fits to the earlier experiments with polar partners are obtained for $n =$

TABLE I: Interaction Parameters

Quantity	CH_3OH^a	H_2O^a	NH_3^a	CH_3NO_2
Dipole moment, D	1.7	1.8	1.5	3.5
C , 10^{-57} erg cm^6	11.0	13.0	16.0	34.5
C' , 10^{-57} erg cm^6	0.5	0.6	0.4	2.8
E' , kcal/mol	46	46	45	46
E , kcal/mol	1.0	0.9	0.5	0.8
n	3.5	4.0	3.5	6.0
τ/τ_R	0.2–0.4	0.2–0.4	0.2–0.4	1.25

^a Reference 2a.

3.5 for CH_3OH and NH_3 and for $n = 4.0$ for H_2O , consistent with excitation of only the transitional modes.

Potassium bromide velocity distributions for the scattering of KBr^+ by CH_3NO_2 are shown as points in Figure 1. The area under the distribution at a given angle is proportional to the total scattered flux at that angle, as measured in an experiment in which the entire interaction region is viewed without velocity analysis. The solid lines in Figure 1 are laboratory distributions calculated for $n = 6$ and $\tau/\tau_R = 1.25$. There is no angle-to-angle adjustment of the relative intensities of the calculated distributions. The collision complex model produces good agreement not only with experimental velocity distribution shapes but also with observed relative intensities. Incompletely understood problems associated with data acquisition at small laboratory angles cause the disagreement at $\theta = 10^\circ$. The broken curve is the calculated distribution scaled to have the same maximum intensity as the experimental points. Peak location in the calculation at 10° agrees fairly well with experiment, indicating that much of the discrepancy arises from uncertainty in the small angle normalization. For the calculations on $\text{KBr}^+-\text{CH}_3\text{NO}_2$, the term for nearly elastic scattering is $\sim 15\%$ smaller than in previous studies,^{2a} but its form is unchanged. Nearly elastic scattering is important only at the smaller laboratory angles; for larger angles ($\theta \geq 35^\circ$), the complex contribution strongly dominates the calculation. Varying n by one produces noticeable changes in the shapes of the laboratory velocity distributions, particularly at the larger scattering angles. As in earlier studies,^{2a} satisfactory agreement between calculated and experimental curves is obtained only for n within one of the best fit value. The best-fit parameters for the previously studied polar partners and for CH_3NO_2 are listed in Table I. A comparison between the calculated laboratory distributions for $n = 3.5$ and $n = 6$ is shown for three laboratory angles in Figure 2. Even if arbitrary adjustments are made in the intensities at each angle, the calculated distributions for the smaller n do not agree with experiment. The magnitude of n required to fit the data clearly indicates that some of the partner modes participate in energy randomization.

An increase in n from 3.5 to 6 is observed in going from CH_3OH to CH_3NO_2 as a collision partner. In the context of the energy transfer model, this indicates that roughly three internal CH_3NO_2 modes are active, with perhaps one of these participating as an internal rotation. It must be emphasized that detailed speculation on the meaning of small variations ($\sim 1/2$) in n is not warranted by the precision of the determination. The three lowest frequency vibrational modes in CH_3NO_2 are associated with motion of the NO_2

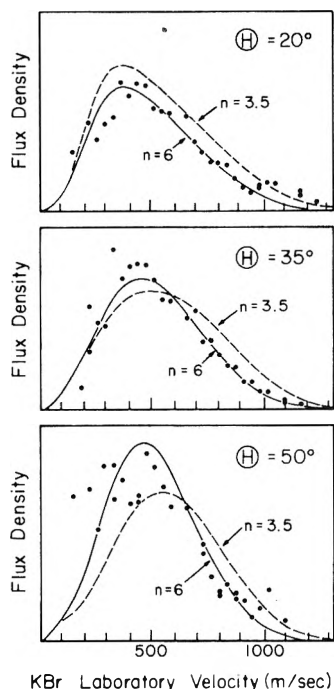


Figure 2. Calculated velocity distributions showing the sensitivity of the calculations to the parameters. The solid curves are calculations for $\text{KBr}^+-\text{CH}_3\text{NO}_2$ with $n = 6$ and $\tau/\tau_R = 1.25$; the broken curves are for $n = 3.5$ and $\tau/\tau_R = 0.25$. Points are the experimental measurements.

group.⁵ A calculated charge distribution for nitromethane¹⁴ indicates that the two oxygens are very negative and that the nitrogen is very positive compared to the rest of the molecule; hence, the molecular dipole is essentially located on the nitro group. Because electrostatic forces orient the dipoles of the collision pair, the motions of the NO_2 group should be coupled quite effectively to the KBr^+ vibration. Thus it seems that three modes of CH_3NO_2 are active because they have low frequencies ($<650\text{ cm}^{-1}$) and are coupled favorably to the KBr^+ vibration by the geometry of the complex.

Because the probability of having the necessary energy in the appropriate mode for decay (the "reaction coordinate") decreases with an increasing density of states, participation of more modes in energy randomization leads to a longer complex lifetime. This feature is reflected in an increased value of the parameter, τ/τ_R , which affects the variation of intensity with CM angle. Relative intensities in the laboratory also are influenced by τ/τ_R , and comparison of the best fit value of this quantity for $\text{KBr}^+-\text{CH}_3\text{NO}_2$ with that for the other systems further supports the conclusion that energy is randomized among more modes in the present case. The sensitivity of the calculated intensities to τ/τ_R is not great enough to allow its precise determination, but it is possible to conclude that $(\text{KBrCH}_3\text{NO}_2)^+$ complexes live substantially longer than those of KBr^+ with CH_3OH , NH_3 , or H_2O . For $\text{KBr}^+-\text{CH}_3\text{NO}_2$, the value $\tau/\tau_R = 1.25$ gives good agreement between the calculated and experimental intensities; for the other systems, τ/τ_R falls in the range 0.2–0.4. The broken curves in Figure 2 are calculated distributions for the $\text{KBr}^+-\text{CH}_3\text{NO}_2$ system using $\tau/\tau_R = 0.25$ and $n = 3.5$. The relative intensities decrease too rapidly with angle to agree with the measured distributions, indicating that the short lifetimes appropriate for the

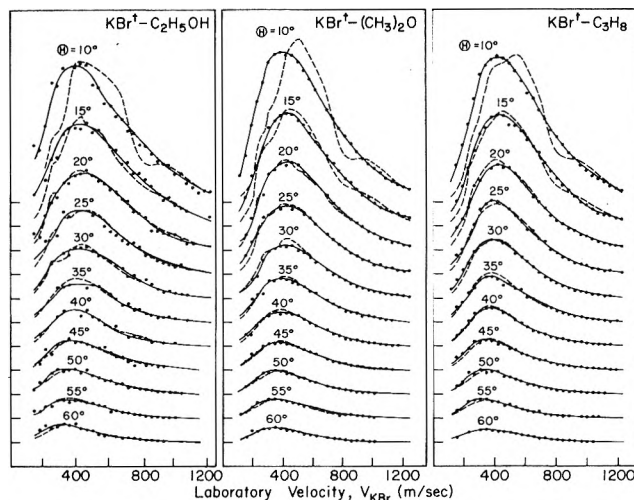


Figure 3. Laboratory velocity distributions of scattered potassium bromide for the systems $\text{KBr}^+-\text{C}_2\text{H}_5\text{OH}$, $\text{KBr}^+-\text{(CH}_3)_2\text{O}$, and $\text{KBr}^+-\text{C}_3\text{H}_8$. Points are experimental data, solid lines are smoothed data used for computer analysis, and broken lines are calculations using the computer generated CM cross sections. The direction of the KBr^+ beam is at a laboratory angle of $\theta = 0^\circ$; the partner beam is at $\theta = 90^\circ$.

partners CH_3OH , NH_3 , and H_2O are not applicable to the interaction of KBr^+ with CH_3NO_2 .

Evidence for redistribution of energy among less than all the vibrational modes in a complex has been obtained for nonreactive decay in this laboratory^{2a} and for reactive decay in several other studies.¹⁵ Shobatake, Lee, and Rice¹⁵ have emphasized the subtleties involved in inferring from the comparison of a calculated distribution with experiment that incomplete randomization of energy is occurring. They point out that features of the potential energy surface which are not well enough known to be included in theory can lead to erroneous conclusions. It is clear, however, that incomplete randomization of energy is an experimental fact which needs to be more completely understood. A nice feature of comparing changes in parameters rather than absolute magnitudes is that possible uncertainties in the theory are often less important. The reason for studying CH_3NO_2 as a partner was to explore the proposal^{2a} that internal modes might be active if a large frequency gap did not exist between them and the transitional modes. As such a test, the experiment and analysis reported here are unambiguous: some internal modes of CH_3NO_2 must be assumed active for the calculation to agree with the data.

Propane, Dimethyl Ether, and Ethanol

Data obtained using the partners C_3H_8 , $(\text{CH}_3)_2\text{O}$, and $\text{C}_2\text{H}_5\text{OH}$ are shown in Figure 3. The points are measured flux densities of scattered potassium bromide as a function of velocity at the indicated laboratory angles. Solid lines are the smoothed data used as input to a numerical analysis routine which generates CM intensities by performing a least-squares fit to the laboratory data. This analysis routine is a modified version⁸ of one developed by Riley and Siska¹⁶ and has been used to aid interpretation of previous tandem molecular beam experiments.² Broken curves in Figure 3 are distributions obtained by transforming the calculated CM intensity to the laboratory. The agreement between the calculated and smoothed experimental distributions for $\text{C}_2\text{H}_5\text{OH}$, $(\text{CH}_3)_2\text{O}$, and C_3H_8 is comparable to that obtained in earlier studies.^{2b} Figure 4 shows the com-

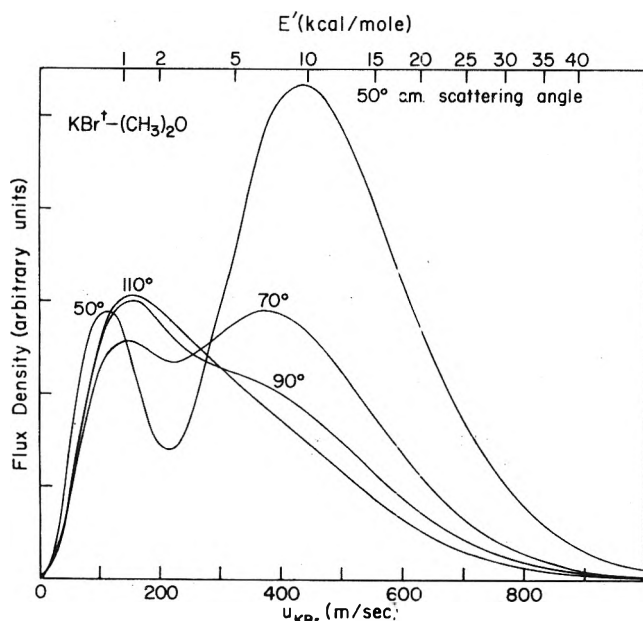


Figure 4. Computer generated CM flux density as a function of final CM velocity at several CM scattering angles for the $\text{KBr}^+(\text{CH}_3)_2\text{O}$ system. The final relative translational energy of the collision pair is shown on the upper axis.

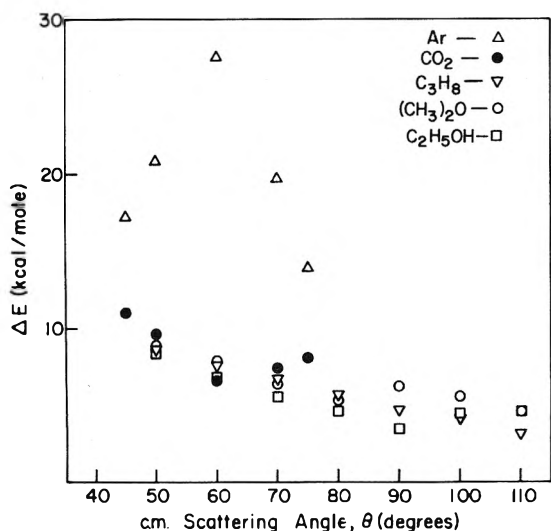


Figure 5. Characteristic energy transfer, ΔE , as a function of CM angle for the scattering of KBr^+ by the partners Ar, CO_2 , C_3H_8 , $(\text{CH}_3)_2\text{O}$, and $\text{C}_2\text{H}_5\text{OH}$. The results for the partners Ar and CO_2 are from earlier experiments (ref 2b) in which the angular range of the data is smaller than that for the experiments reported here.

puter generated CM intensity as a function of potassium bromide final CM velocity, u_{KBr} , at several CM angles for the scattering of KBr^+ by $(\text{CH}_3)_2\text{O}$.¹⁷ The CM intensity distributions for the other two systems are very similar to those shown for $\text{KBr}^+(\text{CH}_3)_2\text{O}$. The shapes of the CM intensity distributions at the smaller laboratory angles are suggestive of the earlier results for nonpolar partners.^{2b} Nearly elastic collisions, in which very little energy is transferred from the vibration of KBr^+ to relative translation of the collision pair, cause the low velocity peak. Strongly inelastic collisions, in which a large amount of vibration-translation, V-T, energy transfer occurs, produce the high velocity peak. At a fixed CM scattering angle, θ , a useful measure of the extent of V-T energy transfer is the differ-

ence between the relative translational energy corresponding to the maximum intensity in the high velocity region and the initial relative translational energy. This quantity is designated ΔE . Initial relative translational energies are determined from the most probable velocities in the beams. A low velocity contribution, whose shape and location are determined from the well-separated peaks at $\theta \sim 50^\circ$, is subtracted from the overall CM distribution at larger CM angles to locate the inelastic peak. Figure 5 summarizes the ΔE 's determined for the present partners as well as those for Ar and CO_2 .^{2b}

Energy transfers for the partners CO_2 , $(\text{CH}_3)_2\text{O}$, $\text{C}_2\text{H}_5\text{OH}$, and C_3H_8 are strikingly similar and very different from those for the partner Ar. The marked difference in the ΔE 's for $\text{KBr}^+\text{-Ar}$ and $\text{KBr}^+\text{-CO}_2$ has been attributed to the presence of internal degrees of freedom in CO_2 which are absent in Ar.^{2b} Vibration-vibration, V-V, energy transfer efficiently competes with V-T processes and, thus, reduces the final relative translational energy of $\text{KBr}^+\text{-CO}_2$ compared to $\text{KBr}^+\text{-Ar}$. The comparison shown in Figure 5 indicates that V-V transfer is also important in collisions of KBr^+ with C_3H_8 , $(\text{CH}_3)_2\text{O}$, and $\text{C}_2\text{H}_5\text{OH}$. The similarity between CO_2 and C_3H_8 as scattering partners is not surprising. They are both nonpolar and have several comparable vibrational frequencies.

Dimethyl ether and ethanol have dipole moments which are similar to those of the previously studied polar partners.^{2a} Because collision complex formation dominates the inelastic scattering of KBr^+ by NH_3 , H_2O , or CH_3OH , it seemed plausible that complexes should be important in the dynamics of the $\text{KBr}^+(\text{CH}_3)_2\text{O}$ and $\text{KBr}^+\text{-C}_2\text{H}_5\text{OH}$ systems. The computer program mentioned in the discussion of CH_3NO_2 was used to generate laboratory distributions based on the decay of an energy randomizing complex. Satisfactory agreement between the calculated and experimental maxima is obtained for $n = 8$ and $\tau/\tau_R = 0.2$, but the calculated and experimental shapes disagree sharply in the high velocity region. Also, this combination of parameters is physically unrealistic because RRKM theory predicts that a $(\text{KBr}(\text{CH}_3)_2\text{O})^+$ or $(\text{KBrC}_2\text{H}_5\text{OH})^+$ complex with $n = 8$ should live a rotational period or longer. Reasons that calculations based on an energy randomizing collision complex model fail to reproduce the observed laboratory data can be seen by examining Figure 4. For small values of θ , the CM distributions, as already remarked, have two peaks, and neither the high nor the low velocity portions can be fit using the collision complex model. At large CM angles, the intensity distributions for the three partners $(\text{CH}_3)_2\text{O}$, $\text{C}_2\text{H}_5\text{OH}$, and C_3H_8 have only a single peak. These distributions are qualitatively similar to those of the decay products of an energy randomizing complex. However, a quantitative comparison reveals that the distributions obtained for all three partners are broader and have more intensity in the high velocity region than the distributions arising from complex decay. The calculated CM distributions, even for large θ , cannot be reproduced using the simple collision complex model for any value of n .

It may be that, in some cases, more than one energy transfer mechanism must be invoked to explain the deexcitation of KBr^+ by a given polyatomic molecule. For instance, dimethyl ether or ethanol may fail to form complexes with KBr^+ in some collisions because the interaction potential is unfavorable for many relative orientations of the salt and partner molecules. For many directions of approach, the charge distribution asymmetry encountered by KBr^+ is too small to produce a strong attraction between

the colliding pair,¹⁸ and the resulting scattering may be dominated by repulsive forces. On the other hand, the striking similarities between the ΔE 's observed for chemically quite different polyatomic molecules suggest that some simple model might account for the dynamics in many systems. Models based on the notion of constrained thermal accommodation¹³ may be useful ones to investigate further but the particular version discussed here and in ref 2a is unable to explain the behavior of any of the systems summarized in Figure 5.

Acknowledgment. The authors are pleased to thank Professor P. R. Brooks for suggesting that nitromethane would be an interesting collision partner to study.

References and Notes

- (1) Address correspondence to this author at Sandia Laboratories, Albuquerque, New Mexico 87115.
- (2) (a) T. Donohue, M. S. Chou, and G. A. Fisk, *Chem. Phys.*, **2**, 271 (1973); (b) F. F. Crim, M. S. Chou, and G. A. Fisk, *ibid.*, **2**, 283 (1973).
- (3) (a) H. J. Loesch and D. R. Herschbach, *J. Chem. Phys.*, **57**, 2038 (1972); (b) D. L. King, H. J. Loesch, and D. R. Herschbach, *Discuss. Faraday Soc.*, **55**, 222 (1973).
- (4) A. L. McClellan, "Tables of Experimental Dipole Moments," W. H. Freeman, San Francisco, Calif., 1963.
- (5) T. P. Wilson, *J. Chem. Phys.*, **11**, 361 (1943).
- (6) J. H. Birely and D. R. Herschbach, *J. Chem. Phys.*, **44**, 1690 (1966).
- (7) C. Maltz, *Chem. Phys. Lett.*, **3**, 707 (1969).
- (8) T. Donohue, Ph.D. Thesis, Cornell University, 1974.
- (9) S. A. Safron, N. D. Weinstein, D. R. Herschbach, and J. C. Tully, *Chem. Phys. Lett.*, **12**, 564 (1972).
- (10) (a) W. B. Miller, S. A. Safron, and D. R. Herschbach, *Discuss. Faraday Soc.*, **44**, 108 (1967); (b) W. B. Miller, S. A. Safron, and D. R. Herschbach, *J. Chem. Phys.*, **56**, 3581 (1972); (c) S. J. Riley and D. R. Herschbach, *ibid.*, **58**, 27 (1973); (d) W. B. Miller, Ph.D. Thesis, Harvard University, 1969.
- (11) (a) G. A. Fisk, J. D. McDonald, and D. R. Herschbach, *Discuss. Faraday Soc.*, **44**, 228 (1967); (b) M. K. Bullitt, C. H. Fisher, and J. L. Kinsey, *J. Chem. Phys.*, **60**, 478 (1974).
- (12) B. Linder, *J. Chem. Phys.*, **44**, 265 (1966).
- (13) Y. N. Lin and B. S. Rabinovitch, *J. Phys. Chem.*, **74**, 3151 (1970).
- (14) W. J. Hehre and J. A. Pople, *J. Amer. Chem. Soc.*, **92**, 2191 (1970).
- (15) K. Shobatake, Y. T. Lee, and S. A. Rice, *J. Chem. Phys.*, **59**, 6104 (1973), and references cited therein.
- (16) S. J. Riley and P. E. Siska, *J. Chem. Phys.*, to be submitted for publication.
- (17) The program parameters are the same as those used for analysis of the data collected for the nonpolar partners.^{2b} A 5X 5 matrix of polynomial coefficients and $u_0 = 70$ m/sec are used for all three systems.
- (18) H. B. A. Bente, Ph.D. Thesis, Cornell University, 1974.

Photochemistry in the Adsorbed Layer. I. Photolyses of Alkyl Ketones in the Presence of Nitric Oxide

Yutaka Kubokawa* and Masakazu Anpo

Department of Applied Chemistry, University of Osaka Prefecture, Sakai, Osaka, Japan 591 (Received December 4, 1973; Revised Manuscript Received March 20, 1974)

Publication costs assisted by the University of Osaka Prefecture

The effect of nitric oxide upon the photolyses as well as phosphorescence spectra of alkyl ketones adsorbed on porous Vycor glass has been investigated. Comparison of the phosphorescence intensities suggests that the excited states of methyl ethyl ketone deactivate more efficiently than those of 2-pentanone. Quenching experiments for 2-pentanone show that 44% of the ethylene formation occurs from the singlet excited states. The lifetime of the triplet excited states as well as of the radicals formed on the surface have been discussed by using the Stern-Volmer relationship. In the adsorbed layer, the lifetime of the propyl radical formed in the primary process is longer than that of the ethyl radical.

Introduction

It would be expected that the features of the photochemical reaction in the adsorbed layer are quite different from those of the corresponding reaction in the gas phase. Especially, it is of interest to investigate how the reactivity of the excited states and of the radicals themselves vary, when they are formed on the surface, from the standpoints of the energy transfer between the solid and the adsorbed species as well as the mechanism of the surface reactions.

Since the classical work of de Boer,¹ the photochemistry and electronic spectra of adsorbed molecules have been investigated by a number of workers.^{2,3} However, there is relatively little work along this line. Consequently, the investigation of the photochemistry of alkyl ketones adsorbed on

porous Vycor glass has been undertaken. Some of the results have already been described by one of the present authors.⁴ However, the nature of the excited state in the adsorbed layer is unclear. For photolyses in the gas phase and solution, information on the nature and reactivity of the excited states has been obtained from studies of the effect of addition of a quencher such as nitric oxide. It seems promising to extend the quenching technique to photolysis in the adsorbed layer. In the present work, therefore, photolyses of alkyl ketones adsorbed on porous Vycor glass have been carried out in the presence of gaseous nitric oxide. Furthermore, the phosphorescence spectra of the alkyl ketones adsorbed have been investigated for direct measurements of the excited states.

Experimental Section

Materials. (a) 2-Pentanone (Tokyo Kasei Kogyo Co., grade, 96 mol %, bp 101°) was purified by means of preparatory chromatography and then vacuum distilled bulb-to-bulb. Analysis by vapor-phase chromatography equipped with flame ionization detection showed one impurity (less than 0.5%) which eluted after 2-pentanone on a polyethylene glycol 1500 column.

(b) Methyl ethyl ketone (Nakarai Chemical Co. grade, 99.9 mol %, bp 79°) was repurified by low-temperature distillation. The ketones were stored in the dark at room temperature.

(c) Nitric oxide (Takachiho Kogyo Co.) was of extra pure grade and used without further purification. Commercial tank oxygen was purified by low-temperature distillation.

(d) Porous Vycor glass (Corning No. 7930) was cut in the form of 2.5 × 2.6 cm from a 1 mm thick sheet and used as adsorbent. Prior to the experiments, the specimen was heated in oxygen at 600° for 7 hr in order to remove carbonaceous materials. On such treatment the color of the porous Vycor glass specimen changed from yellow-brown to blue-white. Its BET surface area⁵ determined by nitrogen adsorption was 160 m²/g.

Apparatus and Procedure. The quartz cell used in the present study was about 30 cm long and 3.0 cm in diameter with a total volume of about 300 ml. The specimen could be moved vertically between the window section at room temperature and the furnace section, so that its temperature could be changed from room temperature to 800°. A conventional vacuum system was used. A ketone sample was allowed to be adsorbed at room temperature on the glass specimen which had been evacuated at 500° for 7 hr. For the samples used, the amount of ketone remaining in the gas phase was negligibly small after adsorption for several hours. Subsequently, nitric oxide was introduced into the cell, its partial pressure being adjusted in the range of 0.01–10 Torr. Then, photolysis was carried out using a Toshiba SHL-100 ultra-high-pressure mercury lamp without filter for 15–60 min. When the photolysis was completed, the specimen was moved up from the window section to the furnace section. The reaction products together with unreacted ketone were desorbed by means of a Toepler pump and cold traps, increasing the temperature of the specimen to 100°. The products were separated by low-temperature distillation using cold traps and a gas-buret collector. The noncondensable gases such as CO and CH₄ were collected from a trap at -215° and the C₂H₄, C₃H₈, C₃H₆, and C₂H₆ fraction at -130°. Analysis was made by vapor-phase chromatography using a 3-m column of Porapak Q for light hydrocarbons and a 2-m column of molecular sieve 5A for the noncondensable gases.

Phosphorescence measurements of the adsorbed ketones were carried out with an Aminco-Bowman spectrophotofluorimeter equipped with a rotating motor sector assembly. Powdered porous Vycor glass was used as the adsorbent, since a quartz cylindrical cell, 4 mm in diameter, was used. The emission spectra were obtained at liquid nitrogen temperature using exciting light of 313 nm. Under such conditions, it was confirmed that no luminescence was detectable from porous Vycor glass.

Results

(1) *Photolyses in the Adsorbed Layer.* Results of photolyses of acetone, methyl ethyl ketone, and 2-pentanone adsorbed on porous Vycor glass are shown in Table I. It is

TABLE I: Photolysis of the Alkyl Ketones Adsorbed at 25°

Compound	Amount adsorbed ml (STP)/g	Yield of main products, ml/hr × 10 ⁻⁵
Acetone ^a	1.06	CH ₄ (12.0), C ₂ H ₆ (8.0)
Methyl ethyl ketone ^b	0.89	CH ₄ (30.0), C ₂ H ₆ (930.0)
2-Pentanone ^c	0.74	CH ₄ (50.0), C ₂ H ₄ (3200.0) C ₃ H ₈ (2400.0)

^a CO was a minor product. ^b CO, C₂H₄, and C₄H₁₀ were minor products. ^c CO, C₃H₆, and C₆H₁₄ were minor products. CH₃COCH₃ was another main product, its amount being not determined.

well known^{6,7} that alkyl ketones with a γ -hydrogen atom, such as 2-pentanone, undergo Norrish type I processes (dissociation into radicals) as well as Norrish type II processes (intramolecular elimination). In the gas-phase photolysis of 2-pentanone at room temperature, the amount of products derived from the type I process ($\text{CH}_3\text{COC}_3\text{H}_7 + h\nu \rightarrow \text{CH}_3\dot{\text{C}}\text{O} + \dot{\text{C}}_3\text{H}_7$) is less than 5% of that from the type II process ($\text{CH}_3\text{COC}_3\text{H}_7 + h\nu \rightarrow \text{C}_2\text{H}_4 + \text{CH}_3\text{COCH}_3$) according to the work of Ausloos, *et al.*⁸ As seen in Table I, the rate of C₃H₈ formation is more than 70% that of C₂H₄ formation. Such an enhancement of the occurrence of the type I process may be ascribed to the presence of surface OH groups; its details will be described in a forthcoming paper.

It is to be noted that negligible formation of CO occurs. Although the true nature of such a phenomenon is unclear at present, it is likely that acetyl radicals formed in the primary process are bound to the surface, rearranging to a stable surface complex. From the results of Table I the photochemical reaction efficiencies of the three ketones can be compared: acetone, 0.01 (CH₄); methyl ethyl ketone, 1.0 (C₂H₆); 2-pentanone, 10.0 (C₂H₄ + C₃H₈). A marked difference can be seen in the efficiencies, in contrast with essentially the same efficiency observed for the gas-phase photolysis^{6,9} of these compounds.

Results of photolyses of the ketones in the presence of nitric oxide are shown in Figures 1 and 2. In the photolysis of 2-pentanone, the rate of ethylene formation (type II process) is decreased by increasing the nitric oxide pressure, leveling off to a constant value. Considering that nitric oxide is an efficient triplet quencher and there is a marked difference in its reactivity toward the excited singlet and triplet states, the amount of nonquenchable reaction (44%) may be attributed to reaction from the excited singlet state, with the remainder of the reaction (56%) occurring from the triplet state. The gas-phase photolysis of 2-pentanone in the presence of oxygen has been investigated by Ausloos, *et al.*,¹⁰ who observed that the nonquenchable fraction of the C₂H₄ formation was 43%, attributing it to reaction from the excited singlet state. Thus, there is little or no difference in the amount of nonquenchable type II process between the photolyses of 2-pentanone in the gas phase and in the adsorbed layer.

Figures 1 and 2 show that the rates of formation of C₃H₈ as well as of C₂H₆ are decreased markedly with increasing nitric oxide pressure, finally approaching zero around 0.3 Torr for C₃H₈ and 1.0 Torr for C₂H₆, as expected from the

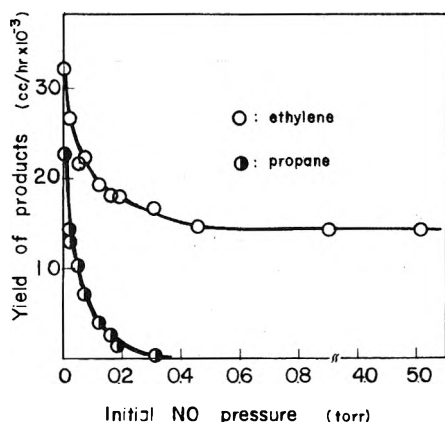


Figure 1. Effect of nitric oxide upon the rate of 2-pentanone photolysis at 25°. The amount of 2-pentanone adsorbed was 3.29×10^{-5} mol/g. During the photolysis nitric oxide was somewhat consumed; it was confirmed, however, that the resulting pressure decrease did not affect the value of the constants A and B in the Stern-Volmer equation.

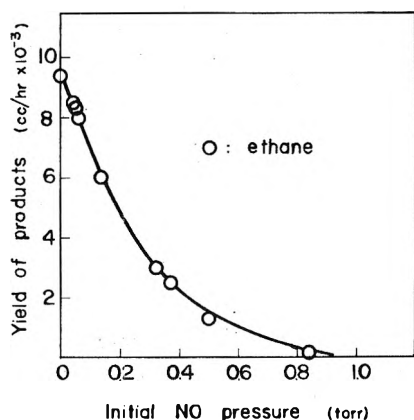


Figure 2. Effect of nitric oxide upon the rate of methyl ethyl ketone photolysis at 25°. The amount of methyl ethyl ketone adsorbed was 3.99×10^{-5} mol/g.

action of nitric oxide as a radical scavenger. It should be noted that, in addition to such scavenging action, the decrease in the rate of formation shown in Figures 1 and 2 is caused by quenching of the excited triplet states with nitric oxide.

(2) *Phosphorescence Spectra in the Adsorbed Layer.* The intensity of the phosphorescence spectra of adsorbed 2-pentanone was about 20 times larger than that of adsorbed methyl ethyl ketone. The phosphorescence of adsorbed acetone was very weak and undetectable. Such behavior is in contrast with the results obtained by O'Sullivan and Testa,¹¹ who observed much less difference in the intensities of the phosphorescence spectra of a series of alkyl ketones in EPA glass. Apart from the intensity, the shapes of the phosphorescence spectra in the adsorbed layer are similar to those observed for the spectra in EPA glass, except that the former exhibits a blue shift.

The effect of addition of nitric oxide as well as oxygen on the phosphorescence intensity was investigated. Figure 3 shows plots of Q_0/Q vs. nitric oxide or oxygen pressure, where Q and Q_0 are the phosphorescence intensity of 2-pentanone in the presence and absence of nitric oxide or oxygen. It is seen that nitric oxide quenches about three times more efficiently than oxygen.

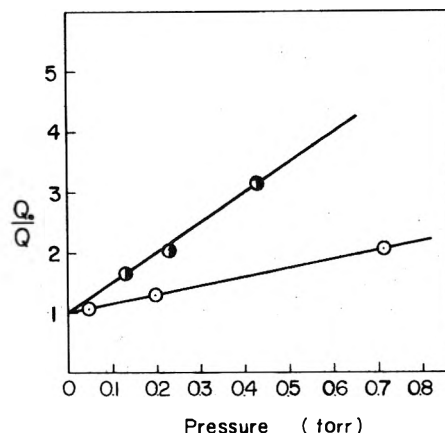
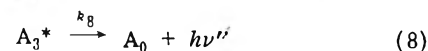
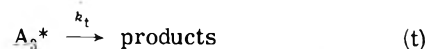
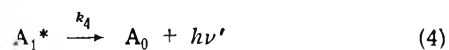
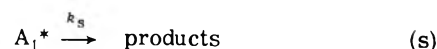
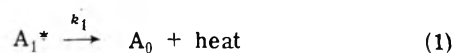
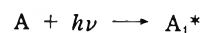


Figure 3. Stern-Volmer plot for quenching of phosphorescence of 2-pentanone adsorbed on porous Vycor glass with nitric oxide or oxygen present at 77°K: excitation wavelength, 313 nm; O, oxygen; ●, nitric oxide.

Discussion

(1) *Phosphorescence Intensity and Photochemical Reaction Efficiency.* The photolyses of the adsorbed ke-

Scheme I



tones may be represented by Scheme I. Using the steady-state approximation in the excited states

$$[T] = \left(\frac{I}{k_1 + k_s + k_4 + k_{isc}} \right) \left(\frac{k_{isc}}{k_5 + k_t + k_8} \right) \quad (\text{I})$$

where $[T]$ is the concentration of the triplet molecules, and I is the intensity of the light absorbed by molecule A . Using the intersystem crossing efficiency, $\Phi_{isc} = k_{isc}/(k_1 + k_s + k_4 + k_{isc})$

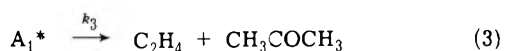
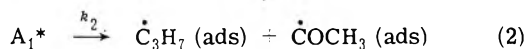
$$[T] = [k\epsilon[A]/(k_5 + k_t + k_8)]\Phi_{isc} \quad (\text{II})$$

where $[A]$ is the amount adsorbed and ϵ is the extinction coefficient. As will be described in part II of this series, in the adsorbed layer the molar extinction coefficient ϵ for 2-pentanone is four times larger than that of methyl ethyl ketone. Considering that the value of Φ_{isc} is 0.9 ± 0.1 for acetone¹² and 0.64 for 2-pentanone,¹³ it appears that there is no marked difference between the Φ_{isc} values for methyl ethyl ketone and for 2-pentanone. By assuming the same Φ_{isc} value for both ketones the denominator of eq II for methyl ethyl ketone is five times larger than that for 2-pentanone, since the phosphorescence intensity of 2-pentanone

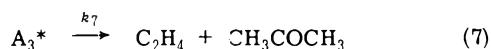
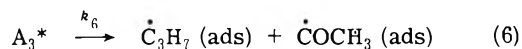
is 20 times higher than that of methyl ethyl ketone as described above. Such a difference in the denominator of eq II may be attributed to the difference in value of k_5 , since neither k_t ¹⁴ nor k_8 ¹¹ for methyl ethyl ketone are expected to be larger than that for 2-pentanone. It is concluded, therefore, that the k_5 value for methyl ethyl ketone will be at least five times larger than that for 2-pentanone. Considering that the blue shift for methyl ethyl ketone is greater, *i.e.*, more strongly hydrogen bonded to the surface OH groups, than that for 2-pentanone, the stronger the adsorption, the more efficient radiationless deactivation (k_5) is and the smaller the resulting extinction coefficient becomes. In fact, with acetone, where the blue shift is the greatest, the smallest ϵ and the largest k_5 values are observed. This conclusion is based upon the phosphorescence measurements at 77°K. A similar trend, however, is expected for the photolysis at room temperature.¹⁵ In fact, the efficiency of the photochemical reaction in the adsorbed layer decreases in the order 2-pentanone > methyl ethyl ketone > acetone in agreement with the above conclusion.

Although in the present work it seems unfeasible to compare the extinction coefficients of these ketones as well as their quantum yields of photolysis between the adsorbed layer and the gas phase, a decrease in the extinction coefficient on adsorption has been reported by a number of workers.¹⁶⁻¹⁸ The following tentative conclusion may therefore be allowed. The photochemical reaction efficiencies of ketones are decreased on adsorption owing to the increase in their efficiency of radiationless deactivation and also to the decrease in their extinction coefficients.

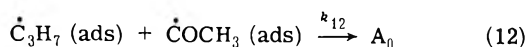
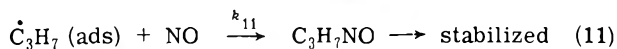
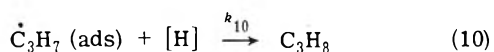
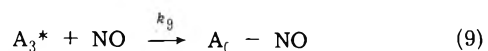
(2) *Effect of Added Nitric Oxide upon Photolyses.* The photolysis of 2-pentanone in the presence of nitric oxide is described as follows. In Scheme I, reaction s is replaced by



and reaction t by



The following reactions are included



In reaction 10, [H] represents a hydrogen donor on the surface. In this reaction scheme α cleavage of 2-pentanone from the excited singlet states (reaction 2) may be neglected, since the striking difference in the reactivity of the excited singlet and triplet states toward α cleavage of alkyl ketones has been emphasized by a number of workers.¹⁹⁻²² Thus, the following Stern-Volmer equation is obtained for the formation of C_3H_8 from 2-pentanone, using the steady-state treatment.

$$Q_0/Q = (1 + A[NO])(1 + B[NO]) \quad (III)$$

where $A = k_9/(k_5 + k_6 + k_7 + k_8)$, $B = k_{11}/([H]k_{10} +$

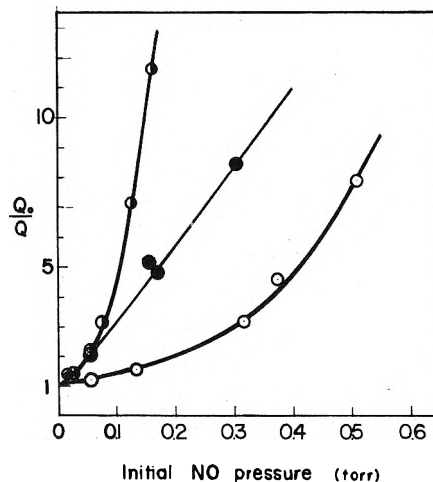


Figure 4. Stern-Volmer plot for products quenched in methyl ethyl ketone and 2-pentanone photolysis in the adsorbed layer at 25°C: O, ethane (methyl ethyl ketone); ◐, propane (2-pentanone); ●, ethylene (2-pentanone).

$[COCH_3]k_{12})$. Q and Q_0 are the rate of C_3H_8 formation in the presence and absence of nitric oxide. The plot of Q_0/Q vs. nitric oxide pressure is shown in Figure 4. The constants A and B are determined such that best fit to the experimental curve is obtained: $A = 3.6 \times 10^5 M^{-1}$, $B = 4.9 \times 10^6 M^{-1}$.²³

As described above, in the photolysis of 2-pentanone C_2H_4 is formed from the singlet as well as the triplet states. The following equation holds for C_2H_4 formation from the triplet state, which is determined by subtracting the non-quenchable amount of C_2H_4 formed with nitric oxide present from the total amount of C_2H_4 formed without nitric oxide present.

$$\frac{Q_0}{Q} = \left(1 + \frac{k_9[NO]}{k_5 + k_6 + k_7 + k_8} \right) = (1 + A[NO]) \quad (IV)$$

Q and Q_0 are the rates of C_2H_4 formation from the triplet state in the presence and absence of nitric oxide, respectively. From the slope of the Stern-Volmer plot (Figure 4) the value of A is $4.26 \times 10^5 M^{-1}$, in agreement with that obtained from eq III. This suggests the reliability of A and B values determined as described above, *i.e.*, the plausibility of the assumption that formation of C_3H_8 from the excited singlet state may be neglected. From the Stern-Volmer plot of the phosphorescence quenching by nitric oxide the value of A is $8.5 \times 10^4 M^{-1}$, being somewhat smaller than that obtained from eq III or IV. Such a discrepancy may be attributed to the difference in the measurement temperature.²⁴

For the formation of C_2H_6 in the photolysis of methyl ethyl ketone, a Stern-Volmer equation similar to eq III is obtained. The corresponding constants for methyl ethyl ketone are determined in a similar manner with the following results: $A' = 9.5 \times 10^4 M^{-1}$, $B' = 2.4 \times 10^5 M^{-1}$.²³ It is seen that the value of A for 2-pentanone is four times larger than that for methyl ethyl ketone. It should be noted that there is a similar difference between the lifetimes of the excited triplet states of both ketones determined from the phosphorescence measurements described above.

Comparison of the values of B for both ketones shows that the value of 2-pentanone is 20 times larger than that of methyl ethyl ketone. Although it is expected that in the adsorbed layer the reactivity of the radicals is different from

that in the gas phase,²⁵ it seems very difficult to attribute such a large difference in *B* only to the difference in *k*₁₁. In other words, $([H]k_{10} + [\dot{C}OCH_3]k_{12})$ for 2-pentanone should be smaller than that for methyl ethyl ketone. It may therefore be concluded that in the adsorbed layer the lifetime of the *n*-propyl radical is longer than that of the ethyl radical. With respect to the nature of such a difference in the lifetime, it is at present impossible to decide between the two possibilities; recombination ($[\dot{C}OCH_3]k_{13}$) and hydrogen abstraction ($[H]k_{10}$) of the radicals.

Acknowledgment. The authors wish to thank Professor H. Tsubomura and Dr. T. Sakata of Osaka University for making the spectrophotofluorimeter available for their present work.

References and Notes

- (1) J. H. de Boer, *Z. Phys. Chem.*, **B 15**, 281 (1932).
- (2) A. N. Terenin, *J. Phys. Chem. USSR*, **14**, 1362 (1940).
- (3) H. P. Leftin and E. Herman, *Proc. Int. Congr. Catal.*, **3rd**, 1964, **1**, 1064 (1965).
- (4) Y. Kubokawa, M. Kubo, and G. Nanjo, *Bull. Chem. Soc. Jap.*, **43**, 3968 (1970).
- (5) S. Brunauer, P. H. Emmett, and E. Teller, *J. Amer. Chem. Soc.*, **60**, 309 (1938).
- (6) J. G. Calvert and J. N. Pitts, Jr., "Photochemistry," Wiley, New York, N.Y., 1966, p 377.
- (7) N. J. Turro, J. C. Dalton, K. Daws, G. Farrington, R. Hautala, D. Morton, M. Niemczyk, and N. Schore, *Accounts Chem. Res.*, **5**, 92 (1972).
- (8) P. Ausloos and E. Murad, *J. Amer. Chem. Soc.*, **80**, 5929 (1958).
- (9) R. B. Cundall and A. S. Davies, *Trans. Faraday Soc.*, **62**, 2444 (1966).
- (10) R. P. Borkowski and P. Ausloos, *J. Phys. Chem.*, **65**, 2257 (1961).
- (11) M. O'Sullivan and A. C. Testa, *J. Amer. Chem. Soc.*, **92**, 258 (1970).
- (12) R. F. Borkman and D. R. Kearns, *J. Chem. Phys.*, **44**, 945 (1965).
- (13) N. C. Yang, S. P. Elliot, and B. Kim, *J. Amer. Chem. Soc.*, **91**, 7551 (1969).
- (14) P. Ausloos and E. Murad, *J. Phys. Chem.*, **65**, 519 (1961).
- (15) R. D. Rauh and P. A. Leermakers, *J. Amer. Chem. Soc.*, **90**, 2246 (1968).
- (16) M. Robin, *J. Chem. Educ.*, **33**, 536 (1956).
- (17) M. Robin and K. N. Trueblood, *J. Amer. Chem. Soc.*, **79**, 5138 (1957).
- (18) J. Kobayashi, *Nippon Kagaku Zasshi*, **80**, 29 (1959).
- (19) R. B. Cundall and A. S. Davies, *Proc. Roy. Soc., Ser. A*, **290**, 563 (1966).
- (20) R. K. Boyd, G. B. Carter, and K. O. Kutschke, *Can. J. Chem.*, **46**, 175 (1968).
- (21) N. C. Yang, E. D. Feit, Man Him Hui, N. J. Turro, and J. C. Dalton, *J. Amer. Chem. Soc.*, **92**, 6974 (1970).
- (22) J. C. Dalton, K. Dawes, N. J. Turro, D. S. Weiss, J. A. Barltrop, and J. D. Coyle, *J. Amer. Chem. Soc.*, **93**, 7213 (1971).
- (23) In the photolysis of 2-pentanone propane formation is quenched more efficiently than ethylene formation (Figure 1), suggesting that *B* should be larger than *A*. Thus, the assignment of the two constants is possible. A similar relation is expected to hold for the photolysis of methyl ethyl ketone. Some evidence supporting it will be given later.
- (24) The temperature dependence of *A* appears to be determined overall by the temperature dependence of the quenching rate constant rather than that of the triplet lifetime, since the latter should decrease with increasing temperature.
- (25) M. I. Christie and J. S. Frost, *Trans. Faraday Soc.*, **61**, 468 (1965).

Photochemistry in the Adsorbed Layer. II. Energy Transfer in the Adsorbed Layer

Masakazu Anpo and Yutaka Kubokawa*

Department of Applied Chemistry, University of Osaka Prefecture, Sakai, Osaka, Japan 591 (Received December 4, 1973; Revised Manuscript Received March 28, 1974)

Publication costs assisted by the University of Osaka Prefecture

In the photolyses of acetone-methyl ethyl ketone and acetone-2-pentanone mixtures adsorbed on porous Vycor glass, the presence of acetone enhanced the rate of photolysis of methyl ethyl ketone as well as that of 2-pentanone. For a methyl ethyl ketone-2-pentanone mixture the rate of photolysis of 2-pentanone was increased by added methyl ethyl ketone, while the photolysis rate of methyl ethyl ketone was decreased by added 2-pentanone. Such behavior suggests that intermolecular energy transfer occurs in the adsorbed layer, its direction being acetone → methyl ethyl ketone → 2-pentanone. The occurrence of this energy transfer was correlated with the lowering of the ground state of ketones owing to hydrogen bond formation with surface OH groups.

Introduction

The intermolecular energy transfer process in gas phase and solution has been studied extensively in the recent years.¹⁻³ However, there seems no report on such energy transfer in the adsorbed layer. It would be expected that the investigation of energy transfer in the adsorbed layer will give useful information on the energy levels of the excited and ground states of molecules on a solid surface. Such information appears to be important for understanding photochemistry in the adsorbed layer.

During the study of the photolysis of alkyl ketones ad-

sorbed on porous Vycor glass,^{4,5} a phenomenon has been found which suggests the occurrence of intermolecular energy transfer. The results are described in the present work.

Experimental Section

Details of the materials, apparatus, and procedures used in the present work have been described in part I of this series. The absorption spectra of adsorbed ketones were determined with a Hitachi EPS 3T type spectrophotometer, measuring transmission through the sample. A quartz cell

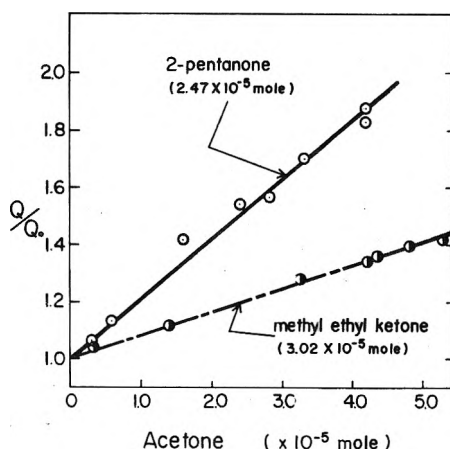


Figure 1. Photolysis of 2-pentanone–acetone and methyl ethyl ketone–acetone mixtures. Q and Q_0 are the rate of photolysis at 25° in the presence and absence of acetone, respectively. These ketones were adsorbed at 25° for several hours. The amount adsorbed was kept constant at 2.47×10^{-5} mol for 2-pentanone and at 3.02×10^{-5} mol for methyl ethyl ketone.

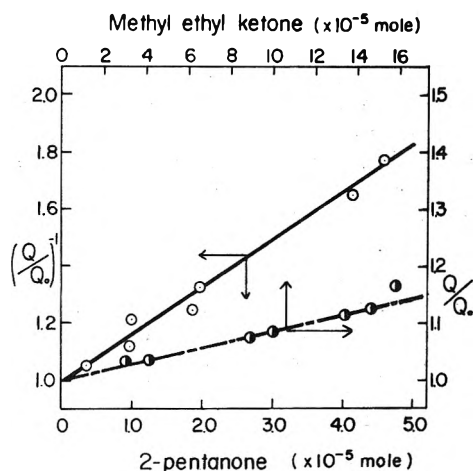


Figure 2. Photolysis of 2-pentanone–methyl ethyl ketone mixtures: \bullet , rate increase of 2-pentanone photolysis by added methyl ethyl ketone; \circ , rate decrease of methyl ethyl ketone photolysis by added 2-pentanone. The amount adsorbed was kept constant at 3.02×10^{-5} mol for methyl ethyl ketone and at 2.29×10^{-4} mol for 2-pentanone.

having two planar windows 10 mm apart was used. The cell was placed just before the photomultiplier in order to minimize scattering error. Another porous Vycor glass sample was pretreated under the same conditions in a separate cell and used as a blank in the reference beam.

Results

(1) *Photolysis of Acetone–Methyl Ethyl Ketone and Acetone–2-Pentanone Mixtures.* As described in part I of this series, the main gaseous products of the photolysis of alkyl ketones in the adsorbed layer are CH_4 and C_2H_6 for acetone, C_2H_6 for methyl ethyl ketone, and C_3H_8 , C_2H_4 , and CH_3COCH_3 for 2-pentanone. It is to be noted that 2-pentanone undergoes a Norrish type I as well as a type II process.^{6,7} The relative quantum yields obtained from the gaseous products are 0.01 (CH_4) for acetone, 1.0 (C_2H_6) for methyl ethyl ketone, and 10.0 ($\text{C}_2\text{H}_4 + \text{C}_3\text{H}_8$) for 2-pentanone. This indicates that in the photolysis of mixtures containing acetone the products from acetone are negligible, leading to the conclusion that it is impossible to determine

TABLE I: Effect of Hydrogen Bond upon the $n\text{--}\pi^*$ Transition (nm) of the Alkyl Ketones at 25°

Compounds	Acetone	Methyl ethyl ketone	2-Pentanone
Gas phase	276.5	278.0	279.0
Heptane ^a	276.7	277.5	279.0
Methanol ^a	270.0	272.0	273.5
Vycor glass	262.0	270.0	273.0

^a Reference 9.

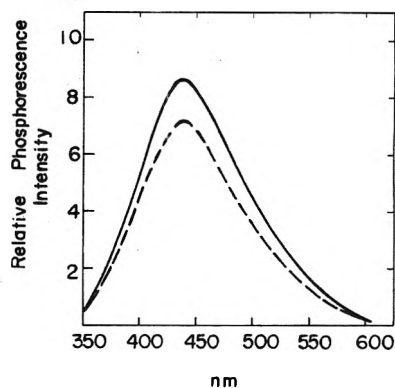


Figure 3. Increase in the phosphorescence intensity of 2-pentanone by added acetone: excitation wavelength, 313 nm. The amounts of 2-pentanone and acetone adsorbed are 3.29×10^{-5} and 1.29×10^{-5} mol/g, respectively: (---) pure 2-pentanone; (—) 2-pentanone–acetone mixture.

how the rate of photolysis of acetone changes in the mixture.

The changes in the rate of photolysis of methyl ethyl ketone as well as of 2-pentanone caused by added acetone are shown in Figure 1. The rates are increased with increasing amount of acetone added, the increase being larger in the case of the acetone–2-pentanone mixture. Essentially the same results were obtained for the case where the order of adsorption of the ketones was reversed. This suggests that adsorption equilibrium is established after adsorption for several hours.

(2) *Photolysis of 2-Pentanone–Methyl Ethyl Ketone Mixtures.* In this case, the effect of added methyl ethyl ketone upon the rate of photolysis of 2-pentanone was investigated by a series of experiments using a constant amount of 2-pentanone and varying amounts of methyl ethyl ketone adsorbed, since the rate of photolysis of 2-pentanone was dependent upon its amount adsorbed. The results are shown in Figure 2. The effect of added 2-pentanone upon the rate of photolysis of methyl ethyl ketone was investigated in a similar manner. As shown in Figure 2, the rate of photolysis of methyl ethyl ketone is decreased with increasing amount of 2-pentanone, while that of 2-pentanone is increased with increasing amount of methyl ethyl ketone. The extent of the increase is much smaller than that of the decrease.

(3) *Phosphorescence Spectra of Acetone–2-Pentanone Mixtures.* Phosphorescence spectra of 2-pentanone as well as of a 2-pentanone–acetone mixture are shown in Figure 3. It is seen that the phosphorescence intensity for the mixture is higher than that for pure 2-pentanone. The phosphorescence of acetone was very weak and not detectable. This suggests that such an increase in the phosphorescence intensity may be attributed to an increase in the intensity of 2-pentanone phosphorescence.

(4) *Absorption Spectra in the Adsorbed Layer.* Acetone, methyl ethyl ketone, and 2-pentanone adsorbed on porous Vycor glass absorb light at shorter wavelengths than the corresponding compound in the gas phase. The wavelengths of maximum absorption are shown in Table I. A marked blue shift is observed with acetone, its magnitude being similar to that found for the acetone-Silica Gel system investigated by Leermakers and Thomas.⁸ Blue shifts of the (n, π^*) bands are observed with ketones in polar solvents, being attributed to hydrogen bond formation with solvents.^{9,10} From a study of ir spectra, Low, *et al.*,¹¹ have concluded that the adsorption force in the ketone-porous Vycor glass system is mainly attributable to hydrogen bonding between the surface OH groups and the C=O groups of the ketones.

It appears that the strength of hydrogen bonding is determined by the acidity of the OH groups and the basicity of the solvents.^{8,9} The blue shifts observed with porous Vycor glass are greater than those obtained with solvents (Table I), suggesting a strong proton-donating power of the surface OH groups. As shown in Table I, the blue shift observed with the adsorbed ketones decreases in the order acetone > methyl ethyl ketone > 2-pentanone. Such a trend can be explained in terms of the concept that an increase in the electron-withdrawing power of the alkyl groups in the ketones increases its ability to accept the hydrogen bond as has been suggested by Balasubramanian and Rao.¹⁰

The spectra of the adsorbed ketones increased in intensity proportional to the amounts adsorbed without changes in relative intensity for the bands from 240 to 320 nm. In Figure 4, the absorbance at the wavelength of maximum absorption for the ketones is plotted against the amount adsorbed, a linear relationship being obtained in the range of amount adsorbed from 1.60×10^{-6} to 3.20×10^{-4} mol/g. It is seen that there is a marked difference in the relative extinction coefficients, the order being 2-pentanone > methyl ethyl ketone > acetone. Although the true nature of such a difference is unclear at present, a marked reduction in the extinction coefficient on adsorption has been already reported by a number of workers.¹²⁻¹⁴

Discussion

The results concerning the photolyses and phosphorescence spectra in the adsorbed layer described above suggest the possibility that an intermolecular energy transfer process takes place in the adsorbed layer, *i.e.*, excitation energy absorbed by an acetone molecule is transferred to a 2-pentanone molecule to give an excited state, the direction of energy transfer being acetone \rightarrow methyl ethyl ketone \rightarrow 2-pentanone.

The situation in the adsorbed layer is similar to that in solution.¹⁵ The donor-acceptor pair is held in a fixed position for a relatively long time ("cage effect"), more efficient energy transfer being expected to occur compared to that in the gas phase. It is well known that the efficiency of the energy transfer process is closely associated with the exothermicity of the transfer process. From the similarities between the adsorbed layer and solution, the blue shifts observed for the ketones adsorbed on porous Vycor glass may be ascribed to the lowering of the ground states rather than of the excited states.^{10,16-18} From the results shown in Table I it is concluded that in the adsorbed layer the ground state is lowered by 5.5 kcal/mol for acetone, by 3.0 kcal/mol for methyl ethyl ketone, and by 2.0 kcal/mol for 2-pentanone compared to that in the gas phase, although

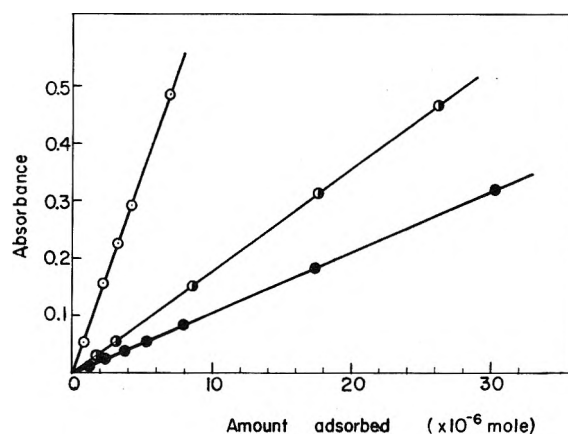
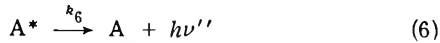
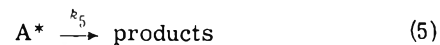
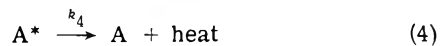
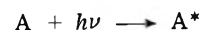
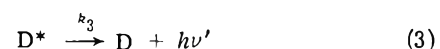
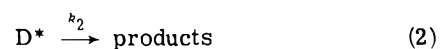
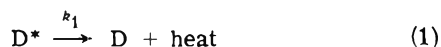
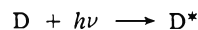


Figure 4. Relationship between absorbance and amounts adsorbed of the alkyl ketones at wavelength of maximum absorption. Porous Vycor glass used in these experiments was about 0.6 g: ●, acetone; ◐, methyl ethyl ketone; ○, 2-pentanone.

the excited state levels are almost the same throughout the three ketones.

Such considerations are applicable to the singlet excited states. In the present system the most probable energy transfer process appears to be triplet-triplet transfer. Although no information is available on the excited triplet state in the adsorbed layer, a similar lowering of the ground state is expected for the transition between the singlet and triplet state.^{19,20} This suggests that the energy difference between the excited triplet and the ground state is larger than in the gas phase, the difference being the largest for acetone and the smallest for 2-pentanone. On such a basis it appears to be understood that the intermolecular energy transfer in the present system occurs in the direction acetone \rightarrow methyl ethyl ketone \rightarrow 2-pentanone.²¹

In order to discuss the energy transfer process quantitatively, the following mechanism is proposed



The rate of photolysis of the ketone A (acceptor) is increased by addition of the ketone D (donor) as described above. Using steady-state treatment such an increase in the rate of photolysis is

$$\frac{Q}{Q_0} = 1 + \frac{I_D k_7 [A]}{I_A (k_1 + k_2 + k_3 + k_7 [A])} \quad (I)$$

TABLE II: Values of $k_7/(k_1 + k_2 + k_3)$ ($\times 10^4$ g/mol) for Mixtures of the Alkyl Ketones at 25°

	CH_3COCH_3 $+$ $\text{CH}_2\text{COC}_3\text{H}_7^a$	CH_3COCH_3 $+$ $\text{CH}_3\text{COC}_2\text{H}_5^a$	$\text{CH}_3\text{COC}_2\text{H}_5$ $+$ $\text{CH}_3\text{COC}_3\text{H}_7^a$	$\text{CH}_3\text{COC}_3\text{H}_7$ $+$ $\text{CH}_3\text{COC}_2\text{H}_5^a$
$k_7/(k_1 + k_2 + k_3)$	25.70	2.70	1.55	1.64

^a The amount adsorbed was kept constant in the mixtures of alkyl ketones.

where Q and Q_0 are the rate of photolysis of ketone A in the presence and absence of ketone D, respectively, I_D and I_A are the intensity of the light absorbed by ketone D and ketone A, respectively. $[A]$ represents the amount of ketone A adsorbed.

As seen in Figure 4, the absorbed light intensity varies linearly with the amount of adsorbed ketones, leading to the eq $I_D \propto \epsilon_D[D]$ and $I_A \propto \epsilon_A[A]$ where ϵ is the molar extinction coefficient. Hence, eq I becomes

$$\frac{Q}{Q_0} = 1 + \frac{\epsilon_D k_7 [D]}{\epsilon_A (k_1 + k_2 + k_3 + k_7 [A])} \quad (\text{II})$$

From Figure 4, values of ϵ_D/ϵ_A are determined as follows: $\epsilon(2\text{-pentanone})/\epsilon(\text{acetone}) = 7.21$, $\epsilon(\text{methyl ethyl ketone})/\epsilon(\text{acetone}) = 1.70$, $\epsilon(2\text{-pentanone})/\epsilon(\text{methyl ethyl ketone}) = 4.00$. Thus, values of $k_7/(k_1 + k_2 + k_3)$ are determined from the slopes of Figures 1 and 2, since the value of ϵ_D/ϵ_A and the amount adsorbed of ketone A are known. The results are shown in Table II. For the case where the rate of photolysis of ketone D is decreased by the presence of ketone A, a similar treatment gives the equation

$$\left(\frac{Q}{Q_0}\right)^{-1} = 1 + \frac{k_7 [A]}{(k_1 + k_2 + k_3)} \quad (\text{III})$$

Hence, from the slope of Figure 2, the value of $k_7/(k_1 + k_2 + k_3)$ for a methyl ethyl ketone–2-pentanone mixture is obtained as 1.64×10^4 g/mol, in agreement with the value determined from the rate increase by addition of ketone D (1.55×10^4 g/mol, in Table II). Such coincidence suggests the plausibility of the energy transfer process represented by step 7.

From the values of $k_7/(k_1 + k_2 + k_3)$ (Table II), it is possible to compare the value of k_7 for the methyl ethyl ketone–acetone and the 2-pentanone–acetone systems, since the denominator is the same in both cases. Thus, it is con-

cluded that the excitation energy of acetone is transferred about 10 times more efficiently to 2-pentanone than to methyl ethyl ketone.

References and Notes

- (1) F. Wilkinson, *Advan. Photochem.*, **3**, 241 (1964).
- (2) A. A. Lamola and N. J. Turro, "Energy Transfer and Organic Photochemistry," Wiley, New York, N.Y., 1969, p 17.
- (3) F. S. Wettack and W. A. Noyes, Jr., *J. Amer. Chem. Soc.*, **90**, 3901 (1968).
- (4) Y. Kubokawa, M. Kubo, and G. Nanjo, *Bull. Chem. Soc. Jap.*, **43**, 3968 (1970).
- (5) Y. Kubokawa and M. Anpo, *J. Phys. Chem.*, **78**, 2442 (1974).
- (6) J. G. Calvert and J. N. Pitts, Jr., "Photochemistry," Wiley, New York, N.Y., 1966, p 377.
- (7) N. J. Turro, J. C. Dalton, K. Cawes, G. Farrington, R. Hautala, D. Morton, M. Niemczyk, and N. Schore, *Accounts Chem. Res.*, **5**, 92 (1972).
- (8) P. A. Leermakers and H. T. Thomas, *J. Amer. Chem. Soc.*, **87**, 1620 (1965).
- (9) C. N. R. Rao, G. K. Goldman, and A. Balasubramanian, *Can. J. Chem.*, **38**, 2508 (1960).
- (10) A. Balasubramanian and C. N. R. Rao, *Spectrochim. Acta*, **18**, 1337 (1962).
- (11) J. C. Mcmanus, Y. Harano, and M. J. D. Low, *Can. J. Chem.*, **47**, 2545 (1969).
- (12) M. Robin, *J. Chem. Educ.*, **33**, 526 (1956).
- (13) M. Robin and K. N. Trueblood, *J. Amer. Chem. Soc.*, **79**, 5138 (1957).
- (14) J. Kobayashi, *Nippon Kagaku Zasshi*, **80**, 29 (1959).
- (15) N. J. Turro, "Molecular Photochemistry," W. A. Benjamin, New York, N.Y., 1967, p 92.
- (16) H. Baba, L. Goodman, and P. C. Valenti, *J. Amer. Chem. Soc.*, **88**, 5410 (1966).
- (17) G. C. Pimentel, *J. Amer. Chem. Soc.*, **79**, 3323 (1957).
- (18) T. Abe, *Bull. Chem. Soc. Jap.*, **39**, 936 (1966).
- (19) D. M. Hercules, "Fluorescence and Phosphorescence Analysis," Wiley, New York, N.Y., 1966, p 81.
- (20) W. G. Herkstroeter, A. A. Lamola, and G. S. Hammond, *J. Amer. Chem. Soc.*, **86**, 4537 (1964).
- (21) In the case where the triplet lifetime of 2-pentanone is shorter than that of acetone, an increase in the rate of photolysis of 2-pentanone by added acetone would be expected, even if both ketones had comparable triplet energies, i.e., the rate constant of the energy transfer from 2-pentanone to acetone was almost the same as that of the reverse transfer. However, such an explanation may be excluded, since, as described in part I of this series, the triplet lifetime increases in the order acetone < methyl ethyl ketone < 2-pentanone.

Dissociation Field Effect and Temperature-Jump Kinetics of Ethanolic and Aqueous Phenolphthalein¹

M. W. Massey, Jr., and Z. A. Schelly*

Department of Chemistry, University of Georgia, Athens, Georgia 30602 (Received March 11, 1974;
Revised Manuscript Received August 20, 1974)

Dissociation field effect and temperature-jump results are presented on ethanolic and aqueous phenolphthalein. It is shown that the steady-state approximation cannot be applied to the hydrolysis equilibria in pure ethanol.

Introduction

The mechanism of proton transfer reactions in aqueous solution can be described by three possible paths: protolysis, hydrolysis, or direct proton exchange between donor and acceptor. The unique structural properties of water allow direct participation in the reaction through secondary and tertiary hydration, where structural diffusion is usually the rate-limiting step in the drift mobility of the proton.² The same is true only to a more limited extent in the lower aliphatic alcohols, e.g., ethanol, where structural diffusion and hydrogen bonding is less pronounced. Nevertheless, the requirements for diffusion-controlled proton exchange rates may be still fulfilled, unless other factors become prevalent.

In the present work we report a study of proton transfer relaxation kinetics involving the acid-base indicator phenolphthalein (di-*p*-dioxydiphenylphthalide) in aqueous and ethanolic solutions. In a previous T-jump study of this system in H₂O, structures for the species in equilibrium were suggested³ different from the ones generally accepted.^{4,5} The present study was undertaken to establish the effects caused by different types of perturbation, and the use of a solvent less polar than water. An investigation using different solvents can reveal the intricate details of the reaction mechanism characteristic to pseudo acids, where intramolecular electronic rearrangement accompanies the proton transfer. In the case of phenolphthalein, the extent of this rearrangement is drastic and can be directly followed under specifically controlled conditions. Information about the "polarization" of the molecular states has been obtained by the alternate use of electric field and temperature-jump perturbations.

Experimental Section

Chemicals. Phenolphthalein (certified ACS) was obtained from Fischer, and purified through precipitation from ethanol with water, and then dried under vacuum. The solutions used in the kinetic experiments were prepared from 3.14×10^{-2} or 5.70×10^{-3} M ethanolic stock solutions.

All water used in the experiments was distilled and doubly deionized with research cartridges Model I from the Illinois Water Treatment Co. US Industrial Chemical Co.'s absolute ethanol was further dried with molecular sieve Linde Type 3A.

J. T. Baker's analytical grade NaOH was washed with and dissolved in absolute ethanol, then a sample of it was

titrated with 0.1 N HCl standard Titrisol in water solution.

The electrolyte used in the ethanolic temperature-jump experiments was tetramethylammonium chloride obtained from J. T. Baker.

Apparatus. Our square wave dissociation field effect (DFE) pulse generator used in the electric field-temperature-jump apparatus closely resembles that described by Olsen, *et al.*⁶

Single 32–50-kV square wave pulses (Figure 1) were generated by discharging a low-inductance 0.005- μ F capacitor from Plastic Capacitors Inc. through EG and G GP-15B triggered spark gaps. The pulse width is variable between 0 and about 30 μ sec. The rise time of the pulse is *ca.* 100 nsec, but the fall time is less than 20 nsec (Figure 1). Typically 40-kV pulses 2–3.5- μ sec long were used in the DFE experiments where the chemical relaxations following the trailing edge of the perturbation pulse were observed, rather than the in-field ones.⁷

Spectrophotometric detection⁸ was used for monitoring the transient concentration changes in the relaxing reaction mixtures at the visible absorption maximum of phenolphthalein (λ 552 nm in water and λ 563 in ethanol). The optical system consisted of a 250-W Osram halogen lamp powered by an Electronics Measurements RE40-10ML regulated power supply, a quarter meter Jarrell Ash monochromator, and a mirror box to focus the light beam passing through the sample cell to the end of a glass fiber optic. The fiber optic terminated at the window of an electromagnetically shielded Fairchild KM2433 photomultiplier tube operated with a 15-kilohm dynode chain, and powered by a Power Design 2K20 power supply. The photomultiplier output was fed directly into a Tektronix 7503 oscilloscope with a 7A13 differential comparator and a 7B52 dual time base. Oscilloscope traces were photographed with a Tektronix C-50 camera, and the pictures evaluated graphically in the usual manner. Using 1.5-kilohm terminating resistor the detection system had a rise time of 30 nsec.

The Plexiglas DFE reaction cell used had an outside diameter of 63.5 mm, an optical path length of 29 mm, and a volume of 9 ml. Highly polished flat surfaces 180° apart served as windows for the analyzing light beam. The T-jump cell with 1-cm path length was manufactured of Teflon and had conical quartz windows. A minimum of 5 ml of solution is needed for an experiment, but only 1 ml is heated. Both cells were equipped with highly polished nonmagnetic stainless steel electrodes located 5 and 10 mm apart in the DFE and T-jump experiments, respectively. The liquids in both cells were thermostated to $\pm 0.1^\circ$ by circulating

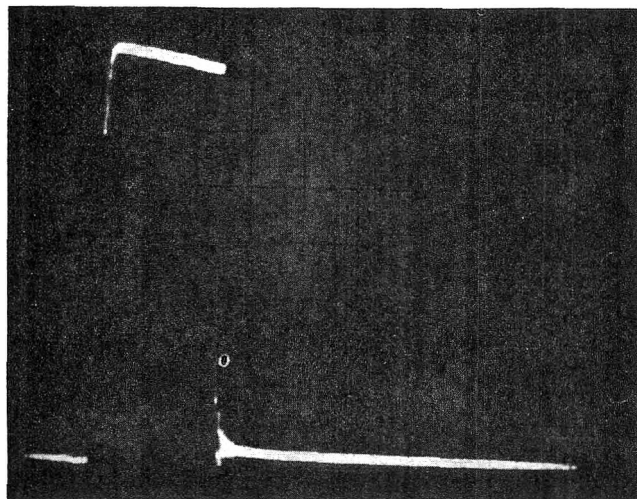


Figure 1. High-voltage square pulse with $3.14 \times 10^{-4} M$ phenolphthalein and $4.76 \times 10^{-4} M$ NaOH ethanolic solution in the cell at 25° : 5×10^3 V/division, $1 \mu\text{sec/division}$.

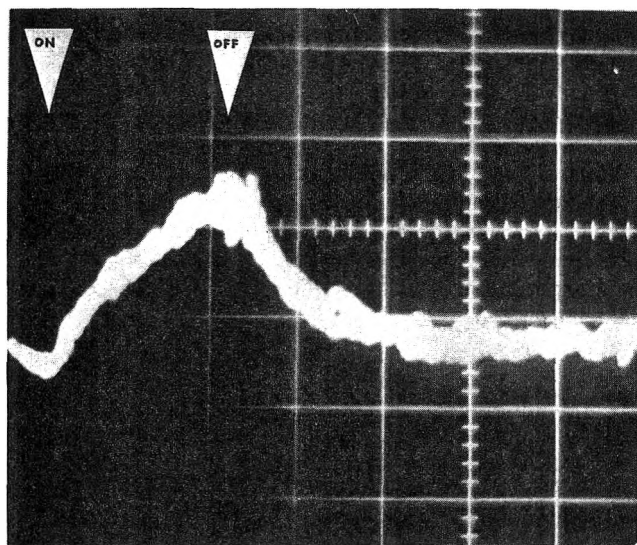


Figure 2. Typical E-jump relaxation of $3.14 \times 10^{-4} M$ ethanolic phenolphthalein at 25° caused by a $2\text{-}\mu\text{sec}$ 40-kV pulse. The location of the perturbation pulse is indicated by arrows. NaOH concentration is $4.76 \times 10^{-4} M$. Direction of increasing analyzing light (λ 563 nm) intensity is toward top of page: vertical axis 100 mV/division , horizontal axis $1 \mu\text{sec/division}$. Two traces superimposed. Due to the high frequency of the noise, relaxation times could be determined from a single trace with a precision of better than 5% in terms of deviation between two extreme possibilities. The reproducibility of the traces was usually better than $\pm 7\%$ in terms of average deviation from the mean.

water through the hollow upper electrodes with a Paratherm U4 thermostat.

Experiments. The E-jump experiments in ethanol were done at 25° , typically using $3 \mu\text{sec}$ or shorter perturbation pulses. Concentration changes during and after the pulse were recorded, however, only the curves obtained at zero field were evaluated. A representative curve is shown in Figure 2. The resistance of the solutions measured in the cell was always greater than 10^4 ohms caused by a maximum ionic strength of $1.03 \times 10^{-3} M$. Maximum heating during the pulse was 0.2° .

All T-jump experiments in ethanol were done at 24.5° as the final temperature, at a $0.3 M$ tetramethylammonium chloride concentration, as the conducting electrolyte. By

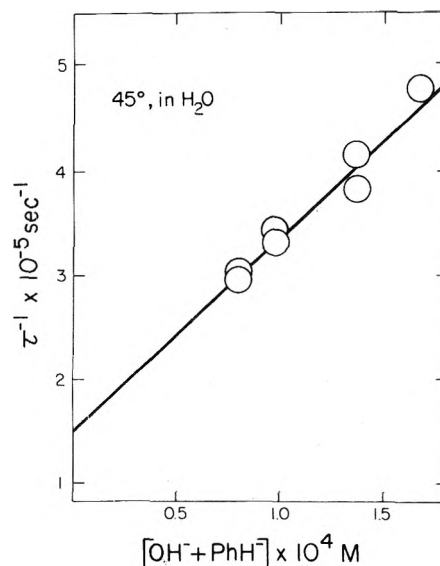


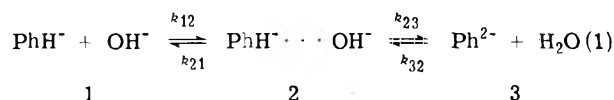
Figure 3. Concentration dependence of the relaxation time τ in the DFE experiments in H_2O at 45° .

not firing the second spark gap, all the energy stored in the capacitor at 35 kV is dissipated in the cell having a resistance of 330 ohms within less than $1 \mu\text{sec}$, causing a temperature rise of 1.6° .

The DFE experiments in water were the most difficult ones reported here, because of the relatively low resistance of the solutions and the long relaxation times observed. Since the second spark gap in most cases would not fire after $8\text{--}10 \mu\text{sec}$, it was necessary to evaluate the in-field relaxation curves. In order to speed up the reactions the perturbation was done at 45° , where the minimum resistance of the solutions in the cell was 4×10^3 ohms, representing a maximum heating of 1.2° within a minimum heating time of $10 \mu\text{sec}$, using 35-kV pulses. The simultaneous increase of the temperature and the electric field strength causes opposing shifts of the equilibria, therefore the experimental conditions had to be carefully optimized in such a way that the effects of the temperature were minimal. Thus only the first $4\text{--}5 \mu\text{sec}$ of the relaxation curves were evaluated, where the heating is about 0.5° . The plots of $\ln \Delta(\text{signal})$ vs. time yielded straight lines and so did the plots of τ^{-1} vs. the appropriate concentration variable (Figure 3). The pH of the reaction mixtures in these experiments was measured immediately before each perturbation with a Leeds and Northrup No. 7401 pH meter using No. 117208 and No. 117169 reference and measuring electrodes, respectively. The maximum ionic strength of the solutions never exceeded $2 \times 10^{-4} M$, where the Debye-Hückel activity coefficients are so close to unity that they can be neglected in the calculations.

Results and Discussion

All our experiments can be interpreted based on Eigen's general hydrolysis mechanism² (with some modification in pure ethanol)



where the meaning of the symbols is explained in Figure 4. There are two possibilities for the kinetic treatment of this

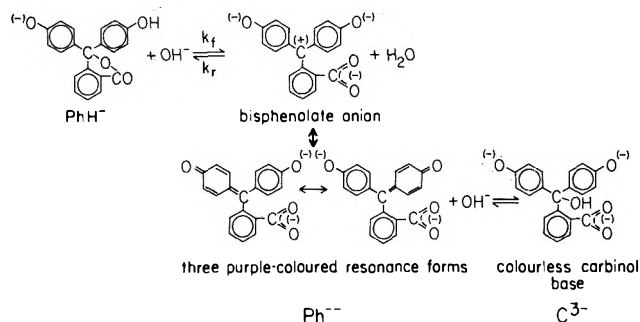


Figure 4. Detailed mechanism of proton transfer and color change of aqueous and ethanolic phenolphthalein.

mechanism, depending on whether the intermediate encounter complex $\text{PhH}^- \cdots \text{OH}^-$ is present in an infinitesimal concentration, that is necessary for a steady-state approximation. The steady-state approximation yields for the overall forward and reverse rate constants $k_f = k_{12}k_{23}/(k_{21} + k_{23})$ and $k_r = k_{32}k_{21}/(k_{21} + k_{23})$. For normal proton transfer $k_{23} \gg k_{21}$ and the frequency of encounter is rate determining.² As, however, the activation energy of step 2-3 increases, caused by internal hydrogen bonding or intramolecular electronic rearrangement accompanying the reaction, the chemical transformation step 2-3 becomes rate determining. Thus if $k_{23} \ll k_{21}$, the rate constants for proton transfer become $k_f = K_{12}k_{23}$ and $k_r = k_{32}$, where $K_{12} = k_{12}/k_{21}$ is the equilibrium constant of step 1-2. In this case, in conjunction with the steady-state approximation, only one relaxation time τ is expected, given by

$$\tau^{-1} = k_f([\text{PhH}^-] + [\text{OH}^-]) + k_r([\text{Ph}^{2-}] + [\text{H}_2\text{O}]) \quad (2)$$

In aqueous solution, where the reaction partner H_2O is in large excess, eq 2 is replaced by

$$\tau^{-1} = k_f([\text{PhH}^-] + [\text{OH}^-]) + k_r \quad (3)$$

but in ethanol eq 2 has to be used. The terms in brackets indicate equilibrium concentrations.

Our T-jump results in ethanol (Figure 5) and DFE experiments in water (Figure 3) are in agreement with eq 2 and 3, respectively. The $[\text{PhH}^-]$ for the aqueous DFE experiments were calculated using Rose and Stuehr's³ spectrophotometrically determined hydrolysis constant $K_h = k_r/k_f = 2.3 \times 10^{-5} M$ at 15° , and $0.1 M$ ionic strength. This value was corrected to 45° ⁹ and zero ionic strength,⁴ corresponding to our experimental conditions. The numerical

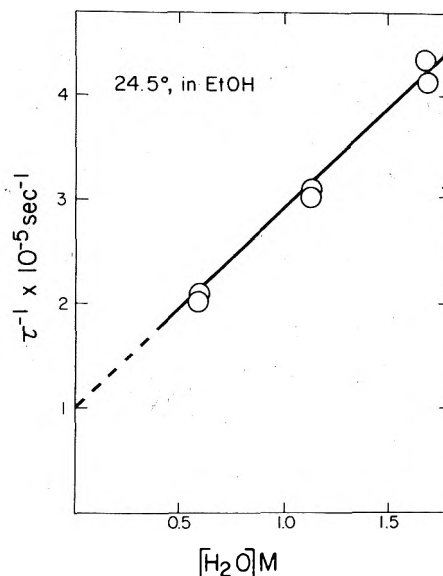


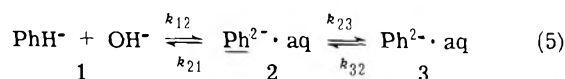
Figure 5. Concentration dependence of the relaxation time τ in the T-jump experiments in ethanol at 24.5° . The curve cannot be linearly extrapolated to pure ethanol because the mechanism apparently changes at low H_2O content of the medium.

values of the obtained rate and equilibrium constants are summarized in Table I.

Since the equilibrium constant is not accurately known in ethanol,¹⁰ the T-jump experiments in this solvent were done at $[\text{OH}^-] = 0.01 M$ and $[\text{H}_2\text{O}]$ between 0.56 to $1.68 M$. The total indicator concentration being $5.70 \times 10^{-5} M$ in each experiment, $[\text{PhH}^-] \ll [\text{OH}^-]$ and $[\text{Ph}^{2-}] \ll [\text{H}_2\text{O}]$, reducing eq 2 to

$$\tau^{-1} = k_f[\text{OH}^-] + k_r[\text{H}_2\text{O}] \quad (4)$$

The E-jump experiments in ethanol were performed without the addition of water. A concentration- and temperature-independent relaxation time $\tau = 0.8 \mu\text{sec}$ was observed (Table II), indicating that mechanism 1 with the steady-state approximation is not valid in this solvent. The results can be interpreted in terms of a modified reaction scheme where the color change takes place in two steps



The first step represents the diffusion-controlled deprotonation of PhH^- , resulting in the still colorless $\text{Ph}^{2-} \cdot \text{aq}$.

TABLE I: Thermodynamic and Kinetic Results of Ethanolic and Aqueous Phenolphthalein

Method	$T, ^\circ\text{C}$	I^a	${}_1E_a,$ kcal mol $^{-1}$	${}_2E_a,$ kcal mol $^{-1}$	$\Delta H,$ kcal mol $^{-1}$	k_t^d $M^{-1} \text{sec}^{-1}$	k_f^e $M^{-1} \text{sec}^{-1}$	$k_r/k_f = K_h^f$	K_h (calcd) ^g
T-Jump in ethanol ^h	24.5	0.3 ^b				2.1×10^7	2.0×10^5	9.5×10^{-3}	
E-Jump in water	45	~ 0	1	7	5	2.0×10^9	1.5×10^5	$7.5 \times 10^{-5} M$	$1.0 \times 10^{-4} M$
T-Jump in water ^c	15	0.1				1.7×10^9	4.7×10^4	$2.7 \times 10^{-5} M$	
E-Jump in ethanol		0				1.4×10^9	$3.4 \times 10^{-5} M$		
See Table II									

^a I = Ionic strength. ^b Corresponding to a $0.3 M$ tetramethylammonium chloride solution. ^c Taken from ref 3, and confirmed experimentally. The values at $I = 0$ were calculated. ^d $k_t = K_{12}k_{23}$ (see eq 1). ^e $k_r = k_{32}$ is for an ion-neutral reaction (see eq 1), thus largely independent of I . ^f From eq 2 and 3. ^g Calculated by temperature and ionic strength corrections on the K_h value in ref 3 (see also ref 9). ^h Water content $0.56 M$ (see Figure 5).

TABLE II: E-Jump Relaxation Times τ_{slow} of Ethanolic Phenolphthalein under Different Conditions

Indicator concn $\times 10^4, M$	NaOH concentration $\times 10^4, M$	$\tau, \mu\text{sec}$	$T, ^\circ\text{C}$
3.14	7.14	0.75, 0.75, 0.75	9.5, 20, 25
	5.85	0.85	25
	4.76	0.80, 0.85, 0.82	25
2.84	4.32	0.85, 0.85, 0.75, 0.75	25
	3.24	0.80, 0.80	25
0.570	4.32	0.80	25
0.314	7.14	0.75	25

^a For error limits see legend of Figure 2.

The much slower intramolecular electronic rearrangement and the opening of the lactone ring take place in the second step, where the pink $\text{Ph}^{2-} \cdot \text{aq}$ is formed.

If the steady-state approximation cannot be applied, reaction 5 has to be treated as two coupled equilibria $1 \rightleftharpoons 2$ and $2 \rightleftharpoons 3$. The usual kinetic analysis yields two simultaneous differential equations¹¹ from which the two relaxation times can be obtained by evaluating the determinant

$$\begin{vmatrix} (a_{11} - \tau^{-1}) & a_{12} \\ a_{21} & (a_{22} - \tau^{-1}) \end{vmatrix} = 0$$

where $a_{11} = k_{12}([\text{PhH}^-] + [\text{OH}^-]) + k_{21}$, $a_{12} = k_{21}$, $a_{21} = k_{23}$, and $a_{22} = k_{32} + k_{23}$. The two relaxation times then are

$$\tau_{1,2}^{-1} = S/2[1 \pm (1 - 4P/S^2)^{1/2}]$$

with $S = a_{11} + a_{22}$ and $P = a_{11}a_{22} - a_{12}a_{21}$.

Under the conditions that $k_{12}, k_{21} \gg k_{23}, k_{32}$ it is evident that $a_{11} \gg a_{22}$ and $a_{12} \gg a_{21}$. Thus the fast relaxation time becomes

$$\tau_{\text{fast}}^{-1} = a_{11} + a_{22} \approx a_{11} = k_{12}([\text{PhH}^-] + [\text{OH}^-]) + k_{21} \quad (6)$$

and slow one

$$\tau_{\text{slow}}^{-1} = \frac{a_{11}a_{22} - a_{12}a_{21}}{a_{11} + a_{22}} \approx \frac{a_{11}a_{22} - a_{12}a_{21}}{a_{11}} = a_{22} - \frac{a_{12}a_{21}}{a_{11}} \quad (7)$$

Low concentrations, and the fact that k_{12} and k_{21} are diffusion controlled simplifies the last term in eq 7 to k_{23} , resulting in

$$\tau_{\text{slow}}^{-1} \approx k_{32} \quad (8)$$

In this case, and if the observation is done on species $\text{Ph}^{2-} \cdot \text{aq}$, only the slow relaxation can be observed which is concentration independent. To observe both relaxations, the concentration of the intermediate $\text{Ph}^{2-} \cdot \text{aq}$ or that of PhH^- has to be followed, which, however, do not absorb in the visible range of the spectrum.

Since step 2-3 is the chemical transformation of the deprotonated lactone to the pink $\text{Ph}^{2-} \cdot \text{aq}$, k_{32} observed through the color change represents the rate of the polarization of the resonance system, and the closing of the lactone ring. Such a rate should be largely temperature independent, which was observed (Table II).

Summary

The detailed reaction mechanisms are shown in eq 1 and 5 where step $2 \rightleftharpoons 3$ represents the color change (see also Figure 4). On heating, a decrease of the concentration of Ph^{2-} results in water, but not in ethanol. In water, the hydrolysis constant $K_h = K_w/K_a$ increases with temperature because K_w gets larger faster than K_a of phenolphthalein.¹² In ethanol the analogous solvolysis constant K_{solvent} and K_a are not known at different temperatures for making a prediction, nevertheless, heating causes the opposite effect.

Dissociation field effect shifts step $1 \rightleftharpoons 2$ to the right in water, leaving step $2 \rightleftharpoons 3$ practically unaffected. As long as the medium contains a sufficient amount of water (>3% v/v) the steady-state treatment of eq 1 is applicable in both solvents, yielding one relaxation time given by eq 3 in water and eq 2 in ethanol.

Using E-jump perturbation in pure ethanol, a discoloration (left shift of step $2 \rightleftharpoons 3$) is the only observable effect. In this solvent eq 5 has to be used, and two relaxation times are expected, given by eq 5 and 8. However, due to the fact that $\text{Ph}^{2-} \cdot \text{aq}$ is monitored, only the slow one can be seen.

The opposite direction of the field effects in water and ethanol is noteworthy, for which specific solute-solvent interactions are responsible. While the resonance structure of the analogous sulfonephthaleins is extremely stable, that of the phthaleins is easily abolished by closing the lactone ring.¹³ The reaction is facilitated if the resonance system is first polarized to a structure similar to that of the bisphenolate anion (Figure 4). The polarization can be achieved either by an external field, or by a highly polar solvent,¹⁴ such as water. However, polarization by a solvent is accompanied by solvation of the sites of high charge density, which can hinder the closure of the ring. This situation is indicated in our case. A comparison of the unperturbed ethanolic and aqueous solutions shows only a negative solvatochromic effect (hypsochromic shift of the absorption band of Ph^{2-}) in H_2O , but no discoloration. Thus, the contribution of the external field to the $2 \leftarrow 3$ shift is larger in ethanol than in H_2O . On the other hand, the $1 \rightarrow 2$ shift caused by DFE is negligible in ethanol compared to that in water. The opposing effects can cancel each other in ethanol-water mixtures, reducing the E-jump relaxation amplitude to zero at an H_2O content of approximately 25% v/v.

Acknowledgment. This work was partially supported by the Research Corporation and the National Science Foundation. The authors are indebted for fruitful discussions with Professor E. M. Eyring and S. L. Olsen on the DFE apparatus. Technical assistance by G. Fielder, R. W. Jones, R. J. Krusberg, R. E. Morton, F. B. Pearson, R. Sexton, and M. W. Williams is gratefully acknowledged.

References and Notes

- (1) Abstracted in part from M. W. Massey, Jr.'s dissertation to be submitted at the University of Georgia.
- (2) M. Eigen, *Angew. Chem.*, **75**, 489 (1963).
- (3) M. C. Rose and J. Stuehr, *J. Amer. Chem. Soc.*, **90**, 7205 (1968).
- (4) E. Banyai, "Indicators," E. Bishop, Ed., Pergamon Press, New York, N.Y., 1972, Chapter III, p 74.
- (5) R. G. Bates, "Determination of pH," 2nd ed, Wiley, New York, N.Y., 1973, p 136.
- (6) S. L. Olsen, R. L. Silver, L. P. Holmes, J. J. Auburn, P. Warrick, Jr., and E. M. Eyring, *Rev. Sci. Instrum.*, **42**, 1247 (1971).
- (7) J. J. Auburn, P. Warrick, Jr., and E. M. Eyring, *J. Phys. Chem.*, **75**, 2488 (1971).
- (8) G. Ilgenfritz, Dissertation, Göttingen, 1966.
- (9) For $K_h = K_w/K_a$ at 45° the dissociation constant K_a was obtained through linear interpolation of $\ln K_a$ known at 18 and 70° (I. M. Kolthoff, *Recl. Trav. Chim. Pays-Bas*, **40**, 775 (1921)). K_w at 45° was taken from

- "Handbook of Chemistry and Physics," 54th ed, Chemical Rubber Publishing Co., Cleveland, Ohio, 1973-1974, p D-131.
- (10) I. M. Kolthoff, *J. Phys. Chem.*, **35**, 2732 (1931).
- (11) M. Eigen and L. DeMaeyer, "Technique of Organic Chemistry," Vol. 8, Part 2, L. Friess and A. Weissberger, Ed., Interscience, New York, N.Y., 1963, Chapter 18.
- (12) H. Eyring and E. M. Eyring, "Modern Chemical Kinetics," Reinhold, New York, N.Y., 1963, p 100.
- (13) G. Schwarzenbach and O. Haggar, *Helv. Chem. Acta*, **20**, 1591 (1937).
- (14) W. Liptay, *Angew. Chem.*, **81**, 195 (1969).
- (15) A. A. Frost and R. G. Pearson, "Kinetics and Mechanism," 2nd ed, Wiley, New York, N.Y., 1961, p 150.

Energy Level Structure and Mobility of Excess Electrons in γ -Irradiated 5 M Potassium Carbonate Aqueous Glasses. Effect of Ions on Trapped and Mobile Electrons in Aqueous Glasses

Shoji Noda and Larry Kevan*

Department of Chemistry, Wayne State University, Detroit, Michigan 48202 (Received May 16, 1974)

Publication costs assisted by the U.S. Atomic Energy Commission

The energy level structure of trapped electrons (e_t^-) in γ -irradiated 5 M K_2CO_3 glassy ice at 77 K has been investigated *via* the wavelength dependence of the photocurrent. Scavenger effects demonstrate that the photogenerated charge carrier is an electron. The photocurrent wavelength response per unit incident photon does not coincide with the optical absorption band of the e_t^- and can be phenomenologically resolved into two bands. The optical absorption band is a symmetrically bleached with monochromatic light and can also be resolved into at least two subbands. The photocurrent band at longer wavelength coincides with the longer wavelength absorption band. Thus the e_t^- in the shallower potential wells appear to have no bound excited state as is the case for e_t^- in 10 M NaOH glassy ice. For e_t^- in the deeper potential wells, the shorter wavelength absorption and photocurrent bands do not coincide and indicate a bound excited state as is found for e_t^- in crystalline ice. The difference between the energy level structure for e_t^- in different aqueous matrices can be understood in terms of a semicontinuum model of electron trapping and the modification of the polarization interactions by the ions present in the matrix. The analysis is supported by the photocurrent wavelength dependence in 4.5 M D-glucose glassy ice. The field and temperature dependence of the photocurrent and the electron drift mobility were also investigated. Superohmic photocurrents are observed in certain dose ranges at 77 K. The electron drift mobility is inversely proportional to field at high fields and exhibits a negative temperature dependence from 80 to 103 K. The dominant scattering mechanism near 77 K for photoexcited mobile electrons is lattice phonon scattering. In contrast to e_t^- in 10 M NaOH ice, the mobility is independent of the hole (CO_3^-) concentration and there appear to be no shallow traps relative to the conduction band associated with CO_3^- . These differences are explained in terms of the different degree of lattice polarization induced by CO_3^- and O^- ions in aqueous matrices.

Introduction

Excess electrons produced by high-energy radiation or by photoionization of a suitable solute are stabilized in a variety of aqueous¹ and organic² glasses. The trapped electrons exhibit diverse energy level structure depending on the nature of the glassy matrix. The trapped electron may also be photoexcited to a mobile state in which their transport mechanisms in the glassy matrix can be probed through their mobility characteristics. In 10 M NaOH glassy ice, the trapped electron appears to have no bound excited state and the optical absorption spectrum is assigned to bound-free transitions.³ Drift and Hall mobility experiments have demonstrated that the photoexcited electron in this glass is quasi-free and that its transport mechanism is well described by a band model.⁴ On the other hand, in less polar organic glasses, such as 2-methyltetrahydrofuran (MTHF), the trapped electron has bound excited states

and can be photoexcited to a mobile state by both one-^{5,6} and two-⁵ photon processes. The mobility of photoexcited electrons in MTHF glass is several orders of magnitude smaller than in 10 M NaOH glassy ice and appears to be best explained by a hopping model.^{7,8} Electrons in alkane glasses, such as 3-methylhexane, seem to have similar energy level structures and mobility characteristics to electrons in MTHF. The influence of matrix polarity on these characteristics of excess electrons has been emphasized.²

It is of importance to determine whether 10 M NaOH glassy ice is typical of aqueous glasses with regard to stabilization of electrons. Previously, it has been suggested that the highly alkaline ice may represent an extreme in effective matrix polarity.^{2,8} In this work we have studied excess electrons in a different aqueous glass, 5 M K_2CO_3 . By photoconductivity and optical bleaching studies we have found that trapped electrons of at least two different types are

formed which are distinguished by their energy level structure. Mobile electrons produced by photoexcitation have a relatively large drift mobility that exhibits characteristics consistent with a band model. Thus it is tentatively concluded that a quasi-free electron state is typical for aqueous glasses.

Experimental Section

The photoconductivity cell and the set-up for the photoconductivity measurements have been described in an earlier work.⁵ The light beam from a 500-W slide projector was directed through semitransparent electrodes. For the wavelength dependence of the photocurrent a Bausch & Lomb high-intensity monochromator with a dispersion of 20 nm was used. Thermocouple measurements showed that the sample temperature increased $<1^\circ$ during bleaching.

Drift mobility was measured with a time-of-flight method. A light flash produces mobile electrons near one electrode by optically detrapping some of the trapped electrons in the γ -irradiated sample. These electrons drift under an applied field to the opposite positive electrode and the time dependence of this current is observed. Experimental details can be seen elsewhere.⁴

All samples were made from nondegassed 5 M K_2CO_3 aqueous solutions. Reagent grade K_2CO_3 , KNO_3 , and D-glucose were used without any further purification. The samples were frozen by plunging into liquid nitrogen and were irradiated in a ^{60}Co γ source at 77 K at a nominal dose rate of 0.27 Mrad/hr. Temperatures above 77 K were obtained by using cold N_2 gas.

Optical absorption measurements were made on a Cary 14 spectrophotometer. Electron paramagnetic resonance (epr) measurements were made in a Varian E-4 epr spectrometer.

Results and Discussion

A. Identity of the Photoinduced Charge Carrier. The observed photocurrent is due to radiation-produced species that are trapped in 5 M K_2CO_3 glassy ice. No photocurrent is seen in the unirradiated 5 M K_2CO_3 glassy ice. A typical photocurrent observed in the glass is shown in Figure 1. This is quite similar to that observed in γ -irradiated 10 M NaOH glassy ice.³ The photocurrent rises instantaneously within the response time of the apparatus and then decreases with time. When the light beam is interrupted the photocurrent drops to zero. When the light is subsequently turned on the current increases to a value about equal to the current measured before the light was interrupted and continues a slow decrease with time; this sequence can be repeated several times. That is, no dark decay of the photocurrent is observed at 77 K.

The main radiation-produced species in this glass at 77 K are CO_3^- and e_t^- .⁹ The photoinduced charge carrier was indicated to be the detrapped electron from the effect of the electron scavenger, KNO_3 , on the photocurrent. As shown in Figure 2, the photocurrent decreases as the concentration of KNO_3 increases. The yields of the trapped electron also decrease with KNO_3 concentration. The e_t^- yields were measured by optical absorption at 450 nm to avoid overlap with the optical absorption of CO_3^- which has a maximum near 620 nm. It is clear that the charge carrier is the electron. The photocurrent decreases faster than the trapped electron yield as a function of scavenger concentration in Figure 2. The photocurrent amplitude depends on the number of mobile electrons and the average

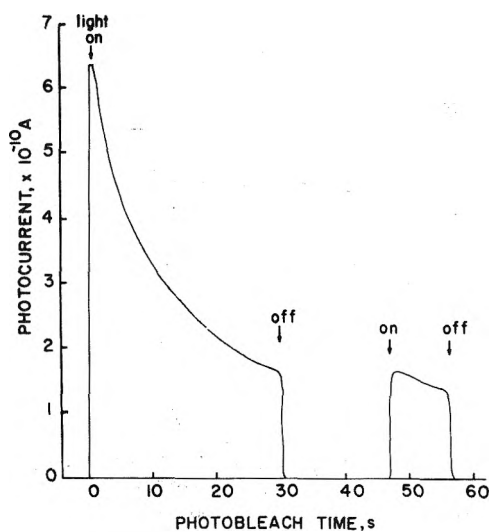


Figure 1. Typical photocurrent curve for γ -irradiated (0.13 Mrad) 5 M K_2CO_3 glassy ice at 77 K with an applied field of 8 kV/cm.

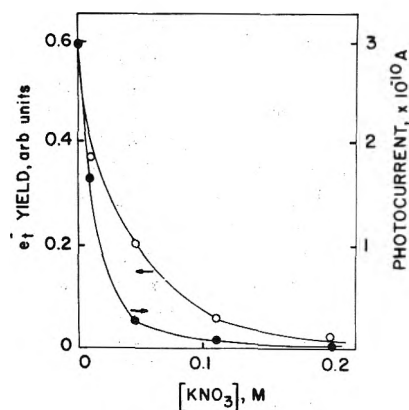


Figure 2. Effect of an electron scavenger, KNO_3 , on the yields of e_t^- and the intensity of photocurrent in γ -irradiated 5 M K_2CO_3 glassy ice at 77 K.

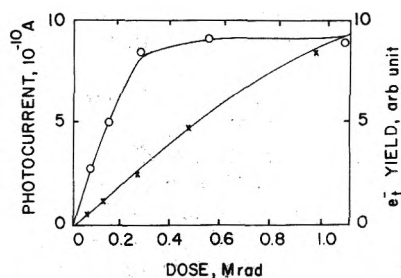


Figure 3. Dose dependence of e_t^- yield and of photocurrent at an applied field of 8 kV/cm in γ -irradiated 5 M K_2CO_3 glassy ice at 77 K.

distance traveled by them. As the electron scavenger concentration increases, not only is the trapped electron yield decreased, but also the average distance traveled by a mobile electron is decreased. This is why the photocurrent decreases faster than the trapped electron yield, however, since there are two variables a unique quantitative analysis seems precluded.

B. Dose Dependence of the Photocurrent. The dose dependence of the photocurrent is given in Figure 3. The photocurrent rises linearly to about 0.07 Mrad where 20% of the light is transmitted at the absorption maximum. It

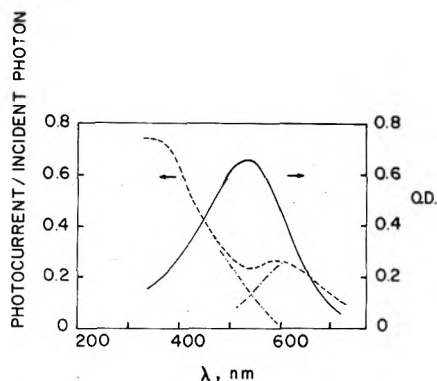


Figure 4. Wavelength dependence of photocurrent in γ -irradiated (0.13 Mrad) 5 M K_2CO_3 glassy ice at 77 K with an applied field of 11 kV/cm: (—) optical absorption curve; (---) photocurrent per number of incident photons. See text for comments on the resolution of the photocurrent curve into part I (···) and II (- · -).

then curves over to a plateau above 0.3 Mrad. At this dose essentially all of the incident light in the e_t^- absorption band is absorbed. The e_t^- yield, measured by epr, at different doses is also plotted. The e_t^- yield increases linearly with dose to at least 0.4 Mrad. Thus the plateau in Figure 3 is simply a consequence of total light absorption.

C. Wavelength Dependence of Photocurrent. The optical absorption spectrum of e_t^- in 5 M K_2CO_3 glassy ice is a broad asymmetric band with a peak at 540 nm at 77 K. The wavelength dependence of the photocurrent per number of incident photons (photocurrent λ response) is shown together with the optical absorption spectrum in Figure 4. There is a shoulder around 600 nm in the photocurrent λ response and then the λ response monotonically increases to high energy until a maximum is reached near 375 nm. This λ response is different from that observed in 10 M NaOH glassy ice, where the photocurrent λ response follows the shape of the absorption band.³

When the γ -irradiated glass was bleached with monochromatic light (the bandwidth was about 40 nm) with no external electric field, the photocurrent λ response was changed and partial bleaching of the optical band was also observed. Bleaching of the glass with 700-nm light removed the shoulder around 600 nm while the other parts of the photocurrent λ response remained almost unchanged (Figure 5). Bleaching with 700-nm light also blue-shifted the λ_{max} of the optical absorption spectrum of e_t^- . On the other hand, illumination by 400-nm light reduced the photocurrent in the high-energy region and increased that in the medium-energy region. The λ_{max} of the optical absorption band was slightly red-shifted (Figure 6). The bleaching experiments indicate that the wavelength dependence of the photocurrent is apparently a composite of at least two or more components as is the optical absorption spectrum. It is noted that light of 750–800 nm, which is in the low-energy tail of the absorption spectrum, produces photocurrent.

The magnitude of the photocurrent was found to be linearly proportional to the light intensity throughout the entire spectral region, and so the photoionization of the trapped electron in 5 M K_2CO_3 glassy ice can be regarded as a one-photon process.

The magnitude of the photocurrent is given by

$$I(\text{A/cm}^2) = eF\mu\tau(V/d) \quad (1)$$

where e is electronic charge, F is the number of charge carriers per cm^3 photoexcited into the conduction band per

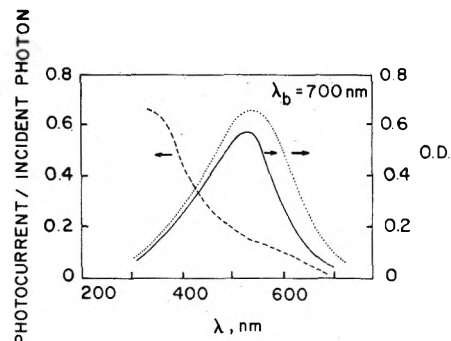


Figure 5. Effects of optical bleaching with monochromatic light on the wavelength dependence of the photocurrent and the optical absorption spectrum in γ -irradiated (0.13 Mrad) 5 M K_2CO_3 glassy ice at 77 K with an applied field of 11 kV/cm: (—) optical absorption spectrum after photobleaching with 700 nm light; (···) optical absorption spectrum before photobleaching; (- · -) photocurrent per number of incident photons after optical bleaching with 700-nm light.

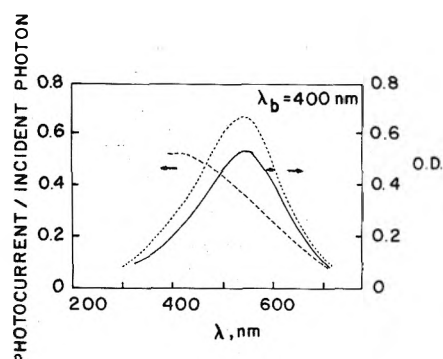


Figure 6. Effects of optical bleaching with monochromatic light on the wavelength dependence of the photocurrent and the optical absorption spectrum in γ -irradiated (0.13 Mrad) 5 M K_2CO_3 glassy ice at 77 K with an applied field of 11 kV/cm: (—) optical absorption spectrum after optical bleaching with 400-nm light; (···) optical absorption spectrum before optical bleaching; (- · -) photocurrent per number of incident photons after optical bleaching with 400-nm light.

second, μ is the mobility of the charge carrier in the conduction band, τ is the average life time of a charge carrier in the conduction band, V is the applied potential, and d is the electrode spacing. F is represented by

$$F = L\sigma C \quad (2)$$

where L is the number of incident photons, σ is the photoionization cross section of the trapped electron, and C is the concentration of trapped electrons. Since μ and τ are normally independent of the photon energy, the photocurrent is linearly proportional to F , or the photocurrent per number of incident photons is proportional to σC

$$I/L \propto \sigma C \quad (3)$$

Since there is a distribution of potential wells for the trapped electrons in the glass, the photocurrent λ response is given by

$$I(\nu)/L(\nu) \propto \sum_i \sigma_i(\nu) C_i \quad (4)$$

where i refers to discrete potential wells of different depth. On the other hand, the optical absorption band is given by

$$\text{OD}(\lambda) \propto \sum_i \epsilon_i(\nu) C_i \quad (5)$$

where ϵ_i is the extinction coefficient of the trapped electron i . Therefore, the wavelength dependence of the photocurrent does not coincide with the optical absorption spectrum, even when all e_t^- are in similar depth potential wells, if optically allowed bound excited states exist. In 10 M NaOH glassy ice the wavelength dependence of the photocurrent and optical absorption do coincide, so the absence of optically allowed bound excited states is suggested and the entire optical absorption spectrum of e_t^- is assigned to the envelope of bound-free transitions. In this case $\epsilon_i(\nu)$ is equal to $\sigma_i(\nu)$ for all i and ν .

The wavelength dependence of the photocurrent in 5 M K_2CO_3 glassy ice can be phenomenologically divided into two parts as shown in Figure 4. Part I photocurrent ($[I(\nu)/L(\nu)]_{\max}$ is ~ 620 nm, $\Delta[I(\nu)/L(\nu)]_{1/2} \approx 0.5$ eV) parallels the optical absorption subband ($\lambda_{\max} \sim 620$ nm, $\Delta OD_{1/2} \approx 0.5$ eV) which is bleached with light of 700 nm and which can be assigned to e_t^- in shallower potential wells. From the arguments given above, coincidence of the wavelength dependence of the photocurrent and the optical absorption is consistent with no bound excited state for e_t^- in the shallower potential wells. The threshold energy is about 1.5 eV (~ 800 nm) and is assigned to the average energy gap between the ground state and the bottom of the conduction band. The maximum cross section for photoionization occurs about 0.5 eV above the bottom of the conduction band at 620 nm; this is consistent with a hydrogenic model of photoionization.¹⁰

The part II photocurrent λ response does not coincide with the optical absorption band. It is therefore similar to the photocurrent λ response of e_t^- in MTHF glass⁵ or in crystalline ice^{8,11} in which optical excitation to both bound and unbound states occurs. This interpretation applies to the e_t^- in the deeper potential wells in 5 M K_2CO_3 glassy ice. Because of the uncertain resolution of the part I and II photocurrents it is not possible to deduce a reliable photoionization threshold for the part II photocurrent.

In summary, our analysis suggests that there is a distribution of trapping potential depths for e_t^- in 5 M K_2CO_3 ice which can be represented by an average shallow potential well and an average deep potential well. The e_t^- in the shallow potential wells appear to have no bound excited state as is the case for e_t^- in 10 M NaOH glassy ice. The e_t^- in the deep potential wells appear to have a bound excited state as found for e_t^- in crystalline ice and in MTHF glass.

D. Energy Level Structure of e_t^- in Aqueous Matrices. In order to understand the energy level structure of trapped electrons in various polar matrices, a semicontinuum potential involving short-range charge dipole interactions and long-range polarization interactions has been used with moderate success in a self-consistent field approximation known as the semicontinuum model.¹² This model accounts for differences in energy level structure of e_t^- on the basis of the matrix properties: density, molecular dipole moment, molecular polarizability, static and optical dielectric constants, and matrix work function for electron photoinjection. With hydrogenic¹² or Gaussian¹³ type wavefunctions, this model always predicts an optically allowed transition to a bound excited state. The only way to avoid this is to ignore the long-range polarization interactions. Then only a bound-free transition is predicted.¹²

We previously argued that it might be justifiable to ignore polarization interactions for e_t^- in 10 M NaOH glassy ice because water molecules beyond the second solvation shell of e_t^- are probably more strongly polarized by OH^-

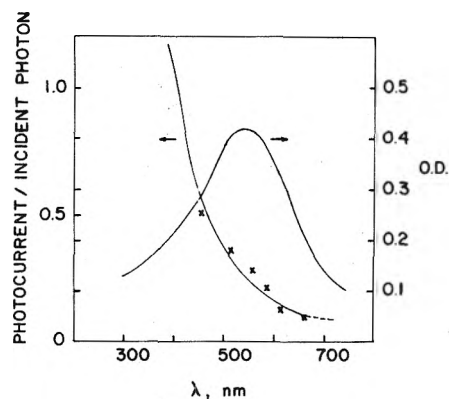


Figure 7. Wavelength dependence of the photocurrent in γ -irradiated (0.24 Mrad) 4.5 M D-glucose glassy ice at 77 K with an applied field of 15 kV/cm: (—) optical absorption curve; (---) photocurrent per number of incident photons.

ions in the matrix rather than by e_t^- . This argument is supported by the observation of a bound excited state for e_t^- in single crystal ice in which there are no other foreign ions to compete with e_t^- . The evidence for a bound excited state in single crystal ice is noncoincidence of the optical bleaching λ response with the optical absorption band of e_t^- .^{8,11}

A more direct test of the above hypothesis is to study e_t^- in a glassy ice containing no ions and to measure the photocurrent λ response. We have carried out such an experiment in 4.5 M D-glucose glassy ice. Electrons are trapped by γ -radiolysis of this matrix with a 100-eV yield (G) of 1.8.^{14,15} Although the glucose molecule is polar, the negatively charged region is diffuse and will probably not compete effectively with e_t^- for polarization of the water dipoles. The results are shown in Figure 7. The photocurrent λ response is as predicted; it does not coincide with the optical absorption band. It is similar in shape to the photocurrent λ response of e_t^- in crystalline ice and in MTHF; and it is consistent with the existence of a bound-bound transition at lower energy and a bound-free transition at higher energy.

The results in 5 M K_2CO_3 glassy ice are intermediate between those in glucose ice and in NaOH ice. The CO_3^{2-} ion should polarize its surrounding water dipoles, but the effect is probably weaker than for OH^- because the negative charge is more diffuse for the CO_3^{2-} ion. Thus we may expect the importance of the polarization interaction felt by the excess electron to be weaker in K_2CO_3 ice than in glucose ice, but stronger in K_2CO_3 ice than in NaOH ice. For the shallow e_t^- trapping potentials in K_2CO_3 ice it appears that the polarization interaction of e_t^- can be ignored, and consequently no bound excited state for e_t^- exists. However, for the deeper e_t^- trapping potentials the polarization interaction becomes significant and gives rise to a bound excited state.

The overall effect of high ion concentration on the energy level structure of e_t^- in various aqueous glasses seems qualitatively clear, and it appears that the energy level structure of e_t^- in aqueous glasses is not fundamentally different from the energy level structure of e_t^- in organic glasses.

E. Field Dependence of Photocurrent and of Electron Drift Mobility. The current-voltage dependence of the photocurrent in 5 M K_2CO_3 glassy ice exhibits an ohmic region and a superohmic region. In the superohmic region the voltage exponent varies from 1 to 2 under different experi-

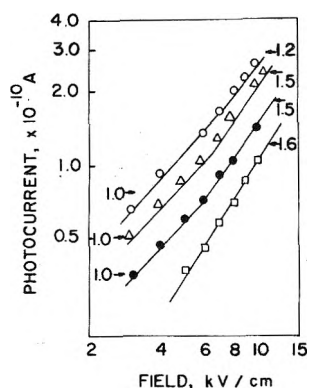


Figure 8. Current-voltage plots for photocurrent in 5 M K_2CO_3 glassy ice at 77 K at different doses: O, 0.83 Mrad; Δ , 0.58 Mrad; \bullet , 0.13 Mrad; \square , 0.05 Mrad. The slopes are indicated.

mental conditions. The transition voltage between the two regions depends on dose and consequently on the concentration of some radiation-produced species. Figure 8 shows current-voltage plots for several different radiation doses at 77 K. At doses above 0.1 Mrad two current-voltage regions are seen. At 0.05 Mrad only the superohmic region is seen with a voltage exponent of about 1.6. Presumably, an ohmic region would be also observed at 0.05 Mrad and lower doses if the current could be observed above the noise at low enough voltage.

γ -Irradiation of 5 M K_2CO_3 glassy ice produces e_t^- and CO_3^- with 100-eV yields (G) of 2.0 ± 0.4 and 3.6 ± 0.7 , respectively.⁹ Another species ($G \sim 0.3\text{--}0.5$), which is not identified, is also observed in the glass by epr after photobleaching.⁹ It is not clear whether this species is originally produced by λ -radiolysis and is counted as part of the CO_3^- initial yield or not. We found that when all the e_t^- are detrapped by optical bleaching, about 30% of CO_3^- remains as measured by epr.

By analogy to λ -irradiated 10 M NaOH glassy ice,³ Coulombic scattering of mobile electrons by the hole species, CO_3^- , may be associated with the nonlinear current-voltage dependence. To test this, the ratio of $[\text{CO}_3^-]$ to $[e_t^-]$ was changed by cycles of successive radiolysis and optical bleaching. Figure 9 shows that for every cycle of successive radiolysis and complete optical bleaching of e_t^- , the photocurrent decreases, even though about the same number of electrons are available for excitation to the conduction band. However, the current-voltage exponent remains unchanged for the samples that were successively bleached and reirradiated at 77 K in contrast to observations on the NaOH matrix. Independent measurements showed that the electron drift mobility was unchanged in samples which were successively bleached and reirradiated at 77 K. This, of course, is consistent with an unchanged current-voltage exponent.

These experiments show that the CO_3^- concentration does not affect the current-voltage dependence, although it does affect the yield of the photocurrent. The decreased photocurrent yield can be explained by capture of mobile electrons by CO_3^- . The independence of the mobility on CO_3^- concentration suggests that Coulombic scattering from CO_3^- is not an important scattering process that limits the electron mobility at 77 K. On the other hand, the dose dependence of the current-voltage exponent suggests that the electron scattering processes are, in part, dose dependent. The dose-dependent component of the electron-

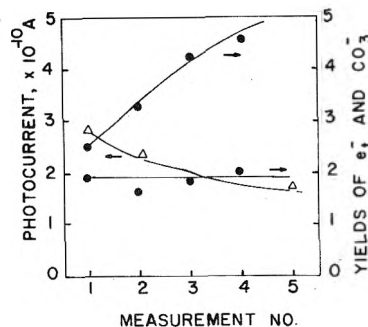


Figure 9. Yields of CO_3^- (\bullet) and e_t^- (O) and photocurrent (Δ) for successive 0.12-Mrad irradiation and bleaching of e_t^- in 5 M K_2CO_3 glassy ice at 77 K.

scattering processes is therefore attributed to Coulombic scattering by e_t^- . At low dose and low e_t^- concentration the mobile electron will be "heated up," so that it is no longer in thermal equilibrium with the lattice, by the applied field more rapidly to reach the range of field-dependent mobility and nonohmic current. At higher doses and higher e_t^- concentration the mobile electron will be "heated up" more slowly by the applied field so that an ohmic photocurrent, indicative of mobile electrons in thermal equilibrium with the lattice, is observed to higher fields.

It is interesting to comment on the difference between electron motion in 5 M K_2CO_3 and 10 M NaOH glassy ices. The hole species in 10 M NaOH ice is O^- and it does affect the mobility and current-voltage exponent at 77 K. Thus the O^- hole appears to be a more effective electron-scattering center than the CO_3^- hole. This is consistent with our previous comments on the extent of lattice distortion or polarization by these two hole centers. For O^- , the lattice is distorted to create a potential barrier around O^- . This makes O^- effective as an electron-scattering center as well as an electron capture center. In contrast CO_3^- causes less lattice distortion and, relative to O^- , is a poorer electron-scattering center and better electron-capturing center.

The existence of hot electrons in 5 M K_2CO_3 glassy ice is clearly demonstrated by electron drift mobility measurements. The sample thickness was usually 1 mm. Since large background signals were observed in the glass irradiated to high dose, the measurements were confined to 0.2 Mrad and below. At these low doses light penetrates a significant distance into the sample and the measured apparent mobility based on the sample thickness must be corrected for the average travel distance of the mobile electrons.⁴ For a sample thickness of 1 mm the average electron travel distance was estimated as 0.85 mm at 0.2 Mrad.

The maximum value of the electron drift mobility is 2.1 $\text{cm}^2/\text{V sec}$ at 10^3 V/cm; measurements at lower voltages were precluded by the low signal-to-noise ratio. Figure 10 shows that this value is not the field-independent mobility but suggests that the field independent mobility is ~ 3 $\text{cm}^2/\text{V sec}$. This electron drift mobility magnitude is similar to the field-independent electron drift mobility of 2 $\text{cm}^2/\text{V sec}$ in 10 M NaOH glassy ice.

The field dependence of the electron drift mobility in 5 M K_2CO_3 glassy ice at 77 K is shown in Figure 10. The observation of field-dependent mobility implies nonohmic photocurrents and shows that the electrons can be "heated up" above their thermal energy distribution in the glassy matrix. This suggests that the mobile electron moves in a reasonably well-defined conduction band. At fields greater

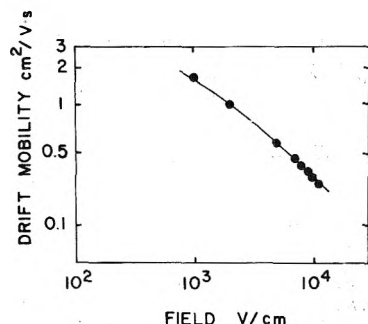


Figure 10. Field dependence of electron drift mobility in γ -irradiated (0.13 Mrad) 5 M K_2CO_3 glassy ice at 77 K.

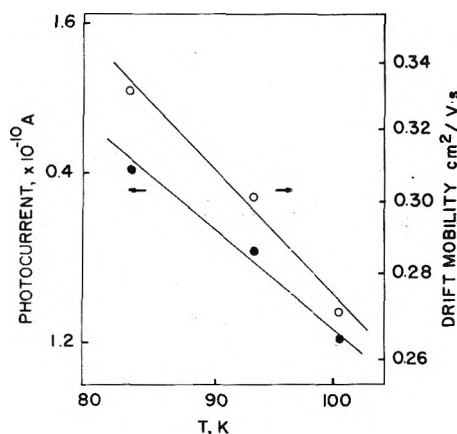


Figure 11. Temperature dependence of the photocurrent and the electron drift mobility in γ -irradiated (0.13 Mrad) 5 M K_2CO_3 glassy ice at an applied field of 6 kV/cm: O, drift mobility; ●, photocurrent. Note that all scales are logarithmic so that the slopes can be compared.

than 6×10^3 V/cm, $\mu_D \propto F^{-1}$. This field dependence suggests that the interaction of mobile electrons with lattice phonon modes is the dominant scattering mechanism¹⁶ in this voltage region at 77 K which is the same mechanism found previously for electrons in 10 M NaOH glassy ice.⁴ This conclusion is consistent with the independence of the electron drift mobility on the CO_3^- concentration.

F. Temperature Dependence of Photocurrent and of Electron Drift Mobility. The temperature dependencies of the photocurrent and of the electron drift mobility are relevant to understanding the photoexcitation process of the trapped electron and the transport mechanism of the mobile electron.

The photodetachment cross section is temperature activated if the optical transition occurs to a bound state from which thermal excitation is required to reach the conduction band. For conduction band transport dominated by lattice phonon scattering the mobility decreases with increasing temperature as has been discussed elsewhere.⁴ The temperature dependence of the photocurrent is the net result of these two temperature effects.

In Figure 11 the temperature dependence of the photocurrent and the electron drift mobility are compared under the same experimental conditions (0.13 Mrad, 6 kV/cm) over the range 83–103 K. In both cases, the temperature dependence is negative and the slopes are about the same within experimental error. Thus it seems that the temperature dependence of the photocurrent can be accounted for by the temperature dependence of the electron drift mobil-

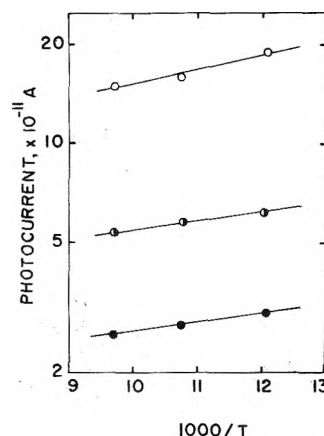


Figure 12. Temperature dependence of photocurrent from 80 to 103 K measured for 0.13 Mrad and different fields in 5 M K_2CO_3 glassy ice: ●, 3 kV/cm; ◐, 6 kV/cm; O, 10 kV/cm.

ity. Consequently, the photodetachment cross section may be regarded as temperature independent. The photoconduction process appears to occur by direct excitation to the conduction state without the intermediacy of a weakly bound excited state near the conduction band.

For mobile electrons in 10 M NaOH glassy ice an additional temperature-dependent process for the photocurrent above 77 K was found.³ A positive temperature dependence was observed, but the magnitude of the temperature dependence was found to be field dependent. This was demonstrated to be due to the existence of a shallow electron trap 0.05 eV below the conduction band associated with the O^- hole. Figure 12 shows the photocurrent temperature dependence in 5 M K_2CO_3 glassy ice at three different fields. At 10 kV/cm the current is superohmic and at 3 kV/cm it is ohmic for the 0.13-Mrad dose used. The same negative temperature dependence is observed for the photocurrent independent of field. Thus, in the 5 M K_2CO_3 glassy ice there does not seem to be a shallow electron trap associated with CO_3^- hole. This is consistent with our previous conclusion about the difference between the CO_3^- and O^- holes in ice matrices. The small matrix distortion associated with CO_3^- is expected to only lead to a deep electron trap.

Conclusions

The energy level structure of e_t^- in aqueous ices is dependent on the nature of the ions, if any, present in the matrix. For small negative ions with a highly localized charge there tend to be no or only weakly bound excited states associated with e_t^- . For larger negative ions e_t^- has a bound excited state. These differences can be understood in terms of a semicontinuum model for electron trapping and the modification of the polarization potential in this model by the type of ions present in the matrix.

Electron drift mobilities are of order $2 \text{ cm}^2/\text{V sec}$ in aqueous glasses near 77 K and are predominately limited by lattice phonon scattering. At sufficiently high applied fields (typically 6 kV/cm) the mobile electrons can be heated above their thermal equilibrium distribution to produce superohmic photocurrents. The superohmic photocurrents are generally dose dependent which implies that Coulombic scattering makes at least some contribution to the electron mobility. The effect of radiation-produced trapped holes in aqueous glasses on the electron-scattering pro-

cesses is dependent on the electrostatic nature of the hole and its local polarization of the matrix.

Acknowledgment. This research was supported by the U. S. Atomic Energy Commission through Contract No. AT(11-1)-2086.

References and Notes

- (1) L. Kevan, *Actions Chim. Biol. Radiat.*, **13**, 57 (1969).
- (2) L. Kevan, "Trapped Electrons in Organic Glasses," in "Advances in Radiation Chemistry," Vol. 4, M. Burton and J. L. Magee, Ed., Wiley-Interscience, New York, N.Y., 1974, p. 181.
- (3) I. Eisele and L. Kevan, *J. Chem. Phys.*, **53**, 1867 (1970).
- (4) T. Huang, I. Eisele, and L. Kevan, *J. Chem. Phys.*, **59**, 6334 (1973).
- (5) T. Huang, I. Eisele, D. P. Lin, and L. Kevan, *J. Chem. Phys.*, **56**, 4702 (1972); J. E. Willard and coworkers do not find evidence for two-photon processes and further experiments on this point are in progress.
- (6) K. F. Baverstock and P. J. Dyne, *Can J. Chem.*, **48**, 2182 (1970).
- (7) T. Huang and L. Kevan, *J. Chem. Phys.*, in press.
- (8) L. Kevan, *J. Phys. Chem.*, **76**, 3830 (1972).
- (9) B. G. Ershow, O. F. Khodzhaev, and A. K. Pikaev, *High Energy Chem. (USSR)*, **2**, 29 (1967).
- (10) K. Fueki, D. F. Feng, and L. Kevan, *J. Chem. Phys.*, **59**, 6201 (1973).
- (11) K. Kawabata, *J. Chem. Phys.*, **55**, 3672 (1971).
- (12) K. Fueki, D. F. Feng, and L. Kevan, *J. Amer. Chem. Soc.*, **95**, 1398 (1973).
- (13) D. F. Feng, D. Ebbing, and L. Kevan, *J. Chem. Phys.*, **61**, 249 (1974).
- (14) J. D. Zimbrick and L. S. Myers, Jr., *J. Chem. Phys.*, **54**, 2899 (1971).
- (15) I. E. Makarov, B. G. Ershow, and A. K. Pikaev, *Izv. Akad. Nauk SSSR, Ser. Khim.*, 447 (1968).
- (16) E. M. Conwell, "High Field Transport in Semiconductors," Academic Press, New York, N.Y., 1967, pp 15-34.

Interactions of Aqueous Electrolytes with Nonelectrolytes. The Enthalpy of Dilution of Urea and *tert*-Butyl Alcohol in Salt Solutions

R. B. Cassel and R. H. Wood*

Department of Chemistry, University of Delaware, Newark, Delaware 19711 (Received April 22, 1974)

The enthalpy of dilution of urea and *tert*-butyl alcohol dissolved in aqueous solutions of LiCl, CsCl, and tetra-*n*-butylammonium chloride has been measured at 25°. Both the diluting solution and the urea or *tert*-butyl alcohol solution always contained the same concentration of salt. The results are a measure of the effects of triplet and quadruplet terms on the enthalpy. Except for the *tert*-butyl alcohol in tetra-*n*-butylammonium chloride system, the effects of the triplet terms in 1 *m* solutions are much smaller than the effects of previously measured pair terms. In 1 *m* solutions, quadruplet terms are normally quite small. An equation for predicting the properties of multicomponent mixtures of electrolytes and nonelectrolytes is proposed. The results show the relative errors expected in the predictions of the equation.

Introduction

One of the long-range goals of a great deal of the research on aqueous solutions is the ability to predict the properties of a multicomponent mixture of electrolytes and nonelectrolytes in aqueous solution from as few basic measurements as possible. A series of papers from this laboratory has dealt with methods for predicting the properties of mixtures of electrolytes.^{1,2} The present results represent a first step toward extending these investigations to mixtures containing both electrolytes and nonelectrolytes. In the first section of this paper, an equation is derived showing all of the interactions present in a mixture. This equation is then used to show how certain specific terms can be measured by designing an experiment which cancels out other terms. The second section presents the results of these measurements: the dilution of a nonelectrolyte in the presence of a constant concentration of an electrolyte. In a third section, the consequences of these measurements for the prediction of mixtures of electrolytes and nonelectrolytes are discussed. In a following paper,³ results for mixtures of the nonelectrolytes urea, sucrose, and glycine are presented.

Theory

The derivation of the equation for predicting the properties of a multicomponent solution of both electrolytes and nonelectrolytes starts with the McMillan-Mayer theory.⁴ If F^{ex} is the excess free energy of a solution of volume V at a pressure equal to the osmotic pressure of the solution plus the standard pressure (1 atm), then

$$-F^{\text{ex}}/VkT = \sum'' c_i c_j B_{ij} + \sum'' c_i c_j c_k B_{ijk} + \dots \quad (1)$$

c_i and c_j are the concentrations of the i th and j th species. B_{ij} is a cluster integral over the species i and j . The first sum on the right-hand side of eq 1 is over all pairs of species. The second sum is over all triplets, the higher sums would include quartets, etc.⁵ In the case of ionic solutions, eq 1 becomes (ref 5, eq 13.44)

$$-F^{\text{ex}}/VkT = \kappa^3/12\pi + \sum_n'' c^n B_n(\kappa) + \dots \quad (2)$$

The first term on the right in this equation is just the Debye-Hückel limiting law. The second term is again the cluster integral sum with the cluster integrals (now functions of the Debye-parameter κ) multiplied by the concentration set c^n . The sum in eq 2 again has contributions

from cluster integrals involving pairs of ions (B_2), triplets (B_3), etc. The corresponding equation under standard conditions (1 atm pressure and concentration units of moles per kilogram of solvent) is

$$Gw^{\text{ex}}/RT = \text{DHLL} + \sum_{i < j} B(i, j) m_i m_j + \sum_{i < j < k} B(i, j, k) m_i m_j m_k + \dots \quad (3)$$

where Gw^{ex} is the excess free energy per kilogram of solvent and the notation $i < j$ means each term is taken only once. The pair term $B(i, j)$ has replaced the pair cluster integral (B_{ij}). The corrections necessary to change from the McMillan–Mayer standard state (eq 2) to the normal standard state^{5,6} will be ignored in this paper. The correction terms contribute to both pair ($B(i, j)$) and triplet ($B(i, j, k)$) terms.⁷ The most important correction involves the volume of the species^{5,6} and does not change the qualitative conclusions of this paper.

Although the equation is formally correct, the expansion in eq 3 would not be very useful for very strongly interacting systems (such as micelle forming systems) because the series in eq 3 would be very slowly converging. In this paper, we shall use the separation implicit in eq 3. This is a reasonable separation, if (1) at constant ionic strength the properties of the solution can be represented by cluster integrals which are independent of the composition of the solution; (2) only the first three terms of the expansion are needed to represent the properties of the solution; and (3) the series is converging in the sense that $(B(i, j) > B(i, j, k) > B(i, j, k, l))$.

Equation 3 could have been derived by assuming that the properties of the solution are represented by a power series in the concentrations of all components with constant coefficients.⁸ Also, the coefficient ($-B(i, j)$) could be identified with the equilibrium constant for the formation of an i - j pair;⁹ that is, $-B(i, j) = K(i, j)$. Although this identification gives a simple physical picture for the interactions, this picture can be misleading because an association constant only has meaning if there is an attractive force between the molecules that leads to association. In the case of two large noninteracting molecules, the cluster integral gives a positive contribution to the free energy because of the excluded volume, and this would formally correspond to a physically absurd, negative equilibrium constant.

Equation 3 has already been used to derive equations for the prediction of mixtures of electrolytes.^{1,2} This is quite difficult because the cluster integrals ($B(i, j)$) are functions of the ionic strength in Mayer's theory of ionic solutions. Once this problem is solved, however, it is not difficult to adapt the equations for a general mixture. This is most easily accomplished by first using previously derived equations to predict the excess free energy per kilogram of solvent (Gw^{ex}) of the solution containing only the electrolytes ($Gw^{\text{ex}}(\text{elect})$). The next step is to use eq 3 to predict Gw^{ex} for the solution containing only the nonelectrolytes ($Gw^{\text{ex}}(\text{nonelect})$). The final step is to predict the excess free energy of transferring the nonelectrolytes from their solution to the electrolyte solution ($\Delta_T G^{\text{ex}}$). The sum of these three steps gives G^{ex} for a mixture of electrolytes and nonelectrolytes.

The excess free energy for the nonelectrolyte solution is easily calculated because the cluster integrals are not functions of the ionic strength, and there is no Debye–Hückel

term. However, before doing this, it will be convenient to change nomenclature. Accordingly, for a mixture of nonelectrolytes N_i ($i = 1, 2, \dots$), we write

$$Gw^{\text{ex}}(\text{nonelect}) = \sum_{i, j} \{N_i N_j\}_g m_i m_j + \sum_{i, j, k} \{N_i N_j N_k\}_g m_i m_j m_k + \dots \quad (4)$$

where the sums now include all terms (both $\{N_i N_j\}$ and $\{N_j N_i\}$), the species within brackets indicate the particles involved in the corresponding cluster integral, and the subscript on the brackets indicates the property being measured.

Equation 4 can be transformed back to a sum which counts each interaction only once, as follows

$$Gw^{\text{ex}}(\text{nonelect}) = \sum_{i < j} A_n \{N_i N_j\}_g m_i m_j + \sum_{i < j < k} A_n \{N_i N_j N_k\}_g m_i m_j m_k + \dots \quad (5)$$

where the coefficient for an n particle term involving n_1 particles of species N_1 , n_2 particles of species N_2 , etc. is

$$A_n = n! / (n_1! n_2! \dots) \quad (6)$$

The interger coefficients A_n added by the change in nomenclature from eq 3 to eq 5 are necessary in order to have $\{N_i N_i\} = \{N_i N_j\} = \{N_j N_j\}$ for three cases in which species i is the same as species j except for some label (such as an isotope) which does not affect the intermolecular forces. A few relationships between the coefficients in eq 3 and 5 will be helpful.

$$\text{RTB}(N_1 N_2) = \{N_1 N_2\}_g + \{N_2 N_1\}_g = 2\{N_1 N_2\}_g$$

$$\text{RTB}(N_1 N_2 N_3) = \{N_1 N_2 N_3\}_g + \{N_2 N_1 N_3\}_g +$$

$$\{N_2 N_3 N_1\}_g + \{N_1 N_3 N_2\}_g + \{N_3 N_1 N_2\}_g + \{N_3 N_2 N_1\}_g =$$

$$6\{N_1 N_2 N_3\}_g = 6\{N_2 N_1 N_3\}_g, \text{ etc.} \quad (7)$$

This nomenclature makes it easy to write approximate equations. For instance, if it is known that two solutes (U and S) are very alike in their structure and interactions with water, the following approximations are reasonable.

$$2\{\text{US}\}_g \simeq \{\text{UU}\}_g + \{\text{SS}\}_g$$

$$3\{\text{USS}\}_g \simeq \{\text{UUU}\}_g + 2\{\text{SSS}\}_g, \text{ etc.} \quad (8)$$

Other approximations are easily derived.

The final step is to calculate the excess free energy of transferring the nonelectrolytes from their solution to the electrolyte solution ($\Delta_T G^{\text{ex}}$). In this step, the electrolyte solution and the nonelectrolyte solution both contain 1 kg of water. After the transfer, the mixture of electrolytes and nonelectrolytes contains 1 kg of water and 1 kg of pure water is left over. In this step, the concentrations of all species and the ionic strength is constant so that the only interactions that change are the ones which contain at least one electrolyte and one nonelectrolyte. Thus, we can write

$$\begin{aligned} \Delta_T G^{\text{ex}} = & \sum_{j, j} \{N_i M_j\}_g m_i E_j + \sum_{i, j} \{N_i X_j\}_g m_i E_j + \\ & \sum_{i, j, k} \{N_i N_j M_k\}_g m_i m_j E_k + \sum_{i, j, k} \{N_i N_j X_k\}_g m_i m_j E_k + \\ & \sum_{i, j, k} \{N_i M_j M_k\}_g m_i E_j E_k + \sum_{i, j, k} \{N_i M_j X_k\}_g m_i E_j E_k + \\ & \sum_{i, j, k} \{N_i X_j X_k\}_g m_i E_j E_k + \dots \quad (9) \end{aligned}$$

where the sums are over all nonelectrolytes (N_1, N_2, \dots) all cations (M_1, M_2, \dots) and all anions (X_1, X_2, \dots). The concentration E_i of an ion M_i is measured in equivalents per kilogram of solvent ($E_i = m_i |Z_i|$). Some of the terms in eq 9 cannot be measured separately because of electroneutrality (for example, the interaction of a nonelectrolyte N with a salt MX includes $\{NM\}_g$ and $\{NX\}_g$). Applying the equation to specific experiments shows what terms can be measured.

The terms in eq 9 all contain at least one ion and, therefore, the cluster integrals and the interaction parameters in eq 9 will be functions of ionic strength. One way of dealing with this problem is to note that strong ionic strength dependence will occur in the Debye-Hückel region (below 0.1 m). The reasons for these expectations are most easily seen in the derivation using equilibrium constants with activity coefficients.^{9,10}

When an extended Debye-Hückel equation with a reasonable distance of closest approach is used for the activity coefficients, it is seen that the great majority of the concentration dependence occurs below $m = 0.1$ mol/kg. Since the interactions are weakest in dilute solutions, eq 9 will not be too far off if the parameters are measured above 0.1 m and assumed to be independent of ionic strength. This is particularly so because the pair term is most important and this term does not have a limiting law.

The equations for other thermodynamic quantities (excess heat content, excess volume, etc.) are easily derived by taking the appropriate derivative of eq 5 and 9.⁵ The result is identical with eq 5 and 9 with Gw^{ex} replaced by Hw^{ex} and $\{US\}_g$ replaced by $\{US\}_h$ etc. The equation for H^{ex} is derived using

$$\partial(G^{\text{ex}}/T)/\partial(1/T) = H^{\text{ex}} \quad (10)$$

So that

$$\{NM\}_h = \partial(\{NM\}_g/T)/\partial(1/T) \quad (11)$$

In this paper, some of the three particle terms in eq 9 are measured by diluting a solution of a nonelectrolyte ($U = \text{urea}$) in a salt (MX) with a solution of the salt. The equivalent concentration of the salt in both solutions is constant (E_{MX}). In this experiment $Hw^{\text{ex(elect)}}$ is unchanged. Using eq 5 and 9 to calculate the changes in the other terms gives the change in enthalpy per mole of nonelectrolyte (n_U).

$$\begin{aligned} \Delta H/n_U = & \{UU\}_h(m_{Uf} - m_{Ui}) + \\ & \{UUU\}_h(m_{Uf}^2 - m_{Ui}^2) + \dots + \{UUM + UUX\}_h \times \\ & (m_{Uf} - m_{Ui})E_{MX} + \{UUMM + UUMX + UUXX\}_h \times \\ & (m_{Uf} - m_{Ui})E_{MX}^2 + \{UUUM + UUUX\}_h \times \\ & (m_{Uf}^2 - m_{Ui}^2)E_{MX} \quad (12) \end{aligned}$$

where m_{Uf} and m_{Ui} are final and initial urea molalities, n_U is the moles of urea present, E_{MX} is the equivalent concentration of electrolyte per kilogram of solvent ($E_{MX} = m_M |Z_M| = m_X |Z_X|$) and $\{UUM + UUX\}_h = \{UUM\}_h + \{UUX\}_h$ etc. The first series of coefficients represent the interactions of nonelectrolyte solute species with themselves: i.e., the interactions present in a pure nonelectrolyte solution. In order to evaluate the higher order interactions the data were fit to

$$\begin{aligned} \Delta H/n_U - \Delta H^0/n_U = & \{UUM + UUX\}_h(m_{Uf} - m_{Ui}) \times \\ & E_{MX} + \{UUMM + UUMX + UUXX\}_h(m_{Uf} - m_{Ui}) \times \\ & E_{MX}^2 + \{UUUM + UUUX\}_h(m_{Uf}^2 - m_{Ui}^2)E_{MX} \quad (13) \end{aligned}$$

where $\Delta H^0/n_U$ is the change in excess enthalpy if a solu-

tion of U is diluted in the same way without the presence of the salt MX .

Experimental Section

A. Materials. The salts used were, with one exception, Fisher certified reagent grade or Baker analyzed reagent, all having a stated impurity of less than 0.1%. The tetra-*n*-butylammonium chloride (Bu_4NCl) was obtained from Eastman Kodak and carried no certification of purity. The *tert*-butyl alcohol and urea used were Fisher certified reagent (impurities < 0.01%). The former was recrystallized twice from methanol, the latter used directly from the bottle. All salts were dried *in vacuo* for 12 hr or more over P_2O_5 at elevated temperatures. The water impurity in *tert*-butyl alcohol was assessed by Karl Fisher titration and found to be negligible (<0.05%).

Nonelectrolyte-electrolyte mixtures were made up by weight freshly each day from pure nonelectrolyte and stock salt solutions.

B. Calorimeter. The calorimeter used is a commercially available heat flow calorimeter.^{11,12} Two identical 14-ml gold cells are arranged symmetrically inside an insulated aluminum block in a constant temperature air bath. The difference between the heats of reaction in the two cells is measured by rotation of the aluminum block allowing the two initial solutions in the two cells to intermix. The blank heat, which is a function of the total weight of solution in the calorimeter cells, was measured after each experiment and subtracted from the apparent heat. The uncertainty in the blank heat was found to be around 100 μcal when dry cell walls were wetted in mixing and around 25 μcal when no wetting occurs. In the results reported here, 1 cal = 4.184 J. A total of 133 experiments were performed.

C. Procedures. In preparation for a dilution experiment, the reaction cell is cleaned and dried. For mixings where the heat of wall wetting is negligible compared to the heat of dilution, the salt solution and salt-nonelectrolyte mixtures are loaded directly by syringe into opposite sides of the cell. For low-heat mixes, the entire cell is rinsed with the diluent salt solution or with the final solution from the previous experiment so that all walls are wetted before mixing. All but about 0.01 g of this solution can be removed from the cell prior to introduction of the solutions. The uncertainty in the completeness of this removal process constitutes a small source of error (<0.3%) in the measurement of the low concentration points.

Special problems arose using this method in the measurement of the *tert*-butyl alcohol dilution because of the relatively high vapor pressure of this nonelectrolyte. Thus upon the introduction of solution to the cell, there is a steady transfer of *tert*-butyl alcohol to the diluent side by diffusion through the air space which joins the two compartments at the top of the cell. This distillation process is roughly a linear function of time and the experimentally obtained heat was, therefore, corrected for the time elapsed between filling and mixing. For a few experiments, 2 hr or more were allowed to elapse before mixing in order to assess the time dependence. The rate of distillation was found to be roughly 5%/hr and the equilibration time for most experiments was around 0.5 hr. Hence, the average correction was about 2.5%. The uncertainty in this rate of distillation is probably the largest single source of error for the *tert*-butyl alcohol dilutions.¹³ The heat generated by this distillation process fluctuated greatly, causing uncertainty in the position of the initial baseline.

In addition to the uncertainties in the blank heat of mixing and those due to distillation, a third source of error was anticipated for all processes. The heat of transfer of water between the liquid and the vapor phase at the time of mixing is function of the osmotic coefficient of the solutions before and after the mixing. However, the volume of vapor space in equilibrium with each initial solution is uncertain since the vapor space is common to both solutions. This uncertainty has been estimated to result in a *maximum* error in ϕ_L of 1 cal/mol and is independent of concentration. An additional *maximum* uncertainty of 5 cal/mol can be expected in the measurement of the heats of dilution of *tert*-butyl alcohol because of the uncertainty in vapor-to-liquid transfer of *tert*-butyl alcohol in mixing.

The raw data can be seen in Table 1M in the microfilm edition of this paper.¹³ The heat of dilution data were weighted according to anticipated error and fitted to eq 13. The parameters obtained for the systems studied can be seen in Table I. The uncertainties tabulated are estimates of the 95% confidence level.¹³ The scatter of points observed when fitting the raw data to eq 13 is reasonable with respect to the expected calorimetric errors. For concentrations of Bu₄NCl higher than 0.5 *m*, a higher order salt-dependent term would be necessary to adequately fit the *tert*-butyl alcohol data. Without such a term, the excess heat predicted by eq 13 for a 1 *m* salt concentration would be about twice that found experimentally. Similarly, a discrepancy of about 30% is found if eq 13 is used to predict the excess heat for urea in a 2 *m* sodium chloride solution. Clearly, higher order salt-dependent terms in eq 13 are necessary to adequately represent the behavior of H^{ex} in more concentrated solutions.

The effects of the presence of a constant concentration of electrolyte on the excess enthalpy per mole of nonelectrolyte can be seen in Figures 1 and 2.¹³

The agreement in the heats of dilution with values found in the literature is satisfactory. The data for urea fall within experimental error of previous results.¹⁴ The limiting slopes obtained of -85.87 and -82.9 compare well with the present result of $\{UU\}_h = -84.4$ cal kg/mol² (see Table I). The limiting slope for the dilution of *tert*-butyl alcohol has been measured by Lange over a concentration range 0.1–0.3 *m* and found to be 145^{15} compared to the present result $\{BB\}_h = 156.9$ cal kg/mol². Recently Krishnan and Friedman¹⁶ found for *tert*-butyl alcohol $\{BB\}_h = 360$. Because of this large discrepancy an independent measurement was made using a different calorimeter and a different sample. The calorimeter¹⁷ used thin glass bulbs to hold the sample and did not require vapor space corrections. A dilution from 0.998 to 0.0186 mol/kg gave off 246 cal/mol (*vs.* 242.5 calculated from the results with the LKB calorimeter).

Discussion

In order to estimate the accuracy of the prediction of the properties of mixtures of electrolytes and nonelectrolytes it is necessary to assess the relative magnitude of the effect of the pair, triplet, and quadruplet terms. We will discuss their effect on the excess enthalpy of a solution in which each solute has a concentration of 1 *m*. Comparison of the present data with values from the literature indicates that, for a wide variety of solutes, the pair term makes a contribution of from +300 to -300 cal/mol, triplet terms contribute ± 30 cal/mol, and quadruplet terms contribute ± 5 cal/mol. Interactions between large nonpolar groups (BuOH–Bu₄NCl) are an important exception to this generalization,

and other exceptions involving systems where strong chemical interactions occur can doubtless be found. As discussed below, the above generalization seems to hold whether the particles are charged or not, except that the interactions are somewhat larger if the interaction is between two ions of opposite sign.

Except for the interactions involving Bu₄NCl all of the triplet and quadruplet terms in Table I are in accord with this generalization. The triplet terms range from +36 to -12 cal kg² mol⁻³ and the quadruplet terms range from -2 to -5 cal kg³ mol⁻⁴. The large effects for BuOH–Bu₄NCl triplet and quadruplet terms (410 cal kg² mol⁻³ and 200 cal kg³ mol⁻⁴) are due to the hydrophobic nature of these molecules and will be discussed below. A quadruplet interaction in the urea–Bu₄NCl system is also much larger than expected. These strong, high-order interactions may make a contribution to the stability of the solid complex Bu₄NCl·6 urea and to the ability of urea to denature proteins.¹⁸

Stern and coworkers have measured the heats of transferring a variety of nonelectrolytes from water into salt solutions. Their results indicate that the contribution of the term involving one nonelectrolyte molecule with one ion at 1 *m* ranges from -66 to $+204$ cal/mol for ethyl acetate–alkali metal halide mixtures^{19a} and from -225 to $+106$ cal/mol for acetic acid–alkali halide mixtures.^{19b} In addition, the NaCl–urea term is 180 cal/mol^{19c} and the NaCl–H₂O₂ term is -150 cal/mol.^{19d}

Turning to the results for the interactions of nonelectrolytes with each other, the result in Table I for the heat of dilution of urea shows that at 1 *m* the term for two urea molecules contributes -84 cal/mol and the term for three urea molecules contributes 5 cal/mol. Similarly the heat of dilution of *tert*-butyl alcohol indicates that the pair terms contribute 157 cal/mol and the triplet terms contribute 89 cal/mol at 1 *m*. The triplet contribution is rather high and again this is due to the hydrophobic bonding present in the nonpolar portion of the *tert*-butyl alcohol molecules. Kozack, Knight, and Kauzmann list data for a wide variety of nonelectrolytes, and these also indicate that nonelectrolyte pairwise and triplet terms are of the same magnitude as other pair and triplet terms.²⁰

The results from a variety of measurements of heats of mixing electrolyte solutions indicate that the interactions between two like-charged ions also conform to the above generalizations. For the alkali halides the interactions vary from -196 for a combination of cesium–lithium pairwise interactions at 1 *m* to $+84$ for a combination of lithium–sodium pairwise interactions at 1 *m*.^{21,22} For the alkali halides, it has been found that the effect of triplet terms on the heat content at 1 *m* is roughly ± 20 cal/mol and that quadruplet terms are much smaller than this.^{22,23} The heats of dilution of electrolytes listed by Parker indicate that the total interactions present in 1 *m* solutions of the alkali halides varies from $+296$ for LiCl to -715 for KNO₃.²⁴ This large spread is due to the interactions of the oppositely charged ions and indicates that these interactions are somewhat larger than the ± 300 cal/mol indicated in the above generalization. This is not too surprising since there is an additional strong electrostatic attraction between these ions which should increase the interaction between them in a 1 *m* solution.

The results for the interaction of *tert*-butyl alcohol with Bu₄NCl show that this behavior is quite different from all of the other cases studied. The triplet term is very large (438 cal/mol at 1 *m*) and higher order terms are important

TABLE I: Interaction Parameters in Eq 13

	LiCl	NaCl	CsCl	Bu ₄ NCl
(A) Urea as Nonelectrolyte (U); {UU} _h = -84.4 cal kg/mol ² , {UUU} _h = +5 cal kg ² /mol ³				
{UUM + UXU} _h , cal kg ² /mol ³	25(5) ^a	33(2)	36(6)	-16(10)
{UUUM + UUUX} _h , cal kg ³ /mol ⁴	-2.0(6)	-2.8(3)	-2.7(5)	-1.5(15)
{UUMM + UUMX + UUXX} _h , cal kg ³ /mol ⁴	-3.2(9)	-4.3(7)	-4.6(12)	+50(20)
(B) <i>tert</i> -Butyl Alcohol as Nonelectrolyte (B); {BB} _h = 156.9 cal kg/mol ² , {BBB} _h = +89.2 cal kg ² /mol ³				
{BBM + BBX} _h , cal kg ² /mol ³	10(4)	4(7)	-12(12)	410(60)
{BBMM + BBMX + BBXX} _h , cal kg ³ /mol ⁴				200(150)

^a The numbers in parentheses are the estimated 95% confidence limits of the least significant digit. For instance, -2.0 ± 0.6 is written as -2.0(6). 1 cal = 4.184 J.

even at fairly low concentrations as evidenced by the fact that eq 13 will not fit the data in 1 *m* Bu₄NCl. The magnitude and sign of these interactions are consistent with that of other hydrophobic interactions if it is assumed that the effect is very roughly proportional to the amount of hydrocarbon present, i.e., the effect of a Bu₄N⁺ ion is approximately 4 times the effect of a *tert*-butyl alcohol molecule. The heat of dilution of *tert*-butyl alcohol given in Table I indicates that triplets contribute 89 cal/mol at 1 *m*. Thus, it would be expected that the interaction of two BuOH molecules with one Bu₄N⁺ ion would be about 4 times this. The results in Table I show that it is actually 5 times this. Considering the gross simplification involved in the above assumption, this agreement is gratifying. Table I gives the pairwise contribution of two BuOH molecules as 157 cal/mol at 1 *m*. Wen and Hung have measured the butane-Bu₄NBr interaction and found 522 cal/mol at 1 *m*.²⁵ Heats of dilution and mixing experiments indicate that the Bu₄N⁺-Bu₄N⁺ interaction is about 2000 cal/mol at 1 *m*. These results are in the ratio of 1:3.3:13 compared to the ratio of 1:4:16 predicted by the above rough approximation. The *t*-BuOH-Bu₄NBr pairwise interaction (2100 cal/mol) measured by Mohanty, Sarma, Subramanian, and Ahluwalia²⁶ is much larger than expected. The interactions in 1 *m* tetrabutylammonium butyrate measured by Levine and Lindenbaum²⁷ (5000 cal) are somewhat larger than expected (2700 cal).

The wide variety of free-energy measurements of nonelectrolyte-electrolyte interactions reviewed by Long and McDevit confirm that the free energies of pairwise terms are also much larger than the free energies of the triplet terms.²⁸ If this were not true the plots of salt effects (log *f_i*) vs. molality would show substantial curvature. The recent results of Spink and Schrier²⁹ show that below 0.1 *m*, the free-energy term involving an acetone molecule with potassium and chloride or sodium and chloride ions increases by 3 or 4%. This effect could be due to changes in the activity coefficients of the ions below 0.1 *m*.

It should be noted that the above comparison depends on the standard concentration (1 *m*). If the interactions were compared at 0.1 *m* instead of 1 *m*, the contribution of pair terms would be reduced by a factor of 10 while the contribution of triplet terms would be reduced by a factor of 100.

The signs and relative magnitudes of the contribution of various triplet and higher order terms to the excess enthalpy show trends which correlate well with other properties of these solutes. Such trends are often rationalized in terms of the solute-water-structure-alteration characteristics of the various ions. Because the interaction of two or more solute species would be expected to result in a transfer of solvent from solute cospheres to the bulk, it would be predicted

that the change in excess enthalpy associated with this transfer would reflect in part the changes in water structure. Since all salts in the present study contained the same anion, it is reasonable to attribute the differences between these chloride salts to the cation contributions.

For contributions to the excess enthalpy, the following trends are observed (B = *tert*-butyl alcohol, U = urea): {B,B,Bu₄N⁺}_h >> {B,B,Li⁺}_h > {B,B,Na⁺}_h > {B,B,Cs⁺}_h; {U,U,Cs⁺}_h > {U,U,Na⁺}_h > {U,U,Li⁺}_h > {U,U,Bu₄N⁺}_h; {U,U,U,Bu₄N⁺}_h > {U,U,U,Li⁺}_h > {U,U,U,Na⁺}_h ≈ {U,U,U,Cs⁺}_h. While the cation trends are intriguing, it is well to remember that these effects reflect a complex and poorly understood physical phenomenon and any further speculation on the reasons for these trends is of questionable value. However, trends like this should be quite useful in estimating interaction constants that have not been measured. For instance {BBK⁺}_h should be between {BBNa⁺}_h and {BBCs⁺}_h.

The fact that the majority of triplet terms measured in this study are comparatively small shows that predictions of the properties of electrolyte-nonelectrolyte mixtures can be made with reasonable accuracy if all pairwise terms are included. Thus reasonable predictions are possible with the knowledge of only a few interactions.

Acknowledgment. The authors are indebted to Peter Thompson for the independent check of the heat of dilution of *tert*-butyl alcohol.

The authors are grateful for the support of this work by the National Science Foundation.

Supplementary Material Available. Figures 1 and 2 and details of the least-squares fit which properly corrects for this distillation phenomenon are found in Appendix I.M which will appear following these pages in the microfilm edition of this volume of the journal. Photocopies of the supplementary material from this paper only or microfiche (105 × 148 mm, 24× reduction, negatives) containing all of the supplementary material for the papers in this issue may be obtained from the Journals Department, American Chemical Society, 1155 16th St., N.W., Washington, D. C. 20036. Remit check or money order for \$3.00 for photocopy or \$2.00 for microfiche, referring to code number JPC-74-2460.

References and Notes

- (1) R. H. Wood and P. J. Reilly, *Annu. Rev. Phys. Chem.*, **21**, 387 (1970).
- (2) The latest in this series is P. J. Reilly and R. H. Wood, *J. Phys. Chem.*, **76**, 3474 (1972).
- (3) R. B. Cassel and R. H. Wood, *J. Phys. Chem.*, **78**, 2465 (1974).
- (4) W. G. McMillan and J. E. Mayer, *J. Chem. Phys.*, **13**, 276 (1945).

- (5) H. Friedman, "Ionic Solution Theory," Interscience, New York, N. Y., 1962, eq. 8.20.
- (6) H. L. Friedman, *J. Solution Chem.*, **1**, 387, 413, 419 (1972).
- (7) The separation into pair and triplet terms is only approximate after conversion to standard conditions. For a discussion, see ref 5, 6, and 20.
- (8) G. Scatchard and S. S. Prentiss, *J. Amer. Chem. Soc.*, **56**, 1486 (1934).
- (9) R. A. Robinson, P. J. Reilly, and R. H. Wood, *J. Chem. Thermodyn.*, **3**, 461 (1971).
- (10) The identification of $B(i,j)$ with $-K(i,j)$ depends on the assumption that the ideal solution has activities equal to molal concentrations. The higher term $B(i,k,k)$ can only be identified with the triplet equilibrium constant, $-K(i,j,k)$, when the pair interactions are small and the same ideal solution rule is assumed.
- (11) LKB 10700-2 Batch Microcalorimeter. LKB Produkter AB 5-16125 Bromma 1, Sweden.
- (12) I. Wadso, *Acta. Chem. Scand.*, **72**, 927 (1968).
- (13) See paragraph at end of text regarding supplementary material.
- (14) (a) F. T. Gucker and H. B. Pickard, *J. Amer. Chem. Soc.*, **62**, 1469 (1940); (b) D. Hamilton and R. H. Stokes, *J. Solution Chem.*, **1**, 223 (1972).
- (15) E. Lange and K. Möhring, *Z. Elektrochem.*, **57**, 660 (1953).
- (16) H. L. Friedman and C. V. Kirshnan, *J. Solution Chem.*, **2**, 119 (1973).
- (17) J. D. Beck, R. H. Wood, and N. N. Greenwood, *Inorg. Chem.*, **21**, 387 (1970).
- (18) S. Saito, M. Lee, and W. Y. Wen, *J. Amer. Chem. Soc.*, **88**, 5107 (1966).
- (19) (a) J. H. Stern and A. Hermann, *J. Phys. Chem.*, **71**, 306 (1967); (b) J. H. Stern, J. P. Sandstrom, and A. Hermann, *ibid.*, **71**, 3623 (1967); (c) J. H. Stern and J. D. Kulluk, *ibid.*, **73**, 2795 (1969); (d) J. H. Stern and W. R. Bottenberg, Jr., *ibid.*, **75**, 2229 (1971).
- (20) J. J. Kozak, W. S. Knight, and W. Kauzmann, *J. Chem. Phys.*, **48**, 675 (1968).
- (21) Y. C. Wu, M. B. Smith, and T. F. Young, *J. Phys. Chem.*, **69**, 1868, 1873 (1965).
- (22) R. H. Wood and R. W. Smith, *J. Phys. Chem.*, **69**, 2974 (1965).
- (23) A. S. Levine, N. Bhatt, M. Ghamkhar, and R. H. Wood, *J. Chem. Eng. Data*, **15**, 34 (1970).
- (24) V. B. Parker, *Nat. Stand. Ref. Data Ser., Nat. Bur. Stand.*, No. 2 (1965).
- (25) W. Y. Wen and J. H. Hung, *J. Phys. Chem.*, **74**, 170 (1970).
- (26) R. K. Mohanty, T. S. Sarma, S. Subramanian, and J. C. Ahluwalia, *Discuss. Faraday Soc.*, **67**, 305 (1971).
- (27) A. S. Levine and S. Lindenbaum, *J. Solution Chem.*, **2**, 445 (1973).
- (28) F. A. Long and W. F. McDevitt, *Chem. Rev.*, **51**, 119 (1952).
- (29) M. Y. Spink and E. E. Schrier, *J. Chem. Thermodyn.*, **2**, 821 (1970).

Heat of Mixing Aqueous Nonelectrolytes at Constant Molality. Sucrose, Urea, and Glycine¹

R. B. Cassel and R. H. Wood*

Department of Chemistry, University of Delaware, Newark, Delaware 19711 (Received April 22, 1974)

The heat of mixing aqueous solutions of sucrose, urea, and glycine at constant molality ($m = 0.1$ – 1.0) has been measured at 25°. Equations are developed for separating the various terms of a power series expansion of the excess enthalpy. The leading terms are the pairwise interaction constants for like and unlike pairs. In the three cases reported the enthalpy effects of two unlike solutes are always more positive than the effect of either solute with itself ($\{N_i N_j\}_h > \{N_i N_i\}_h$ or $\{N_j N_j\}_h$). The result of this is that all enthalpies of mixing are positive. This is quite different from the sign rule observed in mixtures of electrolytes.

Introduction

The prediction of the properties of a multicomponent mixture of electrolytes and nonelectrolytes from as few basic measurements as possible is one of the long-range goals of a great deal of research. In the preceding paper,² a general equation for predicting the properties of a mixture were derived. Also reported were the results of experiments on mixtures of electrolytes and nonelectrolytes which gave information about the sign and magnitude of some three and four particle terms in these mixtures. The present paper reports results on mixtures of nonelectrolytes. A method is presented for measuring the sign and magnitude of the heat effect caused by pairwise interactions between solutes with different effects on the structure of water. There are several previous investigations of mixtures of two nonelectrolytes in water but these either do not cover a low enough concentration to allow reliable estimation of the pairwise interactions^{3a–d} or are limited in accuracy because of the type of calorimeter used.^{3c–e} This is surprising since results in this area are much more amenable to interpretation than the results for the corresponding mixtures of electrolytes which have been extensively investigated. The

corresponding free energies of mixtures of nonelectrolytes in water have received somewhat more attention.^{3f–j}

Experimental Section

Sucrose and urea were Fisher certified ACS grade having an analyzed total impurity of less than 0.06 and 0.01%, respectively. Glycine was obtained from J. T. Baker Co. and was Ultrex certified reagent assayed to be 99.9% pure with less than 0.02% analyzed impurity. Karl Fischer titrations indicated a maximum water content of 0.02, 0.06, and 0.06% by weight for sucrose, urea, and glycine, respectively. Nonelectrolyte solutions were prepared by weight fresh each day to avoid bacterial decomposition. Calculation of the fractional ionization of glycine indicated a negligible contribution to the heat of mixing.

The calorimeter and procedure have been described in the previous paper.² The reaction vessel consists of a gold cell having two compartments (3- and 5-ml capacity) adjoining at the top by a 5-ml vapor space. The two nonelectrolyte solutions are loaded by syringe into the two compartments and allowed to thermally equilibrate. Mixing is initiated by rotation of the cell. For small heats the gold

cell walls are wetted with one, or a mixture of both nonelectrolyte solutions to avoid the substantial and irreproducible heat of wall wetting. The amount of solution left on the walls is reproducible² so the composition of the two solutions being mixed can be calculated.

Results

The calorimetric data appear in Table I. The major source of experimental uncertainty at high concentrations is the heat associated with the transfer of solvent between the solution and the vapor space. For small heats, such as those of mixing at low concentration, the greatest uncertainties are due to the irreproducibility of the heat associated with the mechanical intermixing process and baseline instability. By a comparison of q_{expt} and q_{calcd} in Table I the scatter of points from a smooth curve can be seen to be less than 1% for large heats. The heat of mixing solutions of two pure components can be represented by the equation

$$\Delta_m H = -q = y_A(1 - y_A)m^2W[RTh_0 + RTh_1(1 - 2y_A)] \quad (1)$$

where y_A is the mole fraction of the solute with the higher molecular weight, m is the total solute molality of the initial and final solutions, W is the total weight of water, RTh_0 is a measure of the magnitude of the interaction at $y = 1/2$, and RTh_1 is a measure of the asymmetry (skew) of the mixing curve. This equation is analogous to that used to describe mixtures of electrolytes.⁴ In fitting the actual calorimetric data in Table I, eq 1 was used to calculate q_I , q_{II} , and q_F (the heats of forming the initial solutions (I and II) and the final solution from the pure components). The calculated heat from the actual experiment is then $q_F - q_I - q_{II}$ and a least-squares procedure is used to adjust RTh_0 and RTh_1 to minimize the difference between experimental and calculated heats. The values for the parameters which best fit this data are given in Table II.

The data treatment is entirely analogous to that used for interpreting heats of mixing electrolyte solutions⁵ and the interactions can be related similarly to cluster integrals.^{2,4,6,7} The nomenclature is the same as that used previously.²

The equation for the excess enthalpy per kilogram of solvent (H^{ex}/W) analogous to eq 4 of ref 2 is

$$H^{\text{ex}}/W = \sum_{i,j} \{N_i N_j\}_h m_i m_j + \sum_{i,j,k} \{N_i N_j N_k\}_h m_i m_j m_k + \dots \quad (2)$$

where the sums include all terms (both $\{N_i N_j\}_h$ and $\{N_j N_i\}_h$), m_i is the molality of species N_i , the species within the brackets indicate the particles interacting, the subscript h indicates it is the enthalpy of interaction, and the sum is over all species. If all of the terms in eq 2 for the interaction of n urea molecules (U) and m sucrose molecules (S) are collected, the result is

$$\frac{(n+m)!}{n!m!} \{U^n S^m\}_h m_U^n m_S^m \quad (3)$$

For the mixing process in eq 1, the excess enthalpy of the final solution containing 1 kg of water, $y_S m$ molal sucrose (S), and $(1 - y_S) m$ molal urea (U) is

$$H^{\text{ex}} = \{SS\}_h y_S^2 m^2 + \{UU\}_h (1 - y_S)^2 m^2 + 2\{SU\}_h y_S (1 - y_S) m^2 + \{SSS\}_h y_S^3 m^3 + \{UUU\}_h (1 - y_S)^3 m^3 + 3\{SUU\}_h y_S (1 - y_S)^2 m^3 + 3\{UUS\}_h y_S^2 (1 - y_S) m^3 + \dots \quad (4)$$

Similarly, the excess enthalpy of the initial solution containing y_S kg of water and m molal sucrose is

$$H^{\text{ex}} = y_S \{SS\}_h m^2 + \{SSS\}_h m^3 + \dots \quad (5)$$

The excess enthalpy of the initial solution containing $(1 - y_S)$ kg of water and m molal urea is

$$H^{\text{ex}} = (1 - y_S) \{UU\}_h m^2 + \{UUU\}_h m^3 + \dots \quad (6)$$

Combining eq 4, 5–6 to calculate the excess enthalpy of mixing per kilogram of solvent ($\Delta_m H^{\text{ex}}/W$) gives

$$\Delta_m H^{\text{ex}}/W = y_S(1 - y_S)m^2[2\{SU - SS - UU\}_h + (3m/2)(\{SSU + SUU - SSS - UUU\}_h + (1 - 2y_S)(m)(1/2\{SSS - UUU\}_h + 3/2\{UUU - SSU\}_h)] \quad (7)$$

where $\{SSU + SUU - SSS - UUU\}_h = \{SSU\}_h + \{SUU\}_h - \{SSS\}_h - \{UUU\}_h$ etc. Comparison of this equation and eq 6 shows that

$$RTh_0 = (2\{SU\}_h - \{SS\}_h - \{UU\}_h) + (3m/2)(\{SSU\} + \{SUU\} - \{SSS\} - \{UUU\}_h) \quad (8)$$

and

$$RTh_1 = m(1/2\{SSS - UUU\}_h + 3/2\{SUU - SSU\}_h) \quad (9)$$

Table II gives the results of a least-squares fit of the data in Table I to eq 1. According to eq 8, a plot of RTh_0 vs. m (see Figure 1) gives an intercept of $2\{SU\}_h - \{SS\}_h - \{UU\}_h$ and a slope of $3/2\{SSU + SUU - SSS - UUU\}_h$. Similarly from eq 9 a plot of RTh_1 vs. m should have an intercept of zero and a slope of $1/2\{SSS - UUU\}_h + 3/2\{SUU - SSU\}_h$.

The above equations together with measurements of the heats of dilution of pure nonelectrolytes allow the determination of all of the individual pairwise and triplet terms. This is done using eq 8 and 9 for the mixtures together with eq 2 applied to a solution with only one solute. When only one solute is present (urea) eq 2 becomes

$$H^{\text{ex}}/n = \phi_L = \{UU\}_h m_U + \{UUU\}_h m_U^2 + \dots$$

The heats of dilution of sucrose⁸ and urea² yield $\{UU\} = -84$ and $\{SS\} = +137$. Equation 8 shows that a plot of RTh_0 vs. m for the sucrose-urea mixtures yields an intercept $2\{SU\} - \{SS\} - \{UU\} = 340 \text{ cal mol}^{-2} \text{ kg}$. Combining these results gives $\{SU\} = +197$. The results of similar calculations for the measurements reported in this paper are given in Table III together with the sources of the single solute data.⁹

If heats of dilution are used to classify solutes as structure making or structure breaking,^{10,11} then structure-making solutes are ones which have positive excess enthalpies at low concentrations and structure-breaking solutes are ones that have negative excess enthalpies at low concentrations. On this basis, glycine and urea are structure breakers, while sucrose is a structure maker. An examination of the results in Table II shows that the enthalpy effects of two unlike solutes is more positive than the effect of either solute with itself; that is $\{SU\}_h = 197$ is more positive than $\{SS\}_h = 137$, or $\{UU\}_h = -84$. Similarly $\{SG\}_h = 148$ is more positive than $\{SS\}_h = 137$ or $\{GG\}_h = 107$. When the two similar solutes are mixed the interaction is a little more positive than either of the other two interactions. Estimates of the appropriate correction factors show that this is also true in the McMillan-Mayer standard state.⁶ The result is that all of the $\Delta_m H$ are positive. For the two mixings involving unlike solutes $\Delta_m H$ is large and positive and

TABLE I: Calorimetric Data for Heats of Mixing of Aqueous Nonelectrolyte Solutions at 25° and Constant Molality

Molality, mol/kg	$W_{AI},^b$ g	$W_{BI},$ g	$W_{AII},$ g	$W_{BII},$ g	$-q_{\text{expt}},^c$ mcal	$-q_{\text{calcd}},$ mcal
Sucrose (A)-Urea (B)						
1.0	0	4.152	2.566	0	396.6	395.3
1.0	4.394	0	0	1.879	351.7	353.8
1.0	2.779	0	0	2.044	306.5	307.3
1.0	0.01	3.734	2.538	0.01	375.0	374.7
1.0	4.788	0.01	0.01	1.819	354.1	352.9
0.5	0	4.437	1.960	0	97.1	98.0
0.5	0.01	4.471	1.849	0.01	93.0	93.0
0.5	2.997	0.01	0.01	2.588	102.9	101.9
0.5	0.01	2.702	2.658	0.01	106.5	83.1
0.5	4.533	0.01	0.01	1.455	83.4	88.5
0.5	4.668	0.01	0.01	1.567	87.7	92.4
0.5	0.01	4.475	1.831	0.01	92.2	106.2
0.2	3.088	0.01	0.01	2.428	17.41	17.22
0.2	2.758	0.01	0.01	2.351	16.61	16.56
0.2	0.01	4.270	1.694	0.01	15.01	15.13
0.2	0.01	4.342	1.836	0.01	15.98	16.12
0.2	0.01	4.388	1.782	0.01	16.61	15.82
0.2	4.594	0.01	0.01	1.681	15.17	15.74
0.2	4.371	0.01	0.01	1.578	14.64	14.82
0.1	0.01	4.189	1.723	0.01	3.90	3.83
0.1	4.472	0.01	0.01	1.801	3.82	4.08
0.1	2.729	0.01	0.01	2.553	4.28	4.17
0.1	0.01	3.846	2.195	0.01	4.51	4.96
0.1	4.354	0.01	0.01	2.051	4.45	4.43
Sucrose (A)-Glycine (B)						
1.0	4.824	0	0	1.844	269.9	272.1
1.0	0	4.047	1.747	0	224.0	226.7
1.0	3.548	0	0	2.825	309.8	308.9
1.0	5.178	0	0	1.894	283.0	283.4
1.0	0	4.684	2.186	0	281.6	277.8
0.5	4.645	0	0	1.816	75.4	76.0
0.5	0.00	4.309	1.752	0	69.1	68.8
0.5	4.261	0.00	0	1.865	75.1	75.3
0.5	0.00	4.198	2.112	0	78.6	78.1
0.2	4.241	0.0	0.01	2.360	15.08	15.14
0.2	4.448	0.01	0.01	2.336	15.51	15.25
0.2	0.01	4.277	2.304	0.01	14.82	14.67
0.2	0.01	4.272	2.414	0.01	14.77	15.12
0.1	0	4.123	2.420	0	3.94	4.15
0.1	4.266	0.01	0.01	2.058	3.55	3.51
0.1	0.01	4.106	2.203	0.01	3.58	3.59
0.1	0.01	4.173	2.213	0.01	3.70	3.62
0.1	4.197	0	0	2.310	3.93	3.80
Glycine (A)-Urea (B)						
1.0	0.01	4.227	1.610	0.01	38.92	39.30
1.0	4.224	0.01	0.01	1.767	42.22	42.27
1.0	0.01	4.296	1.727	0.01	42.82	41.54
1.0	4.375	0.01	0.01	1.858	44.65	44.26
1.0	2.668	0.01	0.01	2.074	40.40	39.46
1.0	2.853	0.01	0.01	2.620	44.28	46.24
0.5	0	4.052	2.177	0.01	11.39	11.62
0.5	4.325	0.01	0.01	1.974	11.15	11.10
0.5	0.01	4.407	2.291	0.01	12.48	12.32
0.5	2.690	0.01	0.01	2.501	10.74	10.59
0.5	2.655	0.01	0.01	2.274	9.86	10.00
0.2	0.0	4.317	2.247	0.01	1.73	1.81
0.2	4.477	0.01	0.01	2.273	1.83	1.85
0.2	0.01	2.769	2.647	0.01	1.78	1.65
0.2	0.01	2.500	1.995	0.01	1.67	1.69

^a Component A is the solute with the higher molecular weight. ^b The weights of components A and B are designated W_A and W_B , respectively. The 4- and 2-ml compartments are designated I and II, respectively. For example, in the last experiment listed in the table, a solution made by mixing 0.01 g of 0.2 mol/kg of glycine solution with 2.500 g of 0.2 mol/kg of urea solution is mixed with a solution made by mixing 1.995 g of 0.2 mol/kg of glycine solution and 0.01 g of 0.2 mol/kg of urea solution. The heat absorbed is 1.67 mcal. ^c 1 cal = 4.184 J.

for the mixing involving like solutes $\Delta_m H$ is small and positive. A lot more data will be needed in order to see if these

trends continue when a wide variety of solutes is measured. Ellerton and Dunlop measured the free energy of the su-

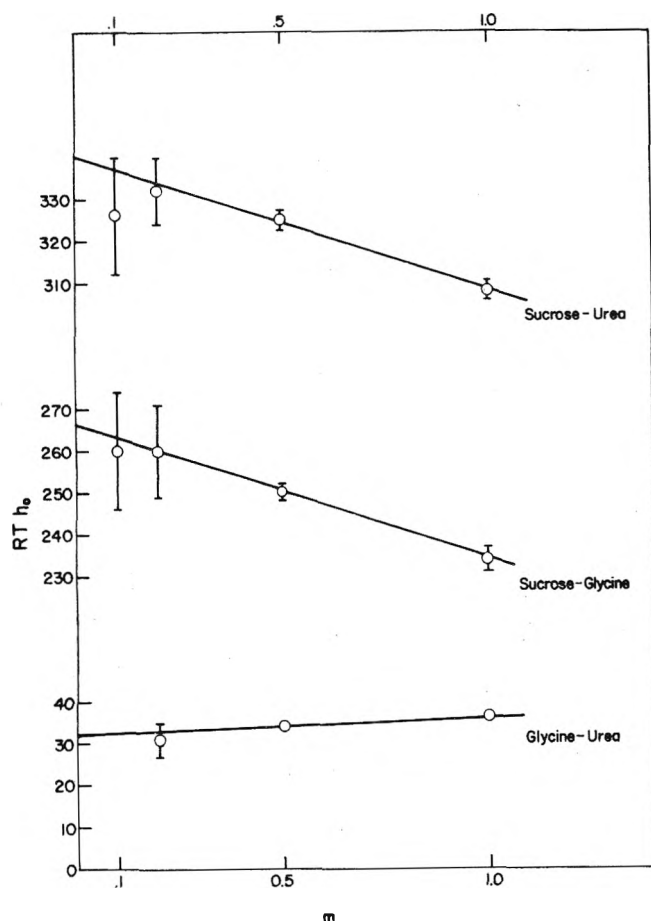


Figure 1. Values of RTh_0 (cal mol⁻² kg) plotted vs. molality (mol kg⁻¹) for various mixtures of nonelectrolytes.

crose-urea-water system using the isopiestic technique.^{3h} Their results can be compared with the present results after converting to the same nomenclature. Using standard thermodynamics transformations on eq 4 of ref 2 (the free-energy analog of eq 2) gives for the osmotic coefficient, ϕ , of a urea-sucrose mixture

$$RT(m_U + m_S)(1 - \phi) = -2\{US\}_g m_U m_S - \{UU\}_g m_U^2 - \{SS\}_g m_S^2 - 6\{USS\}_g m_U m_S^2 - 6\{SSU\}_g m_S^2 m_U - 2\{UUU\}_g m_U^3 - 2\{SSS\}_g m_S^3$$

and for the activity coefficient of urea, γ_U , in a mixture

$$RT \ln \gamma_U = 2\{US\}_g m_S + 2\{UU\}_g m_U + 3\{USS\}_g m_S^2 + 6\{UUS\}_g m_U m_S + 3\{UUU\}_g m_U^2 + \dots$$

and for the change in osmotic coefficient on mixing

$$\Delta = (m_U + m_S)\phi_{\text{mix}} - m_U\phi_U^0 - m_S\phi_S^0 = (2\{US\}_g m_U m_S + 6\{USS\}_g m_U m_S^2 + 6\{UUS\}_g m_U^2 m_S + \dots)/RT$$

where ϕ_U^0 is the osmotic coefficient of a urea solution of molality m_U . Using these equations and the data of Ellerton and Dunlop gives $\{SS\}_g = 42$ cal mol kg⁻², $\{UU\}_g = -26$ cal mol⁻² kg, and $\{US\}_g = -37$ cal mol⁻² kg. These free-energy terms are smaller than the corresponding heat terms. Furthermore, the free-energy effect for two unlike solutes is more negative than the effect of either solute with itself. This is in contrast to the enthalpy data where the unlike solutes give positive enthalpies.

TABLE II: Interaction Parameters for Heats of Mixing Nonelectrolyte Solutions at 25°

System	Molality	RTh_0 , ^a cal mol ⁻² kg	RTh_1 , ^b cal mol ⁻² kg
Sucrose (A)- Urea (B)	1.0	308(2) ^d	2(6)
	0.5	325(2)	-1(6)
	0.2	332(8)	12(22)
	0.1	326(14)	19(43)
	0.0	340 ^c	
Sucrose (A)- Glycine (B)	1.0	234(3)	2(10)
	0.5	250(2)	3(4)
	0.2	260(11)	-6(37)
	0.1	260(14)	-14(47)
	0.0	266 ^c	
Glycine (A)- Urea (B)	1.0	36.5(13)	0(4)
	0.5	34.2(9)	0(3)
	0.2	31(4)	-1(14)
	0.0	32 ^c	

^a See eq 1 and 8. ^b See eq 1 and 9. ^c Extrapolated from results at higher concentrations. ^d The number in parentheses is the estimated 95% confidence level of the last digit. Thus 34.2(9) is 34.2 ± 0.9 .

TABLE III: Enthalpy Effects of Pairwise Interactions^a

	S	U	G
S	137 ^b		
U	197 ^c	-84 ^c	
G	148	-80	-107 ^d

^a S = sucrose, U = urea, G = glycine. The table lists $\{AB\}_h$ (cal mol² kg) under the column labeled A and row labeled B. For instance, $\{SU\}_h = 197$ cal mol⁻² kg. ^b Reference 8. ^c Reference 2. ^d F. T. Gucker, Jr., H. B. Pickard, and W. L. Ford, *J. Amer. Chem. Soc.*, **62**, 2698 (1940).

It is interesting to note that the present results are also quite different from the results observed for electrolyte solutions. Young, Wu, and Krawetz¹² proposed that solutes could be divided into two categories and that mixing similar solutes gave positive enthalpies and mixing unlike solutes gave negative enthalpies. This rule predicts the correct sign for a large number of electrolyte mixtures.¹³ Clearly the structural classification is too simple and a great deal more data will be necessary if these effects are to be unraveled.

It is possible to use the above equations to get individual values for all of the triplet interactions ($\{SUU\}$, $\{SSU\}$, etc.) but this is not too important at the present time, in view of our lack of understanding of even the pairwise interactions as well as the fairly large error involved in measuring the triplet terms.

The enthalpy effect of the pairwise terms between unlike solutes in Table III varies from -80 to +197. This is roughly the same order of magnitude of the effects of two identical solutes which vary from -107 to +137 for the solutes in Table III. An examination of the results in Table II shows that the triplet terms are an order of magnitude smaller. The magnitude of these interactions are in accord with the results for the pairwise and triplet terms of nonelectrolytes with electrolytes given in the preceding paper.² As a rough rule, pairwise terms contribute ± 300 cal/mol at 1 *m* and triplet terms contribute ± 30 cal/mol at 1 *m*. This indicates that fairly accurate predictions of mixtures of nonelectrolytes could be made even if the triplet terms were not measured. With the availability of more data, it may be possible to predict some pairwise interactions from a knowledge of similar pairwise interactions.

Acknowledgment. The authors are grateful for the support of this work by the National Science Foundation.

References and Notes

- (1) Presented at the 166th National Meeting of the American Chemical Society, Chicago, Ill., Sept 1973.
- (2) R. B. Cassel and R. H. Wood, *78*, 2460 (1974).
- (3) (a) E. M. Arnett, W. G. Benrude, J. J. Burke, and P. M. Duggleby, *J. Amer. Chem. Soc.*, **87**, 1541 (1965); (b) G. L. Bertrand, J. W. Farson, L. G. Hepler, *J. Phys. Chem.*, **72**, 4194 (1968); (c) J. H. Stern, O. Yavuz, and T. Swearington, *J. Chem. Eng. Data*, **17**, 183 (1973); (d) J. H. Stern and M. E. O'Connor, *ibid.*, **17**, 185 (1973); (e) C. V. Krishnan and H. L. Friedman, *J. Solution Chem.*, **2**, 119 (1973); (f) R. A. Robinson and R. H. Stokes, *J. Phys. Chem.*, **65**, 1954 (1961); **70**, 2126 (1966); (g) P. O. P. Ts'o, I. S. Melvin, and A. C. Olson, *J. Amer. Chem. Soc.*, **85**, 1289 (1963); (h) H. D. Ellerton and P. J. Dunlop, *J. Phys. Chem.*, **70**, 1831 (1966); (i) E. L. Cussler, Jr., *J. Phys. Chem.*, **71**, 901 (1967); (j) H. Ueda-ira, *Bull. Chem. Soc. Jap.*, **45**, 3068 (1972).
- (4) (a) H. L. Friedman "Ionic Solution Theory," Interscience, New York, N.Y., 1962; (b) H. L. Friedman, *J. Chem. Phys.*, **32**, 1351 (1960).
- (5) J. S. Falcone, Jr., A. S. Levine, and R. H. Wood, *J. Phys. Chem.*, **77**, 2137 (1973).
- (6) H. L. Friedman, *J. Solution Chem.*, **1**, 387, 413, 419 (1972).
- (7) R. A. Robinson, R. H. Wood, and P. J. Reilly, *J. Chem. Thermodyn.*, **3**, 461 (1971).
- (8) F. T. Gucker, Jr., H. B. Pickard, and R. W. Planck, *J. Amer. Chem. Soc.*, **61**, 459 (1939).
- (9) It should be noted that previous results on free energies of nonelectrolyte mixtures^{3d-3f} use the same power series in m to represent the results. The major contribution of the present derivation is to identify each term with its corresponding cluster integral.
- (10) H. S. Frank and A. L. Robinson, *J. Chem. Phys.*, **8**, 933 (1940).
- (11) H. S. Frank and W. Y. Wen, *Discuss. Faraday Soc.*, **24**, 133 (1957).
- (12) T. F. Young, Y. C. Wu, and A. A. Krawetz, *Discuss. Faraday Soc.*, **24**, 37 (1957).
- (13) H. L. Anderson and R. H. Wood, "Thermodynamics of Aqueous Mixed Electrolytes" in "Water: A Comprehensive Treatise," F. Franks, Ed., Plenum Press, New York, N.Y., 1973, Chapter 2.

Theory of Micelle Formation in Aqueous Solutions^{1a}

Charles Tanford^{1b}

Department of Biochemistry, Duke University Medical Center, Durham, North Carolina 27710 (Received July 10, 1974)

Publication costs assisted by the National Science Foundation

Rigorous equations are presented to relate micelle size, the critical micelle concentration, and other micellar properties to a size-dependent free energy of micellization. For micelles formed in aqueous solutions of amphiphiles the free energy can be split into an attractive hydrophobic part and a repulsive part resulting from head group interaction. With the conclusion reached in an earlier paper, that micelles are likely to have an ellipsoidal shape, the hydrophobic component of the free energy and its dependence on micelle size are readily estimated in terms of the area of contact between the hydrophobic core of the micelle and the solvent. The repulsion between polar head groups cannot at present be calculated, but it is shown that quite simple expressions for its dependence on surface area (and thereby on micelle size) can account for the experimentally observed parameters of diverse ionic and nonionic micelles. No matter what form of the repulsive function is used, oblate ellipsoids prove to be thermodynamically favored over prolate ellipsoids for most micelles. Experimental evidence to the contrary is discussed. There are alternative interpretations of these data, and it is not possible to conclude whether or not they represent a real discrepancy from the theoretical prediction.

This paper presents a theoretical treatment for the association of simple amphiphiles to form micelles in aqueous solution. The theory explicitly allows for the variation of micelle properties with micelle size and for the size heterogeneity of micelle populations. The overall approach may be outlined as follows.

(1) Experimentally observable parameters, such as optimal micelle size, micelle size distribution, critical micelle concentration, and their dependence on amphiphile concentration, are related to a size-dependent free energy of micellization by equations that are completely rigorous except for the trivial assumption of ideal solution behavior for monomeric amphiphile. These equations may be used as a framework for any theoretical model for the size-dependent free energy, or they may be employed to deduce the properties of the free-energy function from experimental data.

(2) An approach to the theoretical calculation of the free energy of micellization is made for simple amphiphiles con-

sisting of a single aliphatic hydrocarbon chain with a terminal hydrophilic group. For these substances the free energy of micellization is split into separate attractive and repulsive components. The attractive component is taken as arising entirely from the hydrophobic effect, which seeks to minimize contact between hydrocarbon and water, and is assumed independent of the head group. Both components depend on micelle size and this dependence is here related to the dependence of surface area on micelle size. The ellipsoidal model presented previously² is used for the calculation of surface areas.

(3) Numerical estimates of the hydrophobic component of the free energy can be made within narrow limits on the basis of experimental data for hydrocarbons and their derivatives. Small adjustments within these limits are made on an empirical basis. Since this component of the free energy is the same for all amphiphiles, the repulsion between the polar heads becomes the critical factor determining the unique properties of both ionic and nonionic micelles. This

factor cannot be theoretically evaluated at the present time and what is done in dealing with it is to consider possible functional relationships between the repulsive free energy and surface area, and what effect they have on micelle formation. Quite simple expressions for the repulsive free energy turn out to be able to account for most types of experimentally observed behavior.

(4) Although quantitative predictions for any given micelle-forming system cannot be made until the free energy of repulsion can be evaluated specifically for the head group of that system, some general conclusions can be drawn from calculations based on the simple functional relations that have been used. The most important of these is that a disk-like shape is predicted to be more stable than a rod-like shape for nearly all micelles.

A preliminary paper applying some of the principles used here to two ionic micelles has been published.³

Thermodynamic Formulation

The properties of micelle-forming systems are determined by equilibria between monomeric amphiphile (Z) and aggregates of variable size (Z_m). Assuming thermodynamic ideality, they can be represented by a set of equilibrium constants

$$K_m = [Z_m]/[Z]^m \quad (1)$$

It is desirable to express concentrations in mole fraction units so as to obtain free energies in unitary units.^{4,5} We shall use X_1 to represent the mole fraction of amphiphile in monomeric form and X_m to represent the mole fraction of amphiphile contained in micelles of size m , i.e., $X_m = m[Z_m]$, so that

$$K_m = X_m/mX_1^m \quad (2)$$

Similarly, it is convenient to write the free energy of micellization in terms of the unitary free energy of transfer (ΔG_m°) of a single amphiphile molecule from the monomeric state to a micelle of size m , so that $-RT \ln K_m = m\Delta G_m^\circ$. The fundamental equation for micelle formation then becomes

$$\ln X_m = -m\Delta G_m^\circ/RT + m \ln X_1 + \ln m \quad (3)$$

The assumption of thermodynamic ideality in the derivation of these equations is not a serious limitation. Nonideal behavior of monomer can be taken care of by replacing X_1 by the corresponding thermodynamic activity. Ideality of the micellar species is in fact not assumed unless we consider K_m or ΔG_m° to be constants independent of all variables other than m . We shall actually consider ΔG_m° to be a function of environmental variables as well as micelle size, so that all departures from ideality are implicitly allowed for. For example, counterion binding to ionic micelles is reflected in an effect of counterion concentration of ΔG_m° . Most of the sample calculations to be carried out apply to dilute solutions and it is practical to take ΔG_m° to be independent of amphiphile concentration; but a concentration-dependent term can be included to allow for intermicellar interaction at high concentrations.

Equation 3 is a distribution function, giving the amounts of amphiphile incorporated into micelles of various size. An optimal size m^* can be defined for any given experimental conditions by setting the derivative of $\ln X_m$ with respect to m equal to zero. The derivative is of course taken at constant X_1 since all micelles are in equilibrium with same monomer concentration. The result obtained is that m^* is that value of m for which

$$m \frac{d\Delta G_m^\circ}{dm} = RT \ln X_1 - \Delta G_m^\circ + \frac{RT}{m} \quad (m = m^*) \quad (4)$$

Combining eq 3 and 4 gives an alternative expression

$$\frac{d\Delta G_m^\circ}{dm} = \frac{RT}{m^2} (1 + \ln X_m - \ln m) \quad (m = m^*) \quad (5)$$

which is more useful than eq 4 when the critical micelle concentration (cmc) is unknown and one of the objectives is to calculate it.

The total stoichiometric concentration of amphiphile in a solution is given by

$$X_{\text{total}} = X_1 + \sum_{m=2}^{\infty} X_m \quad (6)$$

and the number and weight average degrees of association by

$$\bar{m}_n = \frac{\sum_{m=2}^{\infty} X_m / \sum_{m=2}^{\infty} X_m / m} \quad (7)$$

$$\bar{m}_w = \frac{\sum_{m=2}^{\infty} mX_m / \sum_{m=2}^{\infty} X_m} \quad (8)$$

The cmc cannot be uniquely defined, as is well known.⁵ It will be defined here as that value of X_{total} at which $\sum X_m$ represents 5% of X_{total} .

The foregoing equations can be used to predict micelle behavior if ΔG_m° is known as a function of m or they can be used to deduce ΔG_m° from experimental data. In either case it is to be kept in mind that X_1 can have only a narrow range of values if micelle concentrations are to be within reasonable limits. Equations 3 and 6 give X_{total} as a function of X_1 and thereby allow properties such as the optimal micelle size to be expressed as a function of total amphiphile concentration. A convenient procedure for making calculations using any assumed free-energy function is given in the Appendix. All calculations were made for a temperature of 20°.

Micelle Dimensions

For simple amphiphiles consisting of a single hydrocarbon chain with a terminal hydrophilic group there is cooperative association between alkyl chains to form the micelle core, which resembles a liquid hydrocarbon droplet.⁵ The hydrophilic head groups extend from the core into the aqueous medium and it is the force of repulsion between them that limits the size to which micelles can grow. The dominant factor in the consideration of micelle shape is the fact that one dimension of the hydrocarbon core cannot exceed the length of two fully extended alkyl chains. This immediately precludes the possibility that micelles in the normally observed size range can be spherical.^{2,6} Since there is no other obvious reason for an irregular shape it is simplest to assume that the micelle core is an oblate or prolate ellipsoid of revolution, with minor axis b limited to being less than the maximal extension l_{max} of an amphiphile alkyl chain, while the major axis a can grow indefinitely.

The expected value of b can actually be fixed more closely. Free-energy calculations of the kind described below show that the sum of the hydrophobic and repulsive free energies is minimized by setting $b = l_{\text{max}}$, but the variation with b is small in comparison with the dependence of the configurational energy of the alkyl chain on its end-to-end distance. The actual length of the alkyl chain in the micelle is thus expected to be close to the optimal length based on configurational energy alone, which can be estimated from the work of Flory and coworkers⁷ with the results given in Table I. These estimates are very approximate because

TABLE I: Length of Flexible Hydrocarbon Chain Equivalent to Minor Ellipsoid Axis^a

Alkyl chain	n_C	l_{max}^b	ρ	$b = \rho l_{max}$
C ₈	7	10.355	0.83	8.59
C ₁₀	9	12.885	0.79	10.18
C ₁₂	11	15.415	0.75	11.56
C ₁₄	13	17.945	0.71	12.74
C ₁₆	15	20.475	0.67	13.72

^a Distances are in ångströms. The parameter ρ is the ratio of a flexible to a fully extended chain, obtained by extrapolation of the calculated distances of Flory⁷ to room temperature. The values must be considered quite approximate. ^b From the relation $l_{max} = 1.5 + 1.265n_C$ given previously.²

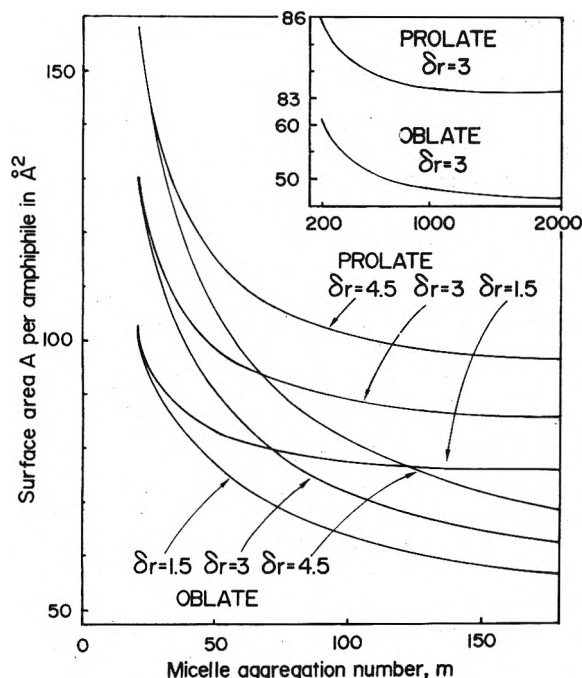


Figure 1. Surface area per amphiphile molecule for micelles formed by dodecyl derivatives ($n_C = 11$) as a function of aggregation number (m) and the distance (δr in Å) from the hydrocarbon core surface. The value of $m = 20$ corresponds to a spherical micelle with radius equal to b .

Flory's data refer to 140° and his temperature coefficient is not applicable to a wide temperature range, but since the calculated micelle characteristics are quite insensitive to the choice of b this is not important. Some of the free-energy calculations have been repeated with the values of ρ increased by 0.05 above those in the table, with no significant effect.

One additional assumption has been made. It has been assumed that the CH₂ group adjacent to the polar head group lies within the hydration sphere of the head group and thus does not have hydrophobic properties.⁵ The number of carbon atoms (n_C) of the alkyl chain that enter into formation of the hydrophobic core is thus one fewer than the total number, as shown in Table I.

The volume of the hydrophobic core (in Å³) for a micelle containing m alkyl chains is given by²

$$v = m(27.4 + 26.9n_C) \quad (9)$$

Combining this with the value of b given by Table I fixes

the major semiaxis a and all other dimensions for given values of m and n_C . Only the choice between prolate and oblate ellipsoids remains.

The dimension of greatest interest is the surface area. The area desired is however usually not the area of the hydrophobic core *per se*, but rather the area at some distance outside the core, e.g., at the distance of closest approach of water molecules (1.5 Å) or at the position where the charges of ionic head groups are located. To calculate these areas we have used ellipsoids with semiaxes $a + \delta r$ and $b + \delta r$, where δr is the distance from the core surface. These ellipsoids are not confocal with the ellipsoid of semiaxes a and b , so that they do not quite correspond to surfaces that are at all points equidistant from the core surface, but they provide a good approximation. Total surface areas have been divided by m to provide the surface area A per amphiphile molecule. This area decreases as m increases as shown by the typical results provided in Figure 1,⁸ but levels off at higher areas for prolate than for oblate ellipsoids. Since diminution of the area of contact between the micelle core and water is the major driving force leading to micelle formation, this difference will be seen to lead to the prediction that large micelles will normally be more stable as oblate rather than prolate ellipsoids.

As has been pointed out previously^{3,9} the surface of the hydrophobic core of a micelle is expected to be undulating rather than smooth. This property is incorporated into the theory indirectly, as shown below, and no attempt has been made to calculate directly the effect this would have on the value of A at a given distance from the core surface.

Hydrophobic Contribution to the Free Energy

For simple alkyl derivatives it is realistic to approach the calculation of ΔG_m° by separation of the contributions from the hydrophobic effect and from head group repulsion. We thus write

$$\Delta G_m^\circ = \Delta U_m^\circ + W_m \quad (10)$$

where ΔU_m° (which will be negative) is the free-energy change associated with the transfer of the alkyl chain from the aqueous medium to the core of a micelle of size m , and W_m (which will be positive) is the free energy associated with the relatively close approach of head groups to each other. The calculation of ΔU_m° will be considered first. It is readily estimated from experimental data to within 10–20%. Adjustments within this uncertainty have been made so as to obtain numerical data within the range of observed micellar properties.

The critical factor in the estimation of ΔU_m° is the recognition that complete removal of alkyl chains from contact with water is not achieved when micelles are formed. If hydrocarbon chains were closely packed, perpendicular to the core surface, all contact with solvent would be avoided. The surface area per chain would then be 21 Å².¹⁰ As Figure 1 shows, micellar surface areas are larger than this, even for quite large values of m . The excess area must represent residual area of contact with the solvent, and reduction in this area is the driving force for micelle growth.

The free energy of contact between water and alkyl chains has been shown empirically (near room temperature) to follow very simple rules. When n -alkyl derivatives are transferred from water to a liquid hydrocarbon the free energy of transfer includes a contribution of –2100 cal/mol per CH₃ group and a contribution of –850 ± 50 cal/mol per CH₂ group.⁵ A more general relation, applicable to cyclic

and branched chains, as well as linear ones, relates the free energy of transfer to the surface area of contact between water and hydrocarbon in the aqueous phase: the free energy of transfer is -25 ± 5 cal/mol per \AA^2 of surface measured at the distance of closest approach of water molecules to the hydrocarbon.^{11,12} In applying these results to the transfer of alkyl chains to the micelle interior it must be recognized that the chains in a micelle are more constrained than they would be in bulk liquid hydrocarbon. Wishnia's measurements of the solubility of small hydrocarbon molecules in sodium dodecyl sulfate micelles¹³ indicate that this constraint has a significant effect on the free energy. The effect should be greater for incorporation of the alkyl chain of an amphiphile into a micelle because it is anchored at one end to the head group. A positive contribution of 100–200 cal/mol per C atom for a linear chain is a reasonable estimate. (The final figure chosen was adjusted on the basis that the coefficient of n_C in eq 11 below represents the major part of the derivative of $RT \ln \text{cmc}$ with respect to chain length.)

The empirical observations of the preceding paragraph suggest a separation of ΔU_m° into two factors, a constant part independent of micelle size which represents the free energy gained for complete immersion of the alkyl chain in the micellar core, and a variable part reflecting the positive free-energy contribution by residual contacts between the core surface and the solvent. An appropriate expression (in cal/mole) is

$$\Delta U_m^\circ = -2000 - 700(n_C - 1) + 25(A_{Hm} - 21) \quad (11)$$

where A_{Hm} is the area in \AA^2 per chain in a micelle of size m at the distance of closest approach of water molecules to the core surface. The excess of this area above 21 \AA^2 represents the residual area of water–hydrocarbon contacts.

The undulating nature of the surface of the hydrophobic core must be taken into account in the calculation of A_{Hm} . This factor arises from the impossibility of bending the alkyl chains emerging from the core so as to make a smooth surface perpendicular to the direction of the chains and was discussed in a previous paper.³ It has the effect of making A_{Hm} larger than the area at a distance of closest approach of water molecules to the smooth ellipsoidal surface that would be obtained by a calculation made at the distance $\delta r = 1.5$ \AA . The simplest way of taking this into account is to continue to use the same model for area calculation, but to increase the value of δr . This procedure is consistent with the requirement that the surface roughness should diminish as the area decreases and vanish when $A_{Hm} = 21$ \AA^2 . The dependence of surface area on δr has these properties. The actual value of δr to be used has been determined empirically. Reasonable results are obtained with $\delta r = 3$ –4 \AA which corresponds to an excess area ascribable to surface roughness in the range of 15–30% of the smooth area ($\delta r = 1.5$ \AA) for the illustrative data of Figure 1. Most of the calculations below have been made with $\delta r = 3$ \AA .

Free Energy of Repulsion between Head Groups

Since both micelle shape and hydrophobic free energy depend only on the length of the alkyl chain, the unique properties of micelles formed by simple n -alkyl amphiphiles must result from the contribution of repulsion between amphiphile head groups to the free energy, i.e., the factor W_m of eq 10. This factor will depend on the separation between head groups, and we may use the available

TABLE II: Sample Calculation of the Effect of the Magnitude of the Repulsive Force on the Cmc and the Optimal Micelle Size^a

$10^{-5}\alpha$, cal $\text{\AA}^2/\text{mol}$	cmc, M	m^* at the cmc
2.00	0.00612	34
1.50	0.00247	50
1.20	0.00205	71
1.00	0.000832	98
0.80	0.000499	159
0.60	0.000281	377
0.50	0.000201	950
0.45	0.000167	2860

^a For oblate ellipsoidal micelles formed by amphiphiles with C_{12} alkyl chains. Equation 12 has been used for W_m and both A_{Rm} and A_{Hm} were calculated at 3 \AA from the smooth core surface. Qualitatively similar results are obtained for prolate ellipsoids. The procedure for calculation is described in the Appendix.

area per head group (A_{Rm}) as a measure of this separation. The distance outside the micelle core at which A_{Rm} is to be evaluated is determined by the geometry of the amphiphile molecule and A_{Rm} cannot in general be equated with A_{Hm} . Both the magnitude of W_m and its functional relation to A_{Rm} can be expected to differ for different head groups and different environmental conditions. It should be a good approximation to consider W_m as independent of the length of the alkyl chain.

The simplest possible relationship (satisfying the necessary condition that W_m vanishes at infinite separation) is

$$W_m = \alpha/A_{Rm} \quad (12)$$

where α is a constant independent of m which would vary in magnitude depending on the magnitude of the repulsive force. Even this simple form for the repulsive free-energy function leads to realistic estimates for the variation in optimal micelle size and cmc with the magnitude of the repulsive force as shown by the sample calculation in Table II. When repulsive interactions are strong, as they would be in ionic micelles, the micelle size is small and the cmc relatively high. Reduction in the repulsive force, as might occur when the ionic strength is increased, leads to a moderate increase in micelle size and to a substantial decrease in the cmc. When the repulsive force becomes much weaker, as it might, for example, for nonionic micelles, the micelle size can become very large. If α is decreased even further m^* becomes infinite, which would signify separation of the amphiphile into a separate phase, as occurs with n -alkyl alcohols.

Equation 12 has been used here as a purely empirical function, without implication of a mechanism for the repulsive interaction. It should be observed, however, that some simple theoretical expressions for W_m have the form of eq 12. The Debye–Hückel equation for the work of charging a sphere of constant radius r_0 , with m charges, is one such example. The excess free energy per charge is

$$W_m = \frac{2\pi\epsilon^2 N r_0 (1 + \kappa a_i)}{D A_{Rm} (1 + \kappa r_0 + \kappa a_i)} \quad (13)$$

where a_i is the average radius of mobile ions in the surrounding electrolyte, ϵ is the electronic charge, D is the dielectric constant of the medium, and κ is the usual Debye–Hückel parameter proportional to the square root of the ionic strength. The area A_{Rm} in this case is the area per charge at the surface of the charged sphere. The Debye–

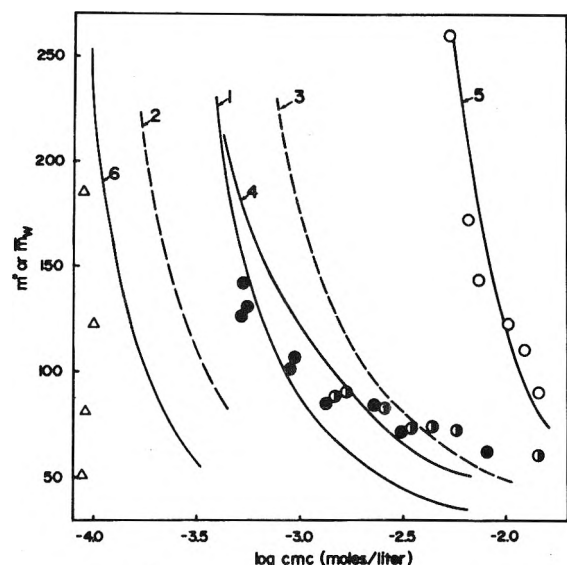


Figure 2. Relation between optimal micelle size (m^*) and the cmc for C_{12} alkyl chains, using different expressions for W_m , as described in the text. Each curve represents a set of calculated results in which only the magnitude of W_m is altered, the dependence on surface area remaining the same. All calculations are for *oblate* ellipsoids. A_{Hm} and A_{Rm} were evaluated at $\delta r = 3 \text{ \AA}$ except for curve 2 (A_{Rm} at $\delta r = 10 \text{ \AA}$) and curve 3 (A_{Hm} at $\delta r = 4 \text{ \AA}$). The points represent typical experimental data, as follows: O, $C_{12}H_{25}NH_3^+Cl^-$ at 30° as a function of ionic strength (data of Kushner, *et al.*¹⁴); ●, $C_{12}H_{25}NMe_3^+Br^-$ as a function of ionic strength at 25° (data of Anacker, *et al.*¹⁵ and of Emerson and Holtzer¹⁶); ●, $C_{12}H_{25}OSO_3^-Na^+$ as a function of ionic strength at 25° (data of Mysels and Princen¹⁷ and of Emerson and Holtzer¹⁶); Δ, $C_{12}H_{25}(OCH_2CH_2)_nOH$ in water as a function of n at 18 and 25° (data of Becher¹⁸ and of Balmbra, *et al.*¹⁹). The size parameter obtained experimentally is the weight average degree of association (\bar{m}_w), but this is expected to be only a few per cent larger than m^* .

Hückel expression for charges on an infinite planar surface has the same form

$$W_m = 2\pi\epsilon^2 N(1 + \kappa a_i)/\kappa D A_{Rm} \quad (14)$$

and so does the corresponding relation for a cylinder of constant diameter.

Figure 2 (curve 1) shows the data of Table II in graphical form. Curve 2 shows the effect of altering the location at which the repulsive interaction occurs from 3 to 10 \AA outside the hydrophobic core surface. Curve 3 shows the effect of altering the surface roughness factor, with A_{Hm} (eq 11) calculated as equivalent to the area at 4 \AA instead of 3 \AA outside the core surface. The figure also shows experimental results for amphiphiles with dodecyl alkyl chains. It is evident that changes in the head group lead to specific effects on the relation between micelle size and cmc that cannot be explained in terms of the magnitude of W_m alone, or in terms of the distance to which head groups extend into the aqueous medium, but require modification of the relation between W_m and micelle size, as reflected in eq 12. Specific affects cannot be explained in terms of changes in ΔU_m° , which by definition is the same for all amphiphiles with the same alkyl chain. Changes in any of the terms of eq 11 simply result in a shift of curve 1 to the right or to the left, as illustrated by curve 3.

It was suggested earlier³ that the problem of obtaining a theoretical expression for W_m can be circumvented by making use of experimental pressure-area curves for amphiphiles at a hydrocarbon-water interface. The requisite data are however difficult to obtain²⁰ and need to be cor-

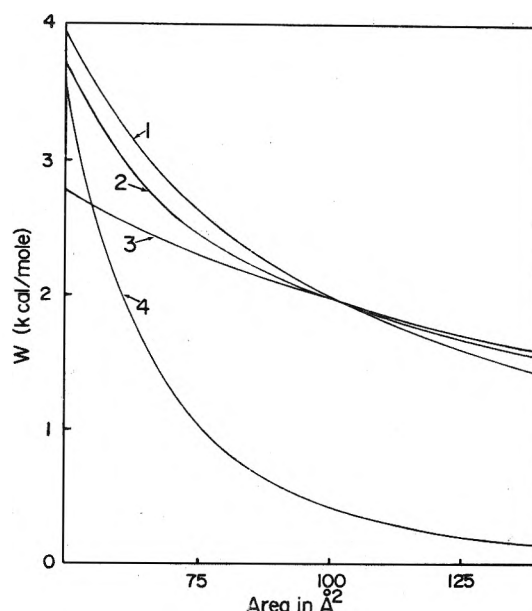


Figure 3. W as a function of surface area per head group. Curve 1 represents eq 12 with $\alpha = 1.93 \times 10^5$, curve 2 is based on experimental pressure-area curves for monolayers of $C_{12}H_{25}OSO_3Na$ at a heptane-water interface (see text), curve 3 is an arbitrary flat curve (eq 15, see text), curve 4 represents $W = 4.5 \times 10^8/A^3$.

rected for surface curvature before they can be applied to the micellar surface. The information from pressure-area curves is at present very limited, but can be used as a guideline for the required alterations in the expression of W_m where available. Figure 3 (curve 2), for example, shows W for $C_{12}H_{25}OSO_3Na$ in 0.1 M NaCl, obtained from pressure-area curves as previously described.^{3,21} The values of W are considerably smaller than would be predicted for a plane surface by a Debye-Hückel type of calculation: eq 14 predicts $W = 3150 \text{ cal/mol}$ at 100 \AA^2 whereas the experimental value is 1980 cal/mol . Equally important is the fact that the experimental curve is flatter than any curve of the type $W = \alpha/A$, as seen by comparison of curve 2 with curve 1, which represents eq 12 with $\alpha = 1.98 \times 10^5$. Such flattening can be incorporated into the theory by replacing eq 12 by a power series

$$W = \alpha/A + \beta/A^2 + \gamma/A^3 \quad (15)$$

Curve 2 is represented by this equation with $\alpha = 2.86 \times 10^5$, $\beta = -1.27 \times 10^7$, $\gamma = 3.86 \times 10^8$.

The relation between micelle size and cmc as a function of the magnitude of W_m is altered when an equation of the type of eq 15 is used for W_m . This is illustrated by curve 4 of Figure 2, which is based on *uniform flattening*, i.e., the coefficients α , β , and γ are kept in the same ratio (in this case as required for the experimental pressure-area curves for $C_{12}H_{25}OSO_3Na$) as the magnitude of W_m is changed. Exact agreement with the experimental data for $C_{12}H_{25}OSO_3Na$ or $C_{12}H_{25}NMe_3Br$ could be obtained if the degree of flattening is itself a function of the magnitude of W_m , i.e., for these results, if it is a function of ionic strength. Monolayer studies that would provide information on this subject are not available.

Both the reduction in the magnitude of W relative to a Debye-Hückel calculation and the flatter W vs. A curve for an ionic amphiphile are qualitatively expected on the basis of the binding of counterions to the micelle surface or to a monolayer surface of similar area. A theoretical treatment

of this subject is difficult, as has been discussed by Mukerjee.^{22,23} The binding of counterions not only alters the force of repulsion between head groups, but also requires the inclusion of a cratic⁴ term in W_m , reflecting the loss of entropy that results from loss of mobility of the bound counterions. In the limiting situation of complete charge neutralization by counterion binding, the variation in W_m with increasing concentration of added salt would arise entirely from this cratic term and W_m at constant ionic strength would become independent of surface area except for the steric repulsion that would set in at very small values of A_{Rm} . This limiting situation is likely to be approached by alkyl ammonium salts: the small radius of the $-\text{NH}_3^+$ group allows counterions to penetrate much closer to the amphiphile charge than is possible for an $-\text{NMe}_3^+$ group and thereby to enter a domain of the surface where the electrostatic force of attraction for counterions is greatly increased. To test this possibility we have investigated the effect of a greater decrease in the dependence of W_m on A_{Rm} , as illustrated by curve 3 of Figure 3, which represents eq 15 with $\alpha = 2.95 \times 10^5$, $\beta = -1.16 \times 10^7$, and $\gamma = 1.92 \times 10^8$. Assuming uniform flattening of this type as W_m changes in magnitude leads to curve 5 of Figure 2, in excellent agreement with the experimental data for $\text{C}_{12}\text{H}_{25}\text{NH}_3\text{Cl}$.¹⁴ It should be emphasized that all parameters other than the equation for W_m are identical in the generation of curves 1, 4, and 5 of this figure.

The cmc values for dodecyl polyoxyethylene glycols, shown by the triangles on the left side of Figure 2, are much lower than for typical ionic micelles. This may be partly the result of having the repulsive interaction removed to a greater distance from the surface of the hydrophobic core (curve 2), but this factor alone is not sufficient. One way of approaching the experimental data is to suppose that the force of repulsion between head groups is in this case purely steric. This would cause W_m to rise rather steeply with decreasing area as the effective physical area of the head group is approached. This situation is simulated by curve 6 of Figure 2, which is based on $W_m = \gamma/A_{Rm}^3$ with increasing values of γ . The shape for one value of γ is shown by curve 4 of Figure 3. A_{Rm} was evaluated at $\delta r = 3$ Å in the calculation of curve 6. The curve is shifted to the left if the repulsive interaction is located further from the core surface.²⁴

All calculations of Figure 2 refer to oblate ellipsoids. The calculations indicate that prolate ellipsoids would not contribute to the micelle population at the cmc within the range of variables selected, as will be discussed later in this paper.

Size Distribution Function

The size distribution function is given by eq 3. The contribution of very small micelles is always negligible because the area of contact between hydrocarbon and water rises steeply for $m < 50$ (see Figure 1). The formation of very large micelles is limited by the cratic term $m \ln X_1$ in eq 3, which becomes increasingly important as $d\Delta G_m^\circ/dm$ becomes less negative for $m > m^*$. Other things being equal, the breadth of the distribution depends on the second derivative of ΔG_m° with respect to m . Since d^2A/dm^2 decreases with increasing m (see Figure 1) the distribution will tend to be broader for large micelles than for small ones when similar W_m functions are used. When different W_m functions are used, the distribution will tend to become broader when the dependence of W_m on A_{Rm} is less.

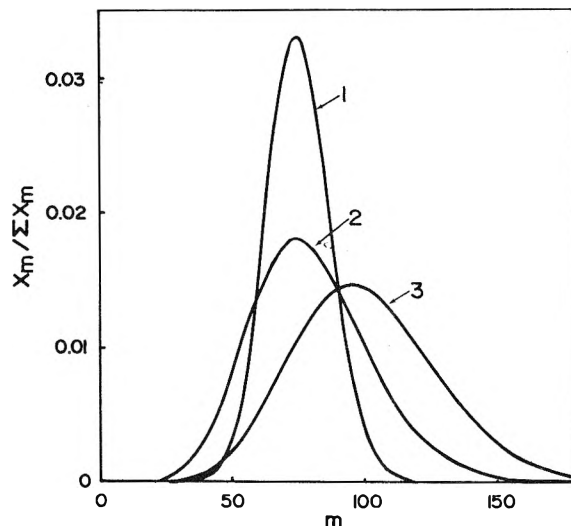


Figure 4. Micelle size distribution functions for amphiphiles with C_{12} alkyl chains forming oblate ellipsoidal micelles with $m^* = 75$ at the cmc. Curves 1 and 2 apply to conditions at the cmc and were obtained by using W functions of the types illustrated by curves 2 and 3 of Figure 3, respectively. Curve 3 is for the same system as curve 2, but at a total amphiphile concentration of 0.028 M. Both A_{Hm} and A_{Rm} were evaluated at $\delta r = 3$ Å.

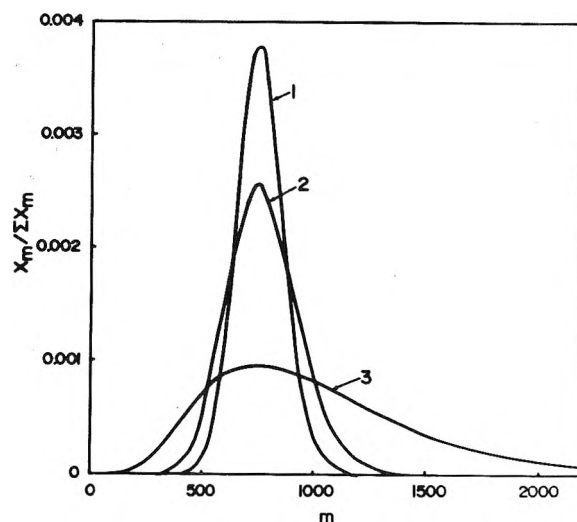


Figure 5. Micelle size distribution functions for prolate and oblate ellipsoids with $m^* = 750$: (curve 1) oblate ellipsoid, $W = \gamma/A^3$, calculated for the cmc; (curve 2) oblate ellipsoid, $W = \alpha/A$, calculated for the cmc; (curve 3) prolate ellipsoid, $W = \alpha/A$, calculated at a total amphiphile concentration of 0.014 M. Both A_{Hm} and A_{Rm} were evaluated at $\delta r = 3$ Å.

These features are illustrated by Figures 4 and 5 which were calculated by use of the different types of W_m functions illustrated by Figure 3. The magnitude of W_m was adjusted in each case so as to lead to $m^* = 75$ or $m^* = 750$.

Figure 5 shows that a steep W - A curve such as was suggested earlier for the alkyl polyoxyethylenes leads to a relatively narrow distribution even for very large oblate micelles. This agrees with the experimental finding of Corkill and Walker²⁵ who found that micelles formed by alkyl polyoxyethylene glycols at 5° behave as if monodisperse. The change in micellar properties observed by these authors at higher temperatures will be discussed below.

Figure 5 also shows a distribution function calculated for a prolate ellipsoidal shape. As is to be expected from the

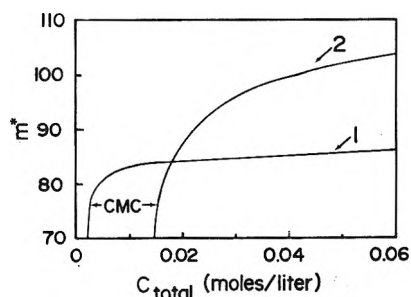


Figure 6. Dependence of m^* on total amphiphile concentration for the two size distributions for oblate ellipsoids given by the curves with corresponding numbers in Figure 4.

flatness of the area curves of Figure 1, the size distribution becomes very broad and skewed toward large m .

Average molecular weights are related to the size distribution by eq 7 and 8. None of the distribution functions for oblate ellipsoids are sufficiently broad to yield experimentally significant differences between \bar{m}_n and \bar{m}_w . Thus $\bar{m}_w/\bar{m}_n = 1.03$ and 1.09 , respectively, for the two distributions of Figure 4, and 1.005 and 1.05 for curves 1 and 2 of Figure 5. Even for the prolate ellipsoidal model used for curve 3 of Figure 5, \bar{m}_w/\bar{m}_n is only 1.26 . These calculations suggest that if larger ratios of \bar{m}_w/\bar{m}_n are experimentally observed (as suggested by Mukerjee²⁶), they do not represent a single continuous size distribution, but instead reflect two populations of micelles, *e.g.*, a mixture of oblate and prolate micelles, or a system in which association between micelles can occur.

Effects of Total Amphiphile Concentration

The dependence of micelle size on total amphiphile concentration is closely linked to the size distribution function.^{26,27} This is illustrated by Figure 6, which compares the effect of concentration on m^* for two micelles, both with $m^* = 75$ at the cmc.²⁸ The effect of increased concentration on m^* is more pronounced for the amphiphile with the broader distribution function. The effect of concentration on the distribution function itself is shown in Figure 4.

The effect of concentration on m^* is particularly pronounced if calculations are made for prolate ellipsoids. Figure 7, for example, shows the calculated data for the prolate micelle corresponding to the distribution function given by curve 3 of Figure 5. The value of m^* is 250 at the cmc, but rises rapidly to over 1000 as the concentration is raised.²⁸ These calculations resemble experimental data obtained for some cationic detergents at high ionic strength²⁹ and for polyoxyethylene derivatives with short polyoxyethylene chains.^{30,31}

A noteworthy feature of Figure 6 is that m^* changes steeply with concentration in the immediate vicinity of the cmc even when the size distribution is relatively sharp. This suggests that it may be futile to attempt to obtain unambiguous micelle molecular weights characteristic of micelles at the cmc. Much of the disagreement between different workers in the determination of micelle size close to the cmc may be due to this aspect of micelle formation.

The effect of total amphiphile concentration on the monomer concentration in equilibrium with micelles is also of interest. This property of the system depends primarily on the average micelle size and it is a good approximation to consider it as governed by a single equilibrium, $mZ \rightleftharpoons Z_m$, with $m = m^*$. This is illustrated by Figure 8, which shows calculated results for the micelles for which the depen-

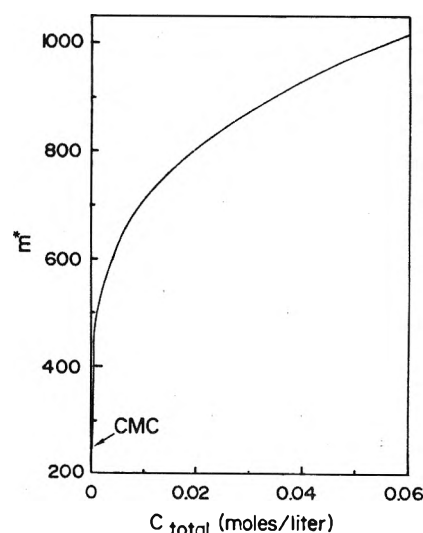


Figure 7. Dependence of m^* on total amphiphile concentration for a prolate ellipsoid with the distribution function given by curve 3 of Figure 5.

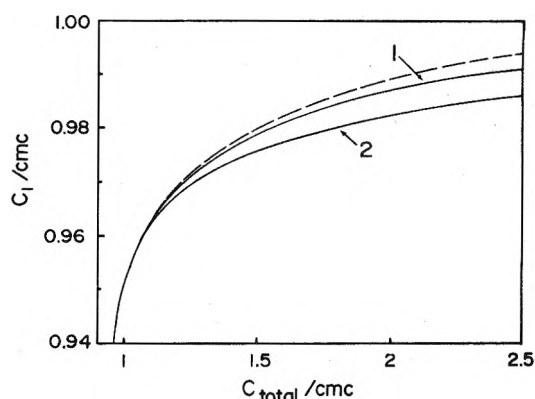


Figure 8. Effect of total amphiphile concentration on the equilibrium concentration of monomer. The dashed line is for a micelle of fixed size ($m = 75$); curves 1 and 2 correspond to the same micelles for which m^* is given in Figure 6.

dence of m^* on total concentration is shown in Figure 6. The dashed line is based on the single equilibrium with $m = 75$. When the calculations are made rigorously, taking size heterogeneity into account, the curves fall only slightly below the dashed line, more so for the broader distribution (curve 2), for which m^* increases above the initial value of $m^* = 75$ more rapidly than for the narrower distribution (curve 1).

Prolate Ellipsoids

The contribution of prolate micelles to the total population of micelles is readily calculated from eq 3, by using the equation twice for each value of m , once for a prolate and once for an oblate shape. In making this calculation it has been assumed that the parameters of eq 11 for ΔU_m° and the parameters of whatever equation for W_m is used are identical for both ellipsoids so that the difference between them depends only on surface area. The result obtained with this assumption is that prolate ellipsoids in fact do not contribute significantly to the total micelle population for moderate or large values of m . It is easy to see why this is so. For $m = 500$, for example, A_{Hm} is about 52 and 84 \AA^2 , respectively, for oblate and prolate ellipsoids, so that the

TABLE III: Transition from Oblate to Prolate Micelles^a

X_{total}	% ΣX_m in prolate micelles	\bar{m}_w		
		Oblate	Prolate	Mixture
0.0003	6.8	53	56	53
0.0010	9.6	55	66	56
0.0041	12.6	56	75	58
0.0200	22.4	58	86	64
0.065	33.6	59	106	75
0.29	56.3	60	134	102

^a For an amphiphile with a C_{12} alkyl chain. Equation 12 was used for W_m , with $\alpha = 2 \times 10^6 \text{ cal } \text{\AA}^2/\text{mol}$. A_{Hm} was evaluated at $\delta r = 4 \text{ \AA}$, A_{Rm} at $\delta r = 3 \text{ \AA}$. The cmc is at 0.01 M , corresponding to $X_{\text{total}} = 0.0002$.

ΔU_m° component of the free energy (eq 11) favors oblate ellipsoids by about 800 cal/mol. If prolate ellipsoids are to be as stable as oblate ellipsoids, W_m must decrease by about 800 cal/mol for a similar difference in A_{Rm} . This requires that W_m must be large and that it must rise steeply with decreasing area. These are however the conditions that lead to the formation of *small* micelles.

For small micelles the procedures used in this paper do predict a marginal contribution from prolate micelles and an increasing contribution from them as the total amphiphile concentration increases to large values, as is illustrated by the calculations shown in Table III. This calculation was based on a somewhat larger surface roughness factor in the calculation of A_{Hm} ($\delta r = 4 \text{ \AA}$ instead of 3 \AA) than has been employed for most of the earlier calculations, and eq 12 was used for W_m . Transition to prolate micelles is not quite reached within the attainable range of amphiphile concentration if δr is set equal to 3 \AA in the calculation of A_{Hm} .³²

The amphiphile concentrations at which the transition to prolate ellipsoids is observed in Table III are very high and under these conditions interaction between micelles is likely to become an important factor (which, formally, would be included in the present treatment as a concentration-dependent contribution to W_m). For example, cylindrical micelles may line up in an ordered array at high concentrations more readily than disk-like micelles and this could promote transition to prolate micelles at high concentrations in situations (e.g., use of $\delta r = 3 \text{ \AA}$ for the calculation of A_{Hm}) for which the present calculations that use a concentration-independent W_m function predict that transition will barely fail to be observed. It is also possible that it is incorrect to assume that ΔU_m° and W_m depend solely on A_{Hm} and A_{Rm} and that they are not affected in any other way by the difference between prolate and oblate ellipsoids. There would however have to be a substantial advantage for prolate ellipsoids to alter the conclusion that prolate ellipsoids attain stability only when the repulsive forces are exceptionally strong. No obvious reason for such an advantage exists.

Effect of Alkyl Chain Length

The effect of alkyl chain length on the cmc and on micelle size provides a rather stringent test of the theory. Since W_m has been defined as independent of alkyl chain length both its numerical value and its functional dependence on surface area must remain fixed as n_C is altered.

The dependence of m^* on chain length results chiefly

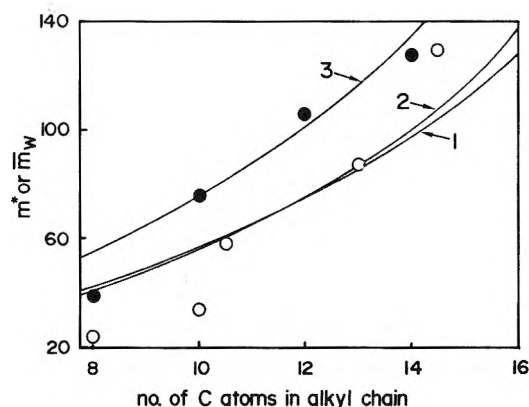


Figure 9. Effect of alkyl chain length on micelle size. Each curve represents the effect of n_C , keeping all other parameters (including the magnitude of W_m as well as its dependence on surface area) the same. Curves 1 and 2 are based on the W_m values giving $m^* = 75$ for C_{12} chains used previously in Figures 4 and 6. Curve 3 is for $W_m = \gamma A^3$, with $\gamma = 1.67 \times 10^6$ chosen to give $m^* \approx 100$ for C_{12} chains. Calculations are for m^* at the cmc, for oblate ellipsoids. Both A_{Hm} and A_{Rm} were evaluated at $\delta r = 3 \text{ \AA}$. The circles represent typical \bar{m}_w values at the cmc obtained experimentally. Open circles are for N -alkyl betaines at 25° (Swarbrick and Daruwala³³), filled circles are for alkyl hexaoxyethylene glycols at 4° (Corkill and Walker²⁵).

from the alteration in the relation between surface area and m (Figure 1) that is produced by changing the ellipsoid minor axis b . An increase in b increases the curvature and leads to larger areas at the same micelle size. The optimal size therefore becomes larger since the optimal surface area will not depend much on n_C . The predicted change in m^* is little affected by the kind of W_m function employed, as is illustrated by curves 1 and 2 of Figure 9, which are for different W_m functions both giving $m^* = 75$ for C_{12} chains. Though neither W_m function is necessarily appropriate for N -alkyl betaines, reasonable agreement with experimental data for these amphiphiles is obtained. Similarly, curve 3 of Figure 9, calculated for the much steeper W_m function suggested previously as possibly simulating steric repulsion between polyoxyethylene head groups, gives reasonable agreement with experimental data for one series of compounds of this type.

In both sets of data shown in Figure 9 the experimental points for the shortest alkyl chains fall below the calculated curves. This could be a reflection of the steep dependence of m^* on total concentration near the cmc, as seen in Figure 6. The cmc values are very high for the short chains (e.g., 0.25 M for the octylbetaine) so that it is feasible to obtain accurate light scattering data at total concentrations very close to the cmc. When the cmc is small light scattering measurements have to be made at concentrations further removed from the cmc to obtain equivalent concentrations of micellar particles. Molecular weights extrapolated from such data may reflect m^* values higher than those at the point designated as the cmc in this paper.

As was noted when numerical parameters were assigned to eq 11, the dependence of the cmc on alkyl chain length is almost entirely determined by the n_C -dependent term of that equation. For all systems discussed here, therefore, $RT \ln \text{cmc}/dn_C$ is calculated as close to -700 cal/mol . Experimental values for the two systems for which \bar{m}_w values are given in Figure 9 are -710 (N -alkyl betaines) and -715 cal/mol (hexaoxyethylene glycols).

TABLE IV: Hydrodynamic Properties

	Micelle size ($m = \bar{m}_w$)	Shear surface $\delta r, \text{\AA}$	$[\eta]$ or D_{20}°		
			Calcd		Obsd
			Prolate	Oblate	
Intrinsic Viscosity, ml/g					
$C_{12}H_{25}OSO_3Na^a$	100	4	6.0	3.4	3.3 ± 0.1
$C_{12}H_{25}NH_3Cl^b$	172	3	12.4	4.1	3.4
	260	3	20.9	4.4	3.8
	430	3	42.6	4.9	4.4
	1170	3	218	6.6	6.0
	3300	3	1340	9.6	15
	(5700)	3	3570	11.9	23
	(9100)	3	8360	14.6	45
$C_{16}H_{33}(EO)_7OH^c$	2600	12	360	5.5	107
	5530	12	1330	6.9	176
	8840	12	3060	8.1	260
Diffusion Coefficient, $cm^2 \text{ sec}^{-1} \times 10^7$					
$C_{12}H_{25}OSO_3Na^d$	85	4	8.4	9.6	9.7
$C_{12}H_{25}(EO)_6OH^e$	105	10	5.9	6.9	7.2
$C_{14}H_{29}(EO)_6OH^e$	127	10	5.4	6.3	6.2

^a Viscosity measurements at ionic strength 0.1–0.2 have been made in several laboratories^{37–39} and confirmed by Dr. J. A. Reynolds in this laboratory. ^b Micelle size and viscosity data as a function of increasing ionic strength from Kushner, *et al.*¹⁴ The authors considered the data in parentheses to be very approximate. ^c EO represents the oxyethylene group. The data represent measurements of Attwood³⁰ at 25, 30, and 35°. ^d Data of McQueen and Hermans⁴⁶ in 0.1 M NaCl at 22°, extrapolated to the cmc. ^e Data of Corkill and Walker,²⁵ measured at 5° and corrected to 20°.

Discussion

This paper has presented a general treatment of micelle formation, adaptable to any theoretical model, and designed to predict the optimal micelle size as well as the cmc. The treatment has been applied to micelles formed in aqueous solution by simple amphiphiles containing a single alkyl chain. The theoretical model proposed for these substances contains elements used in previous approaches to this problem, but is not directly comparable to any of them because its most important feature is the quantitative estimation of the hydrophobic component of the free energy of micellization as a function of micelle size, a problem with which previous theoretical treatments have not dealt. Emerson and Holtzer,^{16,34} for example, split ΔG_m° for ionic micelles into hydrophobic and head group components, as has been done here, but did not treat the hydrophobic component as a size-dependent parameter. Mukerjee²⁶ has used a size-dependent ΔG_m° in calculating the concentration dependence of micelle size, but did not attempt a physical interpretation of the size dependence. He assumed that equilibrium constants for successive additions of monomer are independent of m for $m > 2$, which is equivalent to the assumption that $d\Delta G_m^\circ/dm$ is independent of m . This assumption is not realistic if the variation of ΔU_m° with size is taken into account. When this is done $d\Delta G_m^\circ/dm$ is found to decrease in magnitude with increasing m , as shown, for example, by Figure 3 of my previous paper.³

We have not attempted to make absolute calculations for the free energy of repulsion between head groups (W_m). Previous attempts to make such calculations for ionic micelles have been criticized by Mukerjee²³ and there are no obvious ways to overcome the difficulties in the problem that he has pointed out. This paper has, however, attempted to deal with the formal dependence of W_m on micelle size, and has shown that the striking differences that are observed experimentally in the relation between optimal micelle size and the cmc, for both ionic and nonionic micelles, can be accounted for by variations in the depen-

dence of W_m on m that are appropriate for the different kinds of head groups that are considered. It may be added that the magnitude of W_m required to reproduce experimental data with the appropriate relations are always reasonable. For ionic micelles, for example, W_m turns out to be between 50 and 75% of the value calculated by use of the Debye-Hückel expression for a sphere of appropriate size (eq 13). For nonionic micelles, when the expression $W_m = \gamma/A_{Rm}^3$, which is intended to simulate steric repulsion, is used, the constant γ must be increased as the size of the head group is increased.

Representation of the micelle as an ellipsoid of revolution is essential to the calculations we have made. Since this model unambiguously predicts that oblate ellipsoids should nearly always be more stable than prolate ellipsoids, experimental data regarding micelle shape need to be examined, with special attention to those results that appear to support a rod-like model.

The ellipsoid model predicts preference for the prolate shape only when the repulsion between head groups is very strong. In this situation the micelles formed at the cmc are quite small. As the amphiphile concentration is increased, providing thermodynamic pressure for micelle growth, the prolate shape is favored because its larger surface area keeps head groups farther apart, and a transition such as is illustrated by Table III may be expected to occur. Sufficiently strong repulsion for this situation to arise can be expected for ionic micelles in the absence of added salt, and strong evidence for the existence of rod-shaped micelles comes in fact from micelles of this type; Reiss-Husson and Luzzati³⁵ have observed that several ionic micelles in the absence of added salt undergo a transition at an amphiphile concentration of 25–50% from small particles (indistinguishable by X-ray scattering from spheres) to more extended rods. No similar studies have been made in the presence of added salt. Experiments in more dilute solutions indicate that ionic micelles at moderate ionic strength behave as small particles to the highest concentrations em-

ployed. Intrinsic viscosity measurements invariably indicate that the micelles are compact and globular. Calculations based on the equations provided by Frisch and Simha³⁶ unequivocally support an oblate ellipsoidal shape, as shown by the results for sodium dodecyl sulfate in Table IV. It should be noted that the surface of shear for these calculations has been placed at a geometrically realistic distance from the surface of the hydrophobic core, but the results are in fact not very sensitive to this choice since an increase in δr increases the ellipsoid volume, but decreases the asymmetry, leading to a relatively small effect on $[\eta]$.

When ionic micelles are subjected to even higher concentrations of added salt, a transition in shape is again observed. Light scattering studies indicate a rod-like shape for $C_{16}H_{33}NMe_3Br$ in 0.178 M KBr,⁴⁰ and a dependence of molecular weight on concentration similar to that predicted for prolate micelles in Figure 7 has been reported for $C_{10}H_{21}NH_2CH_3Br$ in 0.5 M NaBr.²⁹ The neutralization of micelle charge by counterions must be virtually complete under these conditions and the idea that electrostatic repulsion exerts a dominant influence on micelle shape would seem to be untenable. Though these results may represent serious disagreement with the theoretical predictions made here, the possibility that the large particles observed are salt-linked aggregates of oblate ellipsoids is not excluded by the available data. The observation by Debye and Anacker⁴⁰ that visible crystals are observed to form in solutions of $C_{16}H_{33}NMe_3Br$ can be viewed as support for this possibility.

A somewhat similar situation is encountered for alkyl polyoxyethylene derivatives. When the number of polyoxyethylene units in the head group is small these amphiphiles form globular micelles below a characteristic threshold temperature. Accurate diffusion coefficients have been determined in one instance, and comparison with calculated diffusion coefficients based on Perrin's equation⁴¹ indicates that they are oblate ellipsoids, as shown in Table IV. Above the threshold temperature the micelle size increases and becomes strongly dependent on concentration in the manner of Figure 7.^{30,31} This concentration dependence, light scattering measurements, and viscosity data (shown in Table IV) all indicate that the micelles are rod-like. The discrepancy seen in Table IV between the measured $[\eta]$ and the calculated values for a rigid prolate ellipsoid is reasonably explained by assuming that the rods are somewhat flexible, as suggested (for another system) by Stigter.⁴² In this case the bulkiness of the head groups could conceivably constitute a driving force favoring the larger surface areas of prolate ellipsoids, but the W_m functions that will account for the very low cmc exhibited by these systems (Figure 2) do not predict this. The pronounced influence of temperature on the formation of these nonglobular micelles suggests moreover that an interaction between head groups is involved, and it is again possible that one is dealing here with a reversible aggregation of small micelles rather than with formation of large extended micelles with a single hydrocarbon core, as has in fact been suggested by all of the investigators who have made the experimental observations on these systems.^{30,31,43,44}

One study frequently cited as evidence for rod-shaped micelles is the study of the viscosity of $C_{12}H_{25}NH_3Cl$ micelles by Kushner, *et al.*¹⁴ These micelles grow to very large size, but have a 100-fold higher cmc than the polyoxyethylene derivatives, as shown in Figure 2. Stigter⁴² has shown that the intrinsic viscosities measured for these mi-

celles are much smaller than expected for stiff rods, but larger than expected for oblate ellipsoids, and has suggested that the micelles are rod-shaped but flexible. We have repeated these calculations and obtain somewhat larger $[\eta]$ values than Stigter, presumably because we have used a smaller minor axis for the ellipsoids to take into account the likely flexibility of the alkyl chains (Table I). As Table IV shows the observed intrinsic viscosities are in fact quite consistent with an oblate ellipsoidal shape, at least to $m = 1200$.

The very large micelles discussed here obviously represent a problem requiring further study. It would be desirable to have experimental data that can distinguish unequivocally between large micelles with a single hydrocarbon core and large micelles formed by loose association of small micelles. If evidence for the existence of large rod-like micelles with a single hydrocarbon core can be established, some modification of the theoretical treatment of this paper will clearly be necessary.

Appendix. Method of Calculation

A computer or large capacity desk calculator⁴⁵ is essential to program the calculation of surface area and dA/dm as a function of micelle size, alkyl chain length, and the distance from the core surface. The program must be linked to an analytical expression for W_m and dW_m/dA (as provided, for example, by eq 15) to evaluate these factors as a function of the same variables.

These programs in effect generate values of ΔG_m° and $d\Delta G_m^\circ/dm$ as a function of m for any desired choice of the adjustable variables. The simplest procedure thereafter is to begin with the optimal size, using eq 5 to estimate $\ln X_{m^*}$ for a series of possible values of m^* . In most cases values of $\ln X_{m^*} < -25$ correspond to solutions below the cmc with a negligible content of micelles. Values of $\ln X_{m^*} > -2$ are physically impossible since ΣX_m must be less than unity. Equation 3 is used with $m = m^*$ to obtain the value of $\ln X_1$ in equilibrium with the micelles of optimal size. This same equation, with $\ln X_1$ fixed, is then used to obtain the size distribution function, numerical integration of which gives ΣX_m , and, by eq 6, the total concentration of amphiphile. The results are then turned around to yield m^* , $\ln X_1$, the size distribution, and the molecular size averages given by eq 7 and 8, all as a function of total amphiphile concentration. The point at which ΣX_m is 5% of X_{total} was designated as the cmc, but any desired definition of the cmc can be used.

For many of the calculations, where a distribution function *per se* was not required, X_m was approximated as a Gaussian distribution

$$X_m = X_{m^*} e^{-s^2(m-m^*)^2} \quad (16)$$

and ΣX_m was obtained as the integral of the right-hand side, from $m = -\infty$ to $m = +\infty$. This does not introduce a significant error in the location of the cmc, but can lead to errors of up to 50% in the absolute values of ΣX_m for high amphiphile concentrations when the distribution function is badly skewed.

Reference and Notes

- (1) (a) This work was supported by Grant No. GB-40559X from the National Science Foundation (b) Recipient of a Research Career Award from the National Institutes of Health, U. S. Public Health Service.
- (2) C. Tanford, *J. Phys. Chem.*, **76**, 3020 (1972).

- (3) C. Tanford, *Proc. Nat. Acad. Sci. U. S.*, **71**, 1811 (1974).
- (4) R. W. Gurney, "Ionic Processes in Solution," McGraw-Hill, New York, N.Y., 1953, pp 88-92.
- (5) C. Tanford, "The Hydrophobic Effect," Wiley, New York, N.Y., 1973, Chapters 1-7.
- (6) H. V. Tartar, *J. Phys. Chem.*, **59**, 1195 (1955).
- (7) (a) P. J. Flory, "Statistical Mechanics of Chain Molecules," Wiley, New York, N.Y., 1969, Chapter V; (b) P. J. Flory and R. L. Jernigan, *J. Chem. Phys.*, **43**, 3509 (1965).
- (8) Accurate values of A and dA/dm as required for the calculations cannot be obtained from this graph but have to be evaluated directly from the formulas for ellipsoid areas.
- (9) D. Stigter and K. J. Mysels, *J. Phys. Chem.*, **59**, 45 (1955).
- (10) D. W. Harkins, "The Physical Chemistry of Surface Films," Reinhold, New York, N.Y., 1952, Chapter 2.
- (11) R. B. Hermann, *J. Phys. Chem.*, **76**, 2754 (1972).
- (12) J. A. Reynolds, D. B. Gilbert, and C. Tanford, *Proc. Nat. Acad. Sci. U. S.*, **71**, 2925 (1974).
- (13) A. Wishnia, *J. Phys. Chem.*, **67**, 2079 (1963).
- (14) L. M. Kushner, W. D. Hubbard, and R. A. Parker, *J. Res. Nat. Bur. Stand.*, **59**, 113 (1957).
- (15) E. W. Anacker, R. M. Rush, and S. S. Johnson, *J. Phys. Chem.*, **68**, 81 (1964).
- (16) M. F. Emerson and A. Holtzer, *J. Phys. Chem.*, **71**, 1898 (1967).
- (17) K. Mysels and L. Princen, *J. Phys. Chem.*, **63**, 1696 (1959).
- (18) P. Becher, *J. Colloid Sci.*, **17**, 325 (1962).
- (19) R. R. Balmbra, J. S. Clunie, J. M. Corkill, and J. F. Goodman, *Trans. Faraday Soc.*, **58**, 1661 (1962).
- (20) J. H. Brooks and B. A. Pethica, *Trans. Faraday Soc.*, **61**, 571 (1965).
- (21) Curve 2 is based on experimental results obtained through the kindness of Dr. J. Mingins of Unilever Research, Port Sunlight, England. The curve differs somewhat from the W curve for $C_{12}H_{25}OSO_3Na$ given earlier (Figure 2 of ref 3) because Dr. Mingins' results differ somewhat from the earlier published data²⁰ from the same laboratory. The up-swing of the curve near $A = 50 \text{ \AA}^2$ may be an artifact of the procedure used for curve fitting: only data for $A > 80 \text{ \AA}^2$ were used for the analysis.
- (22) P. Mukerjee, *Advan. Colloid Interface Sci.*, **1**, 241 (1967).
- (23) P. Mukerjee, *J. Phys. Chem.*, **73**, 2054 (1963).
- (24) Another possibility that might be considered is that there may be a preferred distance between head groups suitable for intercalation of water molecules between oxyethylene groups. In that case W might not increase continuously with decreasing area, but could have a shallow minimum just before the steep rise sets in, as in a Lennard-Jones type of potential function.
- (25) J. M. Corkill and T. Walker, *J. Colloid Interface Sci.*, **39**, 621 (1972).
- (26) P. Mukerjee, *J. Phys. Chem.*, **76**, 565 (1972).
- (27) D. G. Hall and B. A. Pethica in "Nonionic Surfactants," M. J. Schick, Ed., Marcel Dekker, New York, N.Y., 1967.
- (28) The relation between m^* and increasing values of X_1 was calculated rigorously, but the calculation of $\sum X_m$ was made using an approximation which has the effect of making the calculated total concentration somewhat too large. The rise in m^* predicted by a rigorous calculation would thus be slightly steeper than shown.
- (29) R. D. Geer, E. H. Eylar, and E. W. Anacker, *J. Phys. Chem.*, **75**, 368 (1971).
- (30) D. Attwood, *J. Phys. Chem.*, **72**, 339 (1968).
- (31) P. H. Elworthy and C. B. Macfarlane, *J. Chem. Soc.*, 907 (1963).
- (32) As shown in Figure 2, cmc values for the same micelle size are smaller for $\delta r = 3 \text{ \AA}$ than for $\delta r = 4 \text{ \AA}$. This makes the cratic factor of eq 3 ($m \ln X_1$) less favorable to the increase in micelle size that accompanies the transition to prolate micelles.
- (33) J. Swarbrick and J. Daruwala, *J. Phys. Chem.*, **74**, 1293 (1970).
- (34) M. F. Emerson and A. Holtzer, *J. Phys. Chem.*, **69**, 3718 (1965).
- (35) F. Reiss-Husson and V. Luzzati, *J. Phys. Chem.*, **68**, 3504 (1964); *J. Colloid Interface Sci.*, **21**, 534 (1966).
- (36) H. L. Frisch and R. Simha in "Rheology," Vol. 1, F. R. Eirich, Ed., Academic Press, New York, N.Y., 1956, Chapter 14.
- (37) L. M. Kushner, B. C. Duncan, and J. I. Hoffman, *J. Res. Nat. Bur. Stand.*, **49**, 85 (1952).
- (38) R. A. Parker and S. P. Wasik, *J. Phys. Chem.*, **62**, 967 (1958).
- (39) F. Tokiwa and K. Ohki, *J. Phys. Chem.*, **71**, 1343 (1967).
- (40) P. Debye and E. W. Anacker, *J. Phys. Colloid Chem.*, **55**, 644 (1951).
- (41) C. Tanford, "Physical Chemistry of Macromolecules," Wiley, New York, N.Y., 1961, Chapter 6.
- (42) D. Stigter, *J. Phys. Chem.*, **70**, 1323 (1966).
- (43) J. M. Corkill, J. F. Goodman, and T. Walker, *Trans. Faraday Soc.*, **63**, 759 (1967).
- (44) R. H. Ottewill, C. C. Storer, and T. Walker, *Trans. Faraday Soc.*, **63**, 2796 (1967).
- (45) A Wang Model 500 electronic calculator was used in this investigation.
- (46) D. H. McQueen and J. J. Hermans, *J. Colloid Interface Sci.*, **39**, 389 (1972).

Micelle Formation by Ionic Surfactants. II. Specificity of Head Groups, Micelle Structure

Dirk Stigter

Western Regional Research Center, Agricultural Research Service, U. S. Department of Agriculture, Berkeley, California 94710
(Received April 24, 1974)

Publication costs assisted by the Agricultural Research Service, U. S. Department of Agriculture

The critical micelle concentrations (cmc) of various straight chain ionic surfactants in aqueous salt solutions are compared with the cmc's of alkyl sulfates for the same alkyl chain length, ionic strength, and temperature. It is found for five different hydrophilic terminal groups that the cmc is higher when the ionic charge on the head group is closer to the α -carbon atom in the alkyl chain. This correlation is explained by the increase in electrostatic self-potential of the surfactant ion, when in micellization the head group moves from bulk water to the vicinity of the nonpolar core of the micelle. Quantitative agreement requires that the α -methylene groups are contained in the micelle core, and that the core-water interface is located between 0.4 and 1.2 Å from the center of the α -carbon atoms. This approximate distance is confirmed by a free-energy argument, valid for surfactants with sufficiently hydrophilic head groups. From the relatively low cmc's of the decyl substituted 2-, 3-, or 4-pyridinium hydrogen bromides it is concluded that part of the hydrophobic head groups may be contained in the micelle core, depending on the charge distribution in the pyridinium ring. The foregoing conclusions disagree with recent papers on small-angle X-ray scattering and fluorine magnetic resonance of surfactant solutions in which it was concluded that water penetrates between the micellized alkyl chains. However, it is shown that the interpretation in the X-ray paper is not self-consistent; the magnetic resonance experiments might also require reinterpretation.

Introduction

It is well known that micelle formation in aqueous solutions of ionic surfactants depends on various factors. The first paper of this series¹ discussed the dependence on the ionic strength and on the chain length of the surfactant ion. Also the influence of the ionic head group on the critical micelle concentration (cmc) is well documented.² The latter factor is the main topic of this paper.

The specific influence of alkali ions on the cmc of dodecyl sulfate has been correlated with the size of the counterions.³ For sodium dodecyl sulfate (SDS) and dodecyl ammonium chloride (DACl) the adsorption of the counterions at the micelle surface has been explained in terms of electrostatics, allowing for the size of the hydrated head groups and counterions.⁴ A similar model is used in a present study of the electric free-energy changes that accompany micelle formation. Preliminary results show that variations in the size of the head groups and of the counterions cannot explain the large difference between the cmc's of SDS and DACl. It is found that in a satisfactory micelle theory one should include the increase in self-potential of the ionic head group when it moves from the bulk of the aqueous solution to the vicinity of the nonpolar micelle core. This particular aspect of the theory is discussed in the present paper for a variety of surfactants consisting of a straight hydrocarbon chain with a terminal ionic group. Most of the cmc data used in this paper are taken from the critical compilation by Mukerjee and Mysels.² The interesting results for the set of decylpyridinium hydrogen bromides are from a recent paper by Jacobs and Anacker.⁵

The proposed change in self-potential of the surfactant head group upon micellization depends on a rather subtle feature of micelle structure. How far does water penetrate between the micellized hydrocarbon chains? This problem has been studied in recent years by magnetic resonance of fluorinated surfactants.⁶⁻⁸ This work and some other evi-

dence bearing on micelle structure is reviewed in the last part of the paper. A critical discussion is important because there is an apparent discrepancy between the results of different methods of investigation.

Cmc and Self-Potential

In aqueous solutions of ionic surfactants the cmc depends significantly on the length of the straight alkyl chain, on the type of terminal ionic group, and on the presence of foreign salt. The dependence on temperature is not very strong. We compare cmc data recorded at or close to 25°. The information is most complete for the sodium alkyl sulfates. Data for the C_8 to C_{12} compounds are marked in Figure 1 as filled points. The straight lines through these points show the variation of cmc with ionic strength for the particular chain length indicated. We consider only fully ionized compounds in which case all unassociated surfactant contributes to the ionic strength. For this reason the line connecting the cmc's for surfactants in water in Figure 1 has a 45° positive slope.

The lines for the alkyl sulfates in Figure 1 are used as a basis for comparison with other compounds. In each case we compare the cmc's of two surfactants with the same hydrocarbon chain and at the same ionic strength. For instance, the lowest point marked 3 in Figure 1, at 0.0244 *M*, is the cmc of sodium dodecanoate in water. From this point the broken vertical line drops to the C_{11} line at 0.0125 *M*. This is the cmc of sodium undecyl sulfate at ionic strength 0.0244 *M*. Therefore, at this ionic strength the cmc of sodium dodecanoate is a factor 0.0244/0.0125 higher than the cmc of the reference compound, corresponding to a free-energy difference $kT \Delta \ln \text{cmc} = kT \ln (0.0244/0.0125) = 0.65kT$. We have calculated such differences for a number of systems, as indicated by the vertical lines starting from the open circles in Figure 1. It turns out that, within the accuracy of the present cmc data, there is no systematic

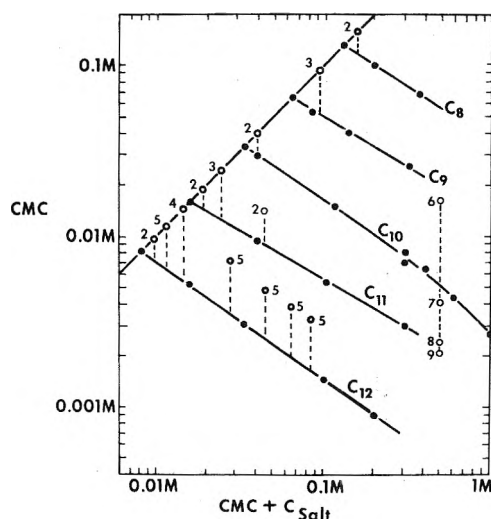


Figure 1. Cmc vs. ionic strength for various surfactants in aqueous salt solutions about 25°: heavy solid line, surfactants in water; filled points and light lines, sodium alkyl sulfates: numbered, open points, 2 = sodium alkylsulfonate, 3 = sodium alkylcarboxylate, 4 = dodecyl ammonium chloride; 5 = dodecyl-1-pyridinium bromide, 6, 7, 8, 9 = decyl-*x*-pyridinium bromide, substituted at position *x* = 1, 2, 3, 4, respectively. KBr or HBr added to pyridinium compounds, NaCl added in other cases to increase ionic strength. Data from table of recommended and selected cmc's in ref 2 and from ref 5.

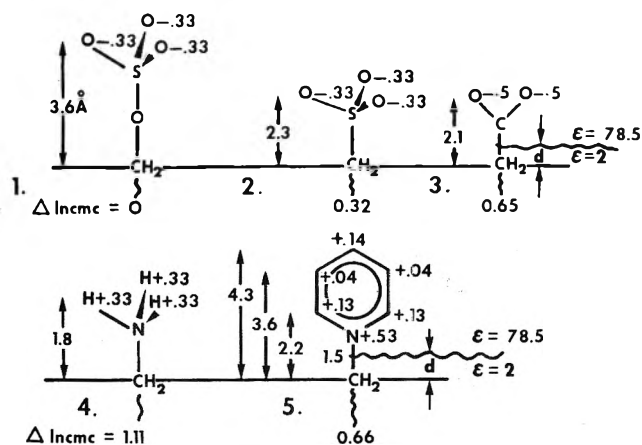


Figure 2. Head groups of surfactants in Figure 1. Vertical distances in angstroms, partial charges in protonic units, cmc differences as defined in text.

change of the calculated free-energy difference with ionic strength or with chain length, but only a dependence on the type of head group. In Figure 2 five different head groups are represented with the (average) values of $\Delta \ln \text{cmc}$. We correlate these data with the charge distribution in the various head groups.

The vertical distances from the α -carbon atoms in Figure 2 are taken from X-ray data.⁹ In groups 1, 2, and 3 we assume that the ionic charge resides on the oxygen atoms, in group 4 on the hydrogen atoms. Strictly speaking, the charge should be smeared out over the entire head group. However, the quantum mechanical details of such distributions are not well known. The situation is somewhat more favorable for the pyridinium group 5. Figure 2 gives the excess charge on the various ring atoms as derived by Jacobs and Anacker⁵ from a Hückel molecular orbital treatment of the π electrons.

Inspection of Figure 2 shows that in the sequence 1 to 4

TABLE I: Change of Self-Potential in Micellization, $\Delta\phi_k$, of Head Groups 1-5 in Figure 2 for Two Values of Distance d , and Comparison with Cmc Difference $\Delta \ln \text{cmc}$ (Flat Interface)

Group $k =$	1	2	3	4	5
$\Delta\phi_k/kT$ for					
$d = 0.5\text{\AA}$	0.522	0.836	0.979	1.167	1.128
$d = 1.1$	0.633	1.135	1.447	1.846	2.133
$(\Delta\phi_k - \Delta\phi_1)/kT$ for					
$d = 0.5$	0	0.31	0.46	0.64	0.61
$d = 1.1$	0	0.50	0.81	1.21	1.50
$\Delta \ln \text{cmc}$	0	0.32	0.65	1.11	0.66

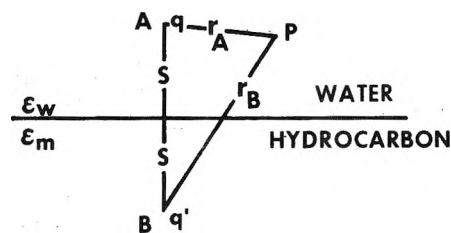


Figure 3. Electrostatic charge q near flat interface, with image charge q' in mirror point.

the vertical distance between the ionic charge and the α -carbon atom decreases, while $\ln \text{cmc}$ increases, that is, it becomes more difficult to form micelles. It is noted that in an early paper¹⁰ Kleven has compared cmc data of several homologous series of ionic surfactants, and concluded that $\ln \text{cmc}$ varies linearly with the total length of the surfactant ion, including the distance between α -carbon and head group charge. However, Figure 2 shows that the latter distance changes not quite linearly with $\Delta \ln \text{cmc}$. So Kleven's empirical relation is a very approximate one. In the following we explain the correlation between $\ln \text{cmc}$ and the vertical distances in Figure 2 with a well-known fact from electrostatics: work is required to move an electric charge closer to a medium of lower dielectric constant.

In Figure 2 we assume that the flat interface between water, with dielectric constant $\epsilon_w = 78.5$, and the hydrocarbon core of the micelle, with $\epsilon_m = 2$, is located at distance d above the α -carbon atoms. A detail is given in Figure 3 where we consider a charge q in point A at a distance s from the interface. The potential field in the aqueous phase is described with the help of a virtual charge in the mirror point B of magnitude $q' = q(\epsilon_w - \epsilon_m)/(\epsilon_w + \epsilon_m)$, the so-called image charge. The potential in point P in water, at a distance r_A from A and r_B from B, is

$$\psi_P = \frac{q}{\epsilon_w r_A} + \frac{\epsilon_w - \epsilon_m}{\epsilon_w + \epsilon_m} \frac{q}{\epsilon_w r_B} \quad (1)$$

In bulk water, when $s = \infty$ in Figure 3, the image term vanishes because $r_B = \infty$.

In order to find the desired change of self-potential, $\Delta\phi$, we move the charge q from bulk water to A in small increments $q d\lambda$. Using eq 1 we find that at a charging stage λ the work increment is

$$\frac{\epsilon_w - \epsilon_m}{\epsilon_w + \epsilon_m} \frac{\lambda q^2}{2\epsilon_w s} d\lambda \quad (2)$$

Integration of this expression between $\lambda = 0$ and $\lambda = 1$ yields the total work, that is, the change of self-potential

$$\Delta\phi = \frac{\epsilon_w - \epsilon_m}{\epsilon_w + \epsilon_m} \frac{q^2}{4\epsilon_w s} \quad (3)$$

TABLE II: Change of Self-Potential in Micellization, $\Delta\phi_k$, of Head Groups 1–5 in Figure 2 for two Values of Distance d , and Comparison with Cmc Difference $\Delta \ln \text{cmc}$ (Curved Interface with 18-Å Radius)

Group $k =$	1	2	3	4	5
$\Delta\phi_k/kT$ for					
$d = 0.7 \text{ Å}$	0.267	0.553	0.703	0.916	0.902
$d = 1.2$	0.344	0.797	1.117	1.569	2.093
$(\Delta\phi_k - \Delta\phi_1)/kT$ for					
$d = 0.7$	0	0.29	0.44	0.65	0.64
$d = 1.2$	0	0.45	0.77	1.23	1.76
$\Delta \ln \text{cmc}$	0	0.32	0.65	1.11	0.66

We now consider a group of charges ($q_1, q_2, \dots, q_i, \dots$) moving from the bulk of the aqueous phase to positions $\vec{r}_1, \vec{r}_2, \dots, \vec{r}_i, \dots$ in the vicinity of the interface, while the mutual distances between the charges are maintained. In this case each charge q_i is in the field of all members of the virtual charge constellation ($q'_1, q'_2, \dots, q'_3, \dots$) at the mirrorpoints ($\vec{r}'_1, \vec{r}'_2, \dots, \vec{r}'_3, \dots$). Generalization of the previous argument yields for the change of self-potential of the group

$$\Delta\phi = \frac{\epsilon_w - \epsilon_m}{\epsilon_w + \epsilon_m} \sum_i \sum_j \frac{q_i q_j}{2\epsilon_w |\vec{r}_i - \vec{r}_j|} \quad (4)$$

We have applied eq 4 to the situations in Figure 2. Results of $\Delta\phi_k$ for group $k = 1$ to 5 and for two values of d are shown in the upper part of Table I. Since group 1 is the reference, the interesting quantity is $\Delta\phi_k - \Delta\phi_1$. This difference should be compared with the free-energy difference $kT \Delta \ln \text{cmc}$, as derived above. The data in the lower part of Table I indicate that for all groups $\ln \text{cmc}$ is bracketed by the values of $(\Delta\phi_k - \Delta\phi_1)/kT$ for $d = 0.5$ and $d = 1.1 \text{ Å}$. In order to evaluate the significance of this result, $d = 0.8 \pm 0.3 \text{ Å}$, we discuss some obvious shortcomings of the model.

First, as already pointed out, we are using approximate charge distributions. It is likely that in groups 1–4 part of the ionic charge is located closer to the α -carbon atom than assumed in Figure 2. The resulting decrease in the best value of d is certainly less than 0.5 Å , perhaps about 0.2 Å .

A second correction is required for the curvature of the micelle surface. For a representative core radius of 18 Å we have recalculated $\Delta\phi_k$, using eq 13 and 19 of ref 4. The results in Table II show that allowing for curvature of the interface increases the best value of d by about 0.15 Å . More accurate calculations cannot be made because the micelle size is not known in all cases and, moreover, the present values of $\Delta \ln \text{cmc}$ are average results. We observe that the correction of d for curvature is opposite to the first correction, and of the same magnitude.

Another source of uncertainty is the nonuniformity of the dielectric constant. The surface layer of a micelle resembles a concentrated electrolyte solution, with a dielectric constant lower than that of bulk water. It is accepted that in aqueous electrolyte solutions, even at high concentrations, the effects of a nonuniform dielectric constant on ionic interactions are minor.¹¹ On this basis refinements in the dielectric constant of the surface layer of the micelle are expected to cause only a small decrease in the best value of d . On the other hand, a small increase of d is expected because in the unassociated state the ionic head group is always close to its attached hydrocarbon tail and, therefore, not completely surrounded by water.

Finally, the distance of closest approach between head

groups and counterions is a factor in the electric free-energy of micelle formation and, hence, influences the cmc. This factor is incorporated in a more complete micelle theory presently under study. Preliminary results for sodium dodecyl sulfate and for dodecyl ammonium chloride suggest that in groups 1–4 of Figure 2 the effects of ionic size are not very different, contributing perhaps about $0.1kT$ to $\Delta\phi_k$.

In summary, the values of $\Delta\phi_k$ in Table I require several corrections which, at least in part, are mutually compensating. With a reasonable estimate of all uncertainties we conclude that for compounds 1–5 in Figure 2 the average location of the core–water interface is at $d = 0.8 \pm 0.4 \text{ Å}$ above the α -carbon atoms.

It is noted in passing that the self-potential of the counterions near the core surface may also change significantly. As pointed out earlier⁴ this may influence the adsorption of the counterions at the micelle surface. However the effects on the cmc of fully ionized surfactants are likely to be small.

Core–Water Interface and Free Energy

In this section the location of the core–water interface found above is tested with an argument used earlier by Levine, Bell, and Pethica¹² in the adsorption of surfactant monolayers at an oil–water interface.

We require the value of d that minimizes the free energy F of the micellar solution, $\partial F/\partial d = 0$. The dependence of F on d derives mainly from hydrophobic and electrostatic interactions and from dehydration of the head group. It was found¹ that, at 25° , the transfer of a methylene group from water to the interior of a micelle decreases the free energy of the system by about $1.25kT$. We adopt this result for all methylene groups and, averaging along the alkyl chain, we take $-1.0kT/\text{Å}$ per monomer as the hydrophobic contribution to $\partial F/\partial d$. This value is reasonable for, e.g., $d < 0.7 \text{ Å}$. For larger d dehydration of the head group is expected to cause a sharp increase in F . This is a short-range repulsion by the core. There is also the long-range electrostatic repulsion of the charged head group by the micelle core, as dealt with in the previous section.

As examples we take alkyl sulfate and alkyl ammonium, compounds 1 and 4 of Figure 2, respectively. In Figure 4 the various free-energy contributions are plotted vs. d . The hydrophobic component is the same for both surfactants, and is given by the lowest curve. This is a straight line with slope as defined above, and with an arbitrary constant added. As shown in Figure 2, the ionic charge of the alkyl ammonium is closer to the α carbon than the charge of the alkyl sulfate. So at a fixed value of d the electrostatic repulsion of the ammonium charge by the core is greater than the repulsion of the sulfate charge. For this reason the composite curve for the alkyl ammonium lies above that of the alkyl sulfate ion. Details of ionic dehydration are not known; the broad arrows are based on the consideration that, in contact with water, the ionic groups are hydrated, but the α -methylene groups are not.

It is noted that, if one disregards the possible effects of hydration, the alkyl ammonium curve in Figure 4 has a minimum around $d = 0.8 \text{ Å}$. For this value of d the ammonium charge is about 1.0 Å above the water–core interface, compare Figure 2. This distance compares well with the equilibrium distance of 1.29 Å , calculated by Levine, *et al.*,¹² between a single surfactant charge and a planar oil–water interface, neglecting possible changes of hydration.

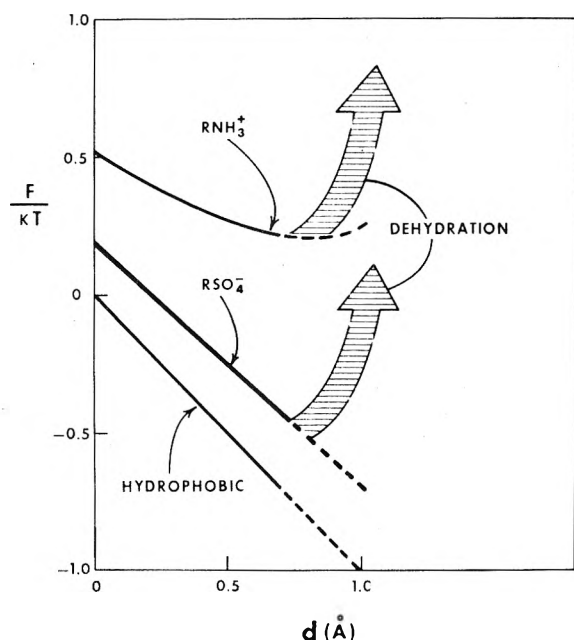


Figure 4. Free energy F vs. distance of immersion of α -carbon atom in micelle core: upper curve, alkyl ammonium; middle curve, alkyl sulfate; lower curve, hydrophobic component; broad arrows, dehydration potential of head groups. Electrostatic contributions calculated for micelle core with radius of 18 Å.

In the latter case the electrostatic repulsion is greater than by the spherical micelle core in Figure 4.

Levine, *et al.*,¹² showed also that, when counterions may penetrate between the adsorbed monolayer charges, the double layer effects diminish the electrostatic repulsion of adsorbed charges by the oil phase. This means that for micelles a treatment which includes such double-layer effects would produce free-energy minima that would be deeper than those in Figure 4. Nevertheless, one expects that the dehydration potential still remains the chief determinant of the equilibrium distance d . For this reason we do not extend the present calculation with a double-layer contribution.

A few remarks about fluctuations are in order. The potential curves in Figure 4 are not symmetrical. Therefore, the equilibrium distance, or average distance $\langle d \rangle$, might be significantly shorter than the value of d for which the free energy is minimal. As an extreme example we consider the hydrophobic curve in Figure 4, combined with an infinitely steep dehydration potential at $d = d_0$

$$F = -dkT \quad d < d_0 \quad (5)$$

$$F = \infty \quad d \geq d_0$$

The average value of d for this potential is

$$\langle d \rangle = \frac{\int_{-\infty}^{+\infty} d \exp(-F/kT) dd}{\int_{-\infty}^{+\infty} \exp(-F/kT) dd} = d_0 - 1 \quad (6)$$

This result shows that the extreme asymmetry of the potential in eq 5 shifts $\langle d \rangle$ by only 1 Å. More realistic free-energy curves will show less asymmetry, causing a shift in $\langle d \rangle$ of only a fraction of 1 Å.

The main conclusion is that the free-energy curves show a not too shallow minimum around the previously derived equilibrium distance $d = 0.8 \pm 0.4$ Å. In view of the uncer-

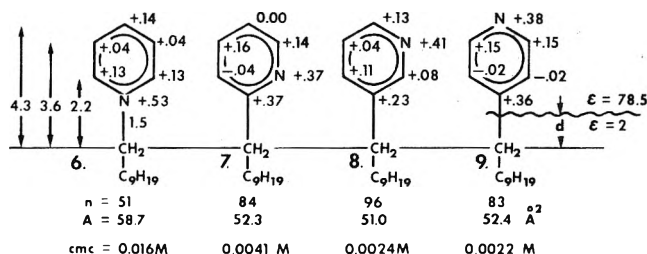


Figure 5. Decyl-substituted pyridinium groups in Figure 1. Micelle numbers n , cmc values, and partial charges from ref 5. Vertical distances in angstroms. A is surface area of micelle core per monomer.

tainty of the dehydration potential the limits on d cannot be narrowed at the present time. It is encouraging that two independent methods give essentially the same location of the core-water interface. One expects that this location does not depend significantly on the particular surfactant, as long as the head group is sufficiently hydrophilic. We now examine some surfactants which do not meet this specification.

Cmc of Decylpyridinium Hydrobromides

Following the work of Jacobs and Anacker⁵ the cmc of decylpyridinium salts depends markedly on the position in which the pyridinium ring is substituted. Figure 5 shows the various isomers, with the ring charges as calculated⁵ with the Hückel molecular orbital method, the association number n ,⁵ and the surface area A available per monomer at the surface of the micelle core. For all compounds the area A , calculated from n and assuming a core density⁴ of 0.789 g/ml, is large enough for the pyridinium rings to lie flat on the core surface. However, such a position would minimize any differences between the four compounds, and the large variations in cmc would be difficult to explain. For this reason we assume that the terminal rings do not lie flat on the micelle surface, but stick out into the water.

We have evaluated the change in self-potential, assuming that the pyridinium rings are perpendicular to the surface of spherical micelles with the experimental n values. The results are shown in Table III for the limits of the range $d = 0.8 \pm 0.4$ Å accepted for compounds 1–5. As before we use 1 as the reference group, and the difference $(\Delta\phi_k - \Delta\phi_1)/kT$ is compared with $\Delta \ln \text{cmc}$. It is noted that the N-substituted group 6 is the same as group 5, and that there is a discrepancy between the values of $\Delta \ln \text{cmc}$ for 5 and 6. A possible reason is the difference in solvent: 0.5M HBr for compound 6, and more dilute KBr solutions for 5. For the purpose of the present argument we have accepted the published cmc data for compounds 6–9, and used sodium decyl sulfate as a reference, see Figures 1 and 5, to obtain $\Delta \ln \text{cmc}$ in Table III.

For group 6 $\Delta \ln \text{cmc}$ is well within the calculated limits in Table III. This is not the case for groups 7–9. In fact, for the present model there is no value of d which produces results for $(\Delta\phi_k - \Delta\phi_1)/kT$ to match the $\Delta \ln \text{cmc}$ data of compounds 7–9. A satisfactory explanation can be constructed when the hydrophobicity of the head groups is considered.

Figure 5 shows that in the order 6, 7, 8 the ring charge moves away from the α -carbon atom. So it is probable that, in this order, the lower part of the pyridinium ring becomes more hydrophobic. As a result one expects d to increase so that the ring moves partly out of the water and into the mi-

TABLE III: Change of Self-Potential in Micellization, $\Delta\phi_k$, of Head Groups 1 in Figure 2, and 6-9 in Figure 4 for Two Values of Distance d , and Comparison with Cmc Difference $\Delta \ln \text{cmc}$ (Spherical Micelles)

Group $k =$	1	6	7	8	9
$\Delta\phi_k/kT$ for					
$d = 0.4 \text{ \AA}$	0.233	0.627	0.565	0.402	0.392
$d = 1.2$	0.344	2.042	1.495	0.865	1.063
$(\Delta\phi_k - \Delta\phi_1)/kT$ for					
$d = 0.4$	0	0.39	0.33	0.17	0.16
$d = 1.2$	0	1.70	1.15	0.52	0.72
$\Delta \ln \text{cmc}$	0	1.12	-0.24	-0.77	-0.86

celle core. The effect is similar to that of lengthening the hydrocarbon tail: it facilitates micelle formation and lowers the cmc, as observed. The relevant contributions to the free energy are difficult to evaluate and, hence, we cannot derive an accurate equilibrium value of d for the present compounds.

It remains to evaluate the possible effect on the cmc of a specific adsorption of bromide ions to the micelle surface by charge transfer (CT) interactions with head groups 6-9 in Figure 5. The formation of CT complexes of pyridinium compounds with various ions is well established,¹³⁻¹⁶ well understood in a qualitative way,¹⁷ and needs no elaboration here. For dodecyl-1 pyridinium micelles in water CT interactions with halogen ions decrease in the order $\text{I}^- > \text{Br}^- > \text{Cl}^-$.¹⁶ This sequence parallels that of the cmc's of the dodecyl-1-pyridinium halogenides:² $0.57 \times 10^{-2} M$ for the iodide, $1.14 \times 10^{-2} M$ for the bromide, and $1.47 \times 10^{-2} M$ the chloride compound in water at 25°. In the micellar solutions there is no spectral evidence of a CT complex of the 1-pyridinium head group with chloride, only with bromide and, particularly, with iodide ions.¹⁶ So for head group 6 (or 5) the CT interaction with bromide ions causes no more than the minor decrease in cmc from 1.47×10^{-2} to $1.14 \times 10^{-2} M$. This decrease is an order of magnitude smaller than the large differences between the cmc's of compounds 6-9 in Figure 5. Furthermore, CT complex formation is quite insensitive to changes in substitution of the pyridinium ring.¹⁴ We conclude that specific adsorption of bromide ions at the micelle surface is not a main factor in the cmc of the compounds under discussion.

Micelle Structure

Light scattering,¹⁸ viscosity,^{19,20} and ultrasonic measurements²¹ in dilute surfactant solutions have produced sound evidence of the presence of small, spherical or larger, worm-like micelles^{22,23} with a liquid core. There is no agreement on the exact composition of the micelle core: pure hydrocarbon, or hydrocarbon mixed with water and counterions. Viscosity data accommodate less than 20% water inside the core of sodium dodecyl sulfate micelles.²² More precise conclusions have been drawn in the previous sections from the specificity of surfactants and from free-energy considerations: no water at all inside the micelle core which comprises the alkyl chains, including the α -carbon groups, and even part of sufficiently hydrophobic head groups. This conclusion disagrees sharply with the widely held view that water penetrates between the alkyl chains into the micelle core at least as far as the β -methylene groups, or even considerably further. Examination shows that the foundations for this view are not particularly solid.

Corkill, *et al.*,²⁴ have measured the effects of micelliza-

tion on the partial molar volume of surfactants as a function of alkyl chain length, and concluded that in micelle formation the hydration of the methylene groups adjacent to the hydrophilic group is retained. This interpretation rests on the doubtful assumption that all volume changes at the micelle surface due to concentration of ionic charges and exposure of the hydrocarbon core surface are much less than 4 ml/mol of micellized surfactant.

Clifford²⁵ has concluded from spin lattice relaxation times of micellized hydrocarbon protons that part of the alkyl chains in the micelle is exposed to water. It is difficult to evaluate this conclusion because of the several implied assumptions concerning micelle lifetimes and statistical averaging near and at the micelle solution interface.

We now discuss some details of interpretation of several other spectroscopic papers^{6-8,26} which support models with water between the micellized alkyl chains.

Small-Angle X-Ray Scattering. Reiss-Husson and Luzati²⁷ first applied small-angle X-ray scattering to study the size and shape of micelles in surfactant solutions. On the basis of model calculations they conclude that in aqueous solutions of sodium dodecyl sulfate at 70° the scattering is consistent with spherical micelles that have a hydrocarbon core of 17 Å radius. This corresponds to about $n = 57$ monomers per micelle.

More recently Svens and Rosenholm²⁶ have investigated micelles of sodium octanoate under a variety of conditions, using essentially the scattering technique and interpretation of ref 27. In aqueous solution at 25° they calculate very small core radii, varying from 4.5 to 6.5 Å, and conclude that water penetrates substantially between the micellized hydrocarbon chains. In evaluating this conclusion it is noted that the X-ray interpretation is based on a simplified model. The authors^{26,27} assume a random distribution of monodisperse micelles, each of which is represented by a hydrocarbon core with a surrounding polar layer of different electron density. Such a stepwise distribution of electron density is unrealistic for the micelle surface and the ionic atmosphere. Moreover, there is mutual repulsion, and hence correlation, between the charged micelles. Perhaps the most questionable is the assumption of monodispersity of the micelles.

The original authors²⁷ well realized the possible shortcomings of the model, and discussed the difficulties in appropriate detail. In fact, they applied a test for monodispersity by calculating a micelle property related to scattering. This property appeared to remain reassuringly constant over a threefold change of concentration of dodecyl sulfate micelles. On the other hand, the data on sodium octanoate in the later work²⁶ fail even such an insensitive test: the calculated core radius increases from 4.5 to 6.5 Å when the octanoate concentration increases from 1 to 1.8 M. Such internal inconsistency renders this particular interpretation of the scattering data of sodium octanoate solutions unconvincing.

Fluorine Magnetic Resonance. Muller, *et al.*, have studied the chemical shift of the fluorine magnetic resonance in solutions of fluorinated surfactants.⁶⁻⁸ The concentration-dependent shift in aqueous solutions above the cmc is resolved in shifts of monomeric and micellar surfactant, δ_w and δ_m , respectively. It is found in all cases that, measured with respect to the same external standard, δ_m is between δ_w and δ_{hc} , the chemical shift in bulk hydrocarbon. "Mixing coefficients," defined as $Z = (\delta_m - \delta_w)/(\delta_{hc} - \delta_w)$, range from 0.51 to 0.59 for $\text{CF}_3(\text{CH}_2)_k \text{COONa}$, with $k = 8, 10$,

and 11, under various conditions of temperature and ionic strength.^{6,7} In the case of sodium perfluorooctanoate⁸ the values calculated from five different sets of fluorine shifts increase from $Z = 0.37$ for the α carbon, or C_2 , to $Z = 0.84$ for the C_8 fluorine. The simplest conclusion, drawn by the authors, is the water penetrates appreciably into the lipophilic core of the micelle.⁶⁻⁸ The disagreement with the conclusion drawn earlier in this paper, no water in the micelle core, cannot be resolved at the present time. We can only offer some possible explanations.

Although micelle sizes for the fluorinated surfactants were not reported, one expects micelle cores with a surface area between 50 and 65 Å² per monomer. This is two or three times the area in tightly packed monolayers. So a substantial portion of the micellized lipophilic chain must be situated at the core surface, in contact with water. One might well argue that in micelles of $CF_3(CH_2)_k COONa$ the CF_3 groups prefer the core surface. Fluorination of the terminal group increases the cmc, possibly because of the large dipole of the CF_3 group. The relatively large size of the CF_3 group might be an additional reason for its preferential location at the core-water interface. This would reconcile the low value $Z = 0.53$ for CF_3 with a water free micelle core. Furthermore, fluorination of the rest of the alkyl chain increases the value for the terminal CF_3 group from $Z = 0.53$ to $Z = 0.84$. This change might support the foregoing argument that fluorination changes the packing of the chain elements inside the core. Very recently, after completion of the present work, Mukerjee and Mysels have presented similar, but more elaborate, arguments in a discussion of some anomalies in the association behavior of partially fluorinated surfactants.²⁸

Finally, the quantitative relation between chemical shift and material properties has not yet been described in any satisfactory way. The relevant properties of the micelle core may well differ from those of bulk hydrocarbon. In fact at least one-third of a micelle core is within 2 Å from the core surface. This means that much of the micellar shift originates at a distance of one atomic diameter or less from the core-water interface. The influence of such an environment on δ_m is largely unknown.

Concluding Remarks

The basic assumptions implied in the present treatment are that all methylene groups in all surfactant ions under study have the same hydrophobic properties and that, at least for the head groups in Figure 2, the average location of the core-water interface is invariant with respect to the α -carbon atoms, that is, d is the same for all surfactants. Although these assumptions yield the simplest and most general micelle model, suitable modifications for particular head groups could explain the cmc data equally well. It will be very difficult to detect minor deviations from our as-

sumptions such as, for example, a somewhat more hydrophilic character of the α -methylene groups in compounds 2-5 in Figure 2 combined with a slightly smaller value of d . Further quantitative work on the pyridine compounds in Figure 5 might be illuminating.

Another point of concern is that all arguments are based on continuum theory, the existence of a shear surface in the rheological treatments, an abrupt change of dielectric constant at the core surface in the electrostatic model. The limits of applicability of these approximations have never been exactly established. In any detailed micelle model one surely operates close to such limits, or perhaps beyond. The only test seems to be the appearance of an incontrovertible inconsistency or contradiction with experiment.

Acknowledgment. The author is indebted to Dr. Robert E. Lundin for corrections in an earlier version of the section on nmr experiments, and to Dr. Karol J. Mysels for reading the manuscript.

References and Notes

- (1) D. Stigter, *J. Colloid Interface Sci.*, **47**, 473 (1974).
- (2) P. Mukerjee and K. J. Mysels, *Nat. Stand. Ref. Data Ser., Nat. Bur. Stand., No. 36* (1971).
- (3) P. Mukerjee, K. J. Mysels, and P. Kapauan, *J. Phys. Chem.*, **71**, 4166 (1967).
- (4) D. Stigter, *J. Phys. Chem.*, **68**, 3603 (1964).
- (5) P. T. Jacobs and E. W. Anacker, *J. Colloid Interface Sci.*, **44**, 505 (1973).
- (6) N. Muller and R. H. Birkhahn, *J. Phys. Chem.*, **71**, 957 (1967).
- (7) N. Muller and R. H. Birkhahn, *J. Phys. Chem.*, **72**, 583 (1968).
- (8) N. Muller and H. Simsohn, *J. Phys. Chem.*, **75**, 942 (1971).
- (9) L. Pauling, "The Nature of the Chemical Bond," Cornell University Press, New York, N.Y., 1960.
- (10) H. B. Klevens, *J. Amer. Oil Chem. Soc.*, **30**, 74 (1953).
- (11) R. A. Robinson and R. H. Stokes, "Electrolyte Solutions," Butterworths, 2nd ed, London, 1959, Chapter 1.
- (12) S. Levine, G. M. Bell, and B. A. Pethica, *J. Chem. Phys.*, **40**, 2304 (1964).
- (13) E. M. Kosower, *J. Amer. Chem. Soc.*, **80**, 3253 (1958).
- (14) E. M. Kosower and J. A. Skorcz, *J. Amer. Chem. Soc.*, **82**, 2195 (1960).
- (15) A. Ray and P. Mukerjee, *J. Phys. Chem.*, **70**, 2138 (1966).
- (16) P. Mukerjee and A. Ray, *J. Phys. Chem.*, **70**, 2144, 2150 (1966).
- (17) R. S. Mulliken, *J. Amer. Chem. Soc.*, **74**, 811 (1952); *J. Phys. Chem.*, **56**, 801 (1952).
- (18) P. Debye and E. W. Anacker, *J. Phys. Colloid Chem.*, **55**, 644 (1951).
- (19) L. M. Kushner, B. C. Duncan, and J. I. Hoffman, *J. Res. Nat. Bur. Stand.*, **49**, 85 (1952).
- (20) L. M. Kushner, W. D. Hubbard, and R. A. Parker, *J. Res. Nat. Bur. Stand.*, **59**, 113 (1957).
- (21) T. Sasaki and K. Shigehara, *Chem., Phys. Appl. Surface Active Subst., Proc. Int. Congr. Surface Active Subst.*, 4th, 1964, **2**, 585 (1967).
- (22) D. Stigter, *Chem., Phys. Appl. Surface Active Subst., Proc. Int. Congr. Surface Active Subst.*, 4th 1964, **2**, 507 (1967).
- (23) D. Stigter, *J. Phys. Chem.*, **70**, 1323 (1966).
- (24) J. M. Corkill, J. F. Goodman, and T. Walker, *Trans. Faraday Soc.*, **63**, 768 (1967).
- (25) J. Clifford, *Trans. Faraday Soc.*, **61**, 1276 (1965).
- (26) B. Svens and B. Rosenholm, *J. Colloid Interface Sci.*, **44**, 495 (1973).
- (27) F. Reiss-Husson and V. Luzzati, *J. Colloid Interface Sci.*, **21**, 534 (1966).
- (28) P. Mukerjee and K. J. Mysels, Presented at the 167th National Meeting of the American Chemical Society, Los Angeles, Calif., April 1974, Abstract No. Coll 107.

Oxidation of Titanium, Tantalum, and Niobium Films by Oxygen and Nitrous Oxide

Jalal M. Saleh* and Mohammed Hashim Matloob

Department of Chemistry, College of Science, University of Baghdad, Baghdad, Iraq (Received July 10, 1974)

Publication costs assisted by the University of Baghdad

The oxidation, by O_2 and N_2O , of evaporated metal films of Nb, Ta, and Ti has been studied in the temperature range 195–473 K. Fast dissociative adsorption of N_2O , which was accompanied by N_2 evolution, occurred on all the three metals at 195 K. At the latter temperature, some incorporation also occurred on Ti film, but the amount adsorbed on Nb was below that required to saturate the film surface with oxygen atoms. Oxygen adsorption on all three metals also took place rapidly at 195 K and the metals showed in general more tendency for oxygen adsorption through O_2 than N_2O . At temperatures ≥ 303 K, the oxidation reaction took place by either O_2 or N_2O with each film at a rate which depended both on the pressure of the reacting gas and the temperature of the metal film. The Ti film was the most, and Nb the least, active of the three metals for O_2 or N_2O oxidation. Both the activation energy (E) and the preexponential factor (A) increased as the extent of oxidation (X or Y) of each film increased so that the experimental rate remained almost constant, suggesting the operation of a compensation effect in the oxidation of the three films. The effect was likely to arise from a relationship between the heat and the entropy of adsorption, leading to a compensation between activation energy and entropy of activation (and hence the preexponential factor). Values of A and E were lower for O_2 adsorption on each film than for N_2O and this was ascribed to the higher heat of oxygen adsorption as compared with that of N_2O . On the other hand, values of A and E for the Ti film were in general smaller than the corresponding values for Ta and Nb films, such data are in parallel with the greater ease with which the oxidation of the Ti film occurred in comparison with the other two films.

Introduction

There have been quite a number of investigations on the interaction of N_2O with bulk metals, reduced powders, and metal filaments but mainly under high N_2O pressures or at elevated temperatures.^{1–4} With evaporated metal films, only a limited number of studies have so far been reported using N_2O gas. Isa and Saleh^{5–7} have studied the interaction of N_2O with films of Fe, Ni, W, Pd, and Pb over the temperature range 195–523 K. Adsorption of N_2O on these metals at 195 K occurred dissociatively with N_2 evolution. On Fe and Ni films, extensive oxidation took place at temperatures ≥ 303 K; a marked compensation existed between the activation energy and the preexponential factor of the oxidation process.

Metals Ti, Ta, and Nb of periodic groups IVa and Va are known to have strong tendencies for oxygen adsorption and the initial heats of oxygen adsorption on these metals were shown to be considerably higher than those on other transition metals.^{8–10} There is a need for a more fundamental investigation of oxygen adsorption to clean surfaces of such metals under controlled conditions of temperature and pressure. Nothing is known concerning the kinetics of the oxidation of the above-mentioned three metals at low pressures and in the temperature range 195–473 K; such data may be of considerable value in accounting for the behavior of the metals in oxidation reactions. It was also attempted to discern the different tendencies of the same three metals toward O_2 and N_2O and this was estimated on the basis of the kinetic data for the oxidation of the metals by either of the two gases.

Experimental Section

The apparatus, materials, and experimental techniques have been described.^{11,12} Metal films of Ti, Ta, and Nb

were prepared from 0.1-mm wire which was obtained from Johnson Matthey Chemicals Ltd. The glass apparatus and the metal filaments were degassed until the rate of degassing with the reaction vessel at 673 K was $<10^{-2}$ N m⁻² hr⁻¹. The evaporation currents were 0.6, 4.0, and 9.0 A for Ti, Nb, and Ta films, respectively, and the reaction vessel was kept open to the pumps throughout the degassing and the subsequent preparation and sintering of the film. Each film was sintered at 343 K for 20 min and, thereafter, its area was measured by krypton adsorption at 78 K. Nitrous oxide was prepared and purified as described before.⁵ Oxygen was obtained from cylinders, but it was further purified before use. Mixtures of N_2 + N_2O were analyzed by condensing the latter gas at 78 K and measuring the remaining pressure of N_2 ; the vapor pressure of N_2O at 78 K as measured by a McLeod gauge was $\sim 10^{-2}$ N m⁻², uncorrected for thermomolecular flow.

Results

The extents of N_2O and O_2 adsorption on each film were expressed in terms of X and Y as follows

$$X = V_{N_2O}/V_{Kr} \quad (1)$$

and

$$Y = V_{O_2}/V_{Kr} \quad (2)$$

where V_{N_2O} and V_{O_2} were the volumes of N_2O and O_2 adsorbed, respectively, and V_{Kr} was the volume of krypton monolayer on the film at 78 K; the volumes were measured in units of microliters (STP).

Because of the very little amount of nitrogen that was retained by a film subsequent to N_2O adsorption, it was reasonable to consider the value of X as a measure of either the coverage of the surface by oxygen atoms or alternatively, when incorporation occurred, of the thickness of the oxide

layer formed. Similarly, when molecular oxygen was used, the value of Y reflected either the coverage of the film surface or of the extent of oxidation in terms of the adsorbed oxygen molecules, the same amount of oxygen uptake may be expressed by a certain value of X or by $2Y = X$ assuming dissociative adsorption of oxygen in each case.

Adsorption of N_2O . The initial adsorption of N_2O on metal films of Nb, Ta, and Ti occurred rapidly (in <1 min) at 195 K to a final pressure of 10^{-3} N m $^{-2}$. Further adsorption of N_2O proceeded at a rate which decreased with increasing values of X . The process of adsorption was accompanied by the evolution of gaseous N_2 . The extent of N_2 desorption on Nb and Ta films was equivalent to that of N_2O adsorption; the total gas pressure always remained constant because one molecule of N_2 appeared in the gas phase for each N_2O molecule that underwent adsorption.

On the Ti film, less N_2 was desorbed than N_2O adsorbed particularly for relatively low values of X at 195 K, and this was reflected in the rapid decrease of the total gas pressure in the initial adsorption of N_2O on Ti film. This was clearly detected in the behavior of the first dose that was admitted to the clean Ti film. In the subsequent adsorption of N_2O which occurred at a measurable rate, there was a slow decrease in the total gas pressure with time as the reaction of N_2O with the film continued. Furthermore, the film of Ti was shown to be more reactive toward N_2O at 195 K than the other two metals, and this is seen in the final values of X (X_{max}) on the three films at this temperature as given in Table I. At such values of X (X_{max}), the rate N_2O uptake becomes $<10^{-4}$ μ l. sec $^{-1}$ cm $^{-2}$ under a gas pressure of 6 N m $^{-2}$ at 195 K.

Some N_2O desorption was observed when a Ti film which had adsorbed N_2O at 195 K to the extent $X_{max} = 4.9$ was warmed to 273 K; the amount desorbed represented only about 10% of the total gas adsorption at 195 K. Thereafter, adsorption of N_2O continued at 273 K at a rate which increased on heating the film to higher temperatures. Dissociative adsorption of N_2O , with complete desorption of N_2 , was the main feature of the N_2O interaction with each of the three metals at temperatures ≥ 303 K. The reaction became faster as the film was heated and, at any temperature, the total gas pressure remained virtually constant as N_2O was consumed at the same rate by which N_2 was desorbed; a typical example for such behavior is shown in Figure 1. At any temperature below 520 K, the Ti film remained the most active among the three metals used in this investigation toward N_2O , i.e., the rates of adsorption at 395 K, under the same pressure, on Nb, Ta, and Ti films were respectively 1.42×10^{11} , 1.46×10^{11} , and 4.2×10^{12} molecules sec $^{-1}$ cm $^{-2}$.

Adsorption of Oxygen. There was a fast instantaneous adsorption of oxygen on metal films of Nb, Ta, and Ti at 195 K. Above $Y = 0.6$, the adsorption occurred at a rate which became slower as Y increased. When the rate of uptake became $<10^{-3}$ μ l. sec $^{-1}$ cm $^{-2}$, the amounts of oxygen adsorbed (Y_{max}) were as given in Table II.

Further interaction took place at and above 303 K. The rate of oxidation increased on increasing the temperature of the film. Above 523 K, some desorption began to occur at an extremely slow rate.

Kinetics of N_2O and O_2 Adsorption

Pressure Dependence. The rate of N_2O or O_2 adsorption on Nb, Ta, and Ti films at any temperature greater than 273 K depended on the pressure of the reacting gas. The

TABLE I: Maximum Values of X (X_{max}) on Nb, Ta, and Ti films at 195 K

Film	X_{max}
Nb	0.82
Ta	1.80
Ti	4.90

TABLE II: Total Amounts of Oxygen Adsorption on Nb, Ta, and Ti films at 195 K

Film	X_{max}
Nb	1.14
Ta	2.00
Ti	2.61

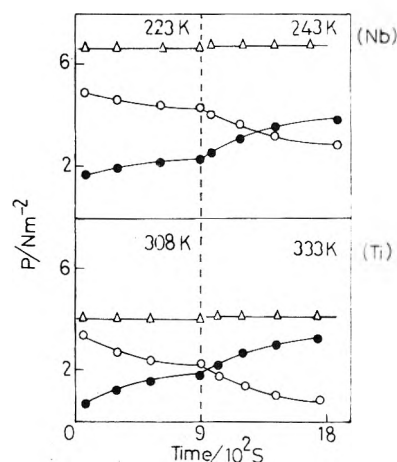


Figure 1. Interaction of N_2O with metal films of Nb and Ti at different temperatures: Δ , total pressure; O , N_2O pressure; \bullet , N_2 pressure.

rate of gas adsorption r_1 at an initial pressure P_1 was first determined, then the pressure was changed to P_2 at which the new rate r_2 was obtained. The dependence (n) of the rate on pressure was evaluated from the relation

$$(P_1/P_2)^n = r_1/r_2 \quad (3)$$

Values of n thus obtained, for the pressure range 1–8 N m $^{-2}$, were close to unity using either N_2O or O_2 . A check for the value of $n = 1$ was to plot $\log P_{gas}$ as a function of time for different films at several temperatures, typical plots of which are indicated in Figure 2.

Effect of Temperature. From the rate of N_2O (or O_2) adsorption at two different temperatures but virtually the same value of X (or Y), the activation energy of adsorption (E) was determined. Values of E for N_2O or O_2 adsorption on each metal film increased as X or Y increased as shown in Figure 3.

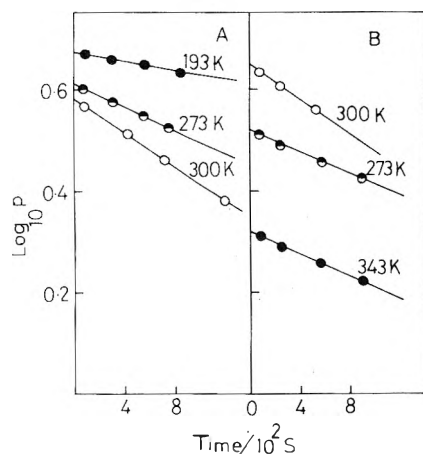
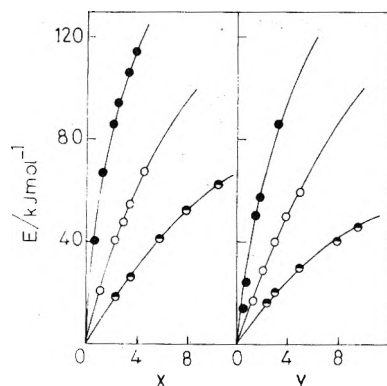
From the rate (r) of gas adsorption at a given temperature T , coverage X (or Y), and appropriate value of E , the value of the preexponential factor A in the Arrhenius type rate equation

$$(r)_{X \text{ (or } Y), T} = A \exp(-E/RT) \quad (4)$$

was obtained. From the values of A at various temperatures and values of X (or Y), the corresponding values of the entropy of activation (ΔS^*) were determined assuming a pressure dependence of $n = 1$. Table III shows that for approximately the same gas pressure (4–7 N m $^{-2}$) the values of A and ΔS^* increased as X (or Y) and E increased on each film so that the experimental rate remained almost constant. Figure 4 shows the relationship

TABLE III: Experimental Values of Activation Energy (E), Frequency (A), and Entropy of Activation (ΔS^*) at Various Values of X or Y on a Ti Film

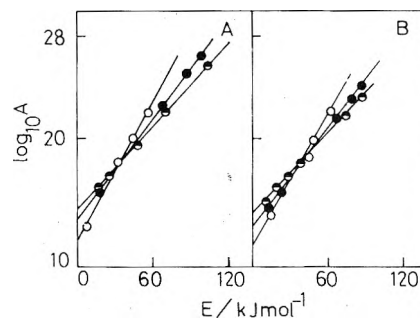
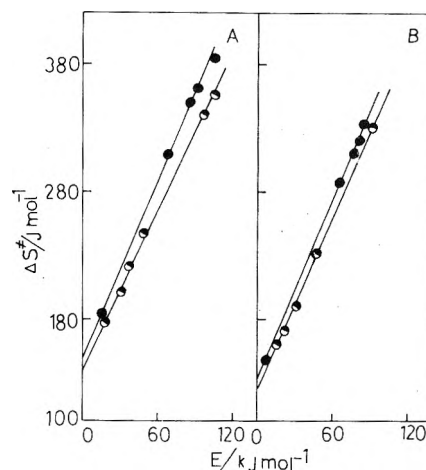
X	Temp, K	Rate, molecules $\text{sec}^{-1} \text{cm}^{-2}$	E , J mol^{-1}	A , molecules $\text{sec}^{-1} \text{cm}^{-2}$	ΔS^* , J mol^{-1}
4.90	273	3.8×10^{12}	18.30	1.1×10^{16}	177.67
7.85	303	1.8×10^{12}	46.65	4.4×10^{19}	246.21
9.41	328	3.4×10^{12}	69.53	5.7×10^{22}	300.88
13.68	393	3.9×10^{12}	106.64	5.33×10^{25}	354.78
Y					
5.08	273	1.53×10^{12}	20.87	4.26×10^{15}	170.17
8.14	308	1.40×10^{12}	30.00	7.89×10^{16}	192.50
9.04	393	1.65×10^{12}	45.07	7.71×10^{18}	233.50
14.79	393	1.28×10^{12}	90.84	1.30×10^{24}	331.67

**Figure 2.** First-order plots for the uptake of N_2O (A) and O_2 (B) on Nb (●), Ta (○), and Ti (◐) films at various temperatures.**Figure 3.** Activation energy (E) plotted against the extent of oxidation X and Y on films of Nb, Ta, and Ti. Symbols are as in Figure 2.

between $\log A$ and E and the variation of ΔS^* values with E is indicated in Figure 5. Values of A , E , and ΔS^* were obtained for each film at a given value of X (or Y) and the results were plotted in Figure 6.

Discussion

Adsorption at 195 K. Dissociative adsorption of N_2O occurred on Nb, Ta, and Ti films even at 195 K as almost all the N_2 of the adsorbed N_2O was desorbed at the same temperature. From the values of X_{max} in Table I one can conclude that surface saturation by oxygen atoms, resulting from the dissociative adsorption of N_2O , was not achieved on Nb film; the value of $X_{\text{max}} = 0.82$ suggests that the adsorbed oxygen atoms of N_2O was only sufficient to cover less than the half of the available surface sites assuming each krypton atom to occupy an area twice as large as the

**Figure 4.** Compensation effect in oxidation of Nb, Ta, and Ti films by N_2O (A) and O_2 (B) gases. Symbols are as in Figure 2.**Figure 5.** Variation of ΔS^* with E for N_2O (A) and O_2 (B) gases in interactions with Nb and Ti films.

oxygen atom. On the other hand, the value of $Y_{\text{max}} = 1.14$ on Nb at the same temperature (Table II) indicates a complete surface saturation by oxygen. The difference in behavior may arise from the higher heat of oxygen adsorption on Nb than of N_2O .

On the Ta film, the value of X_{max} was 1.8 and this value reflects the amount of adsorbed oxygen atoms that are almost sufficient for complete coverage of the film surface. On the same assumption, one would expect $Y_{\text{max}} = 2.0$ on Ta to involve lattice penetration by oxygen in addition to surface saturation. The difference in the heat of adsorption may also account for the different behaviors of the two gases on the same metal.

On the Ti film, the adsorption and incorporation occurred almost to the same extent using either N_2O or O_2 despite the fact that the value of $X_{\text{max}} = 4.9$ corresponded to slightly less oxygen uptake than that expressed by Y_{max}

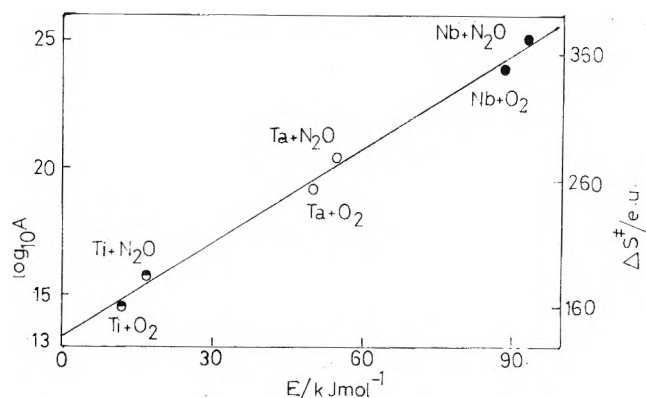


Figure 6. Compensation effect in the oxidation of Nb, Ta, and Ti films by N_2O (at $X = 2.3$) and O_2 (at $Y = 2.3$).

$= 2.6$. The small difference of about $2Y_{\max} - X_{\max} = 0.3$ may account for some nitrogen uptake⁸ in the initial adsorption of N_2O on the Ti film at 195 K in addition to the adsorbed oxygen atoms.

The reactivity of the three metals at 195 K toward the oxygen of the adsorbed N_2O or O_2 occurred in the sequence $Ti > Ta > Nb$. It has been shown⁹ that the initial heats of oxygen adsorption on metals of periodic group IV (as for Ti metal) are higher than on metals of other groups (i.e., Nb and Ta of group V). If the oxidation process involves migration and subsequent outward diffusion of the metal ions to contact the reacting gas, then such factors as the melting point and the ionic radius may be considered to be important in deciding the ease of oxidation; the Ti metal has the lowest melting point and the smallest ionic radius^{13,14} among the three metals used in this investigation. The Ti metal is known to crystallize with a different structure (cph) than that of Ta and Nb (bcc). These and other properties of Ti probably make this metal more favorable for oxidation by either N_2O or O_2 than the other two metals.

Uptake at ≥ 303 K. The results of Figure 4, relating $\log A$ to E , suggest the operation of a compensation effect^{15,16} which may be represented by the relation

$$\log A = UE + W \quad (5)$$

where U and W are constants. The compensation may arise¹⁷ from a relationship between the heat and the entropy of adsorption, and this leads to a compensation between the activation energy and the entropy of activation (and hence the preexponential factor).

The results in Figure 6 indicate a more general picture for the operation of the compensation effect in the oxidation of Nb, Ta, and Ti films by N_2O and O_2 gases. The points representing the oxidation of each metal by O_2 cor-

responded to lower values of $\log A$ and E , and hence to lower values of the entropy of activation, than the points representing the oxidation of the same metal by N_2O . Oxygen adsorption on each metal is likely to take place with a much higher heat of adsorption than that of N_2O . Entropy contributions arising from vibration or rotation of the adsorbed molecule are likely to be more restricted the greater the strength of adsorption; a proportionality between heat and entropy of adsorption is therefore expected. On the other hand, the activation energy of oxygen adsorption is expected to be less than that for N_2O adsorption. The relationship depicted in Figure 5 may suggest that the activated complex for N_2O or O_2 reaction with each metal becomes less restricted as the extent of oxidation increases.

The points representing the oxidation of Ti film by either N_2O or O_2 lie in general (Figure 6) lower than the corresponding points for the other two films. This may be accounted for on the basis of the heat of adsorption and certain other characteristic properties of Ti metal which have been referred to earlier in this work. Moreover, on comparison of the present results with those published previously,⁵ it was found that Ti was, under similar experimental condition, as reactive toward N_2O as Fe and Ni films; the same value of E on Ti, Fe, and Ni metals corresponded to almost the same value of $\log A$. The main difference confined in the fact that a given value of E for Ti film corresponded to a comparatively higher value of X than on Fe and Ni films. This probably assigns a higher reactivity to Ti metal than Fe and Ni. It has been found¹⁰ that the heat of dissociative chemisorption of oxygen increased as one moved from Ni toward Ti due to the some increasing trend in the covalent contribution to metal-oxygen bond formation.

References and Notes

- (1) N. N. Kavtaradze and E. A. Zelyaeva, *Dokl. Akad. Nauk. SSSR*, **172**, 1133 (1967).
- (2) R. M. Dell, F. S. Stone, and P. F. Tiley, *Trans. Faraday Soc.*, **49**, 201 (1953).
- (3) R. P. H. Gasser and C. J. Marsay, *Surface Sci.*, **20**, 116 (1970).
- (4) E. R. S. Winter, *J. Catal.*, **19**, 32 (1970).
- (5) S. A. Isa and J. M. Saleh, *J. Phys. Chem.*, **76**, 2530 (1972).
- (6) J. M. Saleh, *J. Chem. Soc., Faraday Trans. 1*, **68**, 1520 (1972).
- (7) J. M. Saleh, *J. Phys. Chem.*, **77**, 1849 (1973).
- (8) B. M. W. Trapnell, *Proc. Roy. Soc., Ser. A*, **218**, 566 (1953).
- (9) D. Brennan, D. O. Hayward, and B. M. W. Trapnell, *Proc. Roy. Soc., Ser. A*, **256**, 81 (1960).
- (10) Yu. A. Borison and N. N. Bulgacov, *Kinet. Katal.*, **11**, 720 (1970).
- (11) J. M. Saleh, M. W. Roberts, and C. Kemball, *Trans. Faraday Soc.*, **57**, 1771 (1961).
- (12) J. M. Saleh, *Trans. Faraday Soc.*, **64**, 796 (1968).
- (13) G. C. Bond, "Catalysis by Metals," Academic Press, New York, N.Y., 1962, pp 489-490.
- (14) J. E. Huheey, "Inorganic Chemistry," Harper and Row, New York, N.Y., 1972, pp 69-76.
- (15) E. Cremer, *Advan. Catal.*, **7**, 75 (1955).
- (16) C. Kemball, *Proc. Roy. Soc., Ser. A*, **217**, 376 (1953).
- (17) D. H. Everett, *Trans. Faraday Soc.*, **46**, 957 (1950).

Nitric Oxide and Carbon Monoxide Chemisorption on Cobalt-Containing Spinel

H. C. Yao and M. Shelef*

Scientific Research Staff, Ford Motor Company, Dearborn, Michigan 48121 (Received May 28, 1974)

Publication costs assisted by the Ford Motor Company

The chemisorption of nitric oxide and carbon monoxide was investigated on Co_3O_4 and other cobalt-containing normal spinels, such as CoAl_2O_4 and ZnCo_2O_4 . On Co_3O_4 the chemisorption of NO and CO is very similar, with that of the NO being somewhat stronger. Monolayer coverage by NO at 25° is attained at 500 Torr and by CO at 1000 Torr. The NO can coadsorb on a surface covered with preadsorbed CO. Preadsorption of NO prevents the coadsorption of CO. The uptake of NO and CO by ZnCo_2O_4 is the same as by Co_3O_4 . On the other hand, CoAl_2O_4 is almost totally inert for the adsorption. The divalent cobalt ions in CoAl_2O_4 were found by ion-scattering spectroscopy to be largely shielded from the surface. Chemisorption of CO on two crystallographic modifications of cobaltous oxide has shown that the CoO with the NaCl structure is active in chemisorption while the modification having the ZnS structure is not. It is concluded that it is the tetrahedral coordination of the cobaltous ions in CoAl_2O_4 that is responsible for their inactivity in chemisorption rather than their oxidation state.

Introduction

Studies of nitric oxide chemisorption on a series of transition metal oxides¹⁻⁵ and on platinum⁶ have been reported previously. This communication deals with the chemisorption of NO and CO on Co_3O_4 and other cobalt-containing spinels. The chemisorption behavior of this oxide is of particular interest on several accounts. First, this oxide is the most active of the base metals of the first transition series in the catalysis of oxygen-transfer reactions.⁷⁻¹⁰ Secondly, it rapidly becomes deactivated by the solid-state interaction with the most common catalyst support, Al_2O_3 .^{8,11} Thirdly, both the active oxide, Co_3O_4 , and the inactive product of its interaction with Al_2O_3 , CoAl_2O_4 (cobalt aluminate), have the same spinel structure. By examining the chemisorbing surfaces by ion-scattering spectroscopy and the chemisorbed species by infrared spectroscopy, along with the chemisorption measurements, some insight has been gained into the deactivation of Co_3O_4 by interaction with Al_2O_3 to form CoAl_2O_4 .

Since Co_3O_4 has a spinel structure ($\text{Co}^{2+}\text{Co}_2^{3+}\text{O}_4$), with the divalent and trivalent cobalt ions in differently coordinated sites within the crystal, one objective of this study was to elucidate whether these cobalt ions behave differently with respect to chemisorption and catalytic activity. The other cobalt-containing spinels, such as $\text{Co}^{2+}\text{Al}_2\text{O}_4$ and $\text{ZnCo}_2^{3+}\text{O}_4$, with cobalt ions of only one oxidation state and one type of coordination, were used in the chemisorption study for comparison with $\text{Co}^{2+}\text{Co}_2^{3+}\text{O}_4$.

Finally, carbon monoxide chemisorption measurements were also performed on two different samples of cobaltous oxide, one of the commonly observed NaCl structure, with the cobaltous ions in octahedral coordination, and the other of the zinc blende-wurtzite structure, with the cobaltous ions in the tetrahedral coordination.

Experimental Section

A. Adsorbents. Cobalt oxide (Co_3O_4) was prepared by precipitation from an aqueous $\text{Co}(\text{NO}_3)_2$ solution with ammonia. The solid was heated to 400° for 8 hr. The resulting black powder was examined by X-ray diffraction. It had a spinel crystalline structure without impurity lines and had

a BET area of approximately $20 \text{ m}^2/\text{g}$. CoAl_2O_4 was purchased from City Chemical Co. and was preheated to 800° in air prior to use. The heated sample had a BET area of $11 \text{ m}^2/\text{g}$.

ZnCo_2O_4 was prepared by dissolving ZnCO_3 and $\text{Co}(\text{NO}_3)_2$ in HNO_3 solution, using a 1% excess of Zn over the stoichiometric amount. This precaution was taken to assure that no excess of free Co_3O_4 would be present in the end product. The solution was evaporated to near dryness and heated to 400° for 8 hr. The sample was then degassed under vacuum at 800° for 3 hr. The BET area of the sample was $6.2 \text{ m}^2/\text{g}$. Both CoAl_2O_4 and ZnCo_2O_4 were examined by X-ray diffraction and showed a spinel crystalline structure.

ZnO was prepared by the decomposition of ZnCO_3 (Allied Chemical, reagent grade) at about 400° and degassed under vacuum at 400° for 3 hr. The BET area was $19.3 \text{ m}^2/\text{g}$.

The cobaltous oxide of the usual NaCl structure was prepared by the decomposition of CoCO_3 *in vacuo* at 300° for 5 hr and further degassed at 400° for 3 hr.

The CoO with the zinc blende-wurtzite structure was prepared by decomposition of cobalt acetate *in vacuo* at 280° for 20 hr according to the procedure of Redman and Steward.¹² X-ray patterns of the CoO confirmed a zinc blende (3H) structure with minor wurtzite (2H) stacking.

B. Adsorbates. Nitric oxide was purified by several freezing-evaporation cycles and two-thirds of the middle fraction was used in the chemisorption experiments.¹ CP grade carbon monoxide and ultra-pure grade argon (99.9% minimum) were used without further purification.

C. Execution of Measurements. The volumetric measurements were performed in a conventional constant volume adsorption apparatus equipped with a precision pressure gauge linked with a fused quartz Bourdon capsule having a pressure range of 0-1000 Torr (Texas Instruments, Model 145). The mass spectrometric analyses of the gas phase above the adsorbent were carried out by a CEC-614 mass spectrometer equipped with a batch-inlet system and operating at a pressure of 0.1 Torr at the high-pressure side of the gold leak of the analyzer. The infrared spectra were taken with a Perkin-Elmer Model 180 spectrometer.

The ion-scattering spectra were taken by a 3M ion scattering spectrometer using a beam of He^+ ions accelerated to 1000 eV from a static atmosphere of helium at a pressure of 6×10^{-5} Torr.

For the adsorption measurements, the adsorbents were further degassed under vacuum (10^{-5} Torr) at 400° for 3 hr. For the ir measurements, the black powder was pressed in a steel die at a pressure of 20–30 tons/in.² into a wafer-thin, self-supporting disk with a diameter of 15 mm and weighing approximately 50 mg. A sample disk was hung from a quartz carriage with a platinum wire and then placed into a quartz cell similar to that used by Goodsel.¹³ The carriage was manipulated magnetically, placing the sample into a heating zone when degassing at high temperature, or placing it into a cylindrical cell, equipped with NaCl windows, to be inserted into the ir spectrometer operating at room temperature. Before the adsorbates were introduced into the ir cell, the Co_3O_4 sample was degassed at 550° for about 8 hr. To remove a given adsorbate from a pressed disk sample the latter was degassed for 2 hr at 400° .

Samples of cobaltous oxide were handled only under vacuum or in the atmosphere of the CO adsorbate, since the compound is known to undergo spontaneous oxidation in air to Co_3O_4 . For the same reason cobaltous oxide is unsuitable as an adsorbent for NO.

D. Reproducibility of the Adsorption Measurements. Repeated adsorption of NO on all the adsorbents gave reproducible results, indicating that the degassing procedure at 360° and 10^{-6} Torr, which was employed, restored the surface to the original state. The surface shrinkage engendered by this treatment was within the experimental uncertainty of about 5% for an entire series of measurements carried out at a given temperature.

Similar reproducibility was not at first obtained with CO. The uptake of CO decreased in successive adsorption runs, despite degassing by the above procedure between runs. This was judged to be due to the oxygen depletion of the surface during CO desorption at 400° . To correct this, a reoxidation step was used between successive adsorption runs. The adopted procedure consisted of degassing, reoxidation by admission of O_2 at room temperature, and repeated degassing. After such treatment, the sample adsorbed the same amount of CO under identical adsorption conditions.

Results

A. Adsorption Isotherms on Co_3O_4 . The adsorption isotherms for NO and CO on Co_3O_4 at 25° obtained from the volumetric measurements are shown in Figures 1a and 1b, respectively. In both figures, curve A gives the total uptake; curve C the uptake on a surface degassed at 25° after the first adsorption; and curve B the difference between curves A and C. We consider the adsorption associated with curves B and C to be, respectively, the irreversible and reversible parts of the total coverage. As the data in Table I indicate, while the total and irreversible adsorptions decrease for both NO and CO with increasing temperature, the reversible adsorption of NO increases and that of CO decreases with increasing temperature. θ_{NO} is slightly higher than θ_{CO} . The data from Figure 1 are replotted on Figure 2, together with those at other temperatures, in the form of a Freundlich isotherm

$$q = cp^{1/n} \quad (1)$$

TABLE I: Surface Coverage^a of Unsupported Co_3O_4 at 60 Torr Adsorbate Pressure in the 0 – 100° Temperature Range

Adsorbate	$T, ^\circ\text{C}$	θ_t	θ_r	θ_{ir}
NO	0	0.87	0.15	0.72
	25	0.75	0.21	0.54
	100	0.70	0.31	0.39
CO	0	0.79	0.25	0.54
	25	0.67	0.23	0.44
	81	0.58	0.16	0.42

^a θ_t = total coverage; θ_r = reversible part; θ_{ir} = irreversible part.

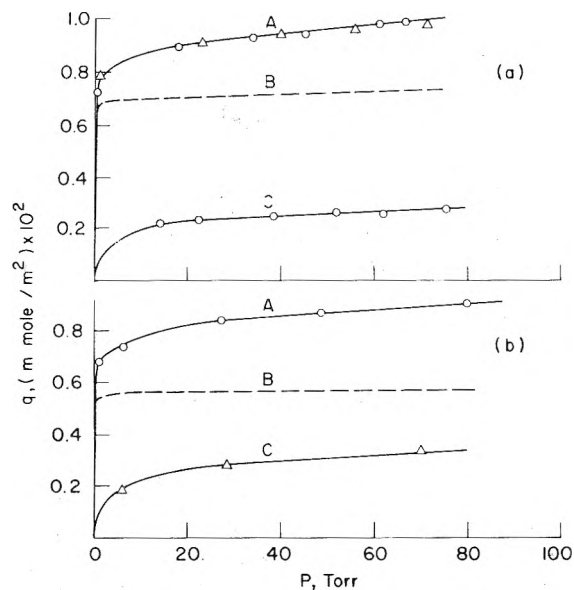


Figure 1. Adsorption isotherms for (a) NO and (b) CO on Co_3O_4 at 25° : A, total uptake; B, irreversible part; C, reversible part. (In a–A, O and Δ are data from two Co_3O_4 samples.)

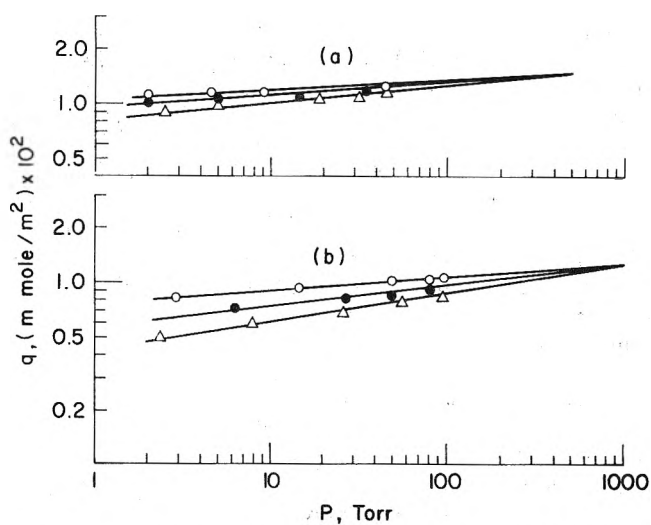


Figure 2. Freundlich Isotherms for (a) NO at 0° (O), 25° (●), and 100° (Δ) and (b) CO at 0° (O), 25° (●), and 81° (Δ) on Co_3O_4 .

In eq 1 q (in mmole per m^2 of area) is the amount of NO or CO adsorbed on the surface and c and n are temperature dependent parameters. The values of c and n are tabulated in Table II. The extrapolation of the straight lines in Figure 2 to the point of intersection gives the monolayer coverage.^{1–4} This amount for both NO and CO is $13 \mu\text{mol}/\text{m}^2$,

TABLE II: Parameters of Freundlich Isotherms for NO and CO Adsorption on Unsupported Co_3O_4

Adsorbate	CO			NO			
	$T, ^\circ\text{K}$	273	298	354	273	298	373
n		12.90	9.75	7.12	19.2	16.0	12.0
$C, \text{mmol/m}^2$		0.00768	0.00634	0.00482	0.0103	0.0076	0.0066
$H_m = nRT/(1 - rT),$ cal/mol		13,000	11,800	12,600	13,800	13,000	13,400
r		1.7×10^{-3}			0.9×10^{-3}		

which is equivalent to an area of 12.8 Å² occupied by one molecule of the adsorbate. As in the case of NiO,³ a higher pressure is required for the monolayer coverage by CO than by NO. These pressures are ~1000 and ~500 Torr, respectively, for the CO and NO on Co_3O_4 as seen in Figure 2.

The logarithmic, refined, form of eq 1 is given by

$$\log q = \log q_m + \frac{RT}{H_m(1 - rT)} \log a_0 + \frac{RT}{H_m(1 + rT)} \log p \quad (2)$$

where r is an adjustable parameter introduced by Halsey¹⁴ to correct for small changes of H_m with temperature so that

$$H_m = nRT/(1 - rT) = \text{constant} \quad (3)$$

Values of H_m and r are also included in Table II. Taking into account the logarithmic change of adsorption heat as a function of surface coverage, inherent in the Freundlich isotherm

$$H_\theta = H_m \ln \theta \quad (4)$$

and using the values of H_m from Table II, the relationship between H_θ and θ is given in Figure 3 for both NO and CO. The experimental points represent the values obtained directly by applying the Clausius-Clapeyron equation to the data of Figure 2. These could be calculated only at $\theta > 0.55$.

B. Coadsorption of NO and CO on Co_3O_4 (Volumetric Results). In order to study the effect of preadsorbed CO on the chemisorption of NO (and vice versa) on Co_3O_4 , the adsorption isotherms of CO and NO were followed in two sequential experiments. In each sequence, one of the gases was chemisorbed first at 25° and then degassed at the same temperature to pump-off the reversible portion of the adsorption. The sample was then contacted at 25° with the other gas. The results, shown in Figure 4a, indicate that there is little change in the amount of total reversible and irreversible NO chemisorption on a Co_3O_4 surface covered with preadsorbed CO, when compared with the adsorption on the "clean" Co_3O_4 (Figure 1a). These results indicate that the NO and CO can coadsorb when the sequence of contact is CO first and NO thereafter.

A different picture prevails when the order of adsorbents is reversed. The amount of CO taken up on a surface covered with the irreversible part of NO adsorption is much less (Figure 4b) than on a clean surface (Figure 1b). In addition the major part of the CO is reversibly adsorbed. It appears as though the reversibly adsorbed CO is accommodated on the sites vacated when the reversible part of NO was pumped off, while the irreversible part represents coadsorption. Comparison of Figures 4a and 4b indicates that coadsorption is much smaller when the adsorption order is NO first, followed by CO.

In order to assess to what extent there is surface interaction taking place at room temperature during successive (CO → NO, NO → CO) or simultaneous (NO + CO) chemisorption experiments, the gas composition was monitored

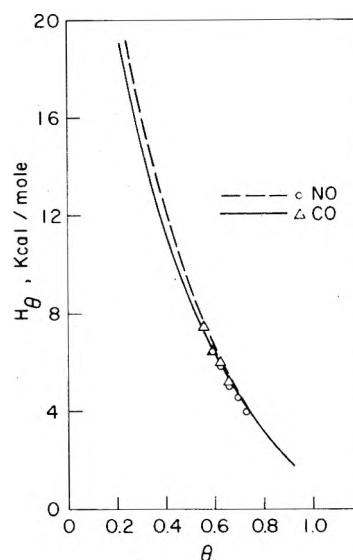


Figure 3. Variation of H_θ with θ from $H_\theta = -H_m \ln \theta$. Experimental points calculated from Figure 2.

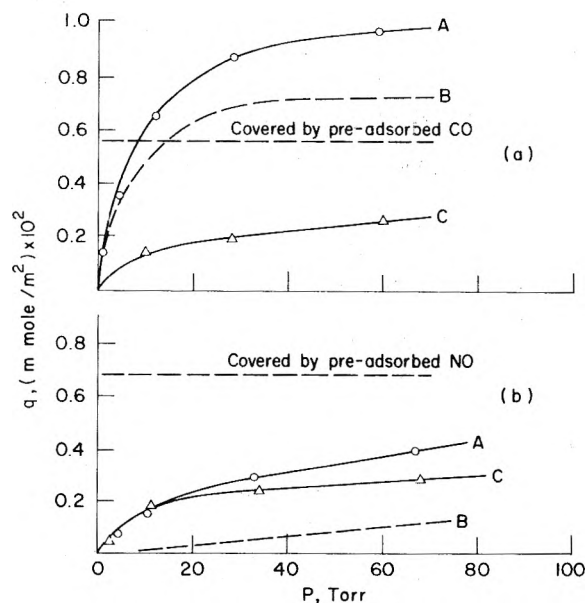


Figure 4. (a) NO adsorption isotherm at 25° on Co_3O_4 with preadsorbed CO; (b) CO adsorption isotherm at 25° on Co_3O_4 with preadsorbed NO: A, total uptake; B, irreversible part; C, reversible part.

mass spectrometrically in separate runs in which a large sample of the adsorbent was contacted with the adsorbates. The mass-spectrometric analyses did reveal, in the gas phase, the products of interaction between NO and CO, even at room temperature, such as N_2 , N_2O and CO_2 . However, it has also shown that the extent of these reactions is confined to a very small fraction of the chemisorbed layer, ~1% of the surface. It can be added that the coadsorption

of NO on a CO-covered surface caused some very minor displacement of the CO into the gas phase. There was no displacement observed in the reverse order of adsorption. While the predominant product of NO reduction in successive adsorptions was N_2O , in the simultaneous coadsorption it was N_2 .

C. Adsorption of NO and CO on $\text{Co}^{2+}\text{Al}_2\text{O}_4$ and $\text{ZnCo}_2^{3+}\text{O}_4$. Adsorption isotherms were taken for these adsorbents with NO and CO at 25° . In order to ascertain what is the uptake of these adsorbates on Al^{3+} and Zn^{2+} ions in the lattice, blank runs were made on $\alpha\text{-Al}_2\text{O}_3$ and ZnO. The results are given in Table III where it is seen that (a) very little adsorption occurs on ZnO or $\gamma\text{-Al}_2\text{O}_3$, (b) almost identical uptake of NO or of CO by $\text{Co}^{2+}\text{Co}_2^{3+}\text{O}_4$ and $\text{ZnCo}_2^{3+}\text{O}_4$ takes place, and (c) the uptake on $\text{Co}^{2+}\text{Al}_2\text{O}_4$ is only about 5% of the uptake on the other two cobalt-containing spinels.

D. Adsorption of CO on Cobaltous Oxide. Since it was noted that CoAl_2O_4 , in which the cobalt is present as cobaltous ions in the tetrahedral position, is almost inactive for the chemisorption of NO or CO, it became of interest to find out whether this behavior is associated with the oxidation state of the cobalt ion or with its coordination number within the structure of the solid. As seen in Table III, the chemisorption of CO on the CoO with the NaCl structure is only somewhat less than that noted on the Co_3O_4 , while the chemisorption on the CoO with the ZnS structure is almost identical with the small uptake on CoAl_2O_4 .

E. Surface Examination by Ion-Scattering Spectrometry. The evaluation of the spinel surfaces by ion-scattering spectrometry (ISS)¹⁵ affords a direct means for the detection of certain ions in the outermost layer. It has been shown that the method is sensitive to the first average atomic surface layer. According to Goff,¹⁵ the identification of surface atoms can be accomplished through measurements of the energy spectra of scattered binary noble gas ions at a given scattering angle. The energy spectra consist of a number of peaks at various energies; the number of peaks corresponds to the number of constituents present in the surface under examination and the energy corresponds uniquely to the mass of each constituent. Within a first approximation, the height of each peak gives a relative measure of the quantity of each constituent present.

In Figure 5 the ion-scattering spectrum of CoAl_2O_4 is presented. The spectrum was taken using He^+ ions of relatively low energy (1000 eV) to minimize the disturbance of the surface layer. As seen in Figure 5, initially the peak associated with Co is not discernible above the background noise. This indicates that on the surface of CoAl_2O_4 the Co ions are absent. As the surface layers are sputtered away in successive scans the Co peak appears in the spectrum. It is plausible to assume that the spectrum after 10 min of He^+ bombardment is representative of the bulk composition of CoAl_2O_4 .

The application of ISS to the examination of the surfaces of complex oxides, which serve as catalysts, will be the subject of a more detailed publication.¹⁶

F. Ir Study of Coadsorption of NO and CO on Co_3O_4 . Ir spectra of coadsorbed NO and CO on Co_3O_4 were taken in two sequential experiments. In each sequence, after the ir spectrum of the "clean" sample was recorded, Co_3O_4 was contacted with one of the gases at 25° and then degassed at room temperature to pump off the reversible portion of the adsorption and a second ir spectrum of the sample was recorded. The sample was then exposed to the second gas at

25° and degassed at room temperature; then the third ir spectrum was taken. These ir spectra are shown in Figure 6. Spectrum 6a-A is that of "clean" Co_3O_4 ; 6a-B is the spectrum after CO adsorption. The broad bands at 1600, 1545, 1370, 1325, and 1135 cm^{-1} were identified by Goodsell¹³ and Hertl¹⁷ as associated with monodentate and bidentate carbonate groups on the surface. The weak band at 2070 cm^{-1} was assigned to the weakly adsorbed CO which can be removed by prolonged pumping. The coadsorption of NO (at 10 Torr) introduces two new bands at 1860 and 1780 cm^{-1} . Since the ir band of gaseous NO is at 1878 cm^{-1} and the NO bands in cobalt nitrosyl compounds are observed at 1859 and 1790 cm^{-1} ,¹⁸ these bands at the surface can be assigned to NO groups covalently or coordinatively bonded to the surface. The carbonate bonds are not significantly affected by the NO coadsorption.

The reversal of the sequence of adsorption (NO first, followed by CO) produces the spectra of Figure 6b. Exposure of an NO-covered surface to 10 Torr of CO suppresses the NO bands somewhat. The existence of the carbonate bands in spectrum 6b-C is due to the incomplete coverage in the preadsorption by NO. An incipient band appears at 2190 cm^{-1} , which is, as noted below, a product of the surface interaction of the coadsorbed molecules.

The 300° temperature treatment of the Co_3O_4 disk by a mixture of CO and NO results in the spectrum 6c-B, which is characterized by a stronger band at 2190 cm^{-1} and broader bands at the lower frequencies assigned to the surface carbonates.

Bands resulting from the CO-NO interaction in this region of the spectrum have recently been identified as associated with surface isocyanate groups. Thus, London and Bell¹⁹ have assigned a band at 2200 cm^{-1} , observed on copper oxide catalyst after the CO-NO reaction at $135\text{--}200^\circ$, to Cu^+NCO . Unland²⁰ has assigned bands at 2267 and 2148 cm^{-1} to isocyanate surface intermediates, formed by the interaction of CO and NO on noble metal catalysts. Following these authors we similarly assign the band at 2190 cm^{-1} to a surface -NCO group.

Discussion

The chemisorption behavior of NO and CO on Co_3O_4 falls into the same general pattern observed in the case of other transition metal oxide adsorbents.

The differences between the chemisorption parameters for the two adsorbates on Co_3O_4 are much narrower than noted previously on NiO .³ There is no difference between the limiting NO and CO monolayer coverages on pure Co_3O_4 ; $13\text{ }\mu\text{mol/m}^2$ (BET) or 7.8×10^{18} molecules/ m^2 (BET). The NO chemisorption is somewhat stronger as judged from the pressures needed to attain monolayer coverage.

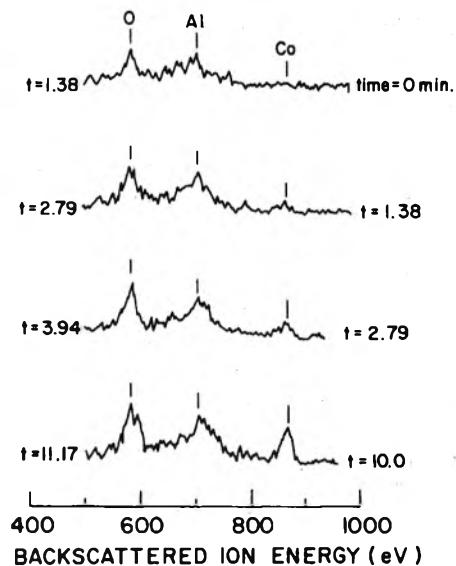
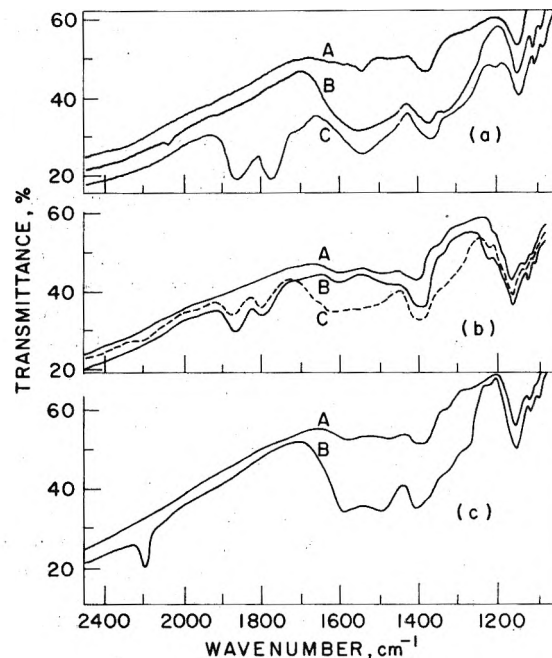
Heats of adsorption of NO and CO differ only slightly on Co_3O_4 . It is interesting to note that among the metal oxides of the first transition series the highest heats of NO chemisorption are found in the spinel oxides, Co_3O_4 and Fe_3O_4 . The H_m values for these two adsorbents are respectively 13.4 and 16.5 kcal/mol. The last value has been corrected upward from the previously published 10.5 kcal/mol² by applying the Halsey¹⁴ correction, not employed in the original publication.

The monolayer of 7.8×10^{18} molecules/ m^2 (BET) for Co_3O_4 is at the upper end of the monolayer coverages as measured on the series of transition metal oxides.

The salient point of the investigation is the almost com-

TABLE III: Surface Coverage of Co-Containing Spinel, CoO, ZnO, and α -Al₂O₃, at 60 Torr Adsorbate Pressure at 25°

Adsorbents	NO			CO		
	θ_t	θ_r	θ_{ir}	θ_t	θ_r	θ_{ir}
ZnCo ₂ O ₄	0.78	0.21	0.57	0.58	0.18	0.40
CoAl ₂ O ₄	0.03	0.025	0.005	0.03	0.02	0.01
Co ₃ O ₄	0.75	0.21	0.54	0.67	0.23	0.44
CoO (NaCl)				0.40	0.07	0.33
CuO (ZnS)				0.03	0.02	0.01
ZnO	0.004	0.003	0.001	0.005	0.004	0.001
α -Al ₂ O ₃	0.003	0.002	0.001	0.004	0.004	0.000
γ -Al ₂ O ₃	0.003	0.002	0.001	0.004	0.003	0.001

**Figure 5.** Ion scattering spectra of CoAl₂O₄ in successive scans.**Figure 6.** Ir spectra of NO and CO chemisorption on Co₃O₄: (a) sequential chemisorption of CO followed by NO at 25°; (b) sequential chemisorption of NO followed by CO at 25°; (c) simultaneous contact of NO and CO at 300°.

plete correspondence of the chemisorption between Co₃O₄ and ZnCo₂O₄ on the one hand and the almost complete absence of chemisorption on CoAl₂O₄. All three adsorbents were chosen to be normal spinels, in which the divalent ions are in the tetrahedral positions in the lattice and the trivalent in octahedral. It is to be noted that a certain degree of randomness, expressed by the subscript x in the overall spinel formula (A_{1-x}B_x)[A_xB_{2-x}]O₄, is present in every case. In the above formula A represents the divalent ion, B the trivalent ion, the parentheses the sites of tetrahedral coordination, and the brackets sites of octahedral coordination. In a normal spinel $x = 0$, in an inverse one $x = 1$; at $x = \frac{2}{3}$ the spinel structure is completely randomized.

Since the Zn²⁺ ion has the largest tetrahedral preference,²¹ x for ZnCo₂O₄ is very small. In Co²⁺Co₂³⁺O₄ (Co₃O₄) the distribution is also normal.²² In the aluminate spinel CoAl₂O₄ there is a certain tendency for the divalent Co²⁺ to occupy the octahedral positions, but the value of x does not exceed 0.1,²¹ at temperatures below 850°^{23,24} because the preference of the Al³⁺ ions for these positions is substantially larger.²¹

The chemisorption results on Co₃O₄ and ZnCo₂O₄ indicate unambiguously that trivalent cobalt ions in octahedral sites chemisorb NO and CO. Divalent cobalt ions in tetrahedral sites do not chemisorb at all, or only very slightly, as shown by the chemisorption on CoAl₂O₄.

Since divalent cobalt ions in octahedral sites, such as are present in the cobaltous oxide with the NaCl structure, do

chemisorb CO, we have to discard as the reason for the inability of the CoAl₂O₄ to chemisorb, the fact that the cobalt ions present therein are divalent. The coverage on CoO is less than on Co₃O₄. This is to be expected, as it is known that the complex-forming ability of the cobaltous ion, which is analogous to chemisorptive ability, is much lower than that of the cobaltic ion.²⁵ On the other hand, the chemisorption behavior of the tetrahedral cobaltous oxide was identical with that of the cobalt aluminate. This is a strong indication that it is the tetrahedral coordination of the cobaltous ion in both cases which is primarily responsible for the absence of chemisorption.

The lower catalytic activity of the metal ions in tetrahedral positions in spinel catalysts has recently been the subject of many investigations. It was noticed first, by Schwab and coworkers,²⁶ for the oxidation of CO. Erofeev²⁷ has shown this general behavior in cyclohexane dehydrogenation over Cu-containing spinels, and Cimino, *et al.*,²⁸ in N₂O decomposition.

It is logical to assume that the relative inability of the metal ions in tetrahedral sites in normal spinels to chemisorb the reactants underlies this behavior.

After it was demonstrated that the divalent cobalt ions do not chemisorb the adsorbates, it was surprising to ob-

serve coverages of NO and CO for Co_3O_4 larger than for the metal oxides studied previously. If the surface composition reflects the bulk composition, one third of the cobalt surface sites were expected to be of the inactive tetrahedral kind, which should have resulted in lower NO (or CO) uptake per m^2 of BET area. The examination of CoAl_2O_4 by ISS has shown that the cobalt is initially not present on the surface (Figure 5). If, by analogy, the same holds true for Co_3O_4 and only Co^{3+} ions are present on the surface, the above discrepancy is explained. Ion-scattering spectrometry is sensitive only to the mass of the surface scatterer and cannot differentiate directly between the cobalt of different coordination or valence in Co_3O_4 .

We should note that we have previously reported the chemisorption of NO on CuAl_2O_4 .⁴ Indeed, the ISS examination of this surface has shown the presence of copper ions on the surface. It should be pointed out that the copper ions in the copper aluminate spinel are randomly distributed with $x = 0.6$.²¹ At the present the generalization that in all spinels the tetrahedral sites are shielded from the surface is not warranted. This subject and its wider implications for the catalytic activity of spinels will be treated separately.¹⁶

The spinel lattice and the atomic layers in the $\langle 100 \rangle$ direction are shown in Figure 7. It appears that, at least, in CoAl_2O_4 , the layers containing the anions and the trivalent cations ($1/8$, $3/8$, and so on) are preferentially exposed on the surface.

Replacement of one adsorbate by the other was not observed in either ir spectra or the volumetric chemisorption data. From the quantitative volumetric measurements of the chemisorption, it becomes clear that, while the access of NO to the CO-covered Co_3O_4 surface is not impeded (Figure 4a), the reverse sequence of chemisorption substantially blocks the access of the CO molecules to the surface of Co_3O_4 .

A phenomenological explanation for this behavior can be provided by the following reasoning. We take, as the adsorbing surfaces in Co_3O_4 , the $1/8$ and $3/8$ atomic planes of Figure 7. The adsorption of CO is pictured schematically in Figure 8a. In accordance with the findings of Goodsel¹³ and Hertl¹⁷ we assume coordination of the CO molecules on the surface through the oxygen anions as surface carbonates. However, the presence of the trivalent Co ions is essential since there is no CO chemisorption on CoAl_2O_4 . The formation of surface carbonates as shown on Figure 8a does not block the subsequent accommodation of the NO molecule. This is shown diagrammatically in Figure 8b, where the chemisorption of NO is assumed to result in the transfer of the electron in the antibonding orbital of NO to the cobalt ion, and the formation of surface nitrosonium ions.²⁹

The reversal of this sequence results, first, in the formation of a positively charged surface nitrosonium ion layer which interacts with the surrounding oxygen anions by electrostatic attraction. The previous studies of the exchange of oxygen in the NO molecules with the surface oxygen in transition metal oxides³⁰ indicate that the chemisorption of NO on oxides results in the formation of surface species which are coordinated both to the transition metal ion and to the oxygen anions. Apparently the stabilization of the oxygen ions on the surface by such interaction is sufficient to prevent the subsequent coordination of the CO to form the surface carbonates.

Note Added in Proof: Dianis and Lester³¹ have recently concluded from the X-ray photoelectron spectra of Co_3O_4

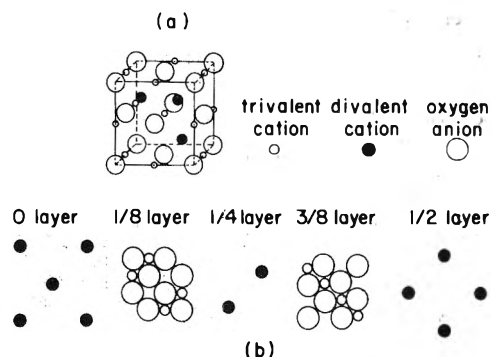


Figure 7. (a) One-eighth of a spinel lattice unit cell. (b) Atomic layers in the $\langle 100 \rangle$ direction.

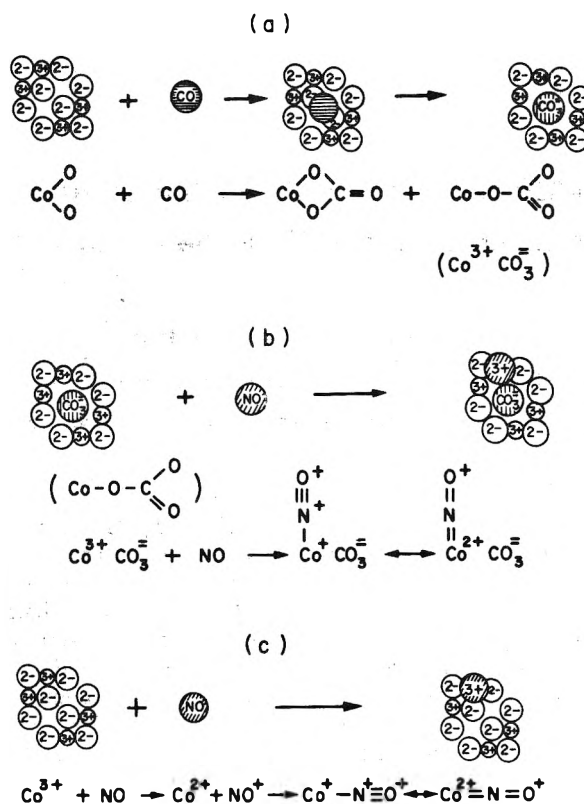


Figure 8. Schematic representation of adsorption on closely packed spinel surfaces: (a) CO on bare surface, (b) NO on CO-covered surface, (c) NO on bare surface.

surfaces that the cobaltous ions are the only species on the surface, which conclusion is exactly opposite to that reached in this paper for cobalt aluminate and implied for Co_3O_4 . Their conclusion was reached by the comparison of the spectra of CoO and Co_3O_4 surfaces which were identical and the assumption that the first surface exposes only cobaltous ions. We think that this assumption was erroneous, since cobaltous ions are unstable in air and it is well known that the surface layer of CoO is oxidized to Co_3O_4 (see last paragraph under "Execution of Measurements" in this paper). Hence, the identity of the spectra obtained by Dianis and Lester reinforces our conclusions.

Acknowledgment. We wish to thank M. A. Z. Wheeler for the ISS spectra and C. Kelly for the X-ray spectra of the adsorbents. Paul Wynblatt suggested the use of ISS for the examination of the spinel surface.

References and Notes

- (1) K. Otto and M. Shelef, *J. Catal.*, **14**, 226 (1969).
- (2) K. Otto and M. Shelef, *J. Catal.*, **18**, 184 (1970).
- (3) H. S. Gandhi and M. Shelef, *J. Catal.*, **24**, 241 (1972).
- (4) H. S. Gandhi and M. Shelef, *J. Catal.*, **28**, 1 (1973).
- (5) H. C. Yao and M. Shelef, *J. Catal.*, **31**, 377 (1973).
- (6) K. Otto and M. Shelef, *J. Catal.*, **29**, 138 (1973).
- (7) G. K. Boreskov, *Discuss. Faraday Soc.*, **41**, 263 (1960).
- (8) Y.-F. Y. Yao, *J. Catal.*, **33**, 108 (1974).
- (9) Y. Moro-oka, Y. Morikawa, and A. Ozaki, *J. Catal.*, **7**, 23 (1967).
- (10) K. C. Stein, T. T. Feenan, G. P. Thompson, J. F. Shults, L. T. E. Hofer, and P. B. Anderson, *Ind. Eng. Chem.*, **52**, 673 (1960).
- (11) (a) H. Schachner, *Cobalt* **No. 2**, 37 (1959); (b) **No. 9**, 12 (1960).
- (12) M. T. Redman and E. G. Steward, *Nature (London)*, **193**, 867 (1962).
- (13) A. T. Goodsel, *J. Catal.*, **30**, 175 (1973).
- (14) G. Halsey, *Advan. Catal.*, **4**, 295 (1952).
- (15) R. F. Goff, *J. Vac. Sci. Technol.*, **10**, 355 (1973).
- (16) M. Shelef, M. A. Z. Wheeler, and H. C. Yao, submitted for publication.
- (17) W. Hertl, *J. Catal.*, **31**, 231 (1973).
- (18) W. Hieber and A. Jahn, *Z. Naturforsch.*, **13b**, 195 (1958).
- (19) J. W. London and A. T. Bell, *J. Catal.*, **31**, 96 (1973).
- (20) M. L. Unland, *J. Phys. Chem.*, **77**, 1952 (1973).
- (21) A. Navrotsky and O. J. Kleppa, *J. Inorg. Nucl. Chem.*, **29**, 270 (1967).
- (22) P. Cossee, *Recl. Trav. Chim. Pays-Bas*, **75**, 2089 (1956).
- (23) H. Schmalzried, *Z. Phys. Chem. (Frankfurt am Main)*, **28**, 203 (1961).
- (24) H. Furuhashi, M. Inagaki, and S. Naka, *J. Inorg. Nucl. Chem.*, **35**, 3009 (1973).
- (25) N. V. Sidgwick, "The Chemical Elements and Their Compounds," Oxford University Press, London, 1950, p. 1383.
- (26) G. M. Schwab, E. Roth, C. H. Grintzos, and N. Mavrikakis, "Structure and Properties of Solid Surfaces," The University of Chicago Press, Chicago, Ill., 1953, p. 464.
- (27) N. N. Nikiforova and B. V. Erofeev, *Vestsi Akad. Navuk Belorus SSR, Ser. Khim. Navuk*, (5), 5 (1971).
- (28) (a) A. Cimino and M. Schiavello, *J. Catal.*, **20**, 202 (1971); (b) A. Schiavello, M. Lo Jacono, and A. Cimino, *J. Phys. Chem.*, **75**, 1051 (1971).
- (29) A. N. Terenin and L. M. Roev, "Actes du Deuxieme Congress International de Catalyse," Vol. 2, Editions Technip, Paris, 1961, p. 2183.
- (30) K. Otto and M. Shelef, *Z. Phys. Chem. (Frankfurt am Main)*, **72**, 316 (1970).
- (31) W. Dianis and J. E. Lester, *Surface Sci.*, **43**, 602 (1974).

Studies of Compound Formation on Alkali/ γ -Aluminum Oxide Catalyst Systems Using Chromium, Iron, and Manganese Luminescence

W. H. J. Stork* and G. T. Pott

Koninklijke/Shell-Laboratorium, Amsterdam, Holland (Received February 19, 1974; Revised Manuscript Received August 19, 1974)

Publication costs assisted by Koninklijke/Shell-Laboratorium

The structures of $\text{Li}_2\text{CO}_3/\gamma\text{-Al}_2\text{O}_3$, $\text{K}_2\text{CO}_3/\gamma\text{-Al}_2\text{O}_3$, and $\text{Cs}_2\text{CO}_3/\gamma\text{-Al}_2\text{O}_3$ catalysts, calcined at different temperatures, have been investigated by a number of techniques including thermal analysis, X-ray diffraction, and phosphorescence spectroscopy. In the phosphorescence technique transition metal ion traces are incorporated into the catalyst, and their spectra compared with those of doped model compounds. A discussion of the phosphorescence spectra of Fe, Cr, and Mn in alkali aluminates is therefore included. Finally, the basicity has been determined with Hammett indicators. In the $\text{Li}_2\text{CO}_3/\gamma\text{-Al}_2\text{O}_3$ catalyst compound formation occurs; at calcination temperatures up to 500° $\alpha\text{-LiAlO}_2$ is formed and at higher temperatures LiAl_5O_8 is formed. In the K and Cs systems no compound formation is observed at calcination temperatures up to 900° . It is concluded that in the last-mentioned catalysts the carbonates react with surface hydroxyl groups to form OK (OCs) groups and that no further reaction with the $\gamma\text{-Al}_2\text{O}_3$ lattice takes place. This difference in behavior is attributed primarily to the difference in ionic radii, the large sizes of K, and especially Cs hampering diffusion into the $\gamma\text{-Al}_2\text{O}_3$ lattice.

I. Introduction

Catalysts consisting of $\gamma\text{-Al}_2\text{O}_3$ supported alkali salts have found wide application in chemical industry. Alkali salts are used in general to enhance the selectivity of alumina-based catalysts and in particular to suppress acid-catalyzed side reactions.

Alkali/ $\gamma\text{-Al}_2\text{O}_3$ catalysts are generally prepared by impregnating $\gamma\text{-Al}_2\text{O}_3$ with an alkali salt, usually the carbonate, followed by drying and calcining. Provided the calcination temperature is high enough, the salt decomposes into the oxide, and in principle the following three processes may occur: (1) The alkali carbonate reacts with surface hydroxyl groups to yield, e.g., OK groups, which cover the surface and do not enter the lattice. (2) The alkali ions react with the $\gamma\text{-Al}_2\text{O}_3$ lattice to give a three-dimensional alkali aluminate compound (compound formation). (3) Some alkali ions penetrate the $\gamma\text{-Al}_2\text{O}_3$ lattice to form a

solid solution. It is highly improbable that the large K and Cs ions will do so, but with Li such a process is conceivable. Ions known to form solid solutions with $\gamma\text{-Al}_2\text{O}_3$ are Fe^{3+} , Co^{2+} , and Cr^{3+} .¹

These three processes (dispersion as crystallites of the catalyst or as a monolayer, compound formation, and dissolution into the support) can occur with all supported oxide catalysts, and are theoretically easy to discern. Experimentally it is difficult to establish the structure of the catalyst, however, this is primarily due to the fact that they occur only at or near the surface of very poorly crystalline materials, which also explains why X-ray diffraction often fails to detect compound formation. It is not surprising, therefore, that only few studies have been reported of the structure of such catalyst systems. Levy and Bauer² measured physical properties such as surface area, density, and pore volume of γ -alumina impregnated with LiNO_3 and KNO_3 . They con-

cluded that Li stabilizes the alumina spinel lattice, presumably through formation of LiAl_5O_8 , whereas K does not enter the γ - Al_2O_3 lattice.

In the present investigation we have studied the structure of $\text{Li}_2\text{CO}_3/\gamma$ - Al_2O_3 , $\text{K}_2\text{CO}_3/\gamma$ - Al_2O_3 , and $\text{Cs}_2\text{CO}_3/\gamma$ - Al_2O_3 catalysts, calcined at different temperatures, using a variety of techniques, such as X-ray diffraction, thermal analysis, and phosphorescence spectroscopy, to establish whether compound formation occurs, and, if so, what compounds are formed. Section II discusses the application of phosphorescence spectroscopy to the study of compound formation; section IV deals with the spectra of Cr, Fe, and Mn tracer in alkali aluminate model compounds; sections V and VI deal with the $\text{Li}_2\text{O}_3/\gamma$ - Al_2O_3 and $\text{K}(\text{Cs})_2\text{CO}_3/\gamma$ - Al_2O_3 systems. The Appendix presents some data on the basicity of alkali carbonate/ γ - Al_2O_3 catalysts.

II. Phosphorescence Spectroscopy as a Tool for Compound-Formation Studies

Phosphorescence spectra of transition metal ions are markedly dependent on the surroundings of the phosphorescent ion, *i.e.*, on the symmetry of, and the distance to, the neighboring ions or molecules. Thus, when dissolved in different host lattices, these ions give rise to different spectra. This dependence on the surroundings is described satisfactorily by crystal-field theory and is discussed elsewhere.³

Since the luminescence spectra of aluminates containing tracer ions, such as the first-row transition metal ions, are characteristic of the compounds into which these ions have been incorporated, luminescence spectroscopy can be used to study the formation of compounds on catalysts. To this end a tracer is built into the catalyst and the resultant spectra are compared with those of the tracer in reference compounds.

Experimentally, the tracer (*e.g.*, Cr^{3+}) is deposited on the carrier in very small amounts (0.01–0.1 wt %) together with the catalyst, here alkali carbonate. The supported catalyst is then calcined as usual, and its phosphorescence excitation and emission spectra are measured. Each catalyst gives a spectrum that consists of the sum of the signals of the tracer in the various compounds present. In case no compound formation occurs, two signals should be observed, one from the tracer in the catalyst and the other from the tracer in the support; in case compound formation does occur, a third signal should be found.

To identify the phases present, the observed signals are compared with spectra of the tracer in appropriate model compounds. For example, to find out what compounds are formed between K and γ - Al_2O_3 , we used Cr as a tracer and prepared and measured separate samples of Cr in α - Al_2O_3 , γ - Al_2O_3 , K_2CO_3 , KAlO_2 , and K β - Al_2O_3 . The phosphorescence spectra thus obtained served as a reference in interpreting the spectrum of the actual K/ γ - Al_2O_3 catalyst (KAlO_2 and K β - Al_2O_3 are the only compounds known to be formed from K_2O and Al_2O_3). The spectra of Cr, Fe, and Mn tracers in the model compounds of importance for the present Li/γ - Al_2O_3 , K/γ - Al_2O_3 , and Cs/γ - Al_2O_3 systems are reported and discussed in section IV.

Thus, the occurrence of phases can be detected from the phosphorescence of the tracer ion. By far the most common method to establish the presence of solid phases is X-ray powder diffraction. We have found, however, that by using the phosphorescence method small amounts of poorly crystalline materials can be observed, which are not detected

by X-ray diffraction. This is due to the following factors. (i) The crystal field at a site is largely determined by the arrangement of the next few layers of ions. Therefore, very small crystallites can be observed, and conditions concerning crystallinity are not so severe. (ii) Phosphorescence can be determined with a very high sensitivity, as it is the emission rather than the absorption that is measured. In this respect the phosphorescence technique has a great advantage over diffuse reflectance spectroscopy. (iii) Phosphorescence spectra consisting of a superposition of different spectra can often be resolved into their component parts with the aid of suitable optical filters. In this way even a weak emission that is overshadowed by another strong emission can be studied. Thus, phosphorescence spectroscopy has a definite advantage over other techniques using tracer ions such as epr spectroscopy. Indeed, in the present investigation it was found that the epr spectra of our samples did not yield such detailed information as phosphorescence measurements. (iv) The possibility of using different tracer ions permits one in principle to choose the tracer most suited to the system under study.

Of course, the method in its present state also has its limitations, the main one being that it is not (yet) quantitative. Phosphorescence studies give no more than a very rough indication of the extent of compound formation for the following reasons. The intensity of the signal due to the tracer X in a particular phase A in the catalyst is, to a first approximation (neglecting quenching effects), proportional to the amount of tracer in A, *i.e.*, to the concentration of X in A times the amount of A present. If the tracer were distributed homogeneously over the system its concentration would be constant and the intensities would reflect the actual amounts of A, B, . . . present (see also below). This will not always be the case, however, because in an equilibrium situation the distribution of the tracer over the phases will follow Nernst's law. Although it should be possible to make (time-consuming) corrections for this effect, the actual catalyst studied will still be different, because equilibrium is hardly ever attained. Moreover, in general the phosphorescence efficiency of the tracer depends on the host lattice, and may vary greatly (which is a disadvantage compared to epr spectroscopy). This effect can be corrected by making a careful study of the model compounds. More serious is the situation in which the tracer does not phosphoresce in one of the phases of interest, or does not enter one of them at all.

As a tracer technique is employed, there is always a chance that the system may become perturbed. Until now, however, we have not found any indication of such effects. Anyhow, the concentrations used are very low (0.01–0.1 wt %).

Notwithstanding these limitations, the phosphorescence technique has enabled us to observe compound formation in some cases where other techniques failed.⁴

III. Experimental Section

Variable-temperature X-ray studies were made with a moving-film Guinier camera.

Thermal analyses were carried out on a Mettler thermoanalyzer TA-2 and on a Rigaku Denki thermoflex analyzer.

Element Analyses. C was measured as CO_3^{2-} . Cs and Al were determined by atomic absorption spectroscopy.

Phosphorescence measurements were carried out as described in ref 5. In order to be able to correct the excitation

TABLE I: Emission Wavelengths and Ligand Field Parameters for Cr Phosphorescence in Various Host Lattices

	λ_{em} , nm	ν_{em} , cm^{-1}		$10Dq$, cm^{-1}	B , cm^{-1}	r_{Al-O} , ^a Å	Ref
α -Al ₂ O ₃	693	14,430	sharp	18,150	700	{ 1.86 1.97	13
γ -Al ₂ O ₃	703 (724)	14,220	br				
α -LiAlO ₂	718	13,930	s	18,300	610	1.90	12
β -LiAlO ₂							
LiAl ₅ O ₈ ^b	716	13,970	s	17,500	800		5
LiAl ₅ O ₈ ^c	695	14,390		17,600			5
	705	14,180		16,600			
	717	13,950		18,200			
Li β -Al ₂ O ₃	700	14,280		17,500	560	2.02-1.82	20
	712	14,050					
KAlO ₂							
K β -Al ₂ O ₃	712	14,050		17,500	560	2.02-1.82	20
CsAlO ₂							
Cs β -Al ₂ O ₃	712	14,050	s	17,500	560	2.02-1.82	20

^a r_{Al-O} for octahedral Al sites. ^b Ordered. ^c Disordered.

TABLE II: Emission Wavelengths and Ligand Field Parameters for Fe Phosphorescence in Various Host Lattices

	λ_{em} , nm	ν_{em} , cm^{-1}	$10Dq$, cm^{-1}	B , cm^{-1}	Excn	r_{Al-O} , ^a Å	Ref
α -Al ₂ O ₃							
γ -Al ₂ O ₃	760	13,160			CT		25
α -LiAlO ₂							
β -LiAlO ₂	735	13,600	8830	630	LF	1.76	16
LiAl ₅ O ₈	680	14,710	8000	644	LF		3
Ordered	752	13,300			CT		
LiAl ₅ O ₈	733	13,640	8000	644	LF		3
Disordered							
Li β -Al ₂ O ₃	758	13,200			CT		
	714	14,000	9000	560	LF	1.68-1.77	20
KAlO ₂	760	13,160	7710	593	LF	1.66	28
K β -Al ₂ O ₃	758	13,200			CT		
	714	14,000	9000	560	LF	1.68-1.77	20
CsAlO ₂	660	15,150	6800	523	LF	1.75	27
Cs β -Al ₂ O ₃	758	13,200			CT		
	714	14,000	9000	560	LF	1.68-1.77	20

^a r_{Al-O} for tetrahedral Al sites.

spectra for the dependence of the lamp intensity on the wavelength, the lamp intensity was measured with a YSI Kettering 65 A radiometer. The spectra given in the figures, however, have not been corrected for light intensity unless stated otherwise.

Model compounds were generally prepared from solutions containing Li₂CO₃, K₂CO₃, or Cs₂CO₃, and Al(NO₃)₃ in stoichiometric amounts. Doped compounds were obtained by adding such an amount of Cr(NO₃)₃, Fe(NO₃)₃, or Mn(NO₃)₂ (all spectroscopically pure) as to yield 0.01 wt % of the tracer in the compound. The solutions were dried and the residues calcined at 800° for β -LiAlO₂, KAlO₂, CsAlO₂ and at 500° for α -LiAlO₂. Since KAlO₂ and CsAlO₂ are very hygroscopic they were handled in a drybox. All compounds prepared were examined by X-ray diffraction.

K- β -alumina was prepared from solutions of K₂CO₃ and Al(NO₃)₃ in concentrations calculated to yield K₂O·7Al₂O₃ (dopants were added as described for α -LiAlO₂). The solutions were evaporated to dryness and calcined at 1200° for 18 hr.

Comparison of our X-ray data with those published by Yamaguchi and Suzuki indicated that our preparations had the β -alumina structure but presumably they contained some excess alkali relative to K₂O·11Al₂O₃.

From **K β -alumina** other β -aluminas were obtained by ion exchange with molten salts.⁶ **NH₄ β -alumina** was pre-

pared by ion exchange with molten NH₄NO₃ at 170°⁶ and was used in turn for the preparation of **Li β -alumina** and **Cs β -alumina** by ion exchange with LiNO₃ and CsNO₃ at 400°. The β -alumina structure was retained throughout these operations, as was evident from X-ray photographs.

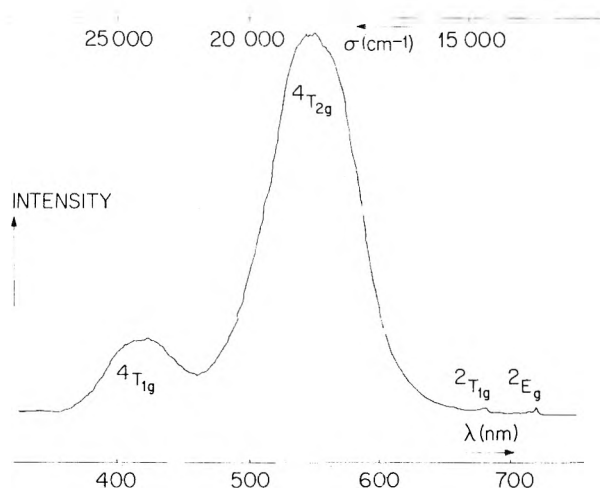
Supported catalysts were prepared by mounting the alkali carbonates (analytical grades) *via* a dry-impregnation procedure. The γ -Al₂O₃ support (surface area 120 m²/g) was obtained from crystalline boehmite (Martinswerk). In the case of Li repeated impregnation was necessary in view of the poor solubility of Li₂CO₃ in water. Samples were dried at 120° and calcined for 18 hr at successively higher temperatures.

IV. Results on Model Compounds

In this section the phosphorescence spectra of the tracer ions in the relevant model compounds are discussed. The following compounds were prepared and dried with Fe, Cr, and Mn: α -LiAlO₂, β -LiAlO₂, Li β -Al₂O₃, KAlO₂, K β -Al₂O₃, CsAlO₂, and Cs β -Al₂O₃. Phosphorescence studies of Fe-, Cr-, and Mn-dried LiAl₅O₈ (both ordered and disordered) have already been reported.^{5,7,8} The above list includes all known Li, K, and Cs aluminates with the exception of α - and β -Li₅AlO₄; as it has been reported⁹ that these compounds cannot be prepared from Li₂CO₃ and Al₂O₃ we have not studied them.

TABLE III: Emission Wavelengths for Mn Phosphorescence in Various Host Lattices

Mn	Red		Green		Ref
	λ_{em} , nm	ν_{em} , cm^{-1}	λ_{em} , nm	ν_{em} , cm^{-1}	
α - Al_2O_3	676	14,790			13
γ - Al_2O_3	700	14,290	507	19,740	
α - LiAlO_2	667, 674	14,990, 14,830			4
β - LiAlO_2	(820)	(12,200)	523	19,110	
LiAl_5O_8	716	13,970	507	19,740	4
Ordered			521	19,190	
LiAl_5O_8	662	15,110	508	19,700	
Disordered					
$\text{Li}\beta$ - Al_2O_3	675	14,810	505	19,800	
	730	13,700			
KAlO_2	727?	13,760?	515	19,420	
$\text{K}\beta$ - Al_2O_3	675	14,810	509	19,650	
	730	13,700			
CaAlO_2					
$\text{Cs}\beta$ - Al_2O_3	675	14,810	505	19,800	
	730	13,700			

**Figure 1.** Excitation spectrum of Cr^{3+} in α - LiAlO_2 .

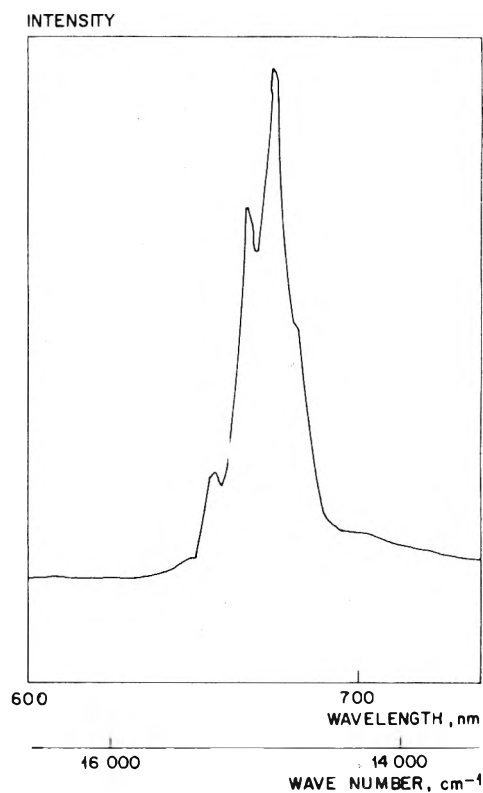
The phosphorescence results on the dried compounds are preceded by a short summary of the phosphorescence from Cr^{3+} , Fe^{3+} , Mn^{2+} , and Mn^{4+} in general. The results are summarized in Tables I–III.

1. Luminescence Properties of Transition Metal Ions in Oxide Host Lattices. In the first-row transition metal ions the electronic transitions observed in excitation and emission spectra are generally confined to the 3d subshell. Electronic repulsion and crystal field split the d levels, as is adequately described by Tanabe and Sugano.¹⁰

Previous papers dealt with the phosphorescence spectra of Fe^{3+} ,⁵ Mn^{2+} ,⁷ Mn^{4+} ,⁷ and Cr^{3+} ⁸ in LiAl_5O_8 (one of the model compounds of interest to the present study). The emission of the d^5 ions Fe^{3+} and Mn^{2+} is due to a ${}^4\text{T}_1({}^4\text{G}) \rightarrow {}^6\text{A}_1({}^6\text{S})$ transition. The emission spectrum is a broad band, because the energy of this transition is crystal-field dependent.

The phosphorescence of the d^3 ions Mn^{4+} and Cr^{3+} is due to a ${}^2\text{E}({}^2\text{G}) \rightarrow {}^4\text{A}_2({}^4\text{F})$ transition and their spectra consist of a narrow line. In the excitation spectra (Figure 1) the broad and narrow bands are easily interpreted with the aid of the Tanabe–Sugano diagram.

The emission observed from Fe^{3+} is always from tetrahedrally coordinated ions,⁵ whereas the Mn^{4+} and Cr^{3+} emis-

**Figure 2.** Emission spectrum of Mn^{4+} in α - LiAlO_2 at 77°K.

sions arise from ions in octahedral coordination.^{7,8} Mn^{2+} emits both in octahedral and in tetrahedral coordination.^{11,12} Although there are many other phosphorescing and fluorescing ions, the choice of first-row transition metal ions as tracers is not arbitrary. The most important reason for using Fe^{3+} , Cr^{3+} , Mn^{2+} , and Mn^{4+} is that they exhibit excitation and emission spectra that are highly sensitive to the environment. Furthermore, these ions generally give intense and well-characterized emission spectra in the visible region. Another class of well-characterized phosphorescing ions is that of the rare earths. Their transitions within the 4f shell are, however, far less dependent on the crystalline environment;¹⁰ moreover, these ions are too big to be easily incorporated into the lattices of interest.

Apart from understanding the phosphorescence of foreign ions located at certain sites in host lattices, it is necessary to consider the way in which such ions are incorporated.^{13,14}

One expects for Cr^{3+} and Fe^{3+} a simple substitution at aluminium sites, as the ionic radii are not too different ($r_{\text{Al}^{3+}(\text{oct})} = 0.53 \text{ \AA}$, $r_{\text{Fe}^{3+}(\text{oct})} = 0.65 \text{ \AA}$, and $r_{\text{Cr}^{3+}(\text{oct})} = 0.62 \text{ \AA}$).¹⁵ This is generally confirmed by our phosphorescence results. Complications arise when only Al ions at tetrahedral sites are present, as Cr^{3+} (d^3) does not substitute at such sites.

Substitution of Mn^{2+} or Mn^{4+} for Al^{3+} , however, requires an additional process to restore electroneutrality, for example, replacement of two Al^{3+} ions by one Mn^{2+} and one Mn^{4+} ion.⁷

Special phenomena arise at high concentrations of dopants and are due to interactions between lattice defects.¹³ As we always used low concentrations of Fe, Cr, and Mn, we shall not discuss them here.

2. α - LiAlO_2 . A. Structure. The structure of α - LiAlO_2 can be described as a distorted NaCl structure elongated

along a threefold axis;^{16,17} all ions have octahedral coordination. The space group is $R\bar{3}m$, the Al-site symmetry $\bar{3}m$.

B. Phosphorescence Results. Fe^{3+} . Phosphorescence due to Fe^{3+} was not observed. This is to be expected since the Al ions in α - $LiAlO_2$ occupy octahedral sites. The Fe^{3+} will therefore also occupy octahedral sites, and at most give rise to phosphorescence in the ir region, which is not covered by our instrument.⁵

Cr^{3+} . Cr emission at 77 K consisted of a sharp line at 13,930 cm^{-1} , with weak vibrational bands at about 13,390, 13,690, and 14,210 cm^{-1} . At room temperature a new line was observed at 14,030 cm^{-1} . The excitation spectrum showed broad bands at 18,340 and 24,650 cm^{-1} (corrected for wave number dependence of lamp intensity), together with weak, sharp bands at 13,940 and 14,760 cm^{-1} (Figure 1). These observations on Cr luminescence follow the general pattern for many host oxides such as α - Al_2O_3 ^{18,19} and $LiAl_5O_8$.⁸ The results are easily explained by assuming the Cr^{3+} ions to be at (octahedral) Al sites ($LiCrO_2$ and $LiAlO_2$ are isostructural²⁰). Quantitative evaluation using the Tanabe-Sugano diagram for a d^3 ion can be made with the following assignment: emission ${}^2E_g \rightarrow {}^4A_{2g}$ (R lines); in excitation two broad bands, ${}^4T_{2g} \leftarrow {}^4A_{2g}$ and ${}^4T_{1g} \leftarrow {}^4A_{2g}$, and a narrow band, ${}^2T_{1g} \leftarrow {}^4A_{2g}$; $10Dq = 18,300$ cm^{-1} ; $B = 610$ cm^{-1} ; $C = 3150$ cm^{-1} .²¹ The second emission line observed at room temperature is due to a splitting of the 2E_g (2G) level in the trigonally distorted cubic symmetry.¹⁰

Mn. At 77 K a strong emission due to Mn^{4+} was observed at 14,990 cm^{-1} with vibrational fine structures at 14,660, 14,830, and 15,240 cm^{-1} (Figure 2). At room temperature a second emission was found at 15,420 cm^{-1} presumably due to splitting of the ${}^2E({}^2G)$ level, as in Cr^{3+} . The excitation spectrum for these emissions consisted of two broad bands (at 23,530 and 30,580 cm^{-1}), together with a weak, sharper band at 14,660 cm^{-1} . Assigning the broad bands to the ${}^4T_{2g}$ and ${}^4T_{1g}$ levels we obtain $10Dq = 23,500$ cm^{-1} ; $B = 650$ cm^{-1} ; $C = 3230$ cm^{-1} . Clearly, the $10Dq$ value is much higher for Mn^{4+} than for Cr^{3+} . This was also found with other compounds, e.g., $LiAl_5O_8$ ^{7,8} and α - Al_2O_3 .¹⁸ In addition, the vibrational structure of the emission was much more pronounced with Mn than with Cr.

Apart from the signal due to Mn^{4+} , there was another Mn emission at wave numbers below 14,000 cm^{-1} . The latter signal was excited *via* a broad band at 20,300 cm^{-1} , and had a slightly shorter lifetime. At present we have no suitable explanation for its occurrence. In summary, Cr^{3+} and Mn^{4+} ions evidently occupy trigonally distorted octahedral Al sites in the α - $LiAlO_2$ lattice, giving rise to characteristic luminescence spectra.

3. β - $LiAlO_2$. A. Structure. β - $LiAlO_2$ is formed from α - $LiAlO_2$ by an irreversible phase transition at temperatures above 600°. ^{16,17} β - $LiAlO_2$ crystals are tetragonal with space group $P4_12_1(D_4)$ ¹⁶ (site symmetry Al: 2). The crystal structure consists of an infinite three-dimensional network of distorted tetrahedra, with aluminium and lithium atoms at the centers and oxygen atoms at the vertices. Each tetrahedron shares one of its edges with that of a different tetrahedron and each of its vertices with those of two additional tetrahedra, one of each kind.

B. Phosphorescence Results. Fe^{3+} . Fe^{3+} emission was very strong and consisted of a broad band at 13,600 cm^{-1} , with a sharp zero-phonon transition⁵ at 14,020 cm^{-1} at low temperatures. This is in good agreement with other findings on the phosphorescence from Fe^{3+} at tetrahedral (Al) sites.⁵

TABLE IV: Observed and Calculated Wave Numbers for Ligand Field Transitions of Fe^{3+} in β - $LiAlO_2$

	4T_1	4T_2	${}^4E_1, {}^4A_1$	${}^4T_2({}^4D)$	${}^4E({}^4D)$
Obsvd				21,300?	
	14,750	16,400	21,300?	21,580	25,580
	15,690	18,420		22,590	25,800
Calcd	14,650	18,100	21,300	23,850	25,710

Excitation took place *via* ligand-field transitions; results are summarized in Table IV. The bands were assigned as indicated, although, of course, further splitting occurred as a result of deviations from cubic symmetry. On the basis of these assignments the ligand-field parameters were found to be $B = 630$ cm^{-1} , $C = 3000$ cm^{-1} , $C/B = 4.73$, and $10Dq = 8830$ cm^{-1} . Table IV shows that the energy levels thus calculated agree reasonably well with the experimental data.

Recently phosphorescence from Fe^{3+} in β - $LiAlO_2$ was also reported by Palumbo.^{22a} The published spectra, which deviated slightly from ours, were interpreted in a widely different way, analogous to the interpretation by Melamed^{22b} and criticized by us in an earlier paper.⁵

Cr^{3+} . No phosphorescence due to Cr^{3+} in β - $LiAlO_2$ was observed. This is in accordance with expectations, as only tetrahedral sites are available.

Mn. Mn-doped β - $LiAlO_2$ gave only a weak phosphorescence signal. Surprisingly, no emission at about 520 nm was observed, although Mn^{2+} in tetrahedral sites often emits at this wavelength.^{7,11}

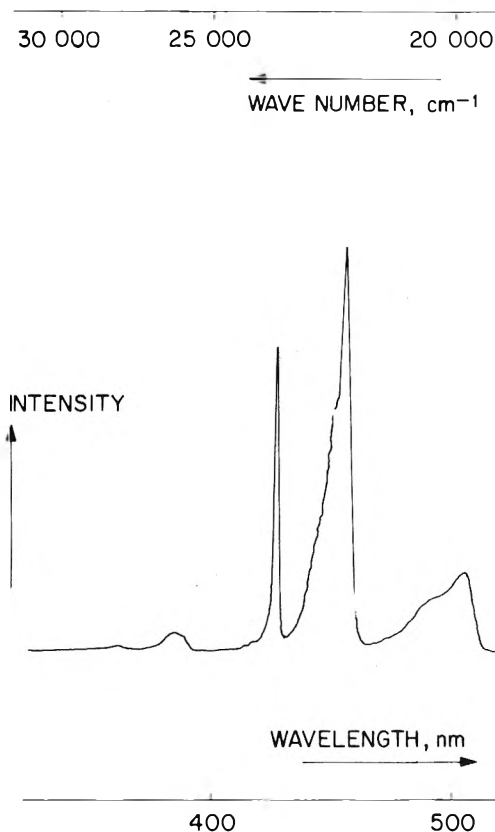
In the red region there was a rather weak, broad emission at about 820 nm, in addition to some emission presumably due to Mn^{4+} in α - $LiAlO_2$. Excitation apparently occurred between 400 and 550 nm. As yet we have no proper explanation for this signal. It might be due to a pair of Mn^{2+} ions, which can replace a set of Li-Al neighbors. In sum, Fe^{3+} emits at 13,600 cm^{-1} , as is expected for tetrahedrally coordinated Fe; Cr does not phosphorescence, again as expected for a host lattice containing only tetrahedral sites. Surprisingly, Mn does not emit in the green region, but yields an emission at about 820 nm.

4. β -Alumina. A. Structure. At present two different β -aluminas are distinguished,²³ viz. β -alumina $NaAl_{11}O_{17}$ and β'' -alumina $NaAl_5O_8$, whose compositions are not exactly stoichiometric. Their structures are similar and consist of layers with a spinel structure (layers of four oxygen atoms) separated by a thin layer containing Na, Al, and O. The stacking of the spinel and alkali-containing layers for the two compounds^{6,24} is different, however. Owing to the excess of sites available the alkali ions are very mobile and can easily be exchanged for other monovalent ions, including NH_4^+ , Tl^+ , and Ag^+ , by using molten salts.⁶ According to the data available the structure does not change much upon exchange; little is known, however, about the stability of β - or β'' -aluminas with ions other than Na^+ .

B. Phosphorescence Results. Fe^{3+} . Fe-doped K β -alumina gave two different phosphorescence signals: a broad emission band at 13,200 cm^{-1} , excited *via* a charge transfer transition at about 28,000 cm^{-1} , and a band at about 14,000 cm^{-1} , excited *via* ligand-field transitions. The first band was also observed in the spectrum of Fe^{3+} -doped γ -alumina.¹ We therefore assumed that this phosphorescence arose from Fe^{3+} at tetrahedral Al sites in the bulk of γ -alumina blocks.⁵ The second signal differed from the first both in spectral characteristics and in decay time. Presumably it

TABLE V: Observed and Calculated Wave Numbers for Ligand Field Transitions of Fe^{3+} in $\text{K } \beta\text{-Al}_2\text{O}_3$

	${}^4\text{T}_1$	${}^4\text{T}_2$	${}^4\text{E}_1, {}^4\text{A}_1$	${}^4\text{T}_2({}^4\text{D})$	${}^4\text{E}({}^4\text{D})$
Obsvd	14,980	17,940	21,660?	21,660?	25,600
	15,450	18,600		22,080	
Calcd	15,000	18,300	21,660	23,800	25,600

**Figure 3.** Excitation spectrum of tetrahedrally coordinated Mn^{2+} in potassium β -alumina.

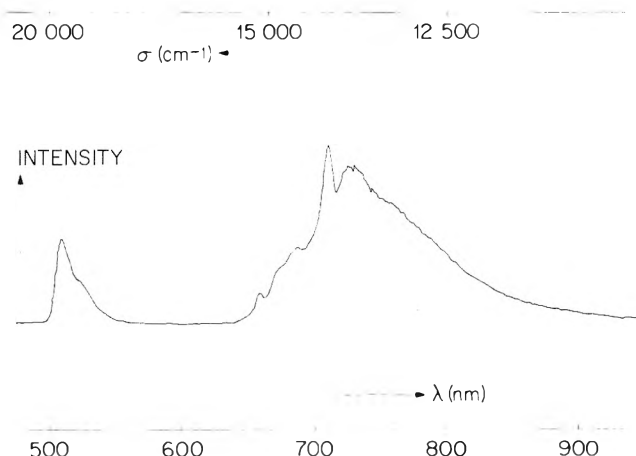
originated from Fe in tetrahedral coordination near the alkali layer, from the sites constituting the spacer columns. It cannot arise from Fe at exchangeable sites since ion exchange did not reduce the signal drastically. The various ligand-field transitions in the excitation spectrum of the emission at $14,000 \text{ cm}^{-1}$ were assigned as indicated in Table V and calculated using $B = 560 \text{ cm}^{-1}$, $C = 3210 \text{ cm}^{-1}$, $C/B = 5.7$, and $10Dq = 9000 \text{ cm}^{-1}$.

Generally speaking, the same results were found for Li^+ , NH_4^+ , and Cs^+ β -aluminas. The phosphorescence at $13,200 \text{ cm}^{-1}$ (excited *via* a charge-transfer band) was more pronounced in Li^+ β -alumina than in K^+ β -alumina. In Cs^+ β -alumina the ligand-field excited phosphorescence was quite strong. Both in emission and in excitation, vibrational structure could be discerned, with a zero phonon transition at $15,040 \text{ cm}^{-1}$. The values of the ligand-field parameters of the various aluminas showed no differences.

Cr^{3+} . Cr in β -alumina gave the usual emission spectrum due to Cr^{3+} in octahedral sites: a sharp emission at $14,050 \text{ cm}^{-1}$. The excitation spectrum, too, was as expected, with strong broad peaks at $17,500$ and $23,420 \text{ cm}^{-1}$ and a weak sharp peak at $14,770 \text{ cm}^{-1}$. Calculation of the ligand field parameters yielded $B = 560 \text{ cm}^{-1}$, $C = 3340 \text{ cm}^{-1}$, and $10Dq = 17,500 \text{ cm}^{-1}$. The same results were found for NH_4^+ and Cs^+ β -alumina. Li^+ β -alumina gave two emis-

TABLE VI: Observed and Calculated Wave Numbers for Ligand Field Transitions of Tetrahedral Mn^{2+} in $\text{K } \beta\text{-Al}_2\text{O}_3$

	${}^4\text{T}_1$	${}^4\text{T}_2$	${}^4\text{E}_1, {}^4\text{A}_1$	${}^4\text{T}_2({}^4\text{D})$	${}^4\text{E}({}^4\text{D})$
Obsvd	19,900	22,220	23,440	25,970	27,800
Calcd	19,750	22,120	23,440	26,480	27,800

**Figure 4.** Emission spectrum of Mn in potassium β -alumina.

sion signals at $14,280$ and $14,080 \text{ cm}^{-1}$; this may be related to the fact that the Li ions are not midway between the layers.⁶

Mn. All β -aluminas investigated gave a green emission at $19,690 \text{ cm}^{-1}$ due to Mn^{2+} at tetrahedral Al sites. The excitation spectrum, too, was characteristic of tetrahedral Mn^{2+} (Figure 3); from this spectrum we derived the following values for the ligand-field parameters: $B = 623 \text{ cm}^{-1}$, $C = 3440 \text{ cm}^{-1}$ ($C/B = 5.5$), $10Dq = 5920 \text{ cm}^{-1}$ (Table VI). No differences were found between the various aluminas.

The spectrum in the red region was far more complicated, since it contained several overlapping signals which were difficult to separate (Figure 4). Measurements using monochromatic filters indicated one emission between 660 and 690 nm , which was excited between 350 and 500 nm , presumably from Mn^{4+} at octahedral sites, and another, broad emission centered around 730 nm , which could be excited over a broad spectral region.

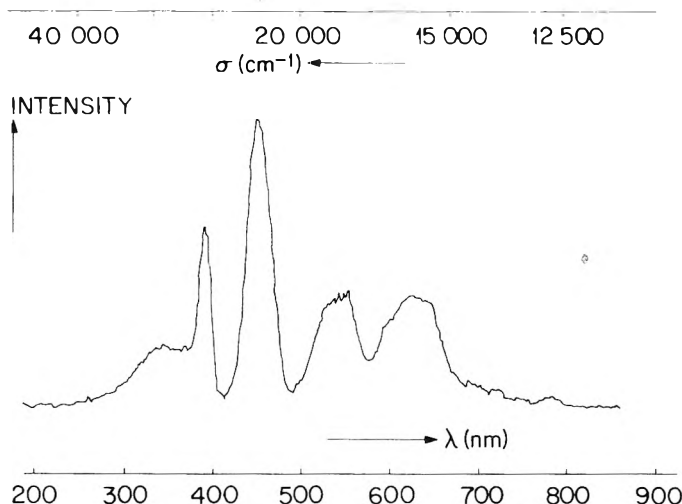
Recently Bergstein and White²⁵ also investigated the luminescence of Mn in $(\text{Na}) \beta\text{-Al}_2\text{O}_3$. They observed the green luminescence at $19,690 \text{ cm}^{-1}$ and, in addition, an emission signal gradually disappeared in favor of the green emission, which demonstrates that the Mn^{2+} ion in exchangeable positions diffuse into the tetrahedral Al sites of the spinel blocks. As our samples were always calcined above 1000° , it is not surprising that we did not observe the signal at 590 nm .

Summarizing, it can be said that phosphorescence of both Fe^{3+} and Cr^{3+} can be observed, in agreement with the presence of both octahedral and tetrahedral sites in the spinel blocks. Mn-doped samples exhibit very complex spectra. All spectra are rather insensitive to exchange of the alkali ions.

5. KAlO_2 and CsAlO_2 . A. Structure. KAlO_2 has a structure similar to that of cubic β -cristobalite (SiO_2) with the Al^{3+} ions at the tetrahedral Si sites, and the alkali ions at the centers of the large holes formed by the AlO_4 tetrahedra.²⁶ The actual structure is probably somewhat deformed

TABLE VII: Observed and Calculated Wave Numbers for Ligand Field Transitions of Fe^{3+} in KAlO_2

	${}^4\text{T}_1({}^4\text{G})$	${}^4\text{T}_2({}^4\text{G})$	${}^4\text{E}_1, {}^4\text{A}_1({}^4\text{G})$	${}^4\text{T}_2({}^4\text{D})$	${}^4\text{E}({}^4\text{D})$	${}^4\text{T}_1({}^4\text{P})$
Obsvd	16,030	18,500		22,190	25,450	(28,900)
Calcd	15,890	18,920	21,300	23,880	25,450	29,970

Figure 5. Excitation spectrum of Fe^{3+} in KAlO_2 for λ_{em} 712 nm.

(space group $P_{2,3}$ instead of $Fd3m$), resulting in trigonally distorted Al–O tetrahedra²⁶ (site symmetry Al: 3). The K^+ ions are 12-coordinated. CsAlO_2 is isostructural with KAlO_2 ,²⁷ with only a small difference in lattice parameter: for KAlO_2 $a = 7.7$ Å, for CsAlO_2 $a = 8.1$ Å.

B. Phosphorescence Results. Cr^{3+} . A very weak emission due to Cr^{3+} was observed at about 710 nm (14,080 cm^{-1}). Since this spectrum was identical with that of Cr^{3+} -K β - Al_2O_3 we attributed this signal to the presence of small amounts of K β - Al_2O_3 in the KAlO_2 , which itself does not show a Cr^{3+} emission.

Fe^{3+} . A broad-banded emission was found near 760 nm; the excitation spectrum consisted of both a charge-transfer band and ligand-field transitions. Detailed investigation using filters showed that the emission consisted of two separate signals: one excited *via* the charge-transfer band, and the other excited *via* the ligand-field transitions. Both emission spectra had their maximum close to 760 nm; their shape was different, however, which enabled us to separate their excitation spectra reasonably well by using interference filters with λ_1 725 nm and λ_2 798 nm (Figure 5). The calculated crystal-field transitions gave a good fit with the observed transitions, with $B = 593$ cm^{-1} , $C = 3074$ cm^{-1} , and $10Dq = 7710$ cm^{-1} (Table VII).

The observed ${}^4\text{T}_1({}^4\text{P})$ level was not firmly established as the observed band may also represent the charge-transfer excitation of the higher-wavelength emission. In addition, it was found that the high-wavelength emission (excited by the charge-transfer band) could also be excited at 720 nm. Possibly, some impurity level was excited, from which by thermal excitation the emission level was reached. This is in agreement with the observation that the intensity of this excitation band increased with increasing temperature.

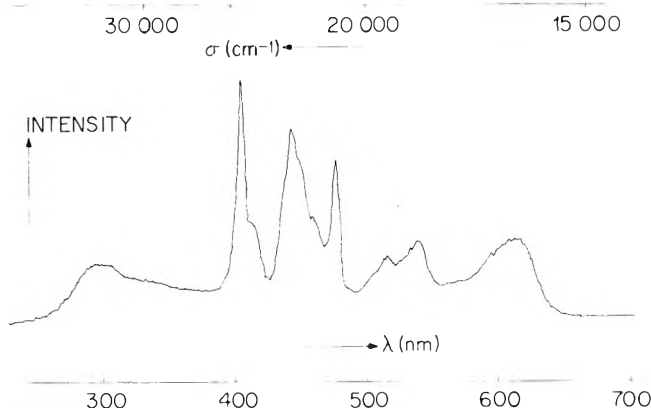
In summary, there were two different signals from Fe^{3+} . From the KAlO_2 structure it is obvious that Fe^{3+} can occupy only one site, namely, that of Al^{3+} (KFeO_2 and KAlO_2 are isomorphous²⁶). Assuming that this species gives rise to one emission, it is difficult to visualize where the other signal originates. In view of the fact that Fe is a very good sub-

TABLE VIII: Observed and Calculated Wave Numbers for Ligand Field Transitions of Fe^{3+} in CsAlO_2

	${}^4\text{T}_1$	${}^4\text{T}_2$	${}^4\text{A}, {}^4\text{E}$	${}^4\text{T}_2$	${}^4\text{E}$
Obsvd	16,360	18,980	20,990	22,150	24,650
Calcd	16,380	18,910	20,990	23,195	24,650

TABLE IX: Observed and Calculated Wave Numbers for Ligand Field Transitions of Tetrahedral Mn^{2+} in KAlO_2

	${}^4\text{T}_1$	${}^4\text{T}_2$	${}^4\text{E}, {}^4\text{A}$	${}^4\text{T}_2$	${}^4\text{E}$
Obsvd	20,090	21,980	23,380	26,270	27,690
Calcd	19,850	22,160	23,380	26,490	27,690

Figure 6. Excitation spectrum of Fe^{3+} in CsAlO_2 .

stitute for Al, the presence of a separate Fe-containing phase seems unlikely and the signal may be due to Fe^{3+} in small amounts of contaminating K β - Al_2O_3 or γ - Al_2O_3 .¹

Fe in CsAlO_2 gave an emission at 660 nm, with a smaller peak at 680 nm. This strong emission was excited by ligand field transitions, as shown in Figure 6. In this spectrum the ${}^4\text{A}, {}^4\text{E}$ transition was clearly present. The spectrum could be fitted with $B = 523$ cm^{-1} , $C = 3152$ cm^{-1} , and $10Dq = 6800$ cm^{-1} (Table VIII).

In addition, there was a weak, broad emission near 760 nm, excited *via* a charge transfer transition. As for KAlO_2 , we suppose that this originated from Fe in γ - Al_2O_3 contamination.¹

Mn. Mn in KAlO_2 was found to emit in the green region at 19,510 cm^{-1} . The emission was typical of Mn^{2+} at tetrahedral sites and has been discussed previously. The excitation spectrum showed the characteristic bands, and could be fitted with $B = 616$ cm^{-1} , $C = 344$ cm^{-1} and $10Dq = 5850$ cm^{-1} (Table IX).

In addition to this signal in the green, an emission was observed in the red (maximum at 727 nm). Again, this emission is unexpected considering the structure of KAlO_2 . Therefore we do not exclude the possibility that this emission originated from Mn in a small amount of a contaminating β - or γ - Al_2O_3 phase. Samples of Mn in CsAlO_2 (and RbAlO_2) were blue; they did not show any phosphorescence.

In summary, it can be said that, in accordance with expectations, Cr^{3+} did not phosphoresce in KAlO_2 or CsAlO_2 ; Fe^{3+} showed complex phosphorescence behavior. Fe^{3+} at Al^{3+} sites in KAlO_2 and CsAlO_2 phosphoresced upon excitation through ligand-field transitions. Both with Fe and with Mn phosphorescence signals were observed which were thought to originate from tracer ions in impurity phases.

6. Summary. The results on the phosphorescence of Cr^{3+} , Mn^{4+} , and Fe^{3+} in alkali aluminates confirm that these tracer ions are incorporated at Al sites. Mn^{2+} possibly also occupies alkali-ion sites, as was found in LiAl_5O_8 : Mn^{2+} .⁷ Cr^{3+} ions only replace aluminium in octahedral coordination, whereas Fe^{3+} phosphoresces only when in tetrahedral coordination. Hence, Cr emission spectra can serve as a fingerprint for compounds with octahedral sites, whereas Fe phosphorescence is useful for the identification of compounds with tetrahedral sites. Mn^{4+} behaves like Cr^{3+} , whereas Mn^{2+} can be incorporated both in octahedral and at tetrahedral sites. Therefore, Mn is in principle the most versatile tracer. Unfortunately, however, its phosphorescence behavior is only partly understood. Since the lattices concerned all have roughly the same Al-O distance, crystal field strength and covalency parameters will be approximately the same and as a result the differences between the spectra will be small. Tables I-III compare the spectra of the tracers in the various host lattices. The results presented confirm the statements made in the preceding paragraph about the use of these tracers in different lattices. Although the differences between the emission wavelengths for Cr^{3+} in the various compounds are small, they are large enough to be detectable and hence Cr tracers are useful for compound formation studies. The same goes for Fe (especially the excitation spectra) and Mn.

V. $\text{Li}_2\text{CO}_3/\gamma\text{-Al}_2\text{O}_3$ Catalysts

Catalysts were prepared with a 5 and 10 wt % Li_2CO_3 loading, corresponding to $\text{Li}_2\text{O} \cdot 14\text{Al}_2\text{O}_3$ and $\text{Li}_2\text{O} \cdot 7\text{Al}_2\text{O}_3$, respectively. Calcination was carried out at temperatures up to 1200° .

X-ray analysis showed that (i) lines due to Li_2CO_3 are observed up to calcination temperatures of 500° (pure Li_2CO_3 decomposes at 723°);²⁸ (ii) lines due to LiAl_5O_8 appear at about 1000° ; (iii) at low temperatures (up to $\sim 170^\circ$) LiAlO_2 hydrate is produced.

Thermal analysis indicated the decomposition of Li_2CO_3 at low temperatures, especially at about 250° (Figure 7). Only a small remainder of Li_2CO_3 decomposes at 720° .

Elemental analysis for C showed that some of the Li_2CO_3 already decomposes upon impregnation, and that after calcination at 500° only some 30% of it is left.

These results clearly demonstrate that when mounted on $\gamma\text{-Al}_2\text{O}_3$ the carbonate decomposes at lower temperatures than the pure compound does. This suggests that there is an interaction between Li_2O and the support; it does not indicate, however, whether small crystallites of a stoichiometric compound are formed, or whether only a surface reaction has occurred.

Phosphorescence Spectroscopy. $\text{Li}_2\text{CO}_3/\gamma\text{-Al}_2\text{O}_3$ catalysts doped with Fe, Cr, and Mn were prepared and calcined at 150 , 350 , 550 , 800 , and 1200° . Their phosphorescence spectra will be discussed separately.

Fe^{3+} . The spectra of Fe-doped catalysts did not provide much information. Upon calcination at temperatures up to

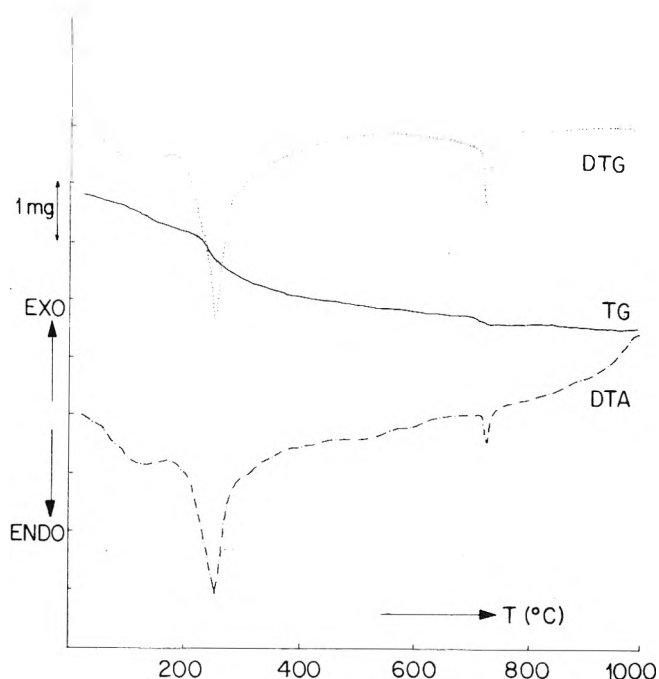


Figure 7. DTA/TGA results for 5% $\text{Li}_2\text{CO}_3/\gamma\text{-Al}_2\text{O}_3$ (265.7 mg).

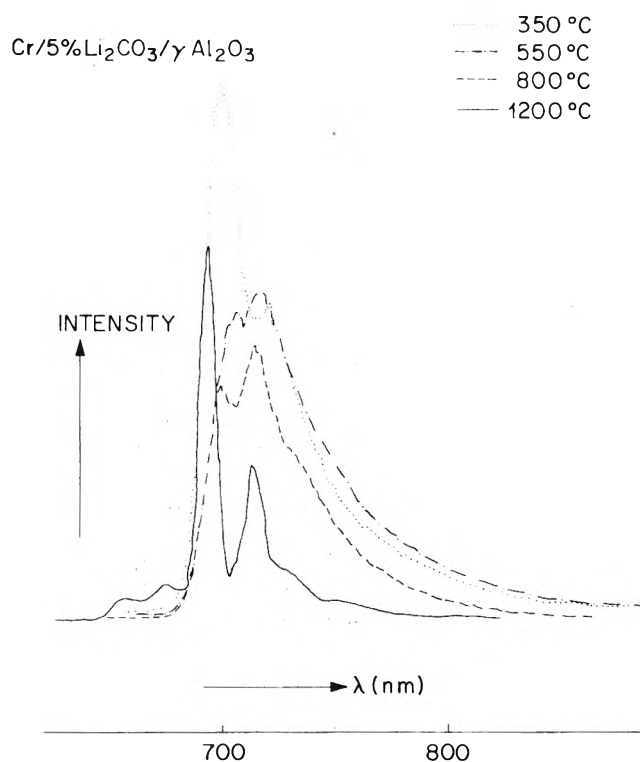


Figure 8. Emission spectra of calcined Cr-doped Li_2CO_3 (5%)/ $\gamma\text{-Al}_2\text{O}_3$ catalysts.

800° a broad emission around 760 nm was always observed. This emission is characteristic of Fe $\gamma\text{-Al}_2\text{O}_3$ and masks other signals, if present. Neither did the excitation spectra offer any evidence for the presence of compounds such as $\beta\text{-LiAlO}_2$ or LiAl_5O_8 , which (unlike Fe $\gamma\text{-Al}_2\text{O}_3$) give rise to strong ligand-field excitation bands. Only in samples calcined at 1200° was the occurrence of the ordered phase of LiAl_5O_8 evident from the sharp emission at 660 nm .

Cr^{3+} . More useful information was obtained from Cr^{3+} luminescence. The emission spectra of 5% $\text{Li}_2\text{CO}_3/\gamma\text{-Al}_2\text{O}_3$ /

TABLE X: Wavelengths of Emission Peaks or Shoulder(s) of Cr-Doped Catalysts Calcined at Different Temperatures

5% Li ₂ CO ₃		10% Li ₂ CO ₃	
Calc'n temp, °C	λ, nm	Calc'n temp, °C	λ, nm
340	701	340	701
	721 (s)		723 (s)
540	718	520	701
			718 (s)
800	714	820	714
	661 (Mn)		693
	677 (Mn)		713
1200	694		
	714		
	730 (s) (Fe)		

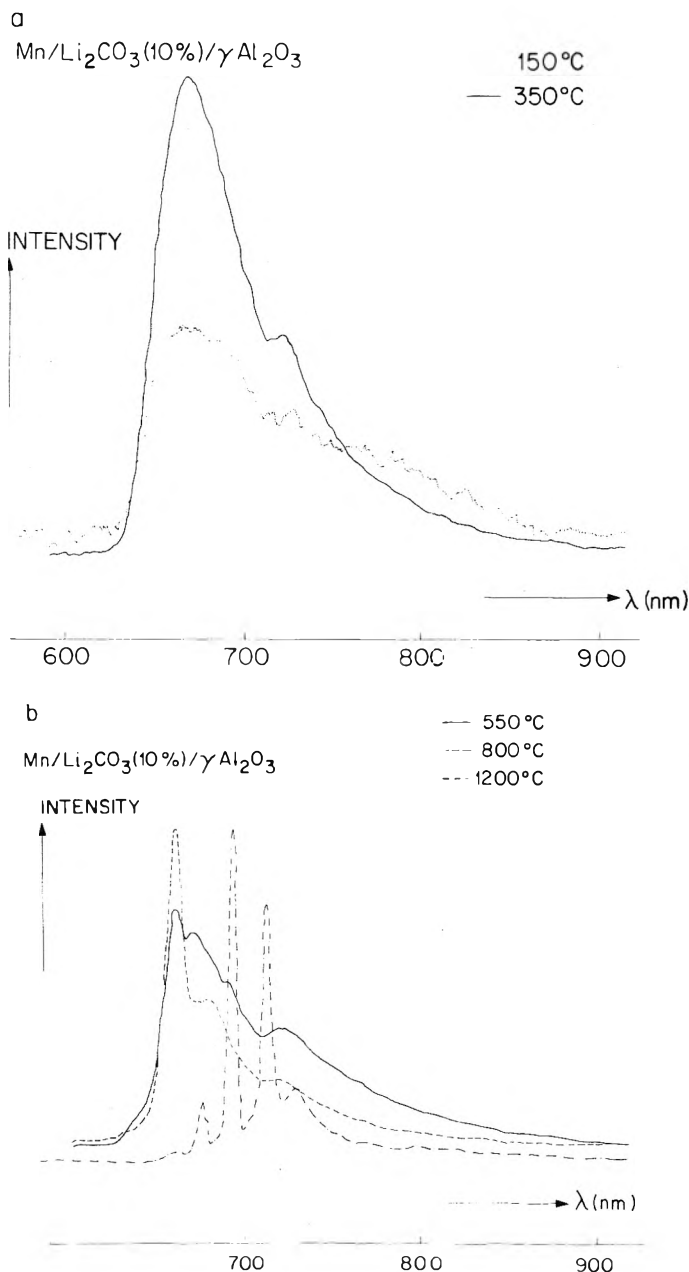
TABLE XI: Wavelengths of Emission Peaks or Shoulders(s) of Mn-Doped Li₂CO₃/γ-Al₂O₃ Catalysts Calcined at Different Temperatures

5% Li ₂ CO ₃		10% Li ₂ CO ₃	
Calc'n temp, °C	λ, nm	Calc'n temp, °C	λ, nm
150	668	150	668
340	675	350	668
540	663, 682 (Fe?)	520	662, 673
	722 (Cr)		692, 720 (Cr)
		820	662, 680 (Fe)
1200	659, 677		719 (Cr)
	693 (Cr), 715	1200	662, 676
	730 (Fe)		693 (Cr), 715, 730 (Fe)

Cr samples calcined at different temperatures are shown in Figure 8. The spectrum of the catalyst calcined at 350° was characteristic of Cr γ-Al₂O₃, featuring a peak at about 703 nm and a shoulder at 724 nm. Calcination at higher temperatures resulted in the appearance of new peaks or shoulders. The wavelengths of these peaks are summarized in Table X; for comparison, the results on the model compounds are given in Table I. The spectra clearly reflect the formation of new compounds, but unambiguous identification is difficult due to the small differences in wavelength between the Cr³⁺ emissions in the various host lattices. Nevertheless, we interpret the peak at 718 nm as a Cr α-LiAlO₂ emission, and the one at 714 nm, observed with samples calcined at 800 and 1200°, as a Cr LiAl₅O₈ (ordered) emission.

Mn. Emission spectra of Mn-doped 10 % Li₂CO₃/γ-Al₂O₃ catalysts are shown in Figure 9 and the relevant data are summarized in Table XI. The wavelengths of the Mn-emission peaks observed with the various host lattices are given in Table III.

The assignment of the various signals can be made with a far higher degree of certainty than in the case of Cr, since the Mn-emission peaks are much wider apart. Thus, the 668-nm peak observed with samples calcined at 150 and 350° is attributed to Mn α-LiAlO₂. (The peak is very broad, indicating that the α-LiAlO₂ formed still has a very low degree of crystallinity.) The 662-nm peak formed at higher temperatures is ascribed to disordered LiAl₅O₈. The peak at 715 nm observed with the 1200° calcined catalyst is probably due to Mn ordered LiAl₅O₈, but may also stem from Cr ordered LiAl₅O₈. As indicated in Table VI, some emission peaks originate from Fe or Cr impurities.

**Figure 9.** Emission spectra of calcined nondoped Li₂CO₃ (10%)/γ-Al₂O₃ catalysts.

In summary, X-ray diffraction, thermal analysis, and elemental analysis show that Li₂CO₃ mounted on γ-Al₂O₃ decomposes at lower temperatures than the pure compound does. The emission spectra of Cr and Mn tracers point to compound formation: α-LiAlO₂ is detected in samples calcined at 150 and 350°, and LiAl₅O₈ in samples calcined at higher temperatures. Very strong evidence for this is provided by Mn phosphorescence, and the conclusions are supported by the results obtained with Cr. In view of the limitations of the present technique the results cannot be given in a quantitative form. On the basis of our phosphorescence data, we assume that compound formation occurs even at low temperatures and that at calcination temperatures under 500° mainly α-LiAlO₂ and at higher temperatures both ordered and disordered LiAl₅O₈ are formed. It is possible that some α-LiAlO₂ is converted into β-LiAlO₂ above 500°, but this is not confirmed by Fe phosphores-

TABLE XII: Basic Properties of Alkali Carbonate/ γ -Alumina Catalysts

Catalyst	Calcn temp, °C	H_0 of most basic sites	mequiv/g	Surface area, m ² /g	mequiv/m ²	H_0 of indicator
5% Li ₂ CO ₃ / γ -Al ₂ O ₃	150	6.8 < H_0 < 12.2	0.35	96	37 × 10 ⁻⁴	6.8
	340	6.8 < H_0 < 12.2	0.35	111	31 × 10 ⁻⁴	6.8
	540	6.8	0.17	103	16 × 10 ⁻⁴	6.8
	800	6.8 < H_0 < 12.2	0.13	67	20 × 10 ⁻⁴	6.8
10% K ₂ CO ₃ / γ -Al ₂ O ₃	340	12.2 < H_0 < 15	1.32	65	200 × 10 ⁻⁴	6.8
			0.21		33 × 10 ⁻⁴	12.2
	550	15	0.45	69	65 × 10 ⁻⁴	6.8
			0.41		60 × 10 ⁻⁴	12.2
20% Cs ₂ CO ₃ / γ -Al ₂ O ₃	800	12.2	0.39	71	55 × 10 ⁻⁴	6.8
			0.32		45 × 10 ⁻⁴	12.2
	370	>17.2	1.27	63	200 × 10 ⁻⁴	6.8
			0.26		41 × 10 ⁻⁴	12.2
20% Cs ₂ CO ₃ / γ -Al ₂ O ₃	520	17.2	0.25		40 × 10 ⁻⁴	15
			0.75	67	113 × 10 ⁻⁴	6.8
			0.40		60 × 10 ⁻⁴	12.2
			0.24		36 × 10 ⁻⁴	15
20% Cs ₂ CO ₃ / γ -Al ₂ O ₃	800	15	0.55	70	78 × 10 ⁻⁴	12.2
			0.41		58 × 10 ⁻⁴	6.8
γ -Al ₂ O ₃		3.3-4.0				
Li ₂ CO ₃		4.0-6.8				
Li ₂ O		6.8-12.2				
K ₂ CO ₃		12.2-15				
α -LiAlO ₂		6.8-12.2				
β -CrAlO ₂		6.8				
LiAl ₅ O ₈		4.0-6.8				
KAlO ₂		>17.2				
K β -alumina		4.0-6.8				
CsAlO ₂		15.0-17.2				

cence. β -LiAlO₂ is not observed, at any temperature, by X-ray diffraction.

These conclusions are corroborated by X-ray data, which demonstrate LiAlO₂ hydrate is present up to 170°, and is presumably converted to α -LiAlO₂ upon heating. (Attempts to detect the hydrate by phosphorescence failed, as the tracers did not phosphoresce in LiAlO₂ hydrate.) On the other hand, the X-ray data indicate the presence of crystalline LiAl₅O₈ at high temperatures. It seems probable that some poorly crystalline LiAl₅O₈ is formed at lower temperatures.

VI. K₂CO₃/ γ -Al₂O₃ and Cs₂CO₃/ γ -Al₂O₃ Catalysts

K₂CO₃/ γ -Al₂O₃ catalysts were prepared with loadings of 9 and 18 wt %, corresponding to K₂O · 16Al₂O₃ and K₂O · 8Al₂O₃, and calcined at temperatures up to 1200°.

X-Ray studies showed the presence, at low temperature, of some KHCO₃ (decomposing at 130°) together with K₂CO₃ and γ -Al₂O₃. The lines due to K₂CO₃ disappeared at about 550° and somewhere near 1150° the γ -Al₂O₃ transformed directly into α -Al₂O₃. At 1050° crystalline β -(K)-alumina was formed.

Thermal Analysis. Upon heating pure K₂CO₃ · xH₂O lost its water of crystallization, with endotherms at 130 and 170°; melting started at 900° and was accompanied by rapid decomposition. Samples of γ -Al₂O₃ impregnated with 9% K₂CO₃ yielded new endotherms (with weight loss), having maxima at 320 and 510°. No melting of K₂CO₃ was observed. In our opinion, these findings suggest that there is some kind of interaction between K₂CO₃ and γ -Al₂O₃ with loss of CO₂. This is also in agreement with results from C analysis (after calcination at 550° about 50% of the carbonate had decomposed).

Phosphorescence spectroscopy was used to detect compounds formed from K₂O and γ -Al₂O₃. The situation here

is simpler than that with Li, as only two such compounds are known to exist, viz. KAlO₂ and K β -Al₂O₃.

Phosphorescence spectra of these compounds doped with Fe, Cr, and Mn are summarized in Tables I-III, and show that the occurrence of potassium β -alumina can be established by using Cr and Fe as tracers and that the presence of KAlO₂ can be deduced from the emission at 760 nm in the Fe excitation spectrum.

Phosphorescence measurements of the doped K₂CO₃ (9 and 18%)/ γ -Al₂O₃ catalysts calcined at different temperatures gave the following results: Fe³⁺ excitation spectra of samples heated up to 900° only featured a charge-transfer band characteristic of Fe³⁺-doped γ -Al₂O₃; spectra of samples doped with Cr³⁺, only showed the presence of Cr γ -Al₂O₃; after calcination above 900° both Cr³⁺- and Fe³⁺-doped samples gave spectra indicative of K β -alumina formation; Mn-excitation spectra failed to yield any useful information, as they were composed of many broad overlapping bands.

We conclude that compound formation is not observed by phosphorescence methods when samples are at temperatures below 900°. As KAlO₂ is very hygroscopic, rapid formation of a hydrate might have prevented its detection. To investigate this possibility we performed a special series of experiments in which the calcined catalysts were carefully handled inside a drybox. However, the results were the same as those obtained previously.

The presence of KAlO₂ and potassium β -alumina was also investigated by ir spectroscopy. Only samples calcined at 1200° yielded absorptions bands due to potassium β -alumina; bands due to KAlO₂ were not observed, irrespective of the calcination temperature adopted.

Probably compound formation does not occur to any appreciable extent under these circumstances. Anyway, it proceeds for more slowly than with Li, which is in line with

results of reactions between powders of Li_2CO_3 , Na_2CO_3 , and Al_2O_3 .^{29,30} This is presumably due to the large size of the K^+ ion. Apparently, K_2CO_3 reacts easily with acidic sites on the surface of the support.

Several reactions can be envisaged: K_2CO_3 might react with surface OH groups to yield OK groups. Furthermore, K_2O resulting from K_2CO_3 decomposition might react with exposed Al^{3+} ions at the surface (Lewis acid centers), again forming Al-OK groups. Finally, K^+ might occupy Al-O vacancies at the surface. Our present data do not allow us to specify the actual state of the K^+ ions in such detail, however.

The situation with Cs is very similar. Again, according to elemental analysis for C, the carbonate mounted on γ - Al_2O_3 decomposes below the decomposition temperature of the pure compound; X-ray analysis does not show the presence of any Cs-containing compound, even in samples calcined at 1200°.

The only compounds known to form from Cs_2O and Al_2O_3 are CsAlO_2 and cesium β -alumina. The spectra obtained with the tracers in cesium β -alumina are identical with those in potassium β -alumina; Fe/ CsAlO_2 emits at 660 nm (ligand-field excitation), Mn and Cr do not phosphoresce in CsAlO_2 .

Phosphorescence measurements performed on the calcined $\text{Cs}_2\text{CO}_3/\gamma\text{-Al}_2\text{O}_3$ catalysts (20 and 40 wt %) did not reveal any compound formation, even with samples calcined at 1200°. This is in line with results of elemental analysis, which indicate that at calcination temperatures above 800° Cs evaporates from the catalyst, so that at 1200° only a trace of Cs is left. It is obvious that this will have important consequences for the preparation, regeneration, and stability of Cs-containing catalysts.

Appendix. Basic Properties of Alkali Carbonate/ γ - Al_2O_3 Catalysts

Alkali carbonate markedly changes the acidic and basic properties of γ - Al_2O_3 based catalysts, and is often used to suppress side reactions, etc. Some results concerning the basic sites on the catalysts are given here and discussed against the background of the structure of the catalyst.

The basicity of these sites was assessed with Hammett indicators³¹ and their number was established by titration with a 0.1 M solution of benzoic acid benzene. Furthermore, by using different indicators we determined the distribution of the basic sites according to their basicity. The following indicators were employed: 4-dimethylaminoazobenzene ($H_0 = 3.3$), phenylazonaphthylamine ($H_0 = 4.0$); Bromothymol Blue ($H_0 = 6.8$); 2,4,6-trinitroaniline ($H_0 = 12.2$); 2,4-dinitroaniline ($H_0 = 15$) and 4-chloro-2-nitroaniline ($H_0 = 17.2$).

The results are summarized in Table XII. Column 3 shows the H_0 values of the most basic sites, determined by color change of the indicators, while column 4 lists the number of basic sites with H_0 equal to or higher than the H_0 of the indicators used in the titration, whose values are given in column 7. Column 6 shows the calculated number of basic sites per unit surface area.

These figures show that $\text{Li}_2\text{CO}_3/\gamma\text{-Al}_2\text{O}_3$ catalysts do not contain highly basic sites; the number of basic sites decrease slowly with increasing calcination temperature, and is always very small considering the amount of Li present (1.3 mequiv/g). This can be explained from what is known

about the structure of the catalyst and the basic properties of the model compounds. At low temperatures most of the Li is present as Li_2CO_3 , which has a H_0 below 6.8. At higher temperatures the carbonate decomposes to yield more basic sites, but this process is counteracted by compound formation, rendering many Li atoms inaccessible.

With K and Cs the situation is different. Catalyst calcined at low temperatures have many weakly basic sites, presumably due to KHCO_3 , and a few more strongly basic sites, the total number roughly corresponding to the amount of K^+ present. The latter sites could be due to K_2CO_3 or a decomposition product. At higher temperatures the weakly basic sites disappear, and the number of strongly basic sites increases. The total number of sites, however, diminishes by a factor of 3. As yet, we have no proper explanation for this phenomenon.

References and Notes

- (1) G. T. Pott and B. D. McNicol, *Discuss. Faraday Soc.*, **52**, 121 (1971).
- (2) R. M. Levy and D. J. Bauer, *J. Catal.*, **9**, 76 (1967).
- (3) G. B. Porter and H. L. Schl  ter, *Ber. Bunsenges. Phys. Chem.*, **68**, 316 (1964).
- (4) W. H. J. Stork, J. G. F. Coolegem, and G. T. Pott, *J. Catal.*, **32**, 497 (1974).
- (5) G. T. Pott and B. D. McNicol, *J. Chem. Phys.*, **56**, 5246 (1972).
- (6) Y. F. Y. Yao and J. T. Kummer, *J. Inorg. Nucl. Chem.*, **29**, 2453 (1967).
- (7) B. D. McNicol and G. T. Pott, *J. Lumin.*, **6**, 320 (1973).
- (8) G. T. Pott and B. D. McNicol, *J. Solid State Chem.*, **7**, 132 (1973).
- (9) H. A. Lehmann and H. Hesselbarth, *Z. Anorg. Allg. Chem.*, **315**, 14 (1962); F. Stewner and R. Hoppe, *ibid.*, **380**, 241 (1971); **381**, 149 (1971).
- (10) B. N. Figgis, "Introduction to Ligand Fields," Interscience, New York, N.Y., 1967; A. B. P. Lever, "Inorganic Electronic Spectroscopy," Elsevier, Amsterdam, 1968; G. B. Porter and H. L. Schl  ter, *Ber. Bunsenges. Phys. Chem.*, **68**, 316 (1964); P. D. Fleischauer and P. Fleischauer, *Chem. Rev.*, **70**, 199 (1970); Y. Tanabe and S. Sugano, *J. Phys. Soc. Jap.*, **9**, 753 (1954).
- (11) D. T. Palumbo and J. J. Brown Jr., *J. Electrochem. Soc.*, **117**, 1184 (1970).
- (12) D. T. Palumbo and J. J. Brown Jr., *J. Electrochem. Soc.*, **118**, 1159 (1971).
- (13) F. A. Kroger, "The Chemistry of Imperfect Crystals," North-Holland Publishing Co., Amsterdam, 1964.
- (14) P. W. Selwood, T. E. Moore, M. Ellis, and W. Wethington, *J. Amer. Chem. Soc.*, **71**, 693 (1949).
- (15) R. D. Shannon and C. T. Prewitt, *Acta Crystallogr., Sect. B*, **25**, 925 (1969).
- (16) M. Marezio and J. P. Remeika, *J. Chem. Phys.*, **44**, 3143 (1966); M. Marezio, *Acta Crystallogr.*, **19**, 396 (1965).
- (17) H. A. Lehmann and H. Hesselbarth, *Z. Anorg. Allg. Chem.*, **313**, 117 (1961).
- (18) S. Geschwind, P. Kisliuk, M. P. Klein, J. P. Remeika, and D. L. Wood, *Phys. Rev.*, **126**, 1684 (1962).
- (19) D. S. McClure, *J. Chem. Phys.*, **36**, 2757 (1962).
- (20) H. P. Fritzer, E. Sliuc, and K. Torkar, *Monatsh. Chem.*, **104**, 172 (1973).
- (21) These data can be compared with those published recently by Fritzer, *et al.*,²⁰ from reflection measurements: $10Dq = 19,000\text{ cm}^{-1}$, $B = 660\text{ cm}^{-1}$.
- (22) (a) D. T. Palumbo, *J. Lumin.*, **4**, 89 (1971); (b) N. T. Melamed, F. de S. Barros, P. J. Viccaro, and J. O. Artman, *Phys. Rev.*, **B**, **5**, 3377 (1972).
- (23) R. C. deVries and W. L. Roth, *J. Amer. Ceram. Soc.*, **52**, 364 (1969); Y. Le Cars, J. Th  ry, and R. Collongues, *C. R. Acad. Sci., Ser. C*, **274**, 4 (1972).
- (24) C. R. Peters, M. Bettman, J. W. Moore, and M. D. Glick, *Acta Crystallogr., Sect. B*, **27**, 1826 (1971); M. S. Wittingham, R. W. Helliwell, and R. A. Huggins, Technical Report, Department of Material Science, Stanford University, Stanford, Calif., 1969; M. Bettman and C. R. Peters, *J. Phys. Chem.*, **73**, 1774; (1969); G. Yamauchi and K. Suzuki, *Bull. Chem. Soc. Jap.*, **41**, (1968); R. Scholder and M. Mansmann, *Z. Anorg. Allg. Chem.*, **321**, 246 (1968).
- (25) A. Bergstein and W. B. White, *J. Inorg. Nucl. Chem.*, **33**, 1629 (1971).
- (26) T. F. W. Barth, *J. Chem. Phys.*, **3**, 323 (1935).
- (27) G. Langlet, *C. R. Acad. Sci.*, **259**, 3769 (1964).
- (28) "Handbook of Chemistry and Physics," 49th ed, The Chemical Rubber Publishing Co., Cleveland, Ohio, 1968.
- (29) V. Frei and V.   slavsk  , *Chem. Z.*, **12**, 399 (1965).
- (30) E. K. Belyaev and V. F. Annopof'sku, *Russ. J. Inorg. Chem.*, **17**, 1078 (1972).
- (31) K. Tanabe, "Solid Acids and Bases," Academic Press, New York, N.Y., 1970.

Nitrogen-15 Nuclear Magnetic Resonance Spectroscopy. Nitrogen-15 Chemical Shifts Determined from Natural-Abundance Spectra^{1a}

John P. Warren and John D. Roberts*

Gates and Crellin Laboratories of Chemistry,^{1b} California Institute of Technology, Pasadena, California 91109 (Received May 23, 1974)

Publication costs assisted by the California Institute of Technology

A number of ¹⁵N chemical shifts, determined at the natural-abundance level of the isotope, are reported for some secondary alkylamines, amides, ureas, urethanes, heterocycles, and miscellaneous compounds. Substituent chemical-shift parameters have been derived for secondary-alkylamine ¹⁵N chemical shifts. The ¹⁵N chemical shifts of secondary alkylamines appear to be potentially useful to determine the number of carbon atoms β to the nitrogen. Effects produced by differences in stereochemistry on the ¹⁵N nmr spectra of di-2-butylamine and di-2-hexylamine have been detected. Possible procedures for accounting for changes in diamagnetic shielding between pairs of compounds are discussed.

Introduction

It has recently been demonstrated that it is possible to obtain ¹⁵N nmr spectra at the natural-abundance level (0.37%) of this isotope,²⁻⁶ although the techniques required are somewhat short of being routine.

At present, it is important for practical detection of natural-abundance ¹⁵N nmr signals by continuous-wave methods that advantage be taken of the nuclear Overhauser effect that arises when proton noise decoupling is used.⁷ When dipole-dipole interactions dominate the ¹⁵N relaxation, the maximum observable nuclear Overhauser effect of -3.9 is obtained. Relaxation mechanisms, such as proton exchange modulation of ¹⁵N-¹H scalar coupling and spin-rotation interactions, reduce the observed nuclear Overhauser effect, requiring very substantial increases in spectral accumulation time to obtain a given signal-to-noise ratio. In unfavorable cases, the opposing effects of dipole-dipole and other interactions can lead to no ¹⁵N signal being observed when proton decoupling is used.

The early natural-abundance ¹⁵N nmr work was done using standard continuous-wave spectral time-averaging methods.^{2,3} Now, Fourier-transform methods are proving valuable in ¹⁵N nmr,^{4,5} although there are potential difficulties with long ¹⁵N relaxation times for those substances where there is no proton directly bonded to nitrogen.^{8,9} However, judicious use of paramagnetic materials (*e.g.*, tris(acetylacetonato)chromium(III)) should help to alleviate problems caused by long ¹⁵N relaxation times,¹⁰ but, of course, at the price of losing the nuclear Overhauser effect.

Most of the data reported here have been obtained using continuous-wave methods, although the Fourier-transform technique was available to us toward the end of the work. The purpose of the study was to probe further the possibilities for natural-abundance ¹⁵N nmr.

Results

The nitrogen chemical shifts are summarized in Table I. Where comparable ¹⁴N (or other ¹⁵N) chemical-shift results were available from other sources, these are given for comparison. No isotope effect upon the chemical shifts is expected.^{11,12} Some of the variations between ¹⁴N and ¹⁵N chemical shifts arise from use of different references and

experimental conditions, and, of course, quadrupolar broadening of ¹⁴N resonances may lead to uncertainty regarding ¹⁴N peak positions. The shifts of ¹⁵N-labeled ammonium chloride, tetramethylammonium iodide, and nitric acid are also given to facilitate relationship of data referenced to tetramethylammonium chloride or to other nitrogen chemical-shift scales used in the literature.^{13,14}

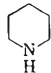
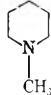
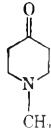
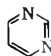
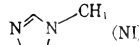
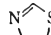
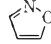
For converting nitrogen chemical shifts from the literature to the tetramethylammonium chloride scale, we have preferred to use shifts given for the tetramethylammonium ion, nitromethane, nitrate ion, or aqueous nitric acid. Where more than one method of interconversion was possible, frequently significant discrepancies were encountered. Shifts measured relative to ammonium ion appear to be less satisfactory than other standards, possibly because of the rather marked sensitivity of ammonium ion shifts themselves to experimental conditions. Thus, there seems to be an uncertainty of a few ppm when various nitrogen chemical-shift scales are compared. This emphasizes the timeliness of Becker's call for an agreed-upon nitrogen chemical-shift scale.¹³

Proton-decoupled ¹⁵N spectra taken by continuous-wave methods of a number of compounds lacking protons directly bonded to nitrogen nevertheless gave inverted resonances, showing that dipole-dipole interactions predominated over other relaxation mechanisms. When using the Fourier-transform technique, it was not convenient to ensure routinely whether peaks were actually inverted, and arbitrary peak phasing was used.

The proton-decoupled ¹⁵N nmr spectra of amides, urethanes, and ureas are obtained with ease when there is a directly bonded proton on nitrogen (although sometimes even in its absence), in contrast to what happens usually with primary and secondary alkylamines. The important factor here is presumed to be the rate of proton chemical exchange from amide nitrogen, which is much slower than from amino nitrogen.¹⁵ For this reason, chemical-exchange modulation of proton-nitrogen scalar coupling is expected to be unimportant with respect to dipole-dipole relaxation for amide nitrogen.

Only a few ¹⁵N chemical shifts of tertiary amines have been measured in this work, because of the long spectral accumulation times required due to long spin-lattice relaxation times and apparently unfavorable nuclear Overhauser

TABLE I: ^{15}N Chemical Shifts^a

Compound	$\delta^{15}\text{N}$, ppm	$\delta^{15}\text{N}$, ppm	$\delta^{15}\text{N}(\text{calcd})$, ppm
D,L-HOCH ₂ CH(CH ₂)NH ₂	-9.3		
CH ₃ CH ₂ CH ₂ CH ₂ NH ₂	-22.5 (-21.7 ^b)	-26; ^c +18 ^d	
CH ₃ NHCH ₂ CH ₃	-15.8		-14.0
(CH ₃ CH ₂) ₂ NH	4.1 (2.7 ^b)	9; ^d 2; ^c -5 ^e	0.3
CH ₃ NHCH ₂ CH ₂ CH ₂ CH ₃	-19.4		-16.1
(CH ₃ CH ₂ CH ₂) ₂ NH	-4.6	-23; ^f -8 ^e	-3.9
[(CH ₃) ₂ CH] ₂ NH	32.3	23 ^e	28.8
(CH ₃) ₃ CNHCH(CH ₃) ₂	38.7		43.0
(CH ₃ CH ₂ CH ₂ CH ₂) ₂ NH	-3.8	-18; ^c -2 ^e	-3.9
meso- and D,L-[CH ₃ CH ₂ CH(CH ₃) ₂ NH	24.1		24.6
[(CH ₃) ₂ CHCH ₂] ₂ NH	23.6		
[CH ₃ (CH ₂) ₄] ₂ NH	-8.7		-8.2
[(CH ₃) ₂ CHCH ₂ CH ₂] ₂ NH	-3.2		-3.9
[(CH ₃) ₂ CHCH ₂ CH ₂] ₂ NH	-3.5		-3.9
[CH ₃ (CH ₂) ₅] ₂ NH	-3.2		-3.9
meso- and D,L-[CH ₃ (CH ₂) ₃ CH(CH ₃) ₂ NH	25.7		24.6
[CH ₃ (CH ₂) ₆] ₂ NH	25.3		
	-3.1		-3.9
	-4.9 (-5.9 ^b)	-7; ^g -12 ^e	
(CH ₃) ₃ SiNHSi(CH ₃) ₃	-16.2	-15 ^h	
(CH ₃ CH ₂ CH ₂ CH ₂) ₃ N	-4.6	-5; ⁱ +15 ^e	
	-4.6		
	-7.0		
NH ₂ CHO	69.0 (70.6; ^j 71.7 ^k)	65.8; ^l 65.1; ^m 70; ⁱ 72 ⁿ	
CH ₃ NHCHO	66.5 (66.5 ^j)	64.2; ^m 66; ⁿ 69.6 ^l	
(CH ₃) ₂ NCHO	60.3	61; ^{i,o} 58.3; ^m 58 ^p	
(CH ₃ CH ₂ CH ₂ CH ₂) ₂ NCHO	82.2		
NH ₂ COOCH ₂ CH ₃	28.5		
CH ₃ CH ₂ NHCOOCH ₂ CH ₃	41.8		
NH ₂ CONH ₂	33.1 (33.1 ^q)	34; ⁱ 16; ^f 31.5; ^r 27 ^s	
(CH ₃) ₂ NCON(CH ₃) ₂	18.9	14.5 ^t	
	251.3	254; ⁱ 253 ^u	
	118.3	126; ^v 116 ^{o,w}	
	279.5	281 ^w	
	339.6	339 ^w	
CH ₃ NO ₂	336.7 (338.1; ^z 339.3 ⁱ)	337; ⁱ 333.5; ^c 336 ^a	
¹⁵ NH ₄ Cl	-18.1 (-18.6; ^y -20.7 ⁱ)	-21 ^{e,i}	
(CH ₃) ₄ ¹⁵ Ni (≈0.3 M)	-1.1	0.1; ^z	
H ¹⁵ NO ₃ (≈10 M)	330.6 (325 ^{aa})	332; ⁱ 334.5 ^c	

^a Downfield from external $\approx 12 M$ aqueous (CH₃)₄¹⁵NCl, ± 0.2 ppm; $\delta^{15}\text{N}(\text{calcd})$ values have been calculated using the substituent parameters for secondary alkylamines (see text). ^b Reference 2. ^c M. Witanowski and H. Januszewski, *Can. J. Chem.*, **47**, 1321 (1969). ^d D. W. Turner, quoted in reference of footnote i. ^e W. Beck, W. Becker, H. Nöth, and B. Wrackmeyer, *Chem. Ber.*, **105**, 2883 (1972). ^f B. E. Holder and M. P. Klein, *J. Chem. Phys.*, **23**, 1956 (1955). ^g P. C. Lauterbur, "Determination of Organic Structures by Physical Methods," Vol. 2, F. C. Nachod and W. D. Phillips, Eds., Academic Press, New York, N.Y., 1962, p 465. ^h K. A. Andrianov, V. F. Andronov, V. A. Drozdov, D. Ya. Zhinkin, A. P. Kreshkov, and M. M. Morgunova, *Proc. Acad. Sci. USSR*, **202**, 58 (1972). ⁱ D. Herbison-Evans and R. E. Richards, *Mol. Phys.*, **8**, 18 (1964). ^j Reference 4. ^k R. J. Chuck, D. G. Gillies, and E. W. Randall, *Mol. Phys.*, **16**, 121 (1969); ^l P. Hampson and A. Mathias, *Mol. Phys.*, **11**, 541 (1966). ^m Reference 40. ⁿ H. Saito, Y. Tanaka, and K. Nukada, *J. Amer. Chem. Soc.*, **93**, 1077 (1971). ^o M. Witanowski, L. Stefaniak, H. Januszewski, and Z. W. Wolkowski, *Tetrahedron Lett.*, 1653 (1971). ^p M. Bose, N. Das, and N. Chatterjee, *J. Mol. Spectrosc.*, **18**, 32 (1965). ^q G. A. Olah and A. M. White, *J. Amer. Chem. Soc.*, **90**, 6087 (1968). ^r Reference 45. ^s M. Witanowski, *J. Amer. Chem. Soc.*, **90**, 5683 (1968). ^t M. Witanowski, L. Stefaniak, S. Peksa, and H. Januszewski, quoted in M. Witanowski and G. A. Webb, Eds., "Nitrogen NMR," Plenum Press, London, 1973, p 190. ^u M. Witanowski, L. Stefaniak, H. Januszewski, Z. Grabowski, and G. A. Webb, *Bull. Acad. Pol. Sci., Ser. Sci. Chim.*, **20**, 917 (1972). ^v H. Saito, Y. Tanaka, and S. Nagata, *J. Amer. Chem. Soc.*, **95**, 324 (1973). ^w M. Witanowski, L. Stefaniak, H. Januszewski, Z. Grabowski, and G. A. Webb, *Tetrahedron*, **28**, 637 (1972). ^x E. D. Becker, private communication. ^y M. Alei, Jr., A. E. Florin, and W. M. Litchman, *J. Phys. Chem.*, **75**, 1758 (1971). ^z E. D. Becker, *J. Magn. Resonance*, **4**, 142 (1971). ^{aa} J. B. Lambert, B. W. Roberts, G. Binsch, and J. D. Roberts, "Nuclear Magnetic Resonance in Chemistry," B. Pesce, Ed., Academic Press, New York, N.Y., 1965, p 269.

er effects. Now that Fourier-transform techniques are available, investigation of natural-abundance ¹⁵N chemical shifts of tertiary amines should be more practical, as the greater sensitivity of these techniques will offset the sacrifice of some or all of the nuclear Overhauser enhancement that results from use of paramagnetic material to shorten spin-lattice relaxation times.¹⁰

The stability of our Fourier transform system with internal deuterium lock, relative to our former continuous-wave system employing an external water lock, allowed for much better resolution and precise determination of chemical-shift effects. For example, Fourier-transform spectra of di-2-butylamine and di-2-hexylamine each showed two peaks, separated by 0.5₆ and 0.3₇ ppm, respectively, as corresponds to the meso and D,L forms, although at this time, we do not know which peaks should be assigned to each. Similar stereochemical effects are well established in ¹³C nmr spectra.¹⁶⁻²⁰ Especially pertinent here is that carbon 4 of 3,5-dimethylheptane shows a chemical-shift difference of 0.2 ppm between its meso and D,L isomers¹⁷ which is very comparable to the 0.6 ppm ¹⁵N-shift difference observed for di-2-butylamine, the nitrogen analog of 3,5-dimethylheptane.

Discussion

Empirically derived substituent parameters have proved very useful in summarizing a large body of ¹³C chemical-shift data,^{17,21,22} and analogous ¹⁵N parameters have been derived for primary alkylamines² and methylhydrazines.³ A regression analysis was performed on the secondary alkylamine ¹⁵N chemical shifts measured in the present work with

$$\delta_N = n_\beta\beta + n_\gamma\gamma + C \quad (1)$$

Here, n_β and n_γ are the numbers of carbon atoms two bonds or three bonds removed from the nitrogen, respectively; β and γ are the substituent parameters, and C is a constant. Preliminary analyses had indicated that consideration of parameters for substituents further removed from the nitrogen atom than the γ position was unnecessary, as these parameters were not statistically significant.²³ The final regression analysis gave alkyl substituent parameter values of $\beta = 14.3 \pm 0.5$ ppm, $\gamma = -2.1 \pm 0.5$ ppm, and $C = -28.2$ ppm. The standard deviation of the dependent variable was 2.0 ppm, and the substituent parameters were significant at the 95% level.

For ¹³C nmr shifts, the α -substituent parameter appears to be a composite of diamagnetic and paramagnetic shielding effects arising from the inductive mechanism (and steric influences where the α substituent interacts sterically with other groups present),^{26,27} while the β parameter results predominately from an inductive effect upon the local paramagnetic shielding term. Mason indicates that after correction of the α parameter for local diamagnetic shielding, the ratio of the α and β parameters for ¹³C chemical shifts of alkanes is close to that expected for an inverse-cube law of the internuclear distances.²⁶ The γ effect is considered to be the result of steric interactions.^{22,27-29}

Comparison of primary and secondary amines indicates that substitution of alkyl on ¹⁵N causes a shift of +9 ppm.² With this and calculated values for the local diamagnetic shielding term σ_d^N of methylamine and dimethylamine,³⁰ it appears that the local paramagnetic shielding contribution

TABLE II: Calculated Diamagnetic Shielding Terms, σ_d^N , for Various Alkylamine Partial Structures

Structure	σ_d^N ^a
Free nitrogen atom	-325.5
N-H	-334.8
N-C	-363.8
	-382.4
	-391.3
	-395.7
	-414.2
	-411.4

^a In ppm, with respect to the bare nitrogen nucleus; the shielding contributions of the atoms shown in bold type have been considered. The procedure was that of ref 31.

σ_p^N to the α substituent chemical-shift parameter is offset by -29 ppm from the change in local diamagnetic shielding upon introduction of an extra α alkyl substituent. Thus, for σ_p^N , the substituent parameters are $\alpha = 38$ ppm, $\beta = 14.3$ ppm, and $\gamma = -2.1$ ppm. The distances from the nitrogen atom to the α and β carbon atoms are 1.47 and 2.46 Å, respectively. These distances have r^{-3} factors of 0.32 and 0.067, whose ratio (4.7) is substantially different from the ratio (2.6) of the α and β substituent parameters for σ_p^N . This analysis suggests for secondary alkylamines that other factors beside internuclear distance may be important in determining σ_p^N on alkyl substitution,³² although this conclusion does depend on the choice of appropriate σ_d^N values on alkyl substitution. The best way to proceed is still in doubt. Thus, Grinter and Mason have suggested use of a local σ_d^N , rather than the all-atom σ_d^N employed by Flygare and Goodisman, and by Ramsey.³³⁻³⁵ Comparison of calculated σ_d^N values for various alkylamine partial structures illustrates some of the problems. The σ_d^N values in Table II have been calculated considering the diamagnetic-shielding contributions to the nitrogen atom of the atoms shown in bold type. Replacement of a proton on nitrogen by a carbon is expected to shield the nitrogen by an additional 29 ppm, and a proton on the carbon atom α to nitrogen to give a further increment of 4.4 ppm. A carbon atom β to the nitrogen would contribute shielding amounting to 22.9 ppm. These figures demonstrate that calculated diamagnetic-shielding contributions, governed, as they are, by an inverse linear law for internuclear distance, can be substantial relative to those of directly bonded atoms, even for atoms two or more bonds away from nitrogen, especially for atoms with comparatively large atomic numbers.

Recent publications have considered calculation of the nitrogen shifts of alkylamines by more sophisticated methods.^{36,37} In one investigation,³⁶ increases in diamagnetic shielding of 26 and 44 ppm were found on going from am-

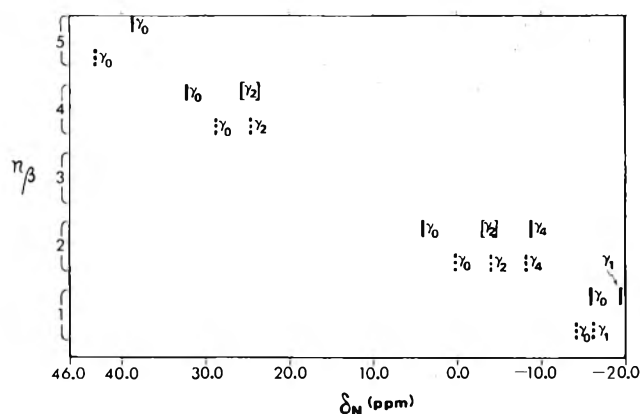


Figure 1. Variation of ^{15}N chemical shifts for secondary amines with varying degrees of alkyl substitution. The ordinate is n_β , the number of alkyl groups on the carbons directly attached to nitrogen. The number of γ substituents for each value of n_β is indicated by γ_n , where n is the number of γ substituents.

monia to methylamine and from methylamine to dimethylamine, respectively. The predicted effects are not additive but are reasonably comparable to the changes in diamagnetic shielding predicted using the Flygare-Mason σ_d^{N} values.^{33,34} On the other hand, Litchman's calculations predicted additive diamagnetic shielding decrements of 4.5 ppm on successive methylations of ammonia.

Use of diamagnetic shielding contributions in discussion of nitrogen shifts has been criticized on the basis that the predicted diamagnetic contributions are usually opposite in direction to the observed shift changes.^{38,39} This argument is hardly compelling, because it has never been claimed that the calculated diamagnetic contributions have done anything more than to help make more clear what the actual magnitude of the dominant paramagnetic contributions are.

Hydrogen bonding is expected to have considerable influence on the shifts of ^{15}N nuclei.^{3,40-43} Ideally, a set of alkyl substituent shift parameters for amines would also include allowance for the variability of hydrogen-bonding possibilities between primary, secondary, and tertiary amines. However, construction of a more sophisticated set of substituent parameters will need to be postponed until more ^{15}N shifts of tertiary alkylamines have been obtained.

The secondary alkylamine substituent shift parameters of $\beta = 14.3$, $\gamma = -2.1$, and $C = -28.2$ ppm are reasonably comparable with the parameters obtained earlier² for primary alkylamines: $\alpha = 8.7$, $\beta = 18.2$, $\gamma = -2.7$, $\delta = 3.0$, $\epsilon = -1.8$, and $C = -48.4$ ppm. Because the data set for the primary alkylamine parameters was relatively small, none of the α to ϵ parameters is statistically significant at the 95% level. A somewhat better fit is possible for a four-parameter equation which neglects the effect of an ϵ substituent and gives $\alpha = 7.8$, $\beta = 18.6$, $\gamma = -2.4$, $\delta = 2.5$, and $C = -48.4$ ppm.⁴⁴

The ^{15}N shift of -16.2 ppm for hexamethyldisilazane is interesting compared to the calculated shift of about 58 ppm for its carbon analog, di-*tert*-butylamine. However, the local diamagnetic shielding term σ_d^{N} suggests that the nitrogen of a disilazane should be more shielded than that of a secondary amine by 91 ppm. Thus, the high-field shift of hexamethyldisilazane seems likely to be due to the larger diamagnetic shielding effect of the two silicon atoms compared to two carbon atoms.

It seems noteworthy that 1,1,3,3-tetramethylurea gives a nitrogen signal 14.2 ppm upfield from that of urea. The pattern of amine substitution would have suggested a downfield shift upon methylation of urea. The observed shift is roughly four times the reported upfield shift of 4 ppm in monomethylurea.⁴⁵

The ^{15}N chemical shifts of secondary alkylamines appear to be useful in qualitative analysis to obtain information about the degree of alkyl substitution close to the nitrogen atom. Figure 1 shows the nitrogen chemical shifts in terms of n_β , the number of substituents on the carbons directly attached to nitrogen. Single solid lines represent single compounds, and brackets the chemical-shift range of a group of compounds. The dashed lines represent the nitrogen chemical shifts predicted from the secondary-alkylamine substituent parameters. Because of the considerable magnitude of the β parameter, there seems to be little possibility of ambiguity in using the experimental nitrogen chemical shift to determine the number of carbon atoms β to the nitrogen atom. The shifts resulting from differences in γ substitution appear, from Figure 1, to have less diagnostic value.

Experimental Section

The unlabeled compounds were commercial products which, in the case of liquids, were distilled before use. The ^{15}N spectra were taken on the neat liquids. The secondary alkylamines were distilled from lithium aluminium hydride in order to minimize proton exchange.⁷ A recent report on formation of secondary amines by base-catalyzed reactions of primary amines⁴⁶ suggests that this may be an inappropriate general method to use in drying amines; previously, sodium hydroxide or potassium hydroxide pellets have been used.²

Much of the early ^{15}N shift data, referenced to nitric acid, were collected by continuous-wave methods on the unmodified DFS-60 spectrometer operating at 6.08 MHz;² the probe temperature was about 45–55° when proton noise decoupling was used. Field stabilization was provided by an external water lock. Later data, referenced to the tetramethylammonium chloride resonance, were collected by Fourier-transform techniques using a Varian DFS-60 spectrometer modified by a Bruker transmitter, probe, receiver, and deuterium internal lock system, and employing a Varian 620i computer and its associated software. The spectra were referenced using a 4-mm o.d. Wilmad precision coaxial capillary containing an approximately 12 M solution of $(\text{CH}_3)_4^{15}\text{NCl}$ in D_2O , mounted inside a 10-mm nmr tube containing the sample. The D_2O signal was used for the internal lock. The $(\text{CH}_3)_4^{15}\text{NCl}$ was synthesized from $^{15}\text{NH}_4\text{Cl}$,^{47,48} or purchased from Merck Sharp and Dohme, Canada Ltd. Chemical-shift scales were interconverted using 330.64 ppm as the chemical shift of nitric acid on the tetramethylammonium chloride scale.¹⁴ Chemical shifts throughout this paper are given on the tetramethylammonium chloride scale unless otherwise indicated. With the spectrometer in the Fourier-transform configuration, the probe was cooled by a stream of air, so that proton decoupling had no significant heating effect. Because of the likely temperature differences between the continuous-wave and Fourier-transform measurements, it was important to show that temperature differences had no important effect on the nitrogen chemical shifts, if the data were to be combined and used in regression analyses to derive substituent chemical-shift parameters. The ^{15}N spectra of

di-*n*-propylamine, diisopropylamine, and di-2-hexylamine taken under the two sets of conditions showed a maximum variation in chemical shifts of 0.15 ppm, so that for a change of about 25° in sample temperatures, there is no significant effect on the nitrogen chemical shifts of these secondary alkylamines.

The ethyl carbamate spectrum was taken of a sample to which the minimum amount of chloroform had been added to give complete solution at the ambient decoupling temperature (approximately 50°).

The regression analyses employed a multiple stepwise linear regression subroutine, REGRES,⁴⁹ run on a PDP-10 computer. The variance ratio (*F* level) of an independent variable, the relative values of variance ratios for the parameters in the regression analysis, and the standard error of the dependent variable were the principal criteria used in assessing the significance of particular regression analyses.

Acknowledgment. We are grateful to Dr. R.L. Lichter for a number of useful discussions, and to Dr. B.L. Hawkins who made the modifications to the spectrometer for Fourier-transform operation.

References and Notes

- (1) (a) Supported by the Public Health Service, Research Grant No. GM-11072 from the Division of General Medical Sciences, and by the National Science Foundation. (b) Contribution No. 4892.
- (2) R. L. Lichter and J. D. Roberts, *J. Amer. Chem. Soc.*, **94**, 2495 (1972).
- (3) R. L. Lichter and J. D. Roberts, *J. Amer. Chem. Soc.*, **94**, 4904 (1972).
- (4) J. M. Briggs, L. F. Farnell, and E. W. Randall, *Chem. Commun.*, 680 (1971).
- (5) P. S. Pregosin, E. W. Randall, and A. I. White, *Chem. Commun.*, 1602 (1971).
- (6) M. G. Gibby, R. G. Griffin, A. Pines, and J. S. Waugh, *Chem. Phys. Lett.*, **17**, 80 (1972).
- (7) R. L. Lichter and J. D. Roberts, *J. Amer. Chem. Soc.*, **93**, 3200 (1971).
- (8) E. Lippmaa, T. Saluvere, and S. Laisaar, *Chem. Phys. Lett.*, **11**, 120 (1971), and references cited therein.
- (9) E. Lippmaa, T. Saluvere, and S. Laisaar, *Eesti NSV Tead. Akad. Toim., Füüs. Mat.*, **21**, 163 (1972).
- (10) L. F. Farnell, E. W. Randall, and A. I. White, *J. Chem. Soc., Chem. Commun.*, 1159 (1972).
- (11) R. Price, Ph.D. Thesis, University of London, 1969.
- (12) E. D. Becker, R. B. Bradley, and T. Axenrod, *J. Magn. Resonance*, **4**, 136 (1971).
- (13) E. D. Becker, *J. Magn. Resonance*, **4**, 142 (1971).
- (14) M. Christl, J. P. Warren, B. L. Hawkins, and J. D. Roberts, *J. Amer. Chem. Soc.*, **95**, 4392 (1973).
- (15) Cf., for example, J. D. Roberts and M. C. Caserio, "Basic Principles of Organic Chemistry," W. A. Benjamin, New York, N.Y., 1964, pp 677-678.
- (16) J. I. Kroschwitz, M. Winokur, H. J. Reich, and J. D. Roberts, *J. Amer. Chem. Soc.*, **91**, 5927 (1969).
- (17) L. P. Lindeman and J. Q. Adams, *Anal. Chem.*, **43**, 1245 (1971).
- (18) C. J. Carman, A. R. Tarpley, Jr., and J. H. Goldstein, *J. Amer. Chem. Soc.*, **93**, 2864 (1971).
- (19) D. Doddrell and N. V. Riggs, *Aust. J. Chem.*, **25**, 2715 (1972).
- (20) H. Eggert and C. Djerassi, *J. Amer. Chem. Soc.*, **95**, 3710 (1973).
- (21) D. M. Grant and E. G. Paul, *J. Amer. Chem. Soc.*, **86**, 2984 (1964).
- (22) B. V. Cheney and D. M. Grant, *J. Amer. Chem. Soc.*, **89**, 5319 (1967).
- (23) The same trend has been noted for alkyl phosphorus compounds, wherein the ³¹P chemical shifts are not affected by substitution beyond the γ position.^{24,25}
- (24) L. D. Quin and J. J. Breen, *Org. Magn. Resonance*, **5**, 17 (1973).
- (25) S. O. Grim, W. McFarlane, and E. F. Davidoff, *J. Org. Chem.*, **32**, 781 (1967).
- (26) J. Mason, *J. Chem. Soc. A*, 1038 (1971).
- (27) D. K. Dalling, D. M. Grant, and E. G. Paul, *J. Amer. Chem. Soc.*, **95**, 3718 (1973).
- (28) D. M. Grant and B. V. Cheney, *J. Amer. Chem. Soc.*, **89**, 5315 (1967).
- (29) J. B. Grutzner, M. Jautelat, J. B. Dence, R. A. Smith, and J. D. Roberts, *J. Amer. Chem. Soc.*, **92**, 7107 (1970).
- (30) The method of calculation has been previously described,^{14,31} with bond lengths taken from "Tables of Interatomic Distances and Configuration in Molecules and Ions," *Chem. Soc., Spec. Publ.*, No. 11, S7, S12, S16 (1958).
- (31) R. Hagen, J. P. Warren, D. H. Hunter, and J. D. Roberts, *J. Amer. Chem. Soc.*, **95**, 5712 (1973).
- (32) See also, R. L. Lichter, "Determination of Organic Structures by Physical Methods," Vol. 4, F. C. Nachod and J. J. Zuckerman, Ed., Academic Press, New York, N.Y., 1971, p 195.
- (33) R. Grinter and J. Mason, *J. Chem. Soc. A*, 2196 (1970).
- (34) W. H. Flygare and J. Goodisman, *J. Chem. Phys.*, **49**, 3122 (1968); see also, T. D. Gierke and W. H. Flygare, *J. Amer. Chem. Soc.*, **94**, 7277 (1972); D. A. Shirley, *Advan. Chem. Phys.*, **23**, 85 (1973).
- (35) N. F. Ramsey, *Phys. Rev.*, **78**, 699 (1950); **83**, 540 (1951); **86**, 243 (1952).
- (36) R. Ditchfield, D. P. Miller, and J. A. Pople, *J. Chem. Phys.*, **54**, 4186 (1971).
- (37) W. M. Litchman, *J. Magn. Resonance*, **12**, 182 (1973).
- (38) M. Witanowski and G. A. Webb, *Annu. Rep. NMR (Nucl. Magn. Resonance) Spectrosc.*, **5A**, 403 (1972).
- (39) M. Witanowski and G. A. Webb, "Nitrogen NMR," Plenum Press, London, 1973, pp 16-18, 28-30.
- (40) H. Kamei, *Bull. Chem. Soc. Jap.*, **41**, 1030 (1968).
- (41) W. M. Litchman, M. Alei, Jr., and A. E. Florin, *J. Amer. Chem. Soc.*, **91**, 6574 (1969).
- (42) M. Alei, Jr., A. E. Florin, and W. M. Litchman, *J. Amer. Chem. Soc.*, **92**, 4828 (1970).
- (43) L. Paolillo and E. D. Becker, *J. Magn. Resonance*, **2**, 168 (1970).
- (44) J. P. Warren, unpublished results.
- (45) P. Hampson and A. Mathias, *J. Chem. Soc. B*, 673 (1968).
- (46) H. G. Richey, Jr., and W. F. Erickson, *Tetrahedron Lett.*, 2807 (1972).
- (47) R. Adams and B. K. Brown, "Organic Syntheses," Collect. Vol. 1, 2nd ed., A. H. Blatt, Ed., Wiley, New York, N.Y., 1941, p 528.
- (48) A. Simon and U. Uhlig, *Chem. Ber.*, **85**, 977 (1952).
- (49) M. A. Efrogmson, "Mathematical Methods for Digital Computers," A. Ralston and H. S. Wilf, Ed., Wiley, New York, N.Y., 1960, p 191.

Electron Nuclear Double Resonance Study of 9-Arylxanthyl Radicals

Yoshio Yamada,* Sadaharu Toyoda, and Kōji Ōuchi

National Research Institute for Pollution and Resources, Kawaguchi, Saitama, Japan 332 (Received January 21, 1974; Revised Manuscript Received May 7, 1974)

Publication costs assisted by the National Research Institute for Pollution and Resources

A series of four 9-arylxanthyl radicals (9-phenyl-, 9-*p*-tolyl-, 9-*o*-tolyl-, and 9- α -naphthylxanthyl) in toluene was investigated by electron nuclear double resonance spectroscopy. The observed endor spectra were analyzed by calculation of the spin density and the assignment of the hyperfine coupling constants was confirmed by computer simulation of the electron spin resonance spectra. The angle between the plane of the xanthyl group and that of the aryl derivative was determined from both the spin densities obtained by experiment and those calculated by the McLachlan SCF-MO method. Consequently, it was found that the plane of *p*-tolyl derivative is twisted by about 52° with respect to that of the xanthyl group and that the 9-phenylxanthyl radical also takes a similar steric arrangement. On the other hand, the angles of twist for 9-*o*-tolyl- and 9- α -naphthylxanthyl radicals were estimated to be about 58 and 65°, respectively. The twisting was found experimentally to be caused by steric hindrance between the xanthyl group and the substituent.

Introduction

Since the first successful electron nuclear double resonance (ENDOR) experiment on a radical in solution,¹ a number of endor measurements have been tried.²⁻⁵ One aim of the application of that technique is to obtain accurate values of hyperfine coupling constants which are too small to be resolvable in the electron spin resonance (ESR) spectrum.

The authors are studying structural changes of aromatic hydrocarbons⁶ in the carbonization process. The radicals produced during carbonization are generally too complex to identify their structure by ESR measurement and endor is a very powerful tool for such cases. In this paper four 9-arylxanthyl radicals (Figure 1) were chosen as a model of thermal cracking of aromatic hydrocarbons. These radicals are easily produced with thermal cleavage of the corresponding dimers^{7,8} and have too complex a structure to be analyzed by ESR alone. Moreover it may be valuable to compare our endor data with those of Sevilla and Vincow⁹ which were obtained for 9-phenylxanthyl by ESR and also to estimate the twisting angle by the steric hindrance of aryl group with the xanthene nucleus.

Experimental Section

All xanthyl radicals were prepared from hydrochloric acid solutions of corresponding xanthenol and vanadium(II) chloride by the method of Conant and Sloan,⁷ except that they were allowed to react under vacuum. The concentration of the solution is approximately 10^{-2} to 10^{-3} M.

Xanthenols were prepared from xanthone and the corresponding Grignard reagents following the method of Gomberg, *et al.*,^{10,11} and purified by recrystallization from benzene or a mixture of benzene and ligroin. The melting points of these compounds are 157–158° for 9-phenylxanthenol, 147–148° for 9-*p*-tolylxanthenol, 163° for 9-*o*-tolylxanthenol, and 196–197° for 9- α -naphthylxanthenol.¹² These values are in nearly good agreement with those of literature.¹³⁻¹⁶

Esr and endor spectra were measured using Japan Elec-

tron Optics Laboratory JES-ME-3X type ESR and ES-EDX1 type endor spectrometers equipped with a variable-temperature attachment.¹⁷

In order to verify the assignment of the coupling constants derived from endor spectra, ESR spectra were calculated on TOSBAC-3400 computer using a program given by Kuwata¹⁸ and compared with the experimental ESR spectra. This program is essentially the same as the SESRS computer program described by Stone and Maki.¹⁹

Results and Discussion

Endor Spectra. As is expected for an equilibrium between radical and dimer, the ESR spectral intensity decreases with decreasing temperature, and the endor signal intensity also decreases. On the other hand, the endor spectral intensity decreases at higher temperatures owing to increasing spin exchange.²⁰⁻²² The most intense signals were observed at -60° for 9-phenyl- and 9-*p*-tolylxanthyl radicals. However, for the 9-*o*-tolyl- and 9- α -naphthylxanthyl radicals, the best enhancement was obtained at -90°. The endor spectra of these radicals are shown in Figure 2. The ESR signals of the former radicals disappeared with decreasing temperature, while those of the latter radicals were observed even at lower temperature near -90°, although their signal intensity decreased considerably. In addition, the toluene solutions of 9-phenyl- and 9-*p*-tolylxanthyl radicals became colorless at lower temperature, but orange-red color remained even at -90° in 9-*o*-tolyl- and 9- α -naphthylxanthyl radicals. From these results the prevention of dimerization of the radicals by steric effect may be a cause of the difference in temperature dependence on signal intensity of the above two groups.

Assignment of Hyperfine Splitting Constants. Two endor lines are usually expected from each group of equivalent protons equally spaced above and below the free-proton frequency. If second-order frequency shift is assumed negligible,²³ the values of the coupling constants are obtained directly from the interval of two lines or from twice of the distance from the free-proton frequency to a line at higher frequency. The values of the coupling constants de-

TABLE I: Proton Hyperfine Splitting of 9-Arylxanthyl Radicals Obtained by Endor (in Gauss)

Position	Xanthyl Radical			
	9-Phenyl- (-60°)	9- <i>p</i> -Tolyl- (-60°)	9- <i>o</i> -Tolyl- (-90°)	9- α -Naphthyl (-90°)
$ a_{3,6}^H $	3.691 ^a (3.809) ^c	3.674 ^a	3.758 ^a	3.756 ^a
$ a_{1,8}^H $	3.191 ^a (3.306) ^c	3.196 ^a	3.252 ^a	3.233 ^a
$ a_{2,7}^H $	0.853 ^b (0.86) ^c	0.866 ^b	0.862 ^b	0.859 ^b
$ a_{4,5}^H $	0.751 ^b (0.74) ^c	0.760 ^b	0.759 ^b	0.766 ^b
$ a_p^H $	0.853 ^b (0.86) ^c	0.866 ^b	0.672 ^b	
$ a_o^H $	0.751 ^b (0.74) ^c	0.760 ^b	0.588 ^b	
$ a_m^H $	0.620 ^b (0.621) ^c	0.639 ^b	0.259 ^{b, d} 0.170 ^{b, e}	
$ a_{2',4'}^H $				0.639 ^b
$ a_{3',5'}^H $				0.532 ^b
$ a_{5',7'}^H $				0.263 ^b
$ a_{6',8'}^H $				0.069 ^b

^a The uncertainty is approximately ± 0.003 G. ^b The uncertainty is approximately ± 0.015 G. ^c See ref 3. ^d This value is assigned to $|a_{5'}^H|$. ^e This value is assigned to $|a_{3'}^H|$.

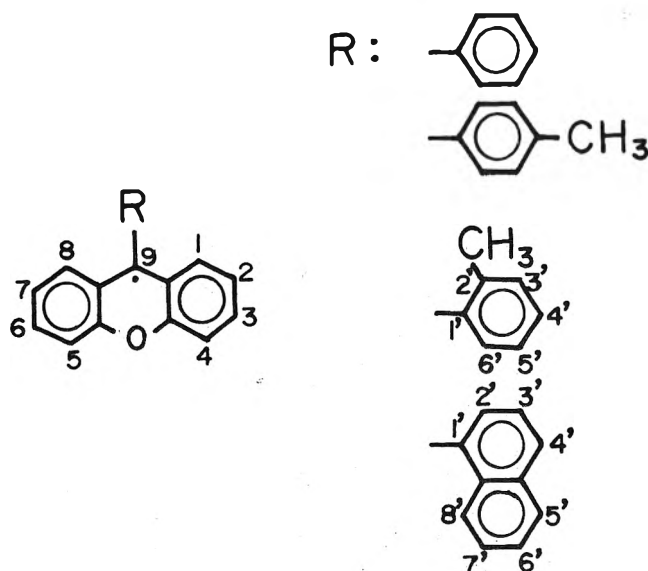


Figure 1. Structural formula and numbering scheme of the 9-arylxanthyl radicals.

terminated on the basis of the assignment described below are given in Table I.

The two signals common to all the spectra were observed near 18–19 MHz, as seen in Figure 2. These lines correspond to coupling constants of about 3.2 and 3.8 G. Sevilla and Vincow assigned the 3.425- and 4.047-G splittings of the xanthyl radical to positions 1 and 3, respectively, by means of experiments.⁸ By analogy with their result, the 3.2- and 3.8-G splittings described above are considered to be due to the protons of positions 1 and 3. The value of the coupling constant $|a_{3,6}^H|$ of 9-*o*-tolyl- and 9- α -naphthylxanthyl radicals is considerably larger than that of 9-phenyl- and 9-*p*-tolylxanthyl radicals (Table I). Also a similar relationship is found for the coupling constant $|a_{1,8}^H|$. These results show that the electron spin of the former radicals is localized in the xanthyl part. It can be explained by considering that the twisting between the xanthyl group and the substituent accompanies the lessening of overlapping of π orbital at positions 9 and 1' and that the structural change inhibits the spin to flow into the substituent through π orbital.

These signal line widths are broader than those in the region of the free-proton frequency and, particularly, a line near 19 MHz in 9-*o*-tolyl- and 9- α -naphthylxanthyl radicals seems to consist of two components. Accordingly, the endor spectra were measured at temperatures ranging from -100 to -40°. Spectral lines weaken at temperatures except for the optimum temperature for endor effect, so that it could not be confirmed experimentally whether broadening of this line is attributable to the difference in conformation.

The assignment of the other lines is not straightforward. The small values of the coupling constants in 9-phenylxanthyl radical are in good agreement with those obtained by Sevilla and Vincow (Table I).⁹ The same endor spectrum was observed for 9-*p*-tolylxanthyl radical. Therefore, the assignment for the two radicals is clear. As can be seen in Table I, the individual splittings $|a_{2,7}^H|$ and $|a_p^H|$ as well as $|a_{4,5}^H|$ and $|a_o^H|$ were not resolved even by means of the endor technique. The endor spectrum of the 9-*o*-tolylxanthyl radical is a little more complicated than that of the 9-phenyl or 9-*o*-tolylxanthyl radical. The magnitudes of the coupling constants are 0.862, 0.759, 0.672, 0.588, 0.259, and 0.170 G. The values of 0.862 and 0.759 G are undoubtedly assigned to the proton coupling constants at positions 2,7 and 4,5 of xanthyl group for the following reason: these values correspond to those in 9-phenyl- and 9-*p*-tolylxanthyl radicals and the small couplings of xanthyl part such as $|a_{2,7}^H|$ and $|a_{4,5}^H|$ have little influence on structural change in the radical. The remaining coupling constants of the 9-*o*-tolylxanthyl radical were assigned, assuming that each coupling constant of the substituent decreases to the same extent as that in the 9-phenyl- or 9-*p*-tolylxanthyl radical. However, the coupling constants of nonequivalent meta positions could not be distinguished. This assignment was made using the calculation of spin density by SCF-MO method. In the same manner, the authors assigned the couplings of the substituent of 9- α -naphthylxanthyl radical which contains many nonequivalent protons. They will be discussed below.

Comparison of Experimental ESR Spectra with Simulated ESR Spectra. All the spectra simulated for these radicals are in fairly good agreement with experiment.²⁴ However, the spectral intensity of the simulated spectra is somewhat different from that of the experiment. One possible explanation



Figure 2. EPR spectra of 9-arylxanthyl radicals: (a) 9-phenyl-, (b) 9-*p*-tolyl-, (c) 9-*o*-tolyl-, and 9- α -naphthylxanthyl radical. The free proton frequency is marked with an arrow.

nation is that a little stronger microwave power was used in order to enhance the wing signal and the spectral lines of the central part might be saturated. The simulated spectra were obtained with the approximation of Lorentzian line shape. This might be another reason for lack of a better fit to the experimental spectrum.

Calculation of the Spin Density and the Angle of Twist. McLachlan SCF-MO spin density has been calculated to investigate the π -electron structure of 9-arylxanthyl radicals.²⁵ Although the results calculated by this method may be insufficient to compare with the accurate values obtained by EPR experiment, this method is considered to be the most elaborate approach to the calculation of spin densities in π radicals.

In the calculations, a semiempirical constant, λ , was chosen as 1.1 since this constant does not depend effectively on the spin densities. Empirical parameters were introduced into the heteroatom model calculation. The Coulomb inte-

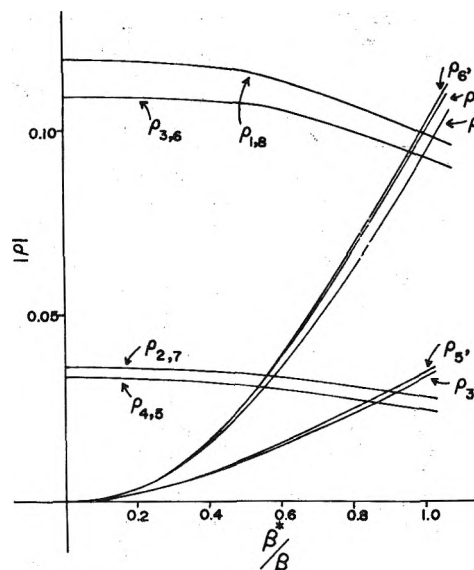


Figure 3. Variation of the absolute value of spin densities with the resonance integral parameter β^*/β for the 9-*o*-tolylxanthyl radical. Numbering of carbon positions is given in Figure 1.

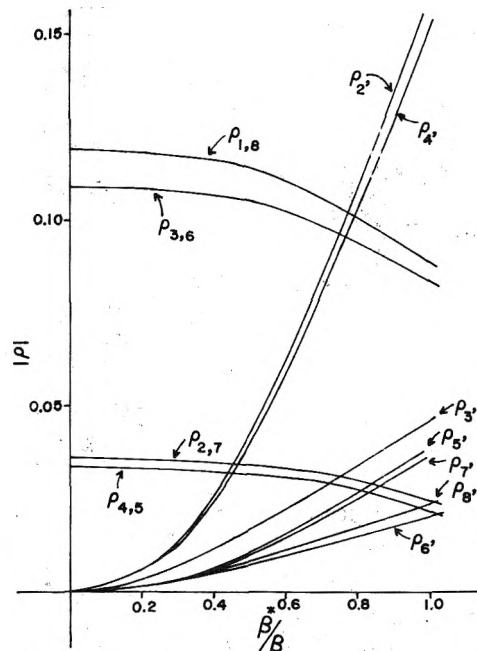


Figure 4. Variation of the absolute value of spin densities with the resonance integral parameter β^*/β for the 9- α -naphthylxanthyl radical. Numbering of carbon positions is given in Figure 1.

gral for the heteroatom becomes $\alpha + h_X\beta$, in which α is the Coulomb integral for benzene carbon, β is the value of resonance integral for two adjacent benzene carbons, and the resonance integral between the benzene carbon, C, and the heteroatom, X, is $k_{C-X}\beta$. For heteroatom parameters for the oxygen atom in xanthyl part, $h_O = 2.0$ and $k_{C-O} = 0.75$ were employed.⁹ The absolute values of calculated spin densities for a function of β^*/β are indicated in Figures 3 and 4, where β^* shows the resonance integral for the bonding between xanthyl group and the substituent. The 9-*p*-tolyl- and 9-*o*-tolylxanthyl radicals contain a methyl group in each substituent. Therefore, the methyl group was treated with hyperconjugation according to the method of Coulson and Crawford.²⁶ The parameters used in this case are

the same values as those for toluene: the Coulomb integrals for the carbon atom and three hydrogen atoms of the methyl group are $h_C = -0.1$ and $h_{H_3} = -0.5$, respectively. The resonance integral for carbon atom-hydrogen atoms of methyl group is $k_{C-H_3} = 2.5$ and that for the methyl group-adjacent carbon atoms is $k_{C-CH_3} = 0.7$.

In Figure 3 the spin density of $|\rho_5|$ is higher than that of $|\rho_3|$ in the range 0.0–1.0 for β^*/β . Hence, $|a_5^H|$ and $|a_3^H|$ were assigned to 0.259 and 0.170 G, respectively (Table I). As is clear from Figure 4, the spin density for the substituent decreases in the following order: $|\rho_2| > |\rho_4| > |\rho_3| > |\rho_5| > |\rho_7| > |\rho_8| > |\rho_6|$ and, in addition, $|\rho_2| \simeq |\rho_4|$, $|\rho_5| \simeq |\rho_7|$, and $|\rho_8| \simeq |\rho_6|$. Therefore, the values of 0.639, 0.532, 0.263, and 0.069 obtained by endor experiment were assigned to $|a_{2,4}^H|$, $|a_3^H|$, $|a_{5,7}^H|$, and $|a_{6,8}^H|$, respectively (Table I).

It is generally known that the spin density of the meta position is not predicted well by the McLachlan's method. Moreover, the value is much smaller than that of ortho or para position (Figure 3). Therefore, in evaluating the angles of twist, $|\rho_d|$ and $|\rho_p|$ were used exclusively and also $|\rho_2|$ and $|\rho_4|$ were chosen in the case of 9- α -naphthyl-xanthyl radical.

The experimental splittings of 9-aryl derivative protons are reduced to the spin densities through the McConnell's relationship²⁷ $a_i^H = Q_i \rho_i^H$, where Q is taken as -27 G, according to Fessenden and Schuler and others.²⁸ From the experimental spin densities in Figures 3 and 4 the angle of twist θ is calculated by use of the following equation: $\beta^* = \beta \cos \theta$. The bond distance between the xanthyl group and the substituent is not in accord with the C–C bond distance in benzene (1.397 Å), so that the above equation does not hold in this case since the resonance integral depends on the C–C bond distance. According to the calculation of Sevilla and Vincow, the equation is transformed as follows: $\beta^* = 0.9\beta \cos \theta$. The calculated angles are summarized in Table II. As the angle of twist for the 9-phenylxanthyl radical, Sevilla and Vincow have given $\theta = 60^\circ$,⁹ being different from that obtained in this work. It seems to arise from the fact that they obtained it by averaging the values not only from $|\rho_p|$ and $|\rho_o|$, but also from $|\rho_s| + \rho_m + \rho_p|$.

It is found clearly from Table II that 9-o-tolyl- and 9- α -naphthylxanthyl radicals are more twisted than the other radicals. Furthermore, the angles for the former radicals may be somewhat larger than the values given in Table II, if the expansion of bond distance between the xanthyl group and the substituent is taken into consideration. Though the values estimated by this method are approximate, it is concluded from them that steric hindrance contributes predominantly to the twisting of the substituent.

McKinley, *et al.*, reported on nuclear magnetic resonance studies of 9-arylxanthene and 9-arylxanthanol that, due to steric interactions between the ortho-substituted group of aryl group and the 1 and 8 hydrogens of xanthyl, the 9-aryl substituent is nearly perpendicular to the xanthyl part.²⁹ Similar conclusions were obtained in relation to some 9-arylxanthyl carbonium ions³⁰ and 9-arylfluorenes.³¹ Since in these compounds there is another substituent at position 9, such as a hydrogen or hydroxyl group, carbon at position 9 is bonded with a sp^3 hybrid orbital. On the contrary, the 9-aryl π orbital of the xanthyl radical interacts with the p π orbital of carbon situated at position 9. The twisting of the ring, owing to steric effect, weakens the sp^2 hybridization and destabilizes the radical because it can not

TABLE II: Angles of Twist of 9-Arylxanthyl Radicals

Xanthyl radical	Angle of twist, deg
9-Phenyl-	54 (60) ^a
9- <i>p</i> -Tolyl-	52
9- <i>o</i> -Tolyl-	58
9- α -Naphthyl-	65

^a See ref 3.

have sp^3 covalent character. Even if severe steric hindrance is added, therefore, the structure perpendicular to the xanthyl group could not be expected for these radicals.

Acknowledgment. The authors wish to express their hearty thanks to Professor Keiji Kuwata of Osaka University for his valuable discussions and helpful advice in McLachlan SCF-MO calculations.

Supplementary Material Available. Figures showing theoretical and experimental spectra will appear following these pages in the microfilm edition of this volume of the journal. Photocopies of the supplementary material from this paper only or microfiche (105 × 148 mm, 24× reduction, negatives) containing all of the supplementary material for the papers in this issue may be obtained from the Journals Department, American Chemical Society, 1155 16th St., N.W., Washington, D. C. 20036. Remit check or money order for \$3.00 for photocopy or \$2.00 for microfiche, referring to code number JPC-74-2512.

References and Notes

- (1) J. S. Hyde and A. H. Maki, *J. Chem. Phys.*, **40**, 3117 (1964).
- (2) L. D. Kispert, J. S. Hyde, C. Boer, D. LaFollette, and R. Breslow, *J. Phys. Chem.*, **72**, 4276 (1968).
- (3) R. D. Allendoerfer and A. S. Pollock, *Mol. Phys.*, **22**, 661 (1971).
- (4) N. M. Atherton, A. J. Blackhurst, and I. P. Cook, *Trans. Faraday Soc.*, **67**, 2510 (1971).
- (5) K. P. Dinse, R. Biehl, K. Mobius, and M. Plato, *J. Magn. Resonance*, **6**, 444 (1972).
- (6) These results will be published in near future.
- (7) J. B. Conant and A. W. Sloan, *J. Amer. Chem. Soc.*, **45**, 2466 (1923).
- (8) (a) M. D. Sevilla and G. Vincow, *J. Phys. Chem.*, **72**, 3635 (1968); (b) *ibid.*, **72**, 3647 (1968).
- (9) M. D. Sevilla and G. Vincow, *J. Phys. Chem.*, **72**, 3641 (1968).
- (10) M. Gomberg and C. S. Schoepfle, *J. Amer. Chem. Soc.*, **39**, 1652 (1917).
- (11) J. B. Conant, L. F. Small, and A. W. Sloan, *J. Amer. Chem. Soc.*, **48**, 1743 (1926).
- (12) All melting points are uncorrected.
- (13) F. Ullmann and G. Engi, *Berichte*, **37**, 2367 (1904).
- (14) H. Bünzly and H. Decker, *Berichte*, **37**, 2931 (1904).
- (15) M. Gomberg and L. H. Cone, *Justus Liebigs Ann. Chem.*, **370**, 142 (1909).
- (16) F. F. Blicke and O. J. Weinkauff, *J. Amer. Chem. Soc.*, **54**, 1446 (1932).
- (17) T. Yamamoto, K. Sato, and T. Miyamae, *Jap. J. Appl. Phys.*, **11**, 1508 (1972).
- (18) K. Kuwata in "Jikken Kagaku Kōza," 2nd series, Vol. 13, Edited by the Chemical Society of Japan, Maruzen Co. Tokyo, 1967, p. 415.
- (19) E. W. Stone and A. H. Maki, *J. Chem. Phys.*, **38**, 1999 (1963).
- (20) J. S. Hyde, *J. Chem. Phys.*, **43**, 1806 (1965).
- (21) J. H. Freed, *J. Phys. Chem.*, **71**, 38 (1967).
- (22) J. S. Hyde, G. H. Rist, and L. E. G. Eriksson, *J. Phys. Chem.*, **72**, 4269 (1968).
- (23) A. H. Maki, R. D. Allendoerfer, J. C. Danner, and R. T. Keys, *J. Amer. Chem. Soc.*, **90**, 4225 (1968).
- (24) See paragraph at end of text regarding supplementary material.
- (25) A. D. McLachlan, *Mol. Phys.*, **3**, 233 (1960).
- (26) C. A. Coulson and V. A. Crawford, *J. Chem. Soc.*, 2052 (1953).
- (27) H. M. McConnell, *J. Chem. Phys.*, **24**, 632 (1956).
- (28) R. W. Fessenden and R. H. Schuler, *J. Chem. Phys.*, **39**, 2147 (1963); L. C. Snyder and A. T. Amos, *ibid.*, **42**, 3670 (1965); M. Karplus and G. K. Fraenkel, *ibid.*, **35**, 1312 (1961).
- (29) S. V. McKinley, P. A. Grieco, A. E. Young, and H. H. Freedman, *J. Amer. Chem. Soc.*, **92**, 5900 (1970).
- (30) S. V. McKinley, J. W. Rakshys, Jr., A. E. Young, and H. H. Freedman, *J. Amer. Chem. Soc.*, **93**, 4715 (1971).
- (31) E. A. Chandross and C. F. Sheley, Jr., *J. Amer. Chem. Soc.*, **90**, 4345 (1968).

Bubble Solution Method for Diffusion Coefficient Measurements. An Experimental Evaluation

William F. Pfeiffer*^{1,2} and Irvin M. Krieger

Departments of Chemistry and Macromolecular Science, Case Western Reserve University, Cleveland, Ohio 44106

(Received February 1, 1974; Revised Manuscript Received August 5, 1974)

The principal limitation to precision and accuracy in the bubble solution method for measuring diffusion coefficients of gases in liquids arises from free convection. The governing dimensionless parameter is the Grashof number, which indicates that convection effects become less important for small bubbles, low gas solubility, and high liquid viscosity. Precision within 5% is obtainable for bubble diameters less than 0.3 mm, and values of a second dimensionless parameter DC_s/η [(diffusion coefficient)(solubility)/(viscosity)] less than 4×10^{-8} . Bubble solution data in pure liquids and in polymer solutions substantiate these conclusions, though the measured values of D appear to be higher than current literature values. The method is particularly suitable for polymer solutions and the data suggest that polymer volume fraction, rather than solution viscosity, is the controlling parameter for diffusion of small molecules in these media.

I. Introduction

The measurement of the diffusion coefficients of dissolved gases in liquids and solutions has been a difficult but important experimental problem for many years. A systematic body of data on the behavior of these simple diffusants would be a helpful guide to understanding the mechanism of mass transport in liquids, and would thereby contribute toward a satisfactory theory of the liquid state. Gas-in-liquid diffusion coefficients are also useful in the design of chemical reactors and in other engineering applications.

There are several well-characterized techniques presently in use for the determination of gas diffusion coefficients in liquids; the literature was reviewed recently by Himmelblau.⁴ The principal experimental problems faced by all workers are elimination of convection due to density and thermal gradients, and accurate measurement of the small quantities of gas involved. If a measurement technique can give a precision of 5% or better, it is generally regarded as acceptable. The liquid jet technique is currently the most popular method, because it is convenient and routinely gives adequate precision for most engineering applications.⁵⁻⁷

Recently, there has been renewed interest in using the rate of solution of a small gas bubble in a liquid to obtain the gas diffusion coefficient. This technique involves suspending a gas bubble in a degassed liquid and measuring its size as a function of time as it dissolves. Knowledge of the gas solubility permits calculation of the gas diffusion coefficient from the radius vs. time data, assuming a Fickian diffusion process. The method is attractive because it gives a direct measure of the gas absorption, it is rapid, and it is relatively easy to analyze because of spherical symmetry. Mache⁸ and Brandstaetter⁹ were the first to use bubble solution techniques in their measurements of the diffusion of air in water. Liebermann¹⁰ measured the diffusion of air in water by bubble collapse at three temperatures, and was able to demonstrate both internal consistency and reasonable agreement with results from other techniques. Manley¹¹ studied the growth and collapse of air bubbles in water and concluded that an "organic skin effect" had to be postulated in order to satisfactorily interpret his observa-

tions. Liebermann had also reported difficulties with impurities at the bubble surface. All of these workers held the sample bubble stationary by attaching it to a flat glass or Perspex plate, and made appropriate corrections for the presence of the surface in extracting the diffusion coefficient from their data.

The first use of the bubble solution technique for a systematic study of the diffusion of gases in liquids was the extensive work of Houghton, *et al.*¹²⁻¹⁵ They reported diffusion coefficients for 14 gases in water from 10 to 60°, claiming reproducibility of better than 4%. Their method involved generating a single bubble of reproducible size, catching it under a flat plastic sheet, and following its rate of collapse microscopically. Although the effect of the plane surface could be accounted for theoretically,^{10,15} Houghton chose to calibrate his method with the known diffusion coefficient of oxygen in water. The values for other gases were somewhat higher than results of other methods, presumably due to this calibration step.⁷

The experimental contribution of Krieger, Mulholland, and Dickey (KMD)¹⁶ to the bubble collapse method was that of catching the bubble on a fine nylon or quartz fiber. This brought the experiment much closer to the theoretical ideal of a free stationary bubble in an infinite liquid. Bubble radius vs. time data were analyzed assuming a Fickian diffusion process, and ideal behavior of the gas and the gas-liquid solution. The differential equation which described the solution process was

$$\frac{da}{dt} = -\frac{D(C_s - C_0)}{a\rho} \left[1 + \frac{a}{\sqrt{\pi Dt}} \right] \quad (1)$$

where a is the bubble radius at time t , D the diffusion coefficient, C_s the gas solubility, C_0 the initial gas concentration, and ρ the gas density. A steady-state solution which predicts a linear dependence of a^2 with t was used by several investigators¹⁰⁻¹⁵ to analyze bubble collapse data, but KMD used an exact solution

$$\ln \left[\frac{a^2}{a_0^2} \left(1 + \frac{\beta\sqrt{\pi Dt}}{a} + \frac{\beta\pi Dt}{a^2} \right) \right] + \frac{2\beta}{\sqrt{4\beta - \beta^2}} \tan^{-1} \frac{\sqrt{4\beta - \beta^2}}{\beta + (2a/\sqrt{\pi Dt})} = 0 \quad (2)$$

where

$$\beta = 2(C_s - C_0)/\pi\rho \text{ (dimensionless)} \quad (3)$$

and a_0 is the bubble radius at $t = 0$. The diffusion coefficient was calculated by fitting eq 2 to the radius vs. time data. KMD measured the diffusion coefficients of O_2 , N_2 , and He in water and a few organic solvents, and reported a reproducibility of 5–10% and reasonable agreement with available literature values. They concluded that the bubble solution technique showed promise as a convenient method which should be particularly suitable for measuring gas diffusion coefficients in viscous liquids and solutions.

This paper describes a more complete evaluation of the experimental utility of the KMD bubble solution method, and an illustration of its use for measuring gas diffusion coefficients in polymer solutions.

Experimental Section

All measurements described in this paper were made at 30.0°.

A. Materials. Water used in this study was purified by a single distillation from alkaline $KMnO_4$ and stored in a plastic bottle. All organic liquids were reagent grade (or better) and were used directly as supplied.

The hydroxyethylcellulose (Cellosize) samples were supplied by Union Carbide Corp. (New York, N.Y.), and the poly(ethylene glycol) (Carbowax) was purchased from the same company. These polymers were commercial samples and were used without further treatment. The poly(vinylpyrrolidone) (PVP) was graciously supplied by GAF Corp. (New York, N.Y.). The K-15, K-30, and K-90 grades were used directly. The K-60 grade, which was supplied in water solution, was purified by precipitation from ether, since the dry material was desired.

B. Solution Viscosity and Gas Solubility Measurements. All gas solubilities used in this work were either measured or taken from the literature as described elsewhere.³ Measurement of solubilities of gases in liquids and solutions was performed using a Van Slyke apparatus.^{17–20} This instrument measures the Bunsen coefficient by outgassing a saturated sample under a Torricellian vacuum. It was found that multiple extractions were necessary for the very viscous liquids, but that a satisfactory equilibrium could be obtained. The solubility C_s (grams of gas/centimeter³ of liquid) was obtained from the Bunsen coefficient α using

$$C_s = \alpha\rho(303.15/273.15) \text{ g/cm}^3 \quad (4)$$

where ρ is the gas density (ideal) at 30.0°.

The viscosities of the pure liquids were obtained from the literature or measured in a modified Ostwald-Cannon-Fenske viscometer. Intrinsic viscosities of the polymers in water were measured using the same equipment. Viscosities of the aqueous hydroxyethylcellulose solutions were estimated using a Brookfield viscometer. The viscosities of the PVP–water solutions and of the Carbowax–water solutions were determined as a function of shear rate with a falling-head capillary viscometer.^{21,22}

C. Diffusion Measurements. The procedure for catching and photographing the dissolving bubble was a modification of that used by Krieger, Mulholland, and Dickey.¹⁶ The entire apparatus, including diffusion cell, water bath, and optical system, was mounted on a pneumatically supported granite table, in order to isolate the system from mechanical vibrations. A procedure for generating and catching a single bubble had been developed by Dr. Her-

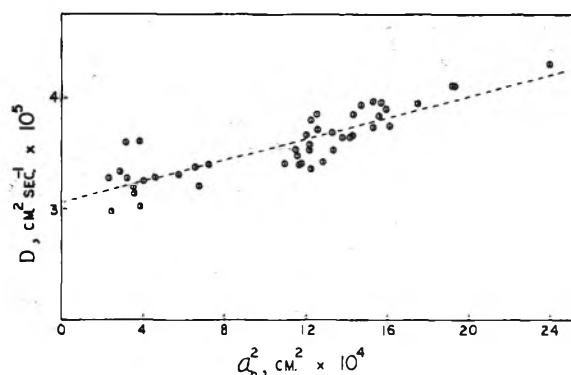


Figure 1. Diffusion coefficient vs. square of initial bubble radius for nitrogen in water at 30°. Line is $D = (4.87 \times 10^{-3})a_0^2 + 3.05 \times 10^{-5}$.

man Bodson (Lake Erie College, Painesville, Ohio) and his method was used here. This was more satisfactory than depending on the fortuitous attachment of one bubble from a stream of bubbles.

All liquids and solutions used for diffusion measurements were completely degassed by aspirating the sample while it was alternately heated and cooled. Degassed polymer solutions were prepared by initially degassing the solvent, introducing the polymer, and continuing to degas while the polymer dissolved. Polymer weight fractions were determined after the diffusion measurements by evaporating weighed aliquots. Volume fractions were calculated using measured solution densities. The theoretical model and fitting procedures used to obtain the diffusion coefficients from the solution rates were exactly those used by KMD.¹⁶

II. Results with Pure Liquids

Despite the experimental improvements mentioned above, the bubble solution technique did not give satisfactory results for diffusion coefficients of gases in pure liquids. Diffusion coefficients obtained for N_2 , O_2 , Ar, and H_2 diffusing in H_2O were higher than literature values, and the measurements gave standard deviations of 8–22%. There was also a significant correlation between the measured diffusion coefficient and the size of the bubble used. These difficulties are illustrated in Figure 1, which is a plot of D vs. a_0^2 for 45 separate determinations of the diffusion of nitrogen in water. The scatter demonstrates the intrinsic nonreproducibility of the measurements. The line in the figure is a least-squares fit which gives a coefficient of correlation of 0.86.^{23,24} Similar results were obtained for the diffusion coefficients of O_2 , H_2 , and Ar in H_2O . This dependence of diffusion coefficient on bubble size indicates that all determinations should be made with bubbles no larger than 3.0×10^{-2} cm in radius. Restriction of the data in this manner gave the results in Table I. The errors are standard deviations of a single observation, and indicate precision of 5–9% of the average value of D . Note also that the values of D are still higher than the range of available literature values.

Insight into the role of the bubble size is given by the Grashof number, which is the dimensionless parameter that controls velocity distributions in free convection.²⁵ The number is defined by

$$Gr = \rho_l^2 g L^3 (\Delta X) Y / \eta^2 \quad (5)$$

where ρ_l is the liquid density, g is the gravitational acceleration, η the liquid viscosity, L a characteristic length, ΔX a

TABLE I: Diffusion Coefficients of Four Gases in Water at 30°^a

Gas	Replica- tions	C_s , g/cm ³ × 10 ⁵	D , cm ² /sec × 10 ⁵	
			Measd	Lit. ^b
N ₂	15	1.72	3.3 ± 0.2	2.1–2.5
O ₂	8	3.749	3.5 ± 0.3	2.2–2.8
Ar	6	5.113	3.1 ± 0.3	2.7
H ₂	4	0.1457	6.4 ± 0.5	4.5
N ₂ ^c	8	1.72	3.0 ± 0.1	2.1–2.5

^a $\alpha_0 = 3.0 \times 10^{-2}$ cm. ^b Values from ref 4 except Ar from ref 13. The Ar value is believed to be high.⁷ ^c Multiple fiber (see text for discussion).

characteristic concentration difference (solute mole fraction), and Y the concentration coefficient of the liquid density. In the bubble solution problem, L is taken as the bubble diameter and ΔX is the gas solubility. The Grashof number predicts that free convection can be reduced by using small bubbles of sparingly soluble gases in highly viscous liquids.

It was found that bubbles could not be caught and held satisfactorily on single fibers in liquids other than distilled water. This difficulty was also encountered by Dickey,²⁶ who solved it by using multiple fibers; his approach was used here. Multiple fibers act as a physical barrier preventing the bubble from rising in the liquid. Surface forces between bubble and fiber are not as important for holding the bubble as in the case of single fibers. The bubble is contacted in two places, and is in close proximity to as many strands as are present (up to four).

The effect of the multiple fibers on the results for N₂ diffusing into H₂O is indicated by comparing the first and last lines of Table I. The significant reduction in D and improvement of the precision were probably due to a combination of three effects: (i) reduction of the solid angle available for mass transport due to the added barrier of multiple strands (a minor effect); (ii) reduction of convection currents in the liquid near the bubble due to the added physical barrier; and (iii) stabilization of the bubble against vibrations and other motions. All of the results described below were obtained using multiple fibers.

The diffusion coefficient of N₂ in aqueous surfactant solution was measured in an effort to estimate the effect of the surface tension. A nonionic surfactant was used (Ultra-pole LDA 9005, Whitco Chemical Co., Patterson, N.J.) at a concentration of ca. 0.01 g/100 ml (3.5×10^{-4} M). The average diffusion coefficient from four measurements was $3.03 \pm 0.04 \times 10^{-5}$ cm²/sec, indicating that the reduction in surface tension did not appreciably affect the measured value of the diffusion coefficient (cf. last line of Table I).

This was in agreement with the findings of Liebermann,¹⁰ who noted no large difference in the diffusion coefficient of air in water when such contaminants as oleic acid, detergent, mineral oil, etc. were present. Interestingly, there is some improvement in precision with the surfactant solutions.

The gas solubility is the source of a rather severe limitation on the utility of the bubble solution technique. The theoretical equations predict that the rate of bubble collapse is proportional to the product DC_s of the diffusion coefficient and the gas solubility (when the initial gas concentration is zero). Since diffusion coefficients of gases in pure liquids do not vary widely, solubility determines the order of magnitude of the DC_s product. It was found in this work that bubbles collapsed too rapidly to photograph conveniently whenever DC_s was greater than 4×10^{-9} g cm/sec. Results for the pure liquid systems studied in this work are given in Table II. The N₂-*o*-dichlorobenzene and N₂-cyclohexanone systems represent the upper limit to the applicability of the technique. It is important to note that systems such as CO₂-water, N₂-benzene, and O₂-ethanol cannot be studied with this bubble solution technique because of their large DC_s products. This limitation could be circumvented by working at lower temperatures, or by starting with partially degassed samples,¹⁶ but neither modification was attempted in this work.

The dimensionless group DC_s/η (approximately the reciprocal of the Schmidt number which governs free convective mass transfer, ref 25, p 581) was found to be an important parameter in the bubble solution method. The diffusion and solubility data from Table II were combined with the liquid viscosities, and similar data were measured for N₂ diffusing in 1% solutions of four viscosity grades of hydroxyethylcellulose (HEC) in water. The solubility of N₂ in the HEC solutions was assumed to be the same as that in pure water. The results, given in Table III, indicated that the standard deviation s of the diffusion coefficient decreased as the parameter DC_s/η decreased. The data are graphed in Figure 2; the line is a least-squares fit and the coefficient of correlation is 0.94. These results indicate that the bubble solution technique could be expected to give acceptable precision only in those systems with DC_s/η less than 4×10^{-8} , where the standard deviation could be expected to be less than 0.1×10^{-5} cm²/sec. It is notable that most solutions of gases in pure water had values of DC_s/η above this approximate "critical" value. Further, it appeared that the best precision obtainable in any system would be ca. 0.05×10^{-5} cm²/sec.

III. Diffusion in Polymer Solutions

The bubble solution technique appeared particularly

TABLE II: DC_s Products for Several Gas-Liquid Systems at 30°

Gas-liquid	D , cm ² /sec × 10 ⁵	C_s , g/cm ³ × 10 ⁵	DC_s , g cm ⁻¹ sec ⁻¹ × 10 ¹⁰
H ₂ -water	6.4 ± 0.5	0.146	0.93
N ₂ -water	3.0 ± 0.1	1.72	5.2
O ₂ -water	3.8 ± 0.2	3.75	14
Ar-water	3.1 ± 0.3	5.11	16
H ₂ -cyclohexanol	1.35 ± 0.06	0.677	0.914
N ₂ -cyclohexanol	0.68 ± 0.03	7.44	5.0
Ar-cyclohexanol	0.80 ± 0.03	20.1	16
N ₂ -ethylene glycol	0.50 ± 0.02	1.90	0.95
H ₂ - <i>o</i> -dichlorobenzene	6.3 ± 0.1	0.471	3.0
N ₂ - <i>o</i> -dichlorobenzene	4.0 ± 0.3	8.67	34
N ₂ -cyclohexanone	3.7 ± 0.4	9.72	36

TABLE III: Standard Deviation and DC_s/η for 13 Systems at 30°

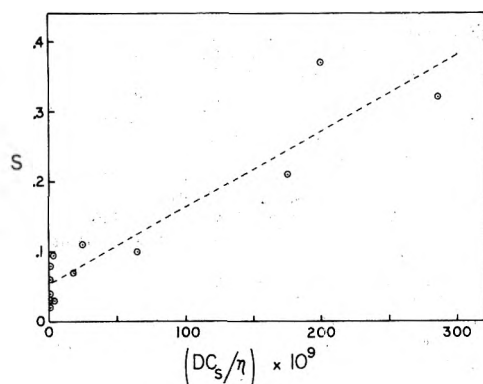
System	η , P	DC_s/η $\times 10^9$	s
N ₂ -o-dichlorobenzene	0.0119	286 ^a	0.32
N ₂ -cyclohexanone	0.0180 ^b	200 ^a	0.37
O ₂ -water	0.008007 ^c	175 ^a	0.21
N ₂ -water	0.008007 ^c	65.0 ^a	0.099
H ₂ -o-dichlorobenzene	0.0119	25.2 ^a	0.11
H ₂ -1% WP-09 HEC	0.025	18.0 ^a	0.071
Ar-cyclohexanol	0.392	4.1	0.033
N ₂ -1% QP-40 HEC	0.11	3.7	0.094
N ₂ -1% QP-300 HEC	0.24	1.6	0.076
N ₂ -cyclohexanol	0.392	1.3	0.039
N ₂ -ethylene glycol	0.137	0.69	0.015
H ₂ -cyclohexanol	0.392	0.233	0.060
N ₂ -1% QP-4400 HEC	2.0	0.17	0.032

^a Only two figures are significant. ^b Reference 27. ^c Reference 28.

TABLE IV: Diffusion Coefficients of Nitrogen in Aqueous Carbowax Solutions at 30°

Carbowax	ϕ^a	D , cm ² /sec $\times 10^5$	C_s , g/cm ³ $\times 10^3$	DC_s/η $\times 10^{10}$
1000	0.183	1.76 \pm 0.05	1.47	70
	0.400	1.15	1.18	8.5
	0.582	0.68 \pm 0.09	0.943	1.26
4000	0.398	0.902	1.18	2.95
	0.409	0.877	1.16	2.49
	0.553	0.63 \pm 0.04	0.978	0.516
6000	0.089	2.02 \pm 0.08	1.61	57.4
	0.176	1.58 \pm 0.06	1.48	12.1
	0.279	1.14 \pm 0.04	1.34	2.59
	0.394	0.690 \pm 0.009	1.18	0.47
	0.440	0.624 \pm 0.004	1.12	0.251
	0.458	0.58 \pm 0.02	1.10	0.198
	0.546	0.451 \pm 0.008	0.986	0.0618

^a Volume fraction.

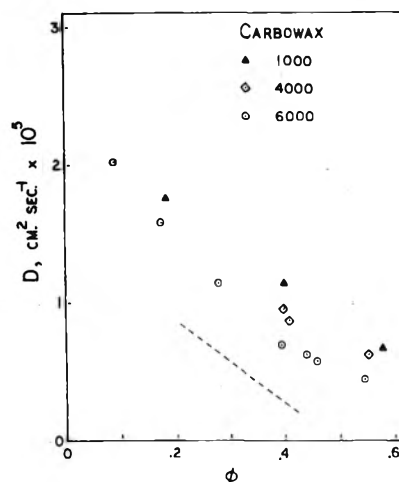
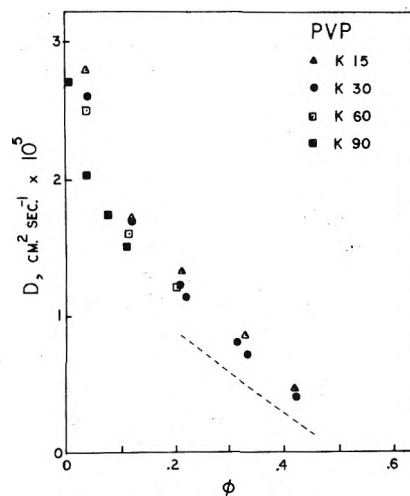
**Figure 2.** Standard deviation vs. DC_s/η for the 13 systems listed in Table III. Line is $s = (1.1 \times 10^{-6})DC_s/\eta + 0.052$.

suitable for studies of the diffusion of gases in viscous liquids and solutions. The problems caused by convection would be minimized by higher viscosities, so that higher precision would be possible. An interesting class of viscous systems is polymer solutions. The diffusion of N₂ in aqueous solutions of poly(ethylene glycol) (Carbowax) and solutions of poly(vinylpyrrolidone) (PVP) was studied in order to examine the suitability of the bubble solution technique for this type of system. The data are reported in Tables IV and V and Figures 3 and 4. The group DC_s/η was small for all of

TABLE V: Diffusion Coefficients of Nitrogen in Aqueous PVP Solutions at 30°

PVP	ϕ^a	D , cm ² /sec $\times 10^5$	C_s , g/cm ³ $\times 10^3$	DC_s/η $\times 10^{10}$
K-15	0.040	2.8 \pm 0.2	1.66	331
	0.122	1.71 \pm 0.08	1.51	46.7
	0.214	1.32 \pm 0.08	1.35	8.81
	0.328	0.86 \pm 0.07	1.17	1.37
	0.420	0.47 \pm 0.06	1.03	0.115
K-30	0.042	2.6 \pm 0.1	1.65	138
	0.123	1.69 \pm 0.07	1.51	16.9
	0.210	1.22 \pm 0.08	1.36	2.44
	0.220	1.13 \pm 0.01	1.34	1.95
	0.313	0.80 \pm 0.07	1.20	0.302
	0.334	0.71 \pm 0.01	1.16	0.132
	0.423	0.40 \pm 0.03	1.03	0.0195
K-60	0.040	2.5 \pm 0.2	1.66	51.7
	0.117	1.6 \pm 0.2	1.52	3.48
	0.204	1.22 \pm 0.09	1.37	0.359
K-90	0.0078	2.7 \pm 0.1	1.71	103
	0.038	2.03 \pm 0.06	1.66	7.04 ^b
	0.076	1.74 \pm 0.03	1.59	0.877 ^b
	0.111	1.50 \pm 0.08	1.53	0.177 ^b

^a Volume fraction. ^b At shear rate = 250 sec⁻¹ (arbitrarily chosen).

**Figure 3.** Nitrogen diffusion coefficient vs. Carbowax volume fraction, ϕ , in water at 30°. Slope of line is -3.0.**Figure 4.** Nitrogen diffusion coefficient vs. PVP volume fraction, ϕ , in water at 30°. Slope of line is -3.0.

the systems studied, and the standard deviations were less than $0.1 \times 10^{-5} \text{ cm}^2/\text{sec}$ in most cases. These standard deviations usually resulted in a reproducibility of better than 5% of the average value of the diffusion coefficient. Difficulty was encountered in very concentrated solutions, in inserting the fiber holder and in catching the bubble. Reproducible values for the diffusion coefficients of N_2 were found in all but the most concentrated solutions.

Addition of polymer to water lowered the gas diffusion coefficient in every case, an observation consistent with the results of Quinn and Blair²⁹ and of Zandi and Turner.³⁰ No enhancement of the diffusion coefficient by the polymer was observed (see Astarita³¹ and Metzner, *et al.*³²⁻³⁴). The most notable feature of the data was that the gas diffusion coefficient did not decrease in proportion to the dramatic increase in solution viscosities for these systems, and was only mildly dependent on molecular weight. The relative viscosity for these solutions ranged from 1 to 100 or more, but the maximum value of the ratio of the diffusion coefficient in water to that in solution was only 7.5. This is in disagreement with widely used theoretical and semiempirical correlations.^{25,35-38} The diffusion coefficient shows an initial sharp decrease at low polymer volume fractions, after which it decreases linearly with increasing polymer volume fraction for volume fractions greater than ca. 0.2. The slope in this region is very nearly equal in magnitude to the diffusion coefficient of N_2 in water ($3 \times 10^{-5} \text{ cm}^2/\text{sec}$), which suggests that the effect of polymer on small penetrants is linear with polymer volume fraction in this concentration range.

Figure 5 shows the same data plotted as the natural logarithm of D/D_0 (the ratio of the N_2 diffusion coefficient in the polymer solution to its value in pure H_2O) vs. polymer volume fraction for four of the more thoroughly studied systems. The least-squares lines in the figure have been forced through the point for pure water. The equations are

$$\text{Carbowax 1000: } \ln(D/D_0) = -2.53\phi \quad (6)$$

$$\text{Carbowax 4000: } \ln(D/D_0) = -2.92\phi \quad (7)$$

$$\text{Carbowax 6000: } \ln(D/D_0) = -3.57\phi \quad (8)$$

$$\text{PVP K-30 } \ln(D/D_0) = -4.48\phi \quad (9)$$

The linearity of these plots suggests that the solution viscosity is not an important factor for diffusion of small penetrants in these systems, but that the polymer volume fraction is the controlling parameter. The authors are presently investigating a model of this diffusion process as a random walk on a solvent lattice where some sites are randomly blocked by dissolved polymer.

Conclusion

In order to obtain acceptable diffusion coefficients by the bubble solution method, certain precautions must be observed. Bubble sizes should not exceed 0.3 mm in radius, and the dimensionless quantity DC/η should be less than 4×10^{-8} , where C is the difference in solute concentration between the saturated solution and the bulk liquid. Outside these ranges, convective effects become serious, causing systematically high values for D and standard deviations in excess of 5%. The method is marginal for aqueous solutions of most gases and best results are obtained with small bubbles, sparingly soluble gases, and viscous liquids, where precision of 2.5% is attainable. Even with these precautions the measured values of D appear to be high when

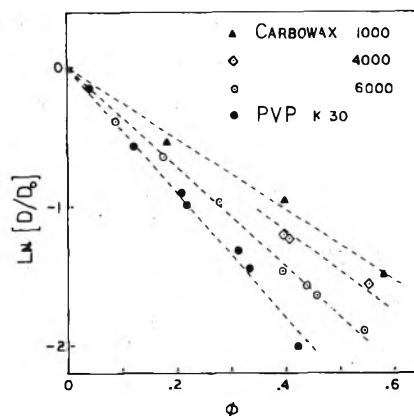


Figure 5. Natural logarithm of the ratio of the N_2 diffusion coefficient in polymer solution (D) to that in water (D_0) vs. polymer volume fraction at 30° for four polymers. Line slopes are -2.53 , -2.92 , -3.57 , and -4.48 for polymers in the order listed.

compared with results of other methods. This inaccuracy may be remedied by a more exact theoretical analysis of the bubble dissolution process. Other authors³⁹⁻⁴¹ have attempted this with somewhat contradictory results, but none has considered the effect of the small movement of the bubble center which occurs experimentally. It is worth noting that more accurate diffusion coefficients have been obtained by Ng and Walkley⁴² using a constant bubble size method.

Application of the KMD bubble solution method to the study of N_2 diffusion in aqueous polymer solutions gave satisfactory precision and the data indicated that polymer volume fraction was the governing parameter for diffusion of small molecules in these media.

References and Notes

- (1) Address correspondence to Department of Chemistry, Utica College, Utica, N.Y., 13502.
- (2) Based on Ph.D. Thesis.³
- (3) W. F. Pfeiffer, Ph.D. Thesis, Case Western Reserve University, 1970.
- (4) D. M. Himmelblau, *Chem. Rev.*, **64**, 527 (1964).
- (5) E. J. Cullen and J. F. Davidson, *Trans. Faraday Soc.*, **53**, 113 (1957).
- (6) Y. P. Tang and D. M. Himmelblau, *AIChE J.*, **11**, 54 (1965).
- (7) J. L. Duda and J. S. Vrentas, *AIChE J.*, **14**, 286 (1968).
- (8) H. Mache, *Wien. Akad.*, **138**, 529 (1929).
- (9) F. Brandstaetter, *Usterr. Akad. Wiss.*, **161**, 107 (1952).
- (10) L. Liebermann, *J. Appl. Phys.*, **28**, 205 (1957).
- (11) D. M. J. P. Manley, *Brit. J. Appl. Phys.*, **11**, 38 (1960).
- (12) G. Houghton, P. D. Ritchie, and J. A. Thomson, *Chem. Eng. Sci.*, **17**, 221 (1962).
- (13) D. L. Wise and G. Houghton, *Chem. Eng. Sci.*, **21**, 999 (1966).
- (14) D. L. Wise and G. Houghton, *Chem. Eng. Sci.*, **23**, 1211 (1968).
- (15) D. L. Wise and G. Houghton, *Chem. Eng. Sci.*, **23**, 1502 (1968).
- (16) I. M. Krieger, G. W. Mulholland, and C. S. Dickey, *J. Phys. Chem.*, **71**, 1173 (1967).
- (17) D. D. Van Slyke, *J. Biol. Chem.*, **30**, 347 (1917).
- (18) D. D. Van Slyke and W. C. Stadie, *J. Biol. Chem.*, **49**, 1 (1921).
- (19) D. D. Van Slyke and J. M. Niell, *J. Biol. Chem.*, **61**, 523 (1924).
- (20) F. S. Orcutt and M. H. Seevers, *J. Biol. Chem.*, **117**, 501 (1937).
- (21) S. H. Maron, I. M. Krieger, and A. W. Sisko, *J. Appl. Phys.*, **25**, 971 (1954).
- (22) M. E. Woods, Ph.D. Thesis, Case Western Reserve University, 1967.
- (23) W. J. Youden, "Statistical Methods for Chemists," Wiley, New York, N.Y., 1951.
- (24) A. Hald, "Statistical Tables and Formulas," Wiley, New York, N.Y., 1952.
- (25) R. B. Bird, W. E. Stewart, and E. N. Lightfoot, "Transport Phenomena," Wiley, New York, N.Y., 1960.
- (26) C. S. Dickey, B.S. Thesis, Case Institute of Technology, 1966.
- (27) J. Timmermans, "Physico-Chemical Constants of Pure Organic Compounds," Vol. 1, Elsevier, Amsterdam, 1950.
- (28) "Handbook of Chemistry and Physics," 40th ed, Chemical Rubber Publishing Co., Cleveland, Ohio, 1959.
- (29) J. A. Quinn and L. M. Blair, *Nature (London)*, **214**, 907 (1967).
- (30) I. Zandi and C. D. Turner, *Chem. Eng. Sci.*, **25**, 517 (1970).

- (31) G. Astarita, *Ind. Eng. Chem., Fundam.*, **4**, 236 (1965).
 (32) S. B. Clough, H. E. Read, A. B. Metzner, and V. C. Behn, *AIChE J.*, **8**, 346 (1962).
 (33) A. B. Metzner, *Nature (London)*, **208**, 267 (1965).
 (34) J. L. Gainer and A. B. Metzner, *AIChE Inst. Chem. Eng. Symp. Ser.*, No. 6, 74 (1965).
 (35) C. R. Wilke and P. Chang, *AIChE J.*, **1**, 264 (1955).
 (36) H. Eyring, *J. Chem. Phys.*, **4**, 283 (1936).
 (37) R. J. Bearman, *J. Phys. Chem.*, **65**, 1961 (1961).
 (38) A. Huq and T. Wood, *J. Chem. Eng. Data*, **13**, 256 (1968).
 (39) J. L. Duda and J. S. Vrentas, *AIChE J.*, **15**, 351 (1969).
 (40) M. Cable and D. J. Evans, *J. Appl. Phys.*, **38**, 2899 (1967).
 (41) D. W. Readey and A. R. Cooper, *Chem. Eng. Sci.*, **21**, 917 (1966).
 (42) W. Y. Ng and J. Walkley, *Can. J. Chem.*, **47**, 1075 (1969).

Conductance Studies of the Alkali Metal Chlorides in Aluminum Chloride–Propylene Carbonate Solution

Jacob Jorné*¹ and Charles W. Tobias

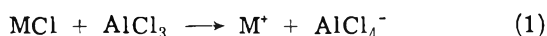
Inorganic Materials Research Division, Lawrence Berkeley Laboratory and Department of Chemical Engineering, University of California, Berkeley, California 94720 (Received February 19, 1974)

Publication costs assisted by the University of California

Conductance of the alkali metal chlorides, LiCl, NaCl, KCl, RbCl, CsCl, in unit molality solution of AlCl₃ in propylene carbonate was measured at 25 and 35°. The measurements were performed in order to characterize the new process for the electrodeposition of the alkali metals at ambient temperature. The results have been interpreted in terms of solvation, ionic equilibrium, and the structure making–breaking ability of the alkali metals in AlCl₃ propylene carbonate solution.

Propylene carbonate (PC) is a polar aprotic solvent which exhibits many useful properties for electrochemical applications. Since the early research on PC was oriented toward the development of high-energy batteries, most of the work was concerned with emf measurements, electrodeposition, stability tests, and conductance at high concentration range. Recently, conductance measurements were performed in the dilute range in order to gain better understanding about the solvent–solute interactions.^{2–5}

The feasibility of the electrodeposition of all the alkali metals from their chlorides in AlCl₃–propylene carbonate solution has been demonstrated.⁶ Lithium, sodium, potassium, rubidium, and cesium were electrodeposited at ambient temperature showing stable and reversible behavior.^{7,8} The alkali metal chlorides are practically insoluble in PC, however, in the presence of AlCl₃ a complex is formed between the chloride and AlCl₃



where M represents the alkali metal.

The electrodeposition of the alkali metals from their chlorides in AlCl₃–PC solution is proposed as a new process for the electrodeposition and refining of the alkali metals at ambient temperature.⁶ In order to characterize such a process, thermodynamic⁷ and kinetic⁸ measurements were performed. This paper presents the results of conductance studies of the alkali metal chlorides in unit molality AlCl₃ solution in PC, at 25 and 35°, over a wide concentration range of up to 1 *m* alkali metal chloride. The role of AlCl₃ is discussed in the light of earlier work^{6–8} and a general evaluation of the results is given.

Previous Work

Most of the data on solubilities and conductivities in PC are summarized in Jasinski's review,⁹ and the reader is referred to Table XIII and XIX in that review.

Conductance measurements in dilute solutions were performed in order to obtain the equivalent conductance at infinite dilution. The equivalent conductances at infinite dilution, Λ_0 , were obtained in most cases by extrapolation of a plot of Λ vs. $c^{1/2}$ to infinite dilution.

Harris¹⁰ obtained Kohlrausch plots for NaI and KI in PC, and the equivalent conductances were 28.3 and 31.0 ohm⁻¹ cm² equiv⁻¹, respectively. The slopes of the straight lines were in good agreement with the Onsager limiting law equation. Fuoss and Hirsch^{2a} studied the conductance of tetra-*n*-butylammonium tetraphenylborate in PC and concluded that ion association was negligible. Wu and Friedman^{2b} investigated the conductances and heats of solution of several alkali metal iodides, perchlorates, trifluoroacetates, and tetraphenylborates in PC. The perchlorates were found to be strong electrolytes, whereas the trifluoroacetates showed considerable ion association. Keller, *et al.*³ measured the equivalent conductance of LiClO₄, LiCl, LiBr, TBABR, and TMAPF₆ in PC, and obtained the equivalent conductance at infinite dilution. Mukherjee and Boden⁴ made conductance and viscosity measurements of LiCl, LiBr, LiClO₄, Et₄NCl, Et₄NClO₄, *n*-Bu₄NBr, and *n*-Bu₄NClO₄ in PC. The method of Fuoss and Accascina¹¹ was used to obtain Λ_0 and the individual ion conductances Λ_+^0 and Λ_-^0 . LiCl and LiBr were found to be associated, whereas no association could be detected for the other salts.

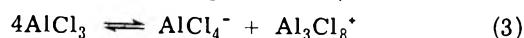
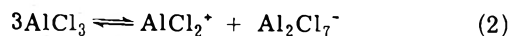
TABLE I: Equivalent Conductance and Ionic Conductance in PC ($\text{ohm}^{-1} \text{cm}^2 \text{equiv}^{-1}$)

Salt	Λ	λ_+	λ_-	Ref
LiCl	25.6			3
	26.2			3
	27.5	7.30	20.20	4
LiBr	26.2			3
	27.35	7.30	20.05	4
LiClO ₄	25.6			3
	26.2			12, 13
	26.08	7.30	18.78	3
NaI	26.3			14
	28.2			10
NaClO ₄	28.3			2b
KI	30.75	11.97	18.78	5
	31.0			10
KClO ₄	30.75	11.97	18.78	5
Et ₄ NClO ₄	32.06	13.28	18.78	5
<i>n</i> -Bu ₄ NClO ₄	28.17	9.39	18.78	5
<i>n</i> -Bu ₄ NBr	28.65	9.39	19.26	5
(<i>i</i> -Am) ₄ N(<i>i</i> -Am) ₄ B	16.37	8.185	8.185	5
(<i>i</i> -Am) ₄ NI	26.95	8.185	18.675	5

Table I presents the equivalent conductances and ionic conductances at infinite dilution for several electrolytes in PC. The ionic conductance of Li⁺ is the lowest, which means that the ion has a large effective size. The ionic conductance of ClO₄⁻, I⁻, Br⁻, and Cl⁻ are approximately the same. Anions are poorly solvated in PC, and their ionic conductance is higher than the conductance of the cations.

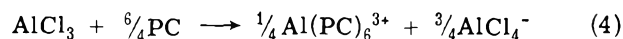
Conductance Measurements of AlCl₃ in PC

AlCl₃, a strong Lewis acid which is very soluble in PC (3.2 M), increases the solubility of salts that are insoluble in pure PC by forming complex ions with the anions of these salts. AlCl₃ in combination with LiCl was investigated as an electrolyte for high-energy batteries (ref 3 and 14–19). Conductance measurements and nmr studies were performed in order to understand the transport properties and the species present in AlCl₃ solutions in PC. Boden¹⁴ measured the specific conductance of AlCl₃ in PC over a wide concentration range. The maximum specific conductance of approximately $10^{-2} \text{ ohm}^{-1} \text{cm}^{-1}$ occurs at an AlCl₃ concentration of 1.2 M. The specific conductance falls off at higher concentrations because of the increasing viscosity of the solution and due to ion association at high concentrations. Breivogel and Eisenberg¹⁵ measured the equivalent conductance of dilute solutions of AlCl₃ and LiCl–AlCl₃ in PC, using a dc conductivity method. The results were interpreted through the Onsager equation, after being corrected for viscosity effect using the Walden rule. The limiting equivalent conductance of LiAlCl₄ was estimated to be $34.5 \text{ ohm}^{-1} \text{cm}^2 \text{equiv}^{-1}$, although the extrapolation was somewhat uncertain.¹⁵ The experimental slope in the case of LiAlCl₄ did not agree with the calculated Onsager slope. Breivogel and Eisenberg¹⁵ attempted to explain the anomalous minimum in the equivalent conductance of AlCl₃ by the presence of different ionic species in different concentration regions. The rapid increase in the equivalent conductance was explained as being caused by an increase in the number of ions per mole of solute as the concentration increases. The following equilibrium reactions were proposed as being able to explain such an increase in the equivalent conductance



Although either of the equations can explain qualitatively the anomalous behavior, further work is required to confirm this hypothesis. A different approach was proposed by Keller, *et al.*,³ who found the same anomalous behavior of AlCl₃ at low concentrations. The minimum in the plot of Λ_0 vs. $C^{1/2}$ was explained by the hydrolysis of AlCl₃ with traces of water to give aluminum hydroxide and HCl.

Keller, *et al.*,³ also studied directly the ionic equilibria of AlCl₃ in PC using nmr techniques. From the ²⁷Al spectra, Keller concluded that the main species are Al(PC)₆³⁺ and AlCl₄⁻, similar to the species present in an AlCl₃ solution in acetonitrile. High-resolution ¹H spectra of 1 M AlCl₃–PC indicate peaks due to coordinated PC as well as bulk PC. From the ¹H and the ²⁷Al spectra, Keller showed that the Al coordination number (*n*) is six. Therefore, the dissolution of AlCl₃ in PC proceeds according to



Furthermore, it was observed that the addition of LiCl to an AlCl₃–PC solution reduces the concentration of the coordinated Al species, and at the saturation point, where the LiCl:AlCl₃ ratio is 1:1, the coordinated Al species disappears. Such observations can be explained by the reaction between LiCl and Al(PC)₆³⁺ to give AlCl₄⁻.

Keller³ discusses the complexing strength of Al³⁺ toward several aprotic solvents and chloride ion. The complexing strength of Al³⁺ toward Cl⁻ is stronger than toward PC, AN, and water, but weaker than toward DMF. This ionic equilibria analysis of AlCl₃ in PC, according to Keller, *et al.*, is in contrast to the analysis of Breivogel and Eisenberg.¹⁵ Neither of these workers succeeded in explaining quantitatively the minimum in the equivalent conductance plot of AlCl₃ in PC.

Experimental Section

Conductivities of the alkali metal chloride in AlCl₃–PC solutions were measured at 25 and 35° using an ac bridge. Sinusoidal signals at 20 kHz and amplitude of around 15 V were generated by an ac generator detector, Model 861 A, Electro Scientific Industries, Portland, Oreg. The cell resistance and capacitance were balanced with an impedance bridge, Model 290 A, Electro Scientific Industries, Portland, Oreg., and with variable decade capacitors, Models CDA-2 and CDA-3, Cornell-Dubilier Electronic Division, Federal Pacific Electric Division.

The conductance cell consisted of two parallel bright platinum disk electrodes. Because of the relatively low conductivities of the nonaqueous solutions, the cell was designed to give a relatively low cell constant, 0.439 cm^{-1} , which was determined using 0.1 and 0.01 N aqueous KCl solution. All electrical wires were shielded. At the frequency of 20 kHz the results were independent of the frequency.

The solutions were prepared in an argon drybox by dissolving weighed amounts of the alkali metal chlorides in 1 M AlCl₃ solution in PC. The volumetric concentrations in moles per liter were calculated from the measured densities of the solutions. The alkali metal chloride concentration varied from 0 to 1 M, all in the presence of AlCl₃ (1 M). The preparation of the solutions was similar to the procedure described for the potential measurements.^{6,7} The AlCl₃ salt was added very slowly to PC to prevent heating and darkening of the solution.

Propylene carbonate (Jefferson Chemical Co., Houston, Tex.) was distilled at 0.5 mm pressure by means of a commercially available distillation column (Semi-CAL series

TABLE II: Specific Conductance of LiCl in AlCl₃ (1 *m*)-PC Solution at 25 and 35°

<i>m</i> , mol/kg of PC	<i>C, M</i>		10 ³ <i>κ</i> , ohm ⁻¹ cm ⁻¹	
	25°	35°	25°	35°
0.02	0.0251	0.0250	6.708	8.315
0.1	0.1262	0.1253	6.741	8.442
1.0	1.2594	1.2512	6.700	8.434

TABLE III: Specific Conductance of NaCl in AlCl₃ (1 *m*)-PC Solution at 25 and 35°

<i>m</i> , mol/kg of PC	<i>C, M</i>		10 ³ <i>κ</i> , ohm ⁻¹ cm ⁻¹	
	25°	35°	25°	35°
0.01	0.0126	0.0125	6.971	8.702
0.10	0.1264	0.1253	6.955	8.693
0.25	0.3163	0.3138	6.910	8.662
0.50	0.6330	0.6279	7.119	8.941

TABLE IV: Specific Conductance of KCl in AlCl₃ (1 *m*)-PC Solution at 25 and 35°

<i>m</i> , mol/ kg of PC	<i>C, M</i>		10 ³ <i>κ</i> , ohm ⁻¹ cm ⁻¹	
	25°	35°	25°	35°
0.0025	0.0031	0.0031	6.915	8.591
0.01	0.0126	0.0125	6.994	8.763
0.10	0.1261	0.1254	7.278	9.108
0.25	0.3167	0.3143	7.754	9.649
0.50	0.6390	0.6330	8.516	10.630
1.00	1.300	1.2920	10.210	12.725

TABLE V: Specific Conductance of RbCl in AlCl₃ (1 *m*)-PC Solution at 25 and 35°

<i>m</i> , mol/ kg of PC	<i>C, M</i>		10 ³ <i>κ</i> , ohm ⁻¹ cm ⁻¹	
	25°	35°	25°	35°
0.0025	0.0031	0.0031	7.157	8.914
0.01	0.0126	0.0125	7.041	8.743
0.05	0.0632	0.0626	7.242	9.020
0.10	0.1272	0.1261	7.294	9.101
0.25	0.3194	0.3168	8.022	9.950
1.00	1.3195	1.3091	11.003	13.719

TABLE VI: Specific Conductance of CsCl in AlCl₃ (1 *m*)-PC Solution at 25 and 35°

<i>m</i> , mol/ kg of PC	<i>C, M</i>		10 ³ <i>κ</i> , ohm ⁻¹ cm ⁻¹	
	25°	35°	25°	35°
0.0025	0.0031	0.0031	6.848	8.508
0.01	0.0126	0.0125	6.732	8.410
0.10	0.1264	0.1259	6.773	8.676
0.25	0.3238	0.3215	7.910	9.756
0.50	0.6597	0.6555	9.070	11.171
1.00	1.3597	1.3481	11.257	13.806

TABLE VII: Densities of the Alkali Metal Chlorides in AlCl₃ (1 *m*)-PC at 25 and 35°

Salt	<i>m</i> , mol/kg of PC	<i>ρ</i> (g/ml)	
		25°	35°
LiCl	0.5	1.262	1.252
	1.0	1.261	1.218
	1.0	1.259	1.251
NaCl	0.01	1.262	1.252
	0.10	1.263	1.253
	0.25	1.265	1.255
KCl	0.50	1.266	1.255
	0.0025	1.261	1.252
	0.01	1.262	1.252
RbCl	0.10	1.261	1.254
	0.25	1.266	1.257
	0.50	1.278	1.267
RbCl	0.01	1.263	1.253
	0.05	1.265	1.253
	0.10	1.272	1.261
CsCl	0.25	1.277	1.267
	1.00	1.319	1.309
	0.0025	1.263	1.253
CsCl	0.01	1.263	
	0.50	1.319	1.310
	1.00	1.359	1.348

liter) and was transferred from the molality basis by multiplying by the density of the solution.

Densities of different molalities of the alkali metal chlorides in AlCl₃ (1 *m*)-PC solution at 25 and 35° are presented in Table VII.

Discussion

The specific conductance of the alkali metal chlorides in AlCl₃ (1 *m*)-PC solution is presented in Figures 1 and 2 at 25 and 35°, respectively. The general trend, with the exception of LiCl, is that the specific conductance increases with an increase in the concentration of the alkali metal chloride, MCl. In the case of NaCl, the specific conductance is almost constant over the entire concentration range. A steady increase in the specific conductance can be observed for KCl, RbCl, and CsCl solutions in AlCl₃ (1 *m*)-PC. Small minima can be observed at low concentrations of LiCl and CsCl. A comparison of the specific conductance of the alkali metal chlorides shows that the specific conductance increases as we pass along the alkali metal series from Li to Cs. Despite the fact that Li is the smallest ion, its chloride solutions have the lowest conductance, while Rb and Cs, which are large ions, have the highest. These observations can be explained on the basis of ionic equilibrium, solvation, and viscosity considerations.

Our measurements yield a value of 6.9×10^{-3} ohm⁻¹ cm⁻¹ for the specific conductance of a 1 *m*, i.e., 1.263 *M*, solution of AlCl₃, as compared to Boden's¹⁴ low-frequency value of 9×10^{-3} ohm⁻¹ cm⁻¹ for a 1 *M* solution of AlCl₃ in PC. However, the present results are in better agreement

3650, Podbielniak, Franklin Park, Ill.) packed with stainless steel helices. The reflux ratio was 60 to 100 and the head temperature 65°. The first 10% and the last 25% of the solvent were discarded. The "as received" solvent contains a few tenths of a per cent of the following impurities: water, propylene glycol, propion aldehyde, and propylene oxide.⁹ Gas chromatographic analysis of the product performed in this laboratory showed the water content to be always below 50 ppm.⁶

The salts were dried in a vacuum oven (Hotpack, Philadelphia, Pa.) at 200° and approximately 50 μ pressure for at least 24 hr. The final solutions were treated with molecular sieves (Linde 4A) in order to remove traces of water. The molecular sieves were treated before use by heating (300°), high vacuum, and several flashes with argon.

Measurements were made at 25 and 35 \pm 0.01°. Densities of solutions of different alkali metal chloride molalities were measured using a pycnometer at 25 and 35°.

Results

The specific conductance of the alkali metal chlorides in AlCl₃ (1 *m*)-PC solution at 25 and 35° is given in Tables II-VI. The concentration is given on molarity basis (mole/

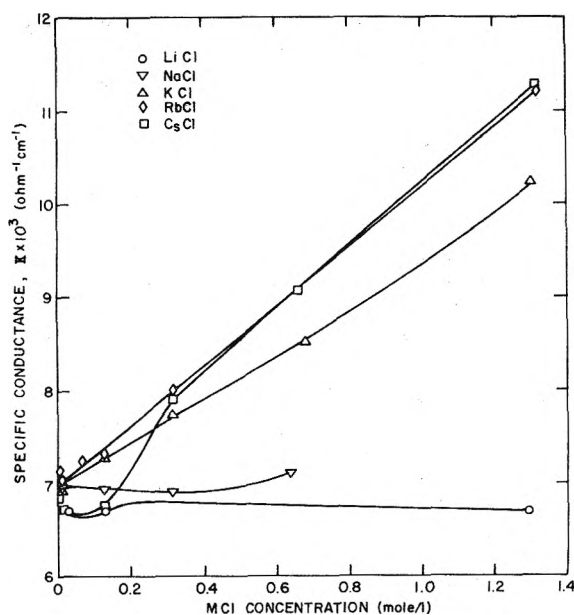


Figure 1. Specific conductance of the alkali metal chlorides in AlCl_3 (1 *m*)-PC solution at 25°.

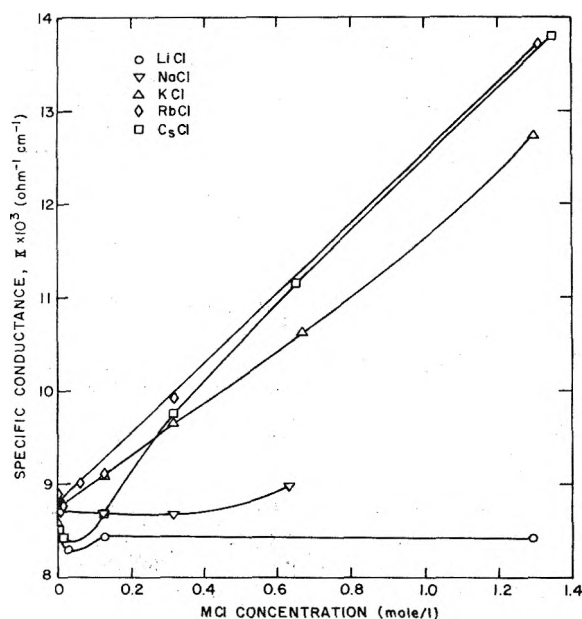
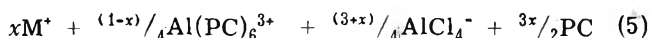
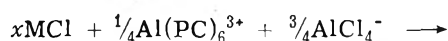


Figure 2. Specific conductance of the alkali metal chlorides in AlCl_3 (1 *m*)-PC solution at 35°.

with the value $6.96 \times 10^{-3} \text{ ohm}^{-1} \text{ cm}^{-1}$ reported by Keller³ for 1 *M* AlCl_3 solution in PC at 25°. Extrapolation of the conductance curve of Breivogel and Eisenberg¹⁵ results in a somewhat smaller value of approximately $6 \times 10^{-3} \text{ ohm}^{-1} \text{ cm}^{-1}$. Chilton and Cook¹⁶ report a specific conductance of approximately 7.1×10^{-3} for AlCl_3 (1 *M*) at 25°. The specific conductance of LiAlCl_4 (1 *m*) at 25° was measured in the present work as $6.7 \times 10^{-3} \text{ ohm}^{-1} \text{ cm}^{-1}$. The molarity of this solution is 1.26 *M*. Keller, *et al.*,³ reports a value of 6.58×10^{-3} for saturated solution of LiCl in AlCl_3 (1 *M*) in PC at 25°, in good agreement with the present results. In addition, Keller's data confirm the present observation that the addition of LiCl to AlCl_3 (1 *m*) solution reduces the conductance of the resultant solution. Eisenberg, *et al.*'s, conductance measurements of LiAlCl_4 in PC¹⁵ were

restricted to concentrations of up to 0.6 *M*. However, crude extrapolation of their data to 1 *M* gives a value of approximately $7 \times 10^{-3} \text{ ohm}^{-1} \text{ cm}^{-1}$ at 25°. The temperature coefficient of the specific conductance of AlCl_3 (1 *m*) solution in PC can be calculated from the data at 25 and 35°. Our value of $0.15 \times 10^{-3} \text{ ohm}^{-1} \text{ cm}^{-1} \text{ }^\circ\text{K}^{-1}$ is in reasonable agreement with $d\kappa/dT = 0.17 \times 10^{-3}$, calculated after Keller, *et al.*³ The temperature coefficient of the specific conductance of LiAlCl_4 (1 *m*) in PC is $0.17 \times 10^{-3} \text{ ohm}^{-1} \text{ cm}^{-1} \text{ }^\circ\text{K}^{-1}$, again in good agreement with a value of 0.18×10^{-3} , after Keller, *et al.*³ In general, good agreement was found between the present results of AlCl_3 and LiAlCl_4 solutions in PC, and the corresponding results found in the literature. This agreement also should lend credibility to the data obtained for the rest of the alkali metal chloride- AlCl_3 system. Unfortunately, the latter results cannot be compared to earlier results obtained elsewhere; previous work was restricted to the LiCl - AlCl_3 system.

The addition of *x* moles of alkali metal chloride, MCl , to AlCl_3 (1 *m*) solution in PC is accompanied by the following reaction



The number of charge carriers increases by 0.5 *x* mol, and therefore, purely on this basis, the specific conductance should increase. The equivalent conductances of all the species are not known. The equivalent conductance of LiAlCl_4 in PC is reported as $34.5 \text{ ohm}^{-1} \text{ cm}^2 \text{ equiv}^{-1}$.¹⁵ The equivalent ionic conductance of Li^+ in PC is $7.30 \text{ ohm}^{-1} \text{ cm}^2 \text{ equiv}^{-1}$. Hence the estimated equivalent conductance of AlCl_4^- is relatively quite high: $27.2 \text{ ohm}^{-1} \text{ cm}^2 \text{ equiv}^{-1}$ (see Table I for comparison). The equivalent ionic conductances of the alkali metal ions in PC increases from Li^+ to Cs^+ , despite the fact that the ionic crystal radius of Li^+ is the smallest, and that of Cs^+ the largest. This reversed trend was observed in most aprotic solvents as well as in water, and is caused by the tightly held sheath of solvent molecules attracted by the intense electric field of the small ion. The equivalent ionic conductances of Li^+ , Na^+ , and K^+ in PC are 7.30, 9.40, and 12.0, respectively (see Table I), and it is expected that the equivalent ionic conductances of Rb^+ and Cs^+ are even higher. The solvated radius of ions in nonaqueous solvents is discussed by Della Monica and Senatore.²⁰ The radii of the solvated metal ions increase from Li^+ to Cs^+ in most solvents (methanol, formamide, *N,N*-dimethylformamide, dimethylacetamide, pyridine, acetonitrile, and sulfolane). The same trend was observed by Yao and Bennion²¹ in DMSO. Mukherjee, Boden, and Lindauer⁵ report equivalent conductances for Li^+ and K^+ in PC of 7.30 and 11.97, respectively.

The addition of MCl to AlCl_3 solution in PC results in two effects: addition of M^+ ions, and a conversion of $\text{Al}(\text{PC})_6^{3+}$ to AlCl_4^- ions. On the basis of the discussion so far, both effects tend to increase the conductance, and the increase is larger as we move along the alkali metal series from Li to Cs . The equivalent conductance of $\text{Al}(\text{PC})_6^{3+}$ is not known since extrapolation to infinite dilution of AlCl_3 in PC is tenuous (because of the minimum at low concentrations) and therefore quantitative analysis is not possible.

Viscosities of electrolytic solutions have been used as an indication of the degree of structure within the solvent. In aqueous solutions the effects are generally ascribed to the

ability of the various ions to increase or decrease the structure of water over that of the pure solvent. Small ions, such as lithium, are structure makers, while large simple ions, such as cesium, are structure breakers. This is the reason why the viscosities of aqueous alkali metal solutions decrease as the cations change along the series from Li^+ to Cs^+ . According to this consideration, the effect should not be observed for solvents exhibiting only a small tendency for structuring. However, Criss and Mastroianni²² discuss this aspect, and show that even in structureless solvents, the B_η coefficients in the Jones-Dole equation²³

$$\eta/\eta_0 = 1 + A_\eta C^{1/2} + B_\eta C \quad (6)$$

decrease with an increase in the size of the ion presumably because of structuring of the solvent by the smaller cations. In the present system, the original solution is AlCl_3 (1 *m*)–PC and not pure PC. This solution possesses a large degree of order to begin with. The addition of LiCl to this solution destroys the previous order by converting $\text{Al}(\text{PC})_6^{3+}$ to AlCl_4^- , but the small Li^+ ion is a structure maker, and therefore the viscosity increases. On the other hand, the addition of CsCl , for example, destroys the initial order, but the large Cs^+ ion is a poor order maker, and it is predicted, therefore, that the increase in the viscosity with concentration will be small or even reversed in the case of RbCl and CsCl solutions in AlCl_3 –PC.

Evidence that in PC viscosity varies with the size of the cation can be found in the viscosity measurements of Mukherjee and Boden.⁴ The B_η coefficient decreases in the order $\text{LiClO}_4 > n\text{-Bu}_4\text{NClO}_4 > \text{Et}_4\text{NClO}_4$, in agreement with the size of the solvated cations.

The minimum in the conductance curve for LiCl in AlCl_3 (1 *m*)–PC can be the result of ionic association of LiCl in PC.^{4,24–26} The association constant for LiCl was estimated to be 557 from conductance measurements,⁴ and as 59 from emf measurements.²⁵ The minimum in the conductance curve of CsCl in AlCl_3 (1 *m*)–PC can be the result of a combination of the opposing factors which determine the conductance of the solution.

The minimum in the plot of the equivalent conductance of AlCl_3 in PC was observed by several workers.^{3,15,16} There is no conclusive explanation for this behavior at low concentration. An attempt to explain the minimum on the basis of the water content of the solvent seems questionable because the minimum was observed by three independent laboratories and the water contents were probably dif-

ferent. Moreover, if we assume that the minimum is the result of the water content, we can extrapolate to infinite dilution, neglecting the minimum, and obtain the molar conductance at infinite dilution, $\Lambda_0 = 18 \text{ ohm}^{-1} \text{ cm}^2 \text{ mol}^{-1}$. The equivalent conductance of AlCl_4^- was estimated before at 27.2, and according to this, the equivalent ionic conductance of $\text{Al}(\text{PC})_6^{3+}$ would be

$$\Lambda_{\text{Al}(\text{PC})_6^{3+}}^0 = \frac{4}{3}(18) - 27.2 = -3.2 \text{ ohm}^{-1} \text{ cm}^2 \text{ equiv}^{-1} \quad (7)$$

Thus it seems that the minimum in the equivalent conductance of AlCl_3 is not due to impurities, but is probably a genuine feature associated with multiple ionic equilibria.

Acknowledgment. This work was conducted under the auspices of the U. S. Atomic Energy Commission.

References and Notes

- (1) Address correspondence to this author at the Department of Chemical Engineering and Material Sciences, Wayne State University, Detroit, Mich. 48202.
- (2) (a) R. Fuoss and E. Hirsch, *J. Amer. Chem. Soc.*, **82**, 1013 (1968); (b) Y. Wu and H. Friedman, *ibid.*, **70**, 501, 2020 (1966).
- (3) R. Keller, *et al.*, Final Report, Contract No. NAS 3-8521, Dec 1969.
- (4) L. Mukherjee and D. Boden, *J. Phys. Chem.*, **73**, 3965 (1969).
- (5) L. Mukherjee, D. Boden, and R. Lindauer, *J. Phys. Chem.*, **74**, 1942 (1970).
- (6) J. Jorñé, Ph.D. Thesis, LBL 1111, University of California, Berkeley, Calif., 1972.
- (7) J. Jorñé and C. W. Tobias, *J. Electrochem. Soc.*, submitted for publication.
- (8) J. Jorñé and C. W. Tobias, *J. Electrochem. Soc.*, **121**, 994 (1974).
- (9) R. Jasinski, *Advan. Electrochem. Electrochem. Eng.*, **8**, 253 (1971).
- (10) W. S. Harris, Thesis, UCRL 8381, University of California, 1958.
- (11) R. Fuoss and F. Accascina, "Electrolytic Conductance," Interscience, New York, N.Y., 1959.
- (12) A. Lyall, H. Seiger, and J. Orshich, Technical Report No. AFAPL-TR-68-71, July 1968.
- (13) A. Dey and M. Rao, Final Report, Contract No. DA-44-009-AMC-1534(T), Nov 1967.
- (14) D. Boden, *Proc. Annu. Power Sources Conf.*, **20**, 63 (1966).
- (15) F. Breivogel and M. Eisenberg, *Electrochem. Acta*, **14**, 459 (1969).
- (16) J. E. Chilton and G. M. Cook, Report No. ASD-TDR-62-837, Sept 1962.
- (17) G. W. Jackson and G. E. Blomgren, *J. Electrochem. Soc.*, **116**, 1483 (1969).
- (18) M. Eisenberg, Forth Quarterly Report, Contract No. N00017-68-C-1401, Sept 1968.
- (19) D. R. Cogley and J. N. Butler, *J. Electrochem. Soc.*, **113**, 1074 (1966).
- (20) M. Della Monica and L. Senatore, *J. Phys. Chem.*, **74**, 205 (1970).
- (21) N. P. Yao and D. N. Bennion, *J. Electrochem. Soc.*, **118**, 1097 (1971).
- (22) C. M. Criss and M. J. Mastroianni, *J. Phys. Chem.*, **75**, 2532 (1971).
- (23) G. Jones and M. Dole, *J. Amer. Chem. Soc.*, **51**, 2950 (1929).
- (24) M. Salomon, *J. Phys. Chem.*, **73**, 3299 (1969).
- (25) M. Salomon, *J. Electroanal. Chem.*, **25**, 1 (1970).
- (26) M. Salomon, *J. Electroanal. Chem.*, **26**, 319 (1970).

COMMUNICATIONS TO THE EDITOR

Effect of Surface-Active Materials in Water on Ortho-Positronium Lifetime and Its Connection to the Bubble Model

Sir: In our recent publication¹ it was pointed out that the empirical relationship between surface tension (γ) and the pick-off annihilation rate of ortho-positronium in molecular liquids as discovered by Tao² is valid for binary mixtures of water-methanol and water-dioxane too. It was also shown³ that the bubble model of positronium formation⁴⁻⁷ could account for the $\gamma^{1/2}$ dependence of pick-off annihilation rate found experimentally.

It seemed to be of interest to examine the effect of surface-active materials on the ortho-positronium lifetime measured in water. It can be supposed that such compounds, by decreasing the surface tension of water significantly even at very low concentrations, may increase the ortho-positronium lifetime, provided they are not positronium quenchers. The same molecules, however, cannot be expected to take part in bubble formation around the positronium atom. At least two arguments support this assumption.

The concentration of such molecules is very low and their size is usually very large as compared to the molecules of the bulk material. Therefore their motion is very slow and they have not enough time to establish equilibrium conditions in the environment of the positronium atom. In addition to this, the very size of these molecules may also hinder them in taking part in bubble formation, since the radius of the latter, and consequently its surface too, is very small. In other words it may well be supposed that in such a case the surface tension observed macroscopically has no effect in the bubble formation of positronium, going on in microscopic measures. In water-methanol or water-dioxane systems, however, where the size and concentration of the two components are comparable, both components are capable to take part in bubble formation to an extent corresponding to their concentration.¹

Here we report the results of our positronium lifetime measurements⁸ obtained for aqueous solutions of two surface-active compounds, namely sodium dodecyl sulfate (c

$= 1.5 \times 10^{-2} M$) and Lerolat N300⁹ ($c = 0.6 \text{ g/dm}^3$). The surface tensions of these solutions as measured by the differential capillary method at 20° were 39 and 50 dyn/cm, respectively. Substituting the constants found by us¹ for the water-methanol and water-dioxane systems into Tao's formula,² the lifetimes to be expected are about 2.3 and 2.1 nsec, respectively. Our lifetime measurements, however, did not show any change in comparison with the 1.80-nsec lifetime observed in pure water.¹⁰

These results support the idea that large surface-active molecules cannot take part in bubble formation. This ineffectiveness of surface-active compounds on ortho-positronium lifetime, in our opinion, does not contradict to the bubble model but, on the contrary, it may provide an indirect proof of its validity. We hope that these results will contribute to a better understanding of the phenomenon.

References and Notes

- (1) B. Lévay, A. Vértés, and P. Hautojarvi, *J. Phys. Chem.*, **77**, 2229 (1973).
- (2) S. J. Tao, *J. Chem. Phys.*, **56**, 5499 (1972).
- (3) B. Lévay and A. Vértés, *Radiochem. Radioanal. Lett.*, **14**, 227 (1973).
- (4) R. A. Ferrel, *Phys. Rev.*, **108**, 167 (1957).
- (5) L. O. Roellig in "Positron Annihilation," L. O. Roellig and A. T. Stewart, Ed., Academic Press, New York, N.Y., 1965, p. 127.
- (6) A. P. Buchikhin, V. I. Goldanskii, A. O. Tatur, and V. P. Shantarovich, *Zh. Eksp. Teor. Fiz.*, **60**, 1136 (1971) (*Sov. Phys. - JETP*, **33**, 613 (1971)).
- (7) A. P. Buchikhin, V. I. Goldanskii, and V. P. Shantarovich, *Pisma Zh. Eksp. Teor. Fiz.*, **13**, 624 (1971) (*JETP Lett.*, **13**, 444 (1971)).
- (8) Our lifetime measurements were performed by a conventional fast-slow coincidence system with ORTEC 437A time-to-amplitude converter. The time resolution was FWHM = 520 psec using 1 in. X 1 in. NE 111 plastic scintillators and XP 1021 photomultipliers. The ²²Na source was deposited and sandwiched between two 1 in. (1.2 mg/cm²) Melinex Type 442 (ICI Ltd.) polyester film.
- (9) Lerolat N300 (Bayer AG) is nonylphenol polyglycolic ether with about 30 ethylene oxide groups per molecule, having a molecular weight of about 1500.
- (10) A reviewer of this paper mentioned that they found similar results using either sodium alkylaryl sulfonate or sodium lauryl sulfate as the surface active agent. S. J. Tao, unpublished data.

Department of Physical
Chemistry and Radiology
L. Eötvös University
Puskín u. 11-13.
1088 Budapest, Hungary

Béla Lévay*
Attila Vértés

Received June 20, 1974

PHYSICAL PHENOMENA

spectroscopy,
thermodynamics,
reaction kinetics,
and other areas
of experimental
and theoretical
physical chemistry
are covered
completely in

THE JOURNAL OF PHYSICAL CHEMISTRY

The biweekly JOURNAL OF PHYSICAL CHEMISTRY includes over 25 papers an issue of original research by many of the world's leading physical chemists. Articles, communications, and symposia cover new concepts, techniques, and interpretations. A "must" for those working in the field or interested in it, the JOURNAL OF PHYSICAL CHEMISTRY is essential for keeping current on this fast moving discipline. Complete and mail the coupon now to start your subscription to this important publication.

The Journal of Physical Chemistry American Chemical Society

1155 Sixteenth Street, N.W.
Washington, D.C. 20036

1975

Yes, I would like to receive the JOURNAL OF PHYSICAL CHEMISTRY at the one-year rate checked below:

	U.S.	Canada**	Latin America**	Other Nations**
ACS Member One-Year Rate*	<input type="checkbox"/> \$20.00	<input type="checkbox"/> \$24.50	<input type="checkbox"/> \$24.50	<input type="checkbox"/> \$25.00
Nonmember	<input type="checkbox"/> \$80.00	<input type="checkbox"/> \$84.50	<input type="checkbox"/> \$84.50	<input type="checkbox"/> \$85.00

Bill me ☐ Bill company ☐ Payment enclosed ☐

Air freight rates available on request.

Name _____

Street _____

Home ☐
Business ☐

City _____

State _____

Zip _____

Journal subscriptions start on January '75

*NOTE: Subscriptions at ACS member rates are for personal use only. **Payment must be made in U.S. currency by international money order, UNESCO coupons, U.S. bank draft, or order through your book dealer.

COMPOSITE MATERIALS

edited by LAWRENCE J. BROUTMAN and RICHARD H. KROCK

Although the development of composite materials has been a subject of intensive interest for the last fifteen years, the concept of using two or more elemental materials combined to form the constituent phases of a composite solid has been employed ever since materials were first used. From the earliest uses, the goal of composite materials development has been to achieve combinations of properties which could not be realized by any of the

materials acting alone; thus, a solid could be prepared from constituents which, by themselves, could not satisfy a particular design requirement. Since this involves physical, chemical, electrical, and magnetic properties, the editors of this multi-volume work have assimilated research from investigators in all of these disciplines to provide a complete treatise of all the major aspects of the science and technology of composite materials.

VOLUME 1/INTERFACES IN METAL MATRIX COMPOSITES

edited by ARTHUR G. METCALFE

CONTENTS: ARTHUR G. METCALFE: Introduction and Review. L. J. EBERT and P. KENNARD WRIGHT: Mechanical Aspects of the Interface. ARTHUR G. METCALFE: Physical Chemical Aspects of the Interface. ARTHUR G. METCALFE and MARK J. KLEIN: Effect of the Interface on Longitudinal Tensile Properties. MARK J. KLEIN: Effect of the Filament-Matrix Interface on Off-Axis Tensile Strength. A. LAWLEY and M. J. KOCZAK: Role of the Interface on Elastic-Plastic Composite Behavior. ELLIOT F. OLSTER and RUSSEL C. JONES: Effect of Interface on Fracture. RICHARD E. TRESSLER: Interfaces in Oxide Reinforced Metals. RICHARD W. HERTZBERG: Interfaces in Directionally Solidified Eutectics. W. BONFIELD: The Effect of Impurity on Reinforcement-Matrix Compatibility.

1974, 432 pp., \$29.00/£13.65/Subscription price: \$24.50*

VOLUME 2/MECHANICS OF COMPOSITE MATERIALS

edited by G. P. SENDECKYJ

CONTENTS: N. J. PAGANO: The Role of Effective Moduli in the Elastic Analysis of Composite Laminates. N. J. PAGANO: Exact Moduli of Anisotropic Laminates. G. P. SENDECKYJ: Elastic Behavior of Composites. R. A. SCHAPERY: Viscoelastic Behavior and Analysis of Composite Materials. DONALD F. ADAMS: Elastoplastic Behavior of Composites. MARK J. BERAN: Application of Statistical Theories for the Determination of Thermal, Electrical, and Magnetic Properties of Heterogeneous Materials. ALLEN C. PIPKIN: Finite Deformations of Ideal Fiber-Reinforced Composites. J. D. ACHENBACH: Waves and Vibrations in Directionally Reinforced Composites. EDWARD M. WU: Phenomenological Anisotropic Failure Criterion. I. M. DANIEL: Photoelastic Investigation of Composites.

1974, 528 pp., \$38.50/£18.50/Subscription price: \$32.70*

VOLUME 3/ENGINEERING APPLICATIONS OF COMPOSITES

edited by BRYAN R. NOTON

TENTATIVE CONTENTS: M. MARTIN: Road Transportation. N. J. MAYER: Civil Aircraft. L. J. KORB: Space Vehicles. P. A. PARMLEY: Military Aircraft. B. R. NOTON: Rail Transportation. S. BERGER and B. R. NOTON: Freight Containers. R. DELLA ROCCA and R. J. SCOTT: Ocean Engineering Industry. A. G. H. DIETZ: Building Industry. J. H. MALLINSON: Chemical Plants. C. E. BACON: Appliances and Equipment. P. C. MURPHY and V. E. HEIL: Electrical Industry. S. G. ABRAHAMSON and R. VALLÉE: Nuclear Industry. B. R. NOTON: Potential High-Volume Applications of Advanced Composites.

1974, in preparation

VOLUME 4/METALLIC MATRIX COMPOSITES

edited by KENNETH G. KREIDER

CONTENTS: KENNETH G. KREIDER: Introduction to Metal-Matrix Composites. E. S. WRIGHT and ALBERT P. LEVITT: Laminated-Metal Composites. E. R. THOMPSON and F. D. LEMKEY: Directionally Solidified Eutectic Superalloys. R. L. MEHAN and M. N. NOONE: Nickel Alloys Reinforced with α -Al₂O₃ Filaments. ROBERT A. SIGNORELLI: Wire-Reinforced Superalloys. ARTHUR G. METCALFE: Fiber-Reinforced Titanium Alloys. E. G. KENDALL: Development of Metal-Matrix Composites Reinforced With High-Modulus Graphite Fibers. KENNETH G. KREIDER and K. M. PREWO: Boron-Reinforced Aluminum.

1974, 508 pp., \$32.50/£15.60/Subscription price: \$27.50*

VOLUME 5/FRACTURE AND FATIGUE

edited by LAWRENCE J. BROUTMAN

CONTENTS: F. F. LANGE: Fracture of Brittle Matrix, Particulate Composites. JOSEPH GURLAND: Fracture of Metal-Matrix Particulate Composites. C. C. CHAMIS: Micromechanics Strength Theories. A. S. ARGON: Statistical Aspects of Fracture. EDWARD M. WU: Strength and Fracture of Composites. J. M. LIFSHITZ: Time-Dependent Fracture of Fibrous Composites. M. J. OWEN: Fatigue Damage in Glass-Fiber-Reinforced Plastics. M. J. OWEN: Fatigue of Carbon-Fiber-Reinforced Plastics. J. R. HANCOCK: Fatigue of Metal-Matrix Composites. G. A. COOPER: Micromechanics Aspects of Fracture and Toughness.

1974, 480 pp., \$34.00/£16.30/Subscription price: \$28.90*

VOLUME 6/INTERFACES IN POLYMER MATRIX COMPOSITES

edited by EDWIN P. PLUEDDEMANN

CONTENTS: PORTER W. EDRICKSON and EDWIN P. PLUEDDEMANN: Historical Background of the Interface Studies and Theories. C. C. CHAMIS: Mechanics of Load Transfer at the Interface. WILLARD D. BASCOM: The Surface Chemistry of Moisture-Induced Composite Failure. MALCOM E. SCHRADER: Radioisotope Studies of Coupling Agents at the Interface. M. W. RANNEY, S. E. BERGER, and J. G. MARSDEN: Silane Coupling Agents in Particulate Mineral Filled Composites. EDWIN P. PLUEDDEMANN: Mechanism of Adhesion through Silane Coupling Agents. DANIEL A. SCOLA: High-Modulus Fibers and the Fiber-Resin Interface in Resin Composites.

1974, 314 pp., \$25.00/£12.00/Subscription price: \$21.25*

VOLUME 7/STRUCTURAL DESIGN AND ANALYSIS—PART I

edited by C. C. CHAMIS

1974, 368 pp., \$32.00/£15.35/Subscription price: \$27.20

VOLUME 8/STRUCTURAL DESIGN AND ANALYSIS—PART II

edited by C. C. CHAMIS

1975, in preparation

*FOR FURTHER INFORMATION, PLEASE CONTACT THE PUBLISHER.

Prices subject to change without notice.

ACADEMIC PRESS, INC.

A Subsidiary of Harcourt Brace Jovanovich, Publishers

111 FIFTH AVENUE, NEW YORK, N.Y. 10003

24-28 OVAL ROAD, LONDON NW1 7DX